



*Development and Analysis of New Ceramic Materials for Electrodeposition*

BIGHARAZ, Masoud

Available from the Sheffield Hallam University Research Archive (SHURA) at:

<http://shura.shu.ac.uk/30520/>

## A Sheffield Hallam University thesis

This thesis is protected by copyright which belongs to the author.

The content must not be changed in any way or sold commercially in any format or medium without the formal permission of the author.

When referring to this work, full bibliographic details including the author, title, awarding institution and date of the thesis must be given.

Please visit <http://shura.shu.ac.uk/30520/> and <http://shura.shu.ac.uk/information.html> for further details about copyright and re-use permissions.

# **Development and Analysis of New Ceramic Materials for Electroadhesion**

**Masoud Bigharaz**

A thesis submitted in partial fulfilment of the requirements of  
Sheffield Hallam University  
for the degree of Doctor of Philosophy

**December 2021**

# *Declaration*

I hereby declare that :

1. I have not been enrolled for another award of the University, or other academic or professional organisation, whilst undertaking my research degree.
2. None of the material contained in the thesis has been used in any other submission for an academic award.
3. I am aware of and understand the University's policy on plagiarism and certify that this thesis is my own work. The use of all published or other sources of material consulted have been properly and fully acknowledged.
4. The work undertaken towards the thesis has been conducted in accordance with the SHU Principles of Integrity in Research and the SHU Research Ethics Policy.
5. The word count of the thesis is 35,347.

Name	Masoud Bigharaz
Award	PhD
Date of Submission	16/12/2021
Faculty	STA
Direct of Study	Prof Paul A Bingham

# Abstract

Fabricating a gripper for industrial robot arms with the capability of handling a variety of objects with different mechanical and material properties is becoming more demanding and electroadhesion (EA) is one potential solution that has proved to be efficient in handling objects with dimensions ranging between micrometres to centimetres.

This study has aimed to develop methods of fabricating EA devices, mostly focusing on fabricating new electroceramic-UV polymer composites to improve the electrical properties of dielectric layers within EA devices and thereby enhancing EA forces between the gripper and the substrate (an object being handled). Results show that using electroceramic materials can improve EA forces obtained by EA devices coated with composites made from UV-cured polymers and electroceramic particles as a result of increasing the relative permittivity of the coating layer. The UV-curable coating was chosen as it is a fast, room-temperature coating technology that enables avoidance of oxidation of the electrodes of EA devices during the coating process.

Numerical simulations were used to find optimal designs for EA devices. In this study, ANSYS MAXWELL was used for simulations which have some advantages over similar software that have previously been used for this purpose, such as using an automotive adapting meshing technique and the capability of considering convergence criteria in simulations. Numerical simulations were carried out to find optimal shapes of electrodes and experimental results were consistent with the modelling results.

Analytical solutions and their limitations for electroadhesion problems were developed. It was also concluded that there is no clear, simple relationship between EA force and the total capacitance of the system. The application of a high voltage dielectric oil as a dielectric layer was tested and showed to be one solution to tackle instability in the performance of EA devices.



# ***List of Contents***

<b><i>Declaration.....</i></b>	<b><i>i</i></b>
<b><i>Abstract.....</i></b>	<b><i>ii</i></b>
<b><i>List of Figures.....</i></b>	<b><i>ix</i></b>
<b><i>List of Tables.....</i></b>	<b><i>xvii</i></b>
<b><i>List of Abbreviations.....</i></b>	<b><i>xx</i></b>
<b><i>Nomenclature.....</i></b>	<b><i>xxii</i></b>
<b><i>Acknowledgements .....</i></b>	<b><i>xxiii</i></b>
<b><i>Dedication .....</i></b>	<b><i>xxiv</i></b>
<b><i>Chapter 1    Introduction.....</i></b>	<b><i>1</i></b>
1.1    Background and purpose of the study.....	1
1.2    Aims and Objectives .....	2
1.3    Layout of the thesis .....	3
<b><i>Chapter 2    Electroadhesion: Principles and Literature Review .....</i></b>	<b><i>5</i></b>
2.1    Introduction .....	5
2.1.1    Electroadhesion Applications .....	6
2.1.2    Components of Electroadhesion Systems .....	10
2.2    Theory .....	11
2.2.1    Electroadhesive Forces on Conductive Substrate Materials .....	11
2.2.2    Electroadhesive Forces on Non-Conductive Materials .....	14
2.2.3    Parameters Influencing Electroadhesion.....	26
2.3    History of Electroadhesion Research .....	27
2.3.1    Empirical relation for EA force .....	27

2.3.2	Effect of Electrode Thickness on EA Force Generation .....	27
2.3.3	Effect of air layer thickness and electrical properties of dielectric layer and substrate on EA force .....	28
2.3.4	Optimal electrode width and spacing for uni and bi-layer EA device .....	30
2.3.5	Effect of electrodes pattern on obtainable EA force .....	32
2.3.6	Effect of Surface texture on obtainable EA force .....	33
2.3.7	Instability of EA devices performance .....	34
<b>Chapter 3</b>	<b><i>Dielectric materials</i></b> .....	<b>39</b>
3.1	Dielectric definition .....	39
3.2	Classification of Dielectric Materials .....	39
3.3	Dielectric Properties .....	39
3.4	Classification of dielectric materials based on relative permittivities and applications 40	
3.4.1	Low relative permittivity materials for interlayer dielectrics .....	40
3.4.2	Low relative permittivity glasses and glass-ceramics for electronic packaging applications .....	40
3.4.3	Ceramic dielectrics .....	41
3.5	Relative permittivity of Polymer-Ceramic composites .....	54
3.6	Liquid dielectrics .....	55
3.7	Gaseous dielectrics .....	56
<b>Chapter 4</b>	<b><i>UV-curable polymer technology</i></b> .....	<b>58</b>
4.1	UV curing .....	58
4.2	Free radical polymerization reaction sequence .....	59
4.3	UV curing ink components .....	60
4.3.1	Monomers .....	60
4.3.2	Oligomers .....	65
4.3.3	Photoinitiators (PIs) .....	66
4.4	The effect of pigments on the UV curing process .....	71
4.4.1	Dispersing agent .....	72
4.4.2	UV and Electron beam exposure devices .....	73
<b>Chapter 5</b>	<b><i>Synthesis of ceramic dielectric materials and UV-electroceramic inks</i></b> .....	<b>78</b>
5.1	Synthesis of electroceramics .....	78
5.2	Solid state reactions .....	78

5.3	Testing and Analysing Techniques and Instruments.....	79
5.3.1	X-Ray diffraction analysis .....	79
5.3.2	Raman spectroscopy analysis .....	80
5.3.3	Scanning electron microscopy.....	80
5.3.4	Electrical property measurement .....	80
5.4	Preparation of BaTiO <sub>3</sub> .....	80
5.5	Dielectric properties measurement.....	85
5.6	Preparation of Ba <sub>0.65</sub> Sr <sub>0.35</sub> TiO <sub>3</sub> .....	85
5.7	Preparation of CaCu <sub>3</sub> Ti <sub>4</sub> O <sub>12</sub> .....	88
5.8	Relative permittivity measurement of CCTO.....	89
5.9	UV curing electroceramic pigmented dielectric preparation .....	89
5.10	Viscosity measurement .....	91
5.11	SEM image .....	92
5.11.1	Sample preparation for SEM analysis .....	92
5.12	Dielectric measurement .....	95
<b>Chapter 6 EA fabrication and testing procedure.....</b>		<b>96</b>
6.1	EA device history and fabrication methods .....	96
6.1.1	Photo-masking process and etching technique .....	96
6.1.2	Conductive inkjet printing .....	97
6.2	Dielectric layer of EA devices .....	98
6.3	Uni-layer and Bi layer electrodes .....	98
6.4	EA device preparation .....	100
6.4.1	EA devices with bare electrodes .....	100
6.4.2	Rigid and Flexible EA devices coated with prefabricated UV- TiO <sub>2</sub> dielectric layer	102
6.4.3	Rigid EA device coated with fabricated UV (without pigment) and UV- electroceramic dielectric layer (BT and CCTO) .....	102
6.4.4	Rigid EA device with high voltage oil dielectric layer .....	106
6.5	History of EA force measurement .....	106
6.6	The experimental setup and procedure of tests .....	107
6.6.1	Repeatability of the instrument.....	108
6.6.2	Denso Robot speed and its effect on data recorded by the force sensor .....	110
6.6.3	Applied voltage measurement before tests .....	110

6.6.4	Testing EA device without charge .....	111
6.6.5	Filtering signal recorded by the sensor .....	111
6.7	Test procedure.....	112
<b>Chapter 7 Numerical Analysis.....</b>		<b>113</b>
7.1	Introduction .....	113
7.1.1	Finite element method .....	113
7.1.2	FEM procedure for high voltage field problems .....	113
7.1.3	Numerical Assumptions .....	115
7.2	Hardware specifications for simulations .....	116
7.3	Simulation procedure in ANSYS Maxwell.....	116
7.4	Simulation procedure in ANSYS MAXWELL .....	118
7.5	Maxwell stress distribution and electroadhesive force calculation in ANSYS MAXWELL	119
7.6	Maxwell stress calculation procedure in ANSYS MAXWELL .....	121
7.7	Parametric simulations .....	122
7.7.1	The relationship between EA force and applied voltage .....	122
7.7.2	The relationship between EA force and relative permittivity of the dielectric layer	123
7.7.3	Parametric simulation to find optimal value of electrodes width and spacing .....	124
7.7.4	Optimizing EA device design with respect to dielectric layer thickness .....	128
7.8	Shape optimization .....	129
7.9	Comparison of obtainable EA force of bi-layer and uni layer EA devices .....	134
7.9.1	Bi-Layer EA devices simulation .....	134
7.9.2	Uni-Layer EA device simulation .....	140
7.9.3	Comparison of obtainable EA force of bi-layer and uni-layer EA devices .....	140
<b>Chapter 8 Results and conclusions.....</b>		<b>141</b>
8.1	Analytical Solution of an interdigitated EA device .....	141
8.1.1	Boundary conditions of the EA problem .....	142
8.1.2	Analytical Solution for constant relative permittivity of system .....	144
8.2	Analytical solution of force obtained by EA device with concentric circles electrode pattern.....	148
8.3	EA force and Total capacitance of the system.....	149
8.4	Experimental Results .....	151

8.4.1	Bare Electrodes.....	151
8.4.2	Considerations for testing EA devices with bare electrodes .....	152
8.4.3	Typical receded force obtained by rigid EA devices .....	152
8.4.4	Relationship between EA force and distance between EA device and substrate ...	153
8.4.5	Effect of spacing between electrodes on obtained EA force .....	154
8.4.6	Effect of voltage on EA force obtained by rigid devices with bare electrodes .....	155
8.4.7	Effect of electrodes pattern on obtainable EA force .....	156
8.4.8	Pros and cons of bare electrodes EA devices:.....	157
8.5	Flexible EA devices .....	157
8.5.1	Typical recorded force obtained by flexible EA devices .....	157
8.5.2	Reproducibility of EA force obtained by flexible EA devices .....	158
8.6	EA device with liquid dielectric .....	159
8.6.1	Consideration in fabricating EA device the with high voltage dielectric oil .....	159
8.6.2	Test procedure of EA devices with liquid dielectric .....	159
8.6.3	Stability in performance of EA devices with liquid dielectric .....	160
8.7	EA devices with UV polymer and electroceramic –UV polymer composites dielectric layer	161
8.7.1	Forces obtained by EA devices with polymer and composites dielectric layer .....	161
8.7.2	Uncertainty in Forces obtained by EA devices with polymer and composites dielectric layer.....	162
8.8	Discussions .....	163
8.8.1	Analytical Solution .....	163
8.8.2	Numerical Analysis.....	164
8.8.3	Relationship between EA force and total capacitance of the system.....	168
8.8.4	Experimental Results .....	169
<b>Chapter 9 Conclusions and further research .....</b>		<b>172</b>
9.1	Conclusion .....	172
9.1.1	Physics of Electroadhesion .....	172
9.1.2	Material development and coating procedure .....	172
9.1.3	Experimental apparatus preparation and test procedure .....	173
9.1.4	Numerical analysis .....	173
9.1.5	Experimental results .....	173

9.2 Further research .....	174
<i>References</i> .....	175
<i>Appendix A</i> .....	184
<i>Appendix B</i> .....	191
<i>Appendix C</i> .....	207

## *List of Figures*

Figure 1-1. Optical image of 3D printed microelectronics components (Wu et al., 2015).....	2
Figure 1-2. Inkjet printed a) single and b) multi-layer capacitors (Correia et al., 2018).....	2
Figure 2-1. Potential Space application: “Spacecrawler” micro inspection robot (Microrobot Inspectors, 2009).....	10
Figure 2-2. Simplified schematic of an electroadhesive device .....	10
Figure 2-3. Schematic of electroadhesive force generation and equivalent circuit (Monkman, 2003; Guo et al., 2016 a).....	11
Figure 2-4. Coulomb and J-R force versus volume resistivity of dielectric (Qin & McTeer, 2007).....	12
Figure 2-5. Schematic showing contact and non-contact area between dielectric and substrate .....	13
Figure 2-6. Application of Gauss’ Law to a differential volume.....	15
Figure 2-7. Polarization within a dielectric medium .....	16
Figure 2-8. Polarization time dependency of an electroadhesive pad (Bamber, Guo & Singh, 2017) .....	17
Figure 2-9. Electric potential profile during charging process in the centre line of interdigitated electroadhesive pad (Bamber et al., 2017).....	18
Figure 2-10. Definition of displacement and charge location for dipole (Melcher, 1981) ....	18
Figure 2-11. Divergence theorem in the region of interest .....	19
Figure 2-12. Simplification of contact interface for electroadhesion system .....	20
Figure 2-13. Electroadhesive force calculation in 2D .....	21
Figure 2-14. Electroadhesive force calculation in 3D .....	22
Figure 2-15. Definition of boundary conditions in Cartesian coordinates .....	23
Figure 2-16. Schwarz-Christoffel transformation .....	24

Figure 2-17. a) Coplanar capacitance domain for theoretical calculation using total capacity of system (Nassr et al., 2008) and b) mapped domain.....	25
Figure 2-18. Independency of electroadhesive force to electrode's thickness (Guo et al., 2016 a).....	28
Figure 2-19. Thickness of air layer effect on electroadhesive force (Mao et al., 2016).....	28
Figure 2-20. Effect of relative permittivity of dielectric layer on EA force (Guo et al., 2016 a).....	29
Figure 2-21. Effect of relative permittivity of dielectric layer on EA force (Akherat et al., 2019).....	29
Figure 2-22. Optimal relative permittivity of a dielectric layer for bi-layer EA devices (Akherat et al., 2019).....	30
Figure 2-23. Effect of electrodes spacing on EA force (Guo et al., 2016 a).....	31
Figure 2-24. Optimal electrode's width for uni-layer EA devices (Guo et al., 2016 a).....	31
Figure 2-25. Optimal electrode widths for bi-layer EA devices (Dadkhah et al., 2019).....	32
Figure 2-26. Optimization of electrodes pattern considering average intensity of electric field of a system (Ruffato et al., 2014).....	32
Figure 2-27. Optimization of electrodes pattern considering total capacitance of a system (Guo et al., 2016 b).....	33
Figure 2-28. Relationship between EA force and surface texture (Guo et al., 2016 c).....	33
Figure 2-29. Instability of EA devices performance (Guo et al., 2016 a).....	34
Figure 3-1. Grain size dependency of BaTiO <sub>3</sub> relative permittivity (Kinoshita & Yamaji, 1976).....	43
Figure 3-2. Grain size dependency of BaTiO <sub>3</sub> relative permittivity (Huan, Wang & Fang, 2014).....	44
Figure 3-3. Relative permittivity of BT doped with different concentration (varies between 0 and 1) of strontium (Tagantsev et al., 2003).....	45
Figure 3-4. Relative permittivity of lanthanum doped barium titanate versus temperature (Ganguly et al., 2013).....	46
Figure 3-5. Relative permittivity of doped BT with different concentration of lead (Vold et al., 2001).....	47
Figure 3-6. Dielectric properties of zirconium doped barium titanate with sintering temperature between 1325°C and 1400°C(Sun, Li & Zheng, 2015).....	47
Figure 3-7. Relative permittivity of tin doped barium titanate versus temperature (Wei & Yao, 2007).....	48



Figure 3-8. Relative permittivity of rare earth doped Barium titanate versus temperature (Li, and Yao, 2012).....	49
Figure 3-9. Relative permittivity of BT doped with different La concentration versus temperature (Paunovic et al., 2016).....	50
Figure 3-10. Relative permittivity of BT doped with 1% of different rare earth oxide (Qi et al., 2012).....	50
Figure 3-11. Relative permittivity temperature stability of $\text{Na}_{1/3}\text{Ca}_{1/3}\text{Bi}_{1/3}\text{Cu}_3\text{Ti}_4\text{O}_{12}$ (Kum-onsa ,Thongbai & Putasaeng, 2015) .....	52
Figure 3-12. Comparison of theoretical and experimental of relative permittivity of PTEF/ $\text{CaTiO}_3$ (Yunxiang et al., 2011).....	55
Figure 3-13. Ceramic particle size effect on relative permittivity of UV polymer /CCTO composite (Choi et al., 2016) .....	55
Figure 3-14. Comparison of actual critical voltage and critical voltage yielded by Paschen's law in air (Gallot-Lavallée, 2013).....	57
Figure 4-1. Market growth of UV ink and coating compositions (Marketandmarket website) .....	59
Figure 4-2. Reaction sequence of free radical polymerisation (Heath and Cooper ,2013) .....	60
Figure 4-3. Chemical structure of IBOA.....	62
Figure 4-4. Chemical structure of TPGDA.....	63
Figure 4-5. Chemical structure of HDDA .....	64
Figure 4-6. Chemical structure of TMPTA .....	65
Figure 4-7. Chemical reactions of PI type I.....	67
Figure 4-8. Chemical structure of TPO .....	68
Figure 4-9. Absorption spectrum of TPO (IGM's material data sheets).....	68
Figure 4-10. Chemical structure of TPO-L.....	69
Figure 4-11. Absorption spectrum of TPO-L (IGM's material data sheets).....	69
Figure 4-12. Chemical structure of 1173.....	70
Figure 4-13. Absorption spectrum of 1173 (IGM's material data sheets).....	70
Figure 4-14. Chemical structure of ITX and reactions in present of UV light .....	71
Figure 4-15. Absorption spectrum of ITX (IGM's material data sheets).....	71
Figure 4-16. High shear mixer used for dispersing pigments (Dispermat LC75).....	73
Figure 4-17. Industrial bead mills used for dispersing pigments.....	73
Figure 4-18. He standard UV lamp, 15 % UV-C 8 % UV-B7 % UV-A 5 % UV-VIS 15 % VIS (Green, 2010).....	74

Figure 4-19. Fe doped UV lamp, 7 % UV-C 5 % UV-B 17 % UV-A 6 % UV-VIS 16 % VIS (Green, 2010).....	75
Figure 4-20. Gallium doped UV lamp, 7 % UV-C 8 % UV-B 5 % UV-A 17 % UV-VIS 24 % VIS (Green, 2010).....	75
Figure 4-21. Comparison of LED's and standard UV lamp spectrums (Photoelcuring website) .....	76
Figure 4-22. Phoseon's FireJet FJ200 for the K600i ink jet printer (12W/cm <sup>2</sup> @ 365nm and 8W/cm <sup>2</sup> @ 385/395/405nm, Phoseon website).....	76
Figure 4-23. EB Lab machine from 80 to 200 keV, format A4 up to 30m/min (Sartomer website) .....	77
Figure 5-1. Flowchart of conventional solid-state reaction.....	79
Figure 5-2. X-Ray diffractograms of BT powder calcined at different temperature.....	81
Figure 5-3. Room temperature X-Ray diffraction pattern of sintered BT at 1200°C.....	82
Figure 5-4. Peak splitting of tetragonal BT at 45 °2θ.....	82
Figure 5-5. Peak spiriting of tetragonal BT at 66 °2θ.....	83
Figure 5-6. Comparison of a) cubic and b) tetragonal structure of BaTiO <sub>3</sub> .....	83
Figure 5-7. Raman spectrum of barium titanate at room temperature .....	84
Figure 5-8. SEM image of prepared BaTiO <sub>3</sub> .....	84
Figure 5-9. Room temperature relative permittivity of BT versus frequency .....	85
Figure 5-10. Room temperature X-ray diffraction pattern of BST.....	86
Figure 5-11. Peak merging at 45°2θ and 66°2θ due to cubic structure of BST.....	86
Figure 5-12. Room temperature Raman spectroscopy of BST.....	87
Figure 5-13. Room temperature relative permittivity of BST versus frequency .....	87
Figure 5-14. Structure of the cubic pseudo-perovskite (Im3) CaCu <sub>3</sub> Ti <sub>4</sub> O <sub>12</sub> .....	88
Figure 5-15. Room temperature X-ray diffraction pattern of CCTO.....	88
Figure 5-16. A CCTO sample prepared for relative permittivity measurement .....	89
Figure 5-17. Room temperature relative permittivity of CCTO versus frequency .....	89
Figure 5-18. Dispermat LC75 E high shear mixer used for dispersing electroceramic particles .....	90
Figure 5-19. Viscosity of mass product screen printing inks and formulated inks versus shear rate.....	92
Figure 5-20. Modified XRF cup to prepare cured ink sample.....	93
Figure 5-21. Cured UV ink sample by electron beam radiated from XRF.....	93
Figure 5-22. Cylindrical sample of cured ink (mixture of BaTiO <sub>3</sub> - UV polymers).....	93

Figure 5-23. SEM image of cured ink (BT-UV polymer) with scale of (a) 50 $\mu\text{m}$ , (b) 20 $\mu\text{m}$ and (c) 4 $\mu\text{m}$ .....	94
Figure 5-24. Comparison of room temperature relative permittivity of cured UV polymer and BT-UV composite versus frequency.....	95
Figure 6-1. Fabricated EA device using conductive ink jet printer (Lessing et al., 2014).....	98
Figure 6-2. Schematic of Uni layer EA devices.....	99
Figure 6-3. Schematic of bi-layer EA devices.....	99
Figure 6-4. Fabricated bi-layer EA devices (Dadkhah et al., 2019) .....	99
Figure 6-5. Printing photo-mask on rigid copper clads using the UV flatbed printer .....	100
Figure 6-6. Printing photo-mask on flexible copper-clad laminate using the UV flatbed printer .....	100
Figure 6-7 a) rigid copper clad after etching and b) rigid copper clad after washing with acetone.....	101
Figure 6-8. Electrode patterns .....	101
Figure 6-9. Flexible EA device with UV-TiO <sub>2</sub> dielectric layer.....	102
Figure 6-10. Fe doped medium pressure mercury UV lamp.....	103
Figure 6-11. Prepared silk screen for UV-electroceramic coating .....	103
Figure 6-12. Schematic of coating layer applied by screen printing technique .....	104
Figure 6-13. Interdigitated EA device coated by formulated inks (with and without pigment).....	105
Figure 6-14. An EA device with high voltage oil as dielectric layer.....	106
Figure 6-15. Schematic of direct method to measure normal force obtained by EA devices.....	106
Figure 6-16. Schematic of indirect method to measure shear force obtained by EA devices.....	107
Figure 6-17. Experimental apparatus used to measure a) normal force (Guo et al., 2016 a) and b) shear force (Dadkhah et al., 2018) obtained by EA devices .....	107
Figure 6-18. Experimental configuration including :(1) Denso robot, (2) DC power suppliers, (3) usb DAQ device, (4) Laptop (5) Substrate holder (6) Robot main controller, (7) interface power supply box of the sensor, (8) EA device, (9) Force sensor, (10) Interface between the robot end effector and the force sensor, (11) Pad holder (12) Substrate.....	109
Figure 6-19. Effect of Denso robot speed on data recorded by the force sensor .....	110
Figure 6-20. High DC voltage probe test TT-HVP40 and multimeter Agilent 34405A .....	111
Figure 6-21. Signal recorded by the force sensor a) before filtering and b) after filtering ...	112
Figure 7-1. Subdividing region of interest into finite elements.....	114

Figure 7-2. Linear interpolation of electric potential in an element .....	114
Figure 7-3. Definition of boundary conditions in Cartesian coordinates .....	117
Figure 7-4. (a) Creating complex geometries in Space Claim, (b) Linking geometries created in Space Claim to ANSYS Maxwell.....	119
Figure 7-5. Pre-processing and processing steps of FEA in ANSYS Maxwell .....	120
Figure 7-6. ANSYS MAXWELL field calculator.....	121
Figure 7-7. 2D modelled EA pressure of interdigitated pattern with electrode width and spacing of 0.5 mm.....	122
Figure 7-8. 2D modelled EA pressure distribution of interdigitated pattern with electrode width of 0.4 mm and spacing of 0.2 mm.....	123
Figure 7-9. The relationship between EA force and relative permittivity of dielectric layer	124
Figure 7-10. Schematic of simulated 2D interdigitated EA devices and its effective area...	125
Figure 7-11. 2D Numerical investigation of the relationship between electrode parameters (width and spacing) and Maxwell stress distribution on nonconductive substrates.....	126
Figure 7-12. 2D Numerical investigation of the relationship between optimum electrode width and spacing to maximize obtainable EA force (N) on non-conductive substrates .....	127
Figure 7-13. 2D Numerical investigation of EA force generated at various electrodes width and spacing on non-conductive substrates.....	127
Figure 7-14. Optimal electrodes width versus dielectric thickness obtained by 2D numerical simulations of interdigitated EA device .....	129
Figure 7-15. Energy error and delta energy b) mesh independency of interdigitated EA pad simulation .....	133
Figure 7-16. Contour of a) electric field, b) pressure obtained by Solid top and interdigitated bottom EA device (1).....	135
Figure 7-17. Contour of a) electric field, b) Pressure obtained by Solid top and interdigitated bottom EA device (2).....	136
Figure 7-18. Contour of a) electric field, b) Pressure obtained by solid top and interdigitated bottom EA device (3).....	136
Figure 7-19. Contour of a) electric field, b) pressure obtained by solid top and concentric circles EA device.....	137
Figure 7-20. Contour of a) electric field, b) pressure obtained by two partially overlapped interdigitated EA device .....	138
Figure 7-21. Contour of a) electric field, b) pressure obtained by two interdigitated electrodes with offset EA device .....	139

Figure 7-22. Contour of a) electric field, b) pressure obtained by two orthogonal interdigitated EA devices.....	139
Figure 7-23. Contour of a) electric field, b) Pressure obtained by uni-layer interdigitated EA device .....	140
Figure 8-1. periodic part of voltage and electric field of 2D interdigitated EA device .....	141
Figure 8-2. 2D Maxwell stress distribution of an EA device with electrode's with of 0.2mm and spacing of 0.4mm obtained by numerical simulation.....	142
Figure 8-3. Fourier transform of periodic part of Maxwell stress of the same EA device ...	142
Figure 8-4. Dirichlet boundary condition at $z=0$ of a interdigitated EA device.....	143
Figure 8-5. .Neumann boundary conditions at $x=\pm(W+S)/2$ of a interdigitated EA device .	143
Figure 8-6. Interfacial boundary conditions .....	144
Figure 8-7. Contour of $\delta$ at $z=0$ for a range of $W$ and $S$ .....	148
Figure 8-8. Simplified geometry of concentric EA device for analitical solution.....	149
Figure 8-9. 2D Modelled potential distribution of coplanar capacitance with 16 electrodes	150
Figure 8-10. Schematic of coplanar capacitance showing simulated area and parameters...	151
Figure 8-11. Relationship between capacitance of coplanar capacitor and electrode width and spacing.....	151
Figure 8-12. A Typical EA force recorded by the sensor during tests of EA devices with bare electrodes.....	152
Figure 8-13. Compression between recorded EA force and filtered one .....	153
Figure 8-14. EA force obtained by interdigitated EA device ( $W$ & $S=5$ ) with bare electrodes versus distance .....	154
Figure 8-15. Comparison of generated EA forces of two interdigitated devices ( $W$ & $S=5$ mm and $W$ & $S=10$ mm) with bare electrodes.....	155
Figure 8-16. Obtained EA force of interdigitated device ( $W$ & $S=5$ mm) with bare electrodes versus applied voltage.....	156
Figure 8-17. Comparison of generated EA forces by sine wave, half hexagonal, interdigitated and concentric circles devices ( $W$ & $S=5$ mm) with bare electrodes .....	157
Figure 8-18. Variation of EA force obtained by a flexible and interdigitated device ( $W$ & $S=5$ ) with bare electrodes during test.....	158
Figure 8-19. Uncertainty in recorded EA force obtained by flexible and interdigitated EA devices ( $W$ & $S=5$ mm) with bare electrodes .....	159
Figure 8-20. A Typical EA force obtained by an interdigitated device (in this case, $W$ & $S=5$ ) with liquid dielectric during test.....	160

Figure 8-21. Comparison of stability in performance of interdigitated EA devices (W & S=5mm) with liquid and rigid dielectric layer.....	161
Figure 8-22. Comparison of EA forces obtained by rigid interdigitated EA devices (W& S=5mm) with different dielectric layer.....	162
Figure 8-23. Comparison of EA forces obtained by rigid interdigitated EA devices (W& S=5mm) with different dielectric layer.....	163
Figure 8-24 EA force versus relative permittivity of dielectric layer of the modelled interdigitated EA device .....	165
Figure 8-25 Pressure distribution of EA devices: (a) Parallel electrodes 45°, (b) offset electrodes, (c) Solid top electrode with bottom orthogonal electrodes, (d) Solid top electrode with concentric circles bottom electrode obtained by 3D simulations (Dadkhah et al. (2018)).....	167
Figure 8-26. Sheer pressure obtained by uni-layer and bi-layer EA devices of substrates with various materials (Dadkhah et al. 2018).....	168
Figure 8-27 Electric potential distribution near two adjacent electrodes with different polarity (Guo et al., 2016 a).....	169
Figure 8-28. Paschen curve of Air at 20°C (Kuffel and Kuffel, 2000).....	170
Figure 8-29. Comparison of obtained EA force of interdigitated EA devices (liquid dielectric layer) with W=3cm, S=1cm and W=5cm, S=5cm, applied voltage 3kV.....	171

## *List of Tables*

Table 2-1. Comparison of astrictive grippers (Monkman, 2003) .....	6
Table 2-2. The history of advances in fabricating EA devices.....	7
Table 2-3 Resistivity of various materials (D physics).....	12
Table 2-4. Laplace's equation in Cartesian and Cylindrical coordinates and solution functions .....	23
Table 2-5. Summary of electroadhesion investigations and optimizations .....	35
Table 3-1. Relative permittivity of low dielectric materials for interlayer dielectrics (Nalwa, 1999).....	40
Table 3-2. Relative permittivity of low relative permittivity glasses and glass-ceramic (Nalwa, 1999) .....	41
Table 3-3. Relative permittivity of low relative permittivity ceramic dielectrics (Nalwa, 1999) .....	42
Table 3-4. Effect of different dopant materials on Curie temperature of BT (Gupta & Gupta, 2015) .....	45
Table 3-5. Room temperature relative permittivity of co-doped BT with different oxides ....	51
Table 3-6. List of relative permittivity of doped CCTO reported (Ahmadipour et al., 2016). 53	
Table 3-7. List of some liquid dielectric and their applications (Mahanta and Laskar, 2017).56	
Table 3-8. comparison of the physical and environmental properties of common dielectric gases (Xiao et al., 2018).....	57
Table 4-1. Chemical structure of typical UV polymers.....	60
Table 4-2. Effect of typical monomers on lowering viscosity of the oligomer (DYMAX's material data sheets) .....	61
Table 4-3. Effect of typical monomers on mechanical properties of cured films (DYMAX's material data sheets) .....	62

Table 4-4. Physical properties of IBOA (Allnex and IGM's material data sheets).....	63
Table 4-5. Physical properties of TPGDA (Allnex and IGM's material data sheets).....	63
Table 4-6. Physical properties of HDDA (Allnex and IGM's material data sheets).....	64
Table 4-7. Physical properties of TMPTA (Allnex and IGM's material data sheets).....	65
Table 4-8. Typical UV oligomers and their chemical structure .....	66
Table 4-9. Typical UV oligomers and their applications (Allnex and IGM's material data sheets).....	67
Table 5-1. Composition of UV-BaTiO <sub>3</sub> ink.....	90
Table 5-2. Composition of UV-CCTO ink .....	91
Table 5-3. Composition of UV ink without pigment.....	91
Table 6-1. Properties of mass product flexible copper-clad laminates .....	97
Table 6-2. Geometric accuracy of the UV flatbed printer .....	101
Table 7-1. Types of B.C used for 2D and 3D simulation .....	117
Table 7-2. Types of elements available in ANSYS Maxwell, discretisation methods and calculation of potential energy .....	118
Table 7-3. Parameters used for 2D interdigitated electroadhesive pad simulation .....	125
Table 7-4. Parameters used for 2D optimization simulations of interdigitated EA device..	128
Table 7-5. Parameters used for 3D interdigitated electroadhesive pad simulation .....	130
Table 7-6. The effect of electrodes design on obtainable attractive forces .....	131
Table 7-7. The effect of electrode shapes on generated electric field and Maxwell stress distribution.....	132
Table 7-8. Statistical information of the grids generated for the last iteration of 3D modelled of the interdigitated pad .....	133
Table 7-9. Parameters used for 3D bi-layer EA devices simulation.....	134
Table 7-10. Device 1 characteristics .....	135
Table 7-11. Device 2 characteristics .....	135
Table 7-12. Device 3 characteristics .....	136
Table 7-13. Device 4 characteristics .....	137
Table 7-14. Device 5 characteristics .....	137
Table 7-15. Device 6 characteristics .....	138
Table 7-16. Device 7 characteristics .....	139
Table 7-17. Uni-layer device characteristics .....	140
Table 8-1 Curve fitting parameters and it's goodness factors.of EA force versus distance..	154



Table 8-2 Curve fitting parameters and goodness criteria of EA force versus applied voltage.....	156
Table 8-3a Comparison of Maxwell stress and obtainable EA force mesh independency ...	166
Table 8-4b Maxwell stress distribution versus number of elements.....	166

# List of Abbreviations

BT	Barium Titanate
BST	Barium Strontium Titanate
CCTO	Calcium Copper Titanate
CM	Conformal Mapping
EA	Electroadhesive
FEM	Finite Element method
HDDA	1,6-Hexanediol diacrylate
IBOA	Isobornyl Acrylate
ITX	2-isopropyl thioxanthene-9-one
LED	Light Emitting Diode
MDM	Medium pressure mercury lamp
PBZ	Lead Barium Zirconate
PI	Photoinitiator
PZT	Lead Zirconate Titanate
S	Spacing between electrodes
SEM	Scanning Electron Microscopy
TMPTA	Trimethylolpropane Triacrylate
TPGDA	Tripropylene Glycol Diacrylate
TPO	(2,4,6-Trimethylbenzoyl) diphenyl Phosphine Oxide
TPO-L	Ethyl(2,4,6-Trimethylbenzoyl)-phenyl phosphinate

UV	Ultra Violet
W	Width of electrodes
XRD	X-ray diffraction
XRF	X-ray fluorescence

# Nomenclature

A	Surface area
C	Capacitance
B	Volume fraction
D	Electric flux density
F	Force
$F_{J-R}$	Johnsen-Rahbek forces
P	Polarisation
$\vec{P}_e$	Electronic polarisation
$\vec{P}_i$	Ionic polarisation
$\vec{P}_o$	Orientational polarisation
$\vec{P}_l$	Interfacial polarisation
Q	Electrostatic charge
R	Electrical Resistivity
S	Space between electrodes
Sq	Root mean square
$\tan \delta$	Dielectric loss tangent
$t_d$	Dielectric layer Thickness
V	Applied DC voltage
$\rho$	Volume resistivity
$\rho_v$	Volume charge density
$\epsilon$	Relative permittivity of a material
$\epsilon_0$	Relative permittivity of vacuum
$x_e$	Polarisability
$\phi$	Electrostatic potential
$\gamma$	Secondary-electron-emission coefficient
$\lambda$	Wavelength

## *Acknowledgements*

I owe my sincere gratitude to my Director of Studies, Prof Paul Bingham for his excellent guidance and continuous support of my PhD study. My sincere thanks also go to Dr Torsten Schenkel for his encouragement, caring and invaluable support during my research work. I would like to extend my appreciation to Prof Jacques Penders who, although no longer with us, continues to inspire by his example and dedication to the students he served over the course of his career.

I am grateful for the support that I have received from the staff in SHU Materials and Engineering Research Institute (MERI) during my study. I would also like to thank the Sheffield Hallam University technicians for all of their help.

I owe my very profound gratitude to my mum, dad, brother, and sister for providing me with continuous support and encouragement through my entire life even when that involves me moving to the other side of the world. I will forever be grateful to my mum and dad for always giving me the incredible support, motivation, encouragement, and positive energy; for being the best parent in the world!

I am very much thankful to my wife and best friend, Helga, without whose love, care, patience, smile, counsel, and immense encouragement, I would not have finished this thesis. During all the challenges that I have faced for my study, she always supported me.

## ***Dedication***

To whom I owe everything:

My father, Javad Bigharaz

My mother: Simin Fahimi

My wife: Helga

# ***Chapter 1***

## ***Introduction***

### **1.1 Background and purpose of the study**

Electroadhesion (EA) has received much attention recently due to the advantages this technology offers to tackle complex problems such as handling delicate objects or micro-size particles (Kim, Jiang, Towell et al., 2019). Research has been carried out to optimise the performance of electroadhesive devices, mainly focusing on design and fabricating these devices with prefabricated dielectric layers (polyimide, Dadkhah et al. 2018 and Akherat, Karimi, Alizadehyazdi et al., 2019). There is presently a lack of systematic research in improving the electrical properties of this layer, and hence the device's performance, for EA applications. This study aimed to find and develop applicable methods to improve EA device performance using novel electroceramic-UV polymer composites as a dielectric layer for these devices.

Recent progress in the manufacturing of microelectronic devices using 3D printers illustrated in figure 1-1 (Wu, Yang, Hsu et al., 2015) and inkjet printers shown in figure 1-2 (Correia, Mitra, Castro et al., 2018) enhance the potential of systematic research for electroadhesion. Considering these opportunities, there are excellent opportunities to develop and fabricate a new generation of EA devices to generate higher attractive forces, be more stable in performance, and have suitable mechanical properties such as flexibility and stretchability for complex applications. On the other hand, development in cold coating systems such as UV-curable polymer coatings (Kim and Willson, 2006) can be brought into play to improve electrical properties of EA devices such as relative permittivity and dielectric breakdown voltage. Development in the numerical analysis of large scale electromagnetic and electrostatic

problems and topology optimisation techniques also can be employed in parallel with these improvements in materials to achieve a more efficient design and thus further enhance the performance of EA devices. In this study, several recently developed technologies have been considered together to design, fabricate, test, and model a new generation of EA devices.

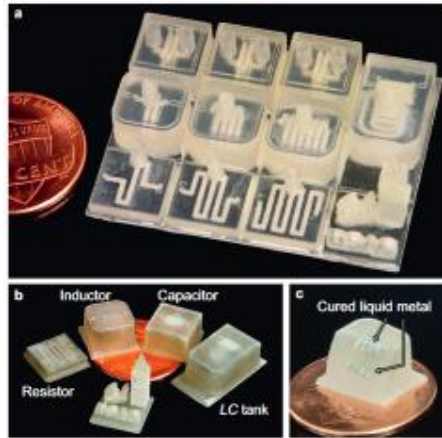


Figure 1-1. Optical image of 3D printed microelectronics components (Wu et al., 2015)

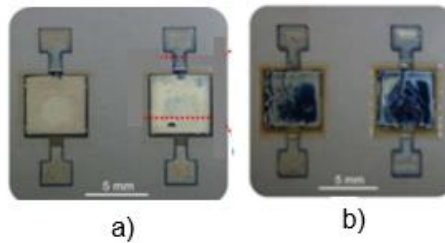


Figure 1-2. Inkjet printed a) single and b) multi-layer capacitors (Correia et al., 2018)

## 1.2 Aims and Objectives

This research aims to improve electroadhesive device performance by finding and developing suitable and applicable electroceramic materials and developing efficient coating methods to manufacture new EA devices with higher clamping forces.

The study's objectives are:

- i. Investigating parameters that influence EA device performance
- ii. Using conventional solid state reaction processing to prepare electroceramic materials for coating onto EA devices.



- iii. Testing and analysing electroceramics with laboratory methods to confirm that the planned phase/s and composition of ceramic materials formed.
- iv. Measuring electrical properties of electroceramics (relative permittivity at room temperature)
- v. Fabricating different types of electrode pattern
- vi. Coating electrodes with electroceramic–UV composites
- vii. Building, testing and measuring EA device performance
- viii. Simulating EA pad performance using finite element methods and verifying findings using experimental results.

### **1.3 Layout of the thesis**

Chapter 2 presents previous research to develop the fundamentals of electroadhesion and summarises the outcome of prior studies. There is also a systematic explanation of the mathematical relationships between applied voltage, electric field, Maxwell stress and obtainable EA force.

Chapter 3 focuses on dielectric materials, including electroceramics, electroceramic–polymer composites, liquid dielectrics, and gaseous dielectrics, to find suitable dielectric materials for manufacturing dielectric components in EA devices.

Chapter 4 focuses on UV technology and explains the commercially available UV-curable ink components, including monomers, oligomers, photoinitiators and UV curing devices, including medium pressure Mercury lamps, LEDs, and electron beam curing devices. The purpose was to select suitable electroceramic pigmented UV-curable ink components and choose an appropriate UV curing device based on these selections. The procedure and devices needed to manufacture pigmented UV-curable ink are explained.

Chapter 5 describes the procedure followed to fabricate electroceramics and UV-curable polymer-electroceramic composites. The material analyses were carried out during and after the fabrication of electroceramics and pigmented UV-curable inks, including XRD, Raman spectroscopy, SEM and viscosity measurements, and dielectric measurements.

Chapter 6 includes two separate sections: first, the fabrication procedures followed in manufacturing rigid and flexible EA devices; and second, the experimental apparatus and procedures followed to test EA device performance.

Chapter 7 presents finite element based 2D and 3D numerical analyses carried out to evaluate and optimise EA device performance. ANSYS Maxwell was used to carry out parametric

simulation in 2D and 3D simulations utilised to find optimum shapes of electrodes. Optimisation analyses were also carried out by coupling ANSYS Maxwell and MATLAB. Chapter 8 presents the results of this study, including analytical solutions, numerical analyses, and experimental results. The limitation of using analytical solutions to calculate EA forces are presented. Experimental results for rigid and flexible EA devices, with and without dielectric layers, are reported.

## ***Chapter 2***

# ***Electroadhesion: Principles and Literature Review***

### **2.1 Introduction**

Electroadhesion is the electrostatic effect of adhesion between two surfaces (electroadhesive device and substrate) subjected to an electrical field, including conductors, semiconductors, and insulators. Compared to other adhesion mechanisms like a vacuum, electroadhesion is more efficient and could be used to pick and release almost every insulating material (e.g., silicon, wood, glass, concrete, and plastic) (Cao, Sun, Fang, 2016). Table 2-1 compared EA technology with a similar adhesive gripping method. Derygin and colleagues first presented Electroadhesion in 1978 (Galembeck & Burgo, 2017). However, due to a lack of reproducible electrostatic measurements and understanding of electrostatic charging, insulator mechanisms did not reach the researcher's attention. However, recently, due to contact-free attraction and vacuum environment applications, electroadhesion has become more important and may offer innovative solutions in many different areas. Some of those applications are explained in the following section.

Table 2-1. Comparison of astrictive grippers (Monkman, 2003)

Astrictive Gripping Method	Object material types suitable for prehension	Typical rise Retention Pressure (N/m <sup>2</sup> )	Steady state Volumetric flowrate (m <sup>3</sup> /s)	Typical rise and fall Time constants —
Vacuum	Any relatively rigid, nonporous surface	50,000	$>10^{-4}$	10 ms, <1s
Magnetic	Magnetically susceptible materials	100,000	$\approx 10^{-3}$	>20 ms
Electrostatic*	Relatively flat, electrical conductors	200	$\approx 2 \times 10^{-3}$	1 ms, 10 ms
Electrostatic <sup>†</sup>	Almost all materials provided these are flat and relatively light	50	$\approx 2 \times 10^{-5}$	100 ms, >1 s

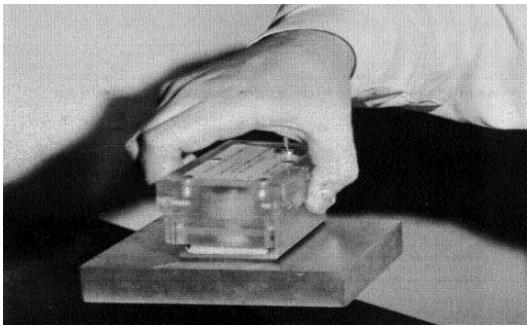
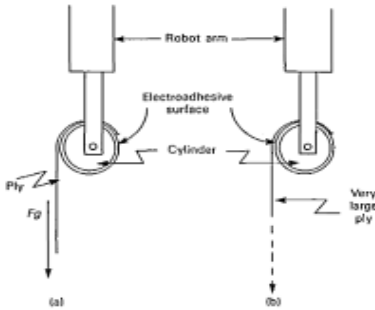
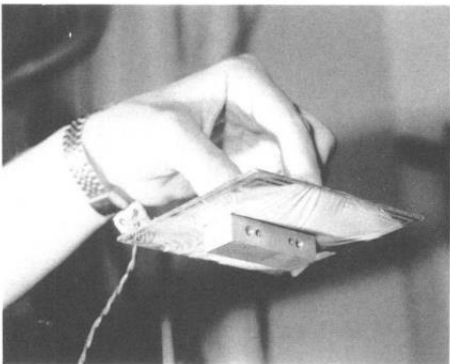
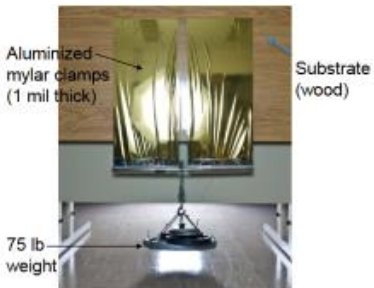
\*Used with electrically conducting object materials

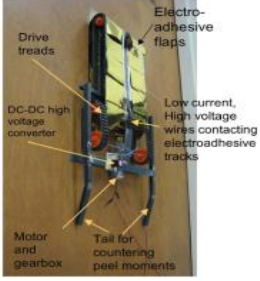
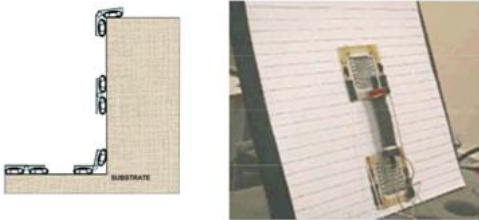
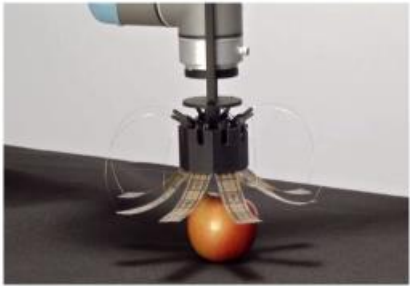

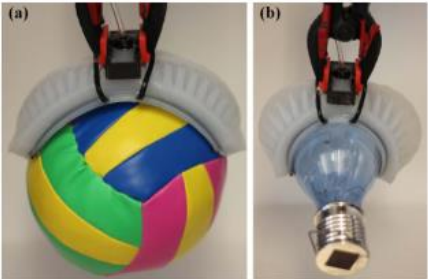
<sup>†</sup>Used with electrically insulating object materials

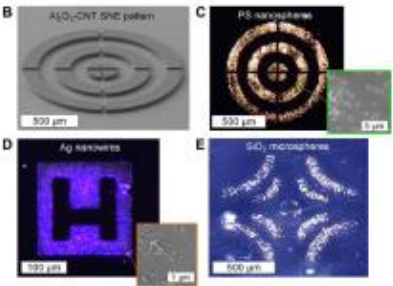


### 2.1.1 Electroadhesion Applications

Electroadhesion has various applications, including wall climbing robots (Liu, Chen & He, 2013) and grippers for handling semiconductor wafers and applications in flat panel display and printing industries (Ruffatto, Shah & Spenko, 2014). It can also potentially be used for various space applications (see figure 2-1), such as tile inspection or solar array inspection (Microrobot Inspectors -NASA, 2009). The other advantage of electroadhesive (EA) devices is that they can be fabricated in various dimensions, from micrometre to centimetre, while producing suitable forces for these applications. Kim, Jiang, Towell et al. (2019) have used EA devices to pick up and deposit nano- and micro-sized particles for electronic applications. Flexible electronics have received attention recently due to advances in 3D printing and the development of complex electronic devices such as wearable and stretchable sensors. Germann, Schubert and Floreano (2014) fabricated and tested a flexible interdigitated EA device prototype. These new and novel technologies are up-and-coming for fabricating advanced EA devices. The history of advances in fabricating EA devices is illustrated in the table 2-1.

Table 2-2. The history of advances in fabricating EA devices

	<p>Hand model EA device lifting Aluminium plate</p> <p>Krape (1968)</p>
	<p>Electroadhesive roller action on fabric</p> <p>Purpose: clothing robotics</p> <p>Monkman, Taylor and Farnworth (1989)</p>
	<p>Electroadhesive gripper with fluid dielectric medium</p> <p>Purpose: adaptive robot end-effectors and Shape optimisation</p> <p>Monkman (1992)</p>
	<p>An initial prototype of flexible EA devices</p> <p>Purpose: Showing the capability of EA device holding 75 lb weight</p> <p>Kaltenbrunner, White, Głowacki et al. (2012)</p>

	<p>Purpose:</p> <p>Application of EA technology in wall climbing robots</p> <p>Kaltenbrunner, White, Głowacki et al. (2012)</p>
	<p>Purpose:</p> <p>Second generation of wall climbing robots with capability for more complex manoeuvres</p> <p>Kaltenbrunner, White, Głowacki et al. (2012).</p>
	<p>Purpose:</p> <p>Soft gripper mounted on industrial arm robot</p> <p>Fabricated by Grabit company (2014)</p>
	<p>Interdigitated Stretchable EA device Using sequential casting method</p> <p>Germann, Schubert, &amp; Floreano (2014)</p>
	<p>More advanced soft robotic gripper with stretchable EA device</p> <p>Guo, Elgeneidy, Xiang et al. (2018)</p>

	<p>Purpose:</p> <p>Deposition of Nano and micron size of particles Using EA devices</p> <p>Towell et al. (2019)</p>
	<p>Robot name: Stackit</p> <p>More advanced robot arm with EA gripper</p> <p>Fabricated by Grabit company</p> <p><a href="https://grabitinc.com/products/">https://grabitinc.com/products/</a></p>
	<p>Device name: Conveyit</p> <p>Advanced conveyer with array of EA devices</p> <p>Fabricated by Grabit company</p> <p><a href="https://grabitinc.com/products/">https://grabitinc.com/products/</a></p>

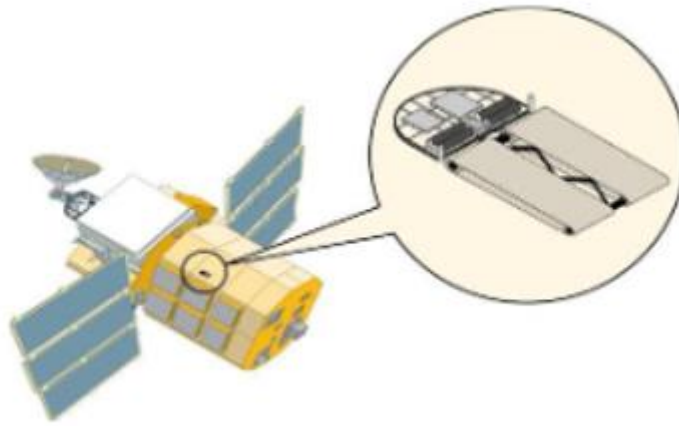


Figure 2-1. Potential Space application: “Spacecrawler” micro inspection robot (Microrobot Inspectors, 2009)

### 2.1.2 Components of Electrodehesion Systems

The components of an electrodehesion system (as shown in figure 2-2) are not complex compared with other adhesion mechanisms. They include a high DC voltage power supply, an electrodehesive pad (electrodes embedded in a dielectric material) and a substrate (the object being picked up). Figure (2-3) schematically shows how the electrodehesive force is generated.

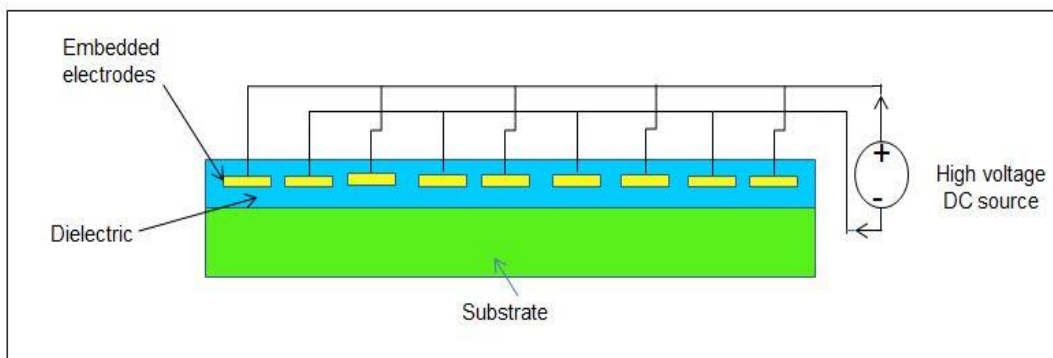


Figure 2-2. Simplified schematic of an electrodehesive device



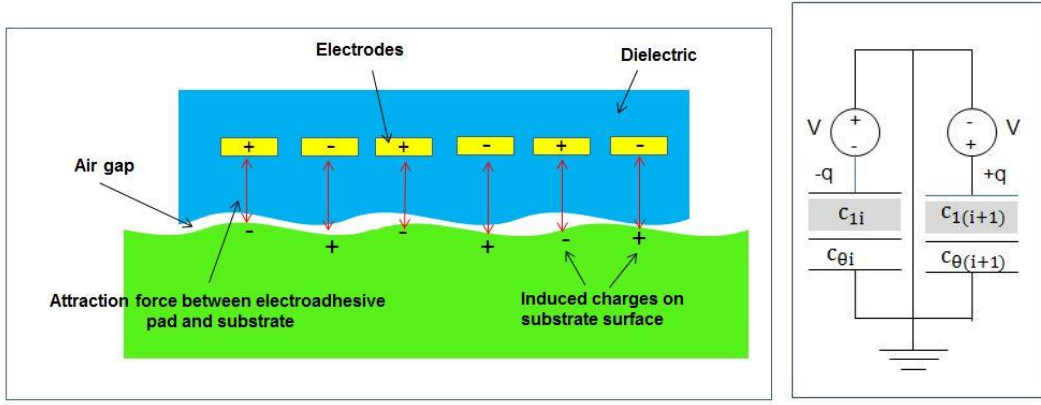


Figure 2-3. Schematic of electroadhesive force generation and equivalent circuit (Monkman, 2003; Guo et al., 2016 a)

## 2.2 Theory

Recently, researchers (Guo et al., 2016 a; Qin & McTeer, 2007) have proven that parameters influencing the attractive forces on conductive and insulating substrates are different and need to be investigated separately. Therefore, first, the electroadhesive forces on conductive substrate materials will be introduced, and then electroadhesive forces on insulating substrate materials will be explained in detail.

### 2.2.1 Electroadhesive Forces on Conductive Substrate Materials

Qin and McTeer (2007) reported that the electroadhesive forces on conductive substrates, in reality, are always a combination of Coulomb ( $F_{\text{coulomb}}$ ) and Johnsen-Rahbek ( $F_{\text{J-R}}$ ) forces and, depending on the volume resistivity of the dielectric material, one of them can be dominant. Figure (2-4) indicates that for a volume resistivity ( $\rho$ ) of less than  $10^{10} \Omega\text{cm}$ , the J-R force is dominant and for  $\rho > 10^{13} \Omega\text{cm}$ , the Coulomb force is dominant. Resistivities of typical materials are listed in table 2-3.

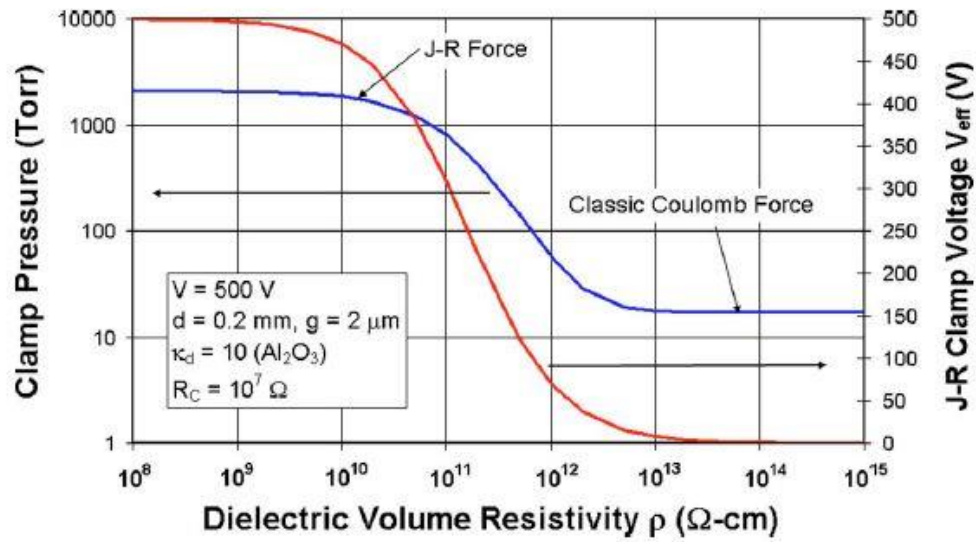


Figure 2-4. Coulomb and J-R force versus volume resistivity of dielectric (Qin & McTeer, 2007)

Table 2-3 Resistivity of various materials (D physics)

Material	Resistivity ( $\rho$ ) [ $\Omega \cdot m$ ]
<b>Conductors</b>	
Silver	$1.6 \times 10^{-9}$
Copper	$1.7 \times 10^{-8}$
Aluminium	$2.7 \times 10^{-8}$
Tungsten	$5.6 \times 10^{-8}$
Iron	$10 \times 10^{-8}$
Platinum	$11 \times 10^{-8}$
Mercury	$89 \times 10^{-8}$
<b>Semiconductors</b>	
Silicon	2300
Carbon (Graphite)	$3.5 \times 10^{-5}$
Germanium	0.46
<b>Insulators</b>	
Silicate glass	$10^{10}$ to $10^{14}$
Hard rubber	$10^{13}$ to $10^{16}$
NaCl	$\sim 10^{14}$
Fused Quartz	$\sim 10^{16}$

### 2.2.1.1 Coulomb Forces

Coulomb forces are calculated as follows (Qin and McTeer, 2007):

$$F_{Coulomb} = \frac{1}{2} \frac{C_{equiv}^2 V^2}{\epsilon_0 A} \quad (2-1)$$

Where A is electrode area; V is potential difference of the DC supply;  $C_{equiv}$  is equivalent capacitance of the dielectric and the gap and is given by:

$$C_{equiv} = \frac{C_g C_d}{C_g + C_d} \quad (2-2)$$

$$C_g = \epsilon_0 \frac{\epsilon_g A}{t}, \quad C_d = \epsilon_0 \frac{\epsilon_d A}{d} \quad (2-3)$$

### 2.2.1.2 Johnsen-Rahbek (J-R) Forces

The gap between the dielectric material and the conductive substrate, in reality, depends on contact pressure and surface roughness, consisting of contact and noncontact area, and is shown schematically in figure (2-5). This and the fact that the volume resistivity of dielectrics is finite together result in the J-R effect

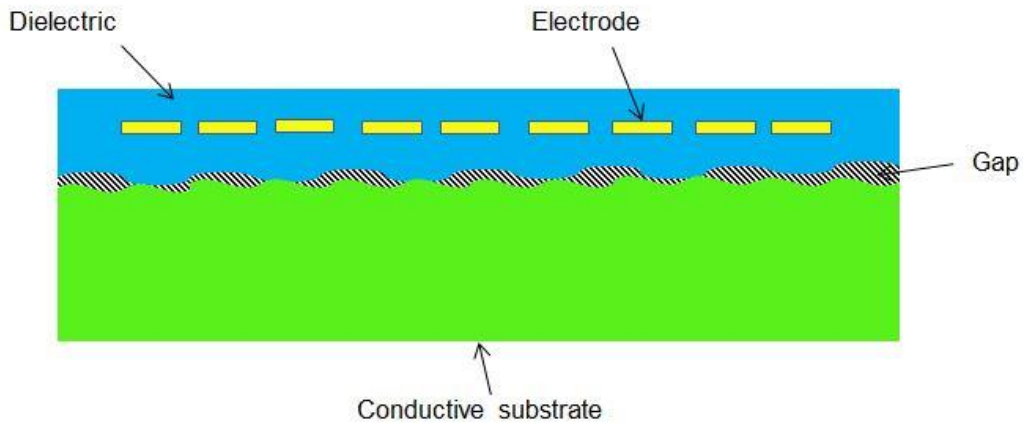


Figure 2-5. Schematic showing contact and non-contact area between dielectric and substrate

The J-R force between the electroadhesive pad and the conductive substrate is given by (Qin and McTeer, 2007):

$$F_{J-R} = \frac{1}{2} \frac{C_{J-R}^2 V_{J-R}^2}{\epsilon_0 A_{J-R}} \quad (2-4)$$

Where:

$A_{J-R}$  is noncontact area between dielectric and substrate

$C_{J-R}$  is capacitance of noncontact area

$V_{J-R}$  is the potential difference across the interface, and is calculated by following:

$$V_{J-R} = \frac{R_c}{R_c + R_d} V \quad (2-5)$$

Where  $R_d$  is the volume resistivity of the dielectric and  $R_c$  is resistivity of contact area.

## 2.2.2 Electroadhesive Forces on Non-Conductive Materials

### 2.2.2.1 Definition of electrostatic field

An electrostatic field is an electric field associated with time-invariant charges at rest, which means that the electric field does not change (in its magnitude and with time, and electric charges are always at rest). Therefore, according to the electroadhesion system, the electric field generated by introducing a high DC voltage to the electrodes is considered electrostatic; therefore, to explain the theory of electroadhesion, equations that govern electrostatic field problems are used.

#### 2.2.2.2 Integral form of Gauss' Law

According to Gauss' Law, in terms of charge distribution, net electric flux within a homogeneous volume of material is equal to the net electric charge of a surface which encloses the volume.

$$\int_V \rho_V dV = \oint_A \vec{D} \cdot d\vec{A} \quad (2-6)$$

#### 2.2.2.3 Differential form of Gauss' Law

The differential form of Gauss' Law can be driven by applying Gauss' Law to the infinitesimal parallelepiped as shown in figure (2-6) and using a first-order Taylor Series approximation of the electric flux density and assuming  $\rho_V$  as a total charge within the volume can be written as follows:

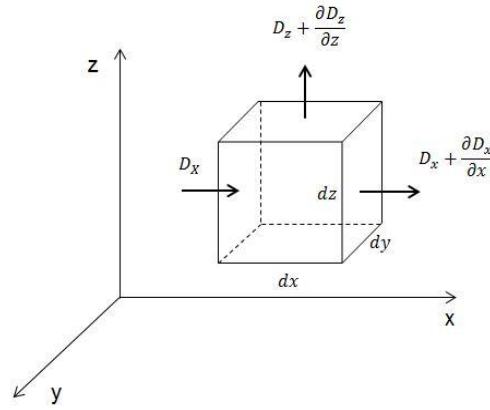


Figure 2-6. Application of Gauss' Law to a differential volume.

$$\frac{\partial D_x}{\partial x} + \frac{\partial D_y}{\partial y} + \frac{\partial D_z}{\partial z} = \rho_V \text{ or } \vec{\nabla} \cdot \vec{D} = \rho_V \quad (2-7)$$

Equation (2-7) is known as the first Maxwell equation.

#### 2.2.2.4 Poisson's and Laplace's Equations

Finding relationships between electric potential and charge density is desirable as electric potential is a scalar quantity compared to electric field intensity and electric flux intensity, which are vector quantities. Once the electric potential has been calculated, the other electric parameters can be determined using suitable mathematical operations.

The relationship between electric flux density and electric field intensity for a homogeneous medium with uniform dielectric permittivity is given by:

$$\vec{D} = \epsilon_0 \vec{E} + \vec{P} = \epsilon \vec{E} \quad (2-8)$$

Combining the above equation with the first Maxwell equation, it may be written that:

$$\vec{\nabla} \cdot \vec{E} = \frac{\rho_V}{\epsilon} \quad (2-9)$$

Also the electric field intensity and electric potential are related as  $\vec{E} = -\nabla \phi$  therefore the relationship between electric potential and electric charge density can be written as follows:

$$\vec{\nabla} \cdot (-\nabla \phi) = \frac{\rho_V}{\epsilon}, \text{ or, } \vec{\nabla} \cdot \nabla \phi = -\frac{\rho_V}{\epsilon}, \text{ or, } \vec{\nabla}^2 \phi = -\frac{\rho_V}{\epsilon} \quad (2-10)$$

This is known as Poisson's equation (Chakravorti, 2015).

### 2.2.2.5 Laplace's Equation

Assuming dielectric media to be ideal insulators reduces equation (2-10) to give the Laplace equation since the volume charge density ( $\rho_V$ ) within the field region is zero. Below is the Laplace equation in different forms:

$$\vec{\nabla}^2 \phi = 0, \text{ or, } \frac{\partial^2 \phi}{\partial x^2} + \frac{\partial^2 \phi}{\partial y^2} + \frac{\partial^2 \phi}{\partial z^2} = 0 \quad (2-11)$$

### 2.2.2.6 Polarisation

In order to understand how an electroadhesive force on an insulating material is generated, polarisation is defined and then the polarisation force for an individual dipole is derived. Finally, the force density within a medium is calculated.

Inducing electric fields in dielectric materials results in alignments of dipoles in the direction of the external electric field, which is called polarisation (see figure 2-7). There are four main kinds of polarization. Electronic ( $\vec{P}_e$ ) and ionic ( $\vec{P}_i$ ) polarizability are elastic processes and, compared to inelastic orientational ( $\vec{P}_o$ ) and interfacial ( $\vec{P}_l$ ) polarizability, are extremely fast (Chakravorti, 2015). Therefore, the total polarisation of the medium is the sum of all these effects.

$$\vec{P}_{total} = \vec{P}_e + \vec{P}_i + \vec{P}_o + \vec{P}_l + \vec{P}_{others} \quad (2-12)$$

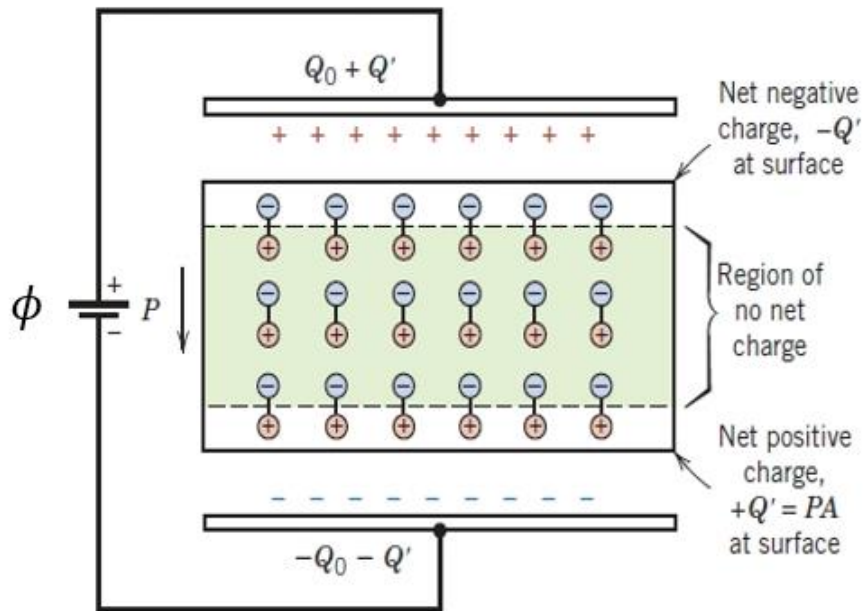


Figure 2-7. Polarization within a dielectric medium

In reality, most of the physical properties are tensors, which means there are different behaviours in different directions, and these are defined as a tensor with nine directions. As result, polarizability( $\chi_e$ ) of a substance will be given by:

$$\begin{bmatrix} \chi_{exx} & \chi_{exy} & \chi_{exz} \\ \chi_{eyx} & \chi_{eyy} & \chi_{eyz} \\ \chi_{ezx} & \chi_{ezy} & \chi_{ezz} \end{bmatrix} \quad (2-13)$$

And polarization is found through:

$$\vec{P} = \varepsilon_0 \chi_e \vec{E} \quad (2-14)$$

It is well known that the polarisation of materials is time dependent, and much research has been established that explains how long it takes for each type of polarization to be influenced by an external electric field (Kao, 2004). Figure (2-8) shows the time dependency of polarization. Previous research (Bamber, Guo & Singh, 2017) carried out at SHU to measure the electric potential distribution of an interdigitated electroadhesive pad showed that it takes roughly 30 minutes for that pad (230mm  $\times$  190mm) to become fully charged. This proved that electroadhesion is an unsteady-state phenomenon for a specific period and measuring a stabilized attraction force should be considered carefully. Figure (2-9) depicts a certain period before the electroadhesive pad becomes fully charged. Therefore, it cannot yet be concluded confidently, based on literature, which types of polarization should be considered in investigations of electroadhesion and further research is required.

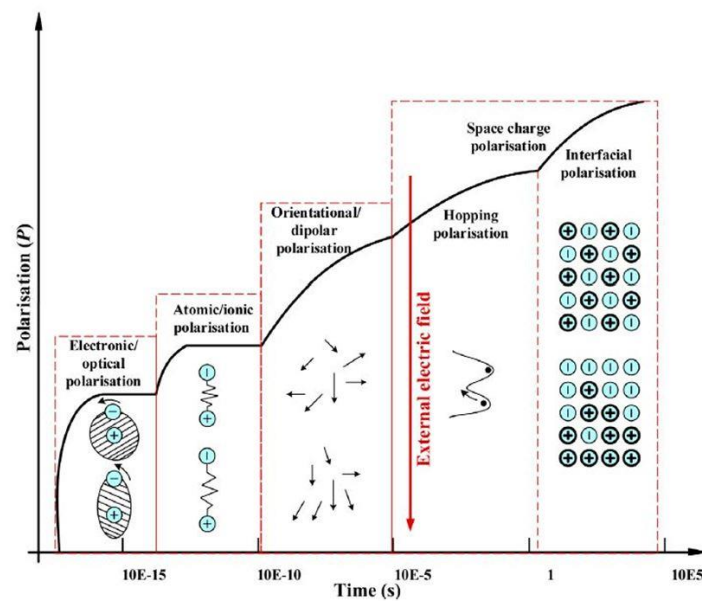


Figure 2-8. Polarization time dependency of an electroadhesive pad (Bamber, Guo & Singh, 2017)

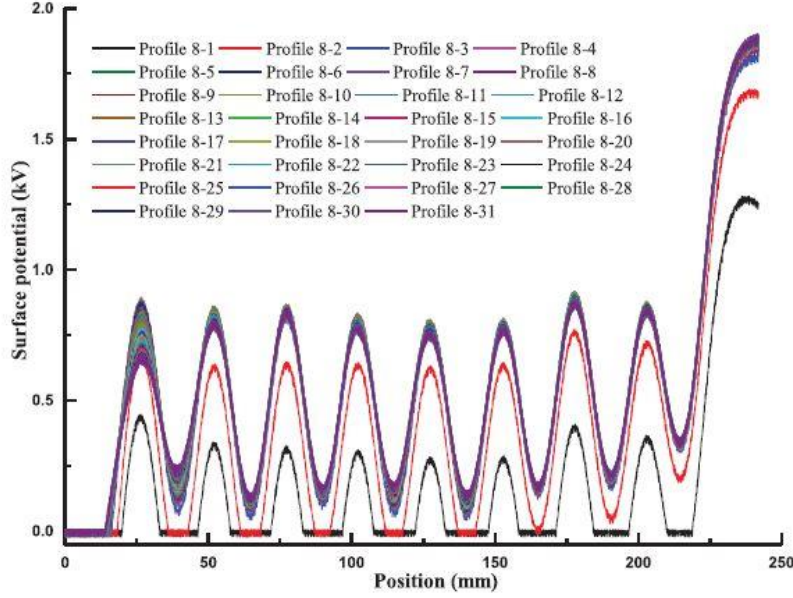


Figure 2-9. Electric potential profile during charging process in the centre line of interdigitated electroadhesive pad (Bamber et al., 2017)

The dielectric of an electroadhesive pad consists of many randomly oriented crystals; therefore, there is no preferred orientation. As a result, polarisability can be treated as a scalar quantity whose magnitude equals the average of all dimensions of the polarizability tensor. The polarisation force for an individual dipole (see figure 2-10) (Melcher, 1981) is given by:

$$f_i = \lim_{d \rightarrow 0} q [E_i(\vec{r} + \vec{d}) - E_i(\vec{r})] \quad (2-15)$$

$$f_i = \lim_{d \rightarrow 0} q \left[ E_i(\vec{r}) + \frac{\partial E_i}{\partial x_j} d_j - E_i(\vec{r}) \right] = p_j \frac{\partial E_i}{\partial x_j} \quad (2-16)$$

$$\vec{f} = \vec{p} \cdot \nabla \vec{E} \quad (2-17)$$

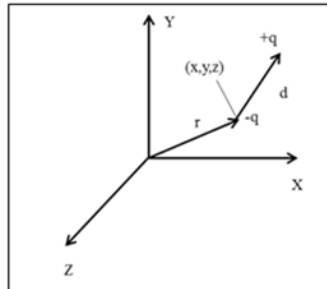


Figure 2-10. Definition of displacement and charge location for dipole (Melcher, 1981)

By averaging the polarization force for all dipoles within a medium and considering the polarisation density as  $\vec{P} = n\vec{p}$ , the Kelvin polarization force density is found:



$$\vec{F} = \vec{P} \cdot \nabla \vec{E} \quad (2-18)$$

As in electrostatics or electroquasistatics, the E-field is conservative or irrotational ( $\frac{\partial E_i}{\partial x_j} = \frac{\partial E_j}{\partial x_i}$ ), Eq. (2-18) becomes (Melcher, 1981):

$$\vec{F} = \nabla \left[ \frac{1}{2} (\epsilon - \epsilon_0) \vec{E} \cdot \vec{E} \right] \quad (2-19)$$

### 2.2.2.7 Electrostatic force and Maxwell stress tensor

The relationship between the electrostatic force and the Maxwell stress tensor can be driven using the Divergence Theorem. The Divergence Theorem states that under suitable conditions, the outward flux of a vector field across a closed line equals the double integral of the divergence of the field over the two-dimensional region enclosed by the line. The outward flux of a vector field across a closed surface equals the triple integral of the divergence of the field over the three-dimensional region enclosed by the surface (Chakravorti, 2015).

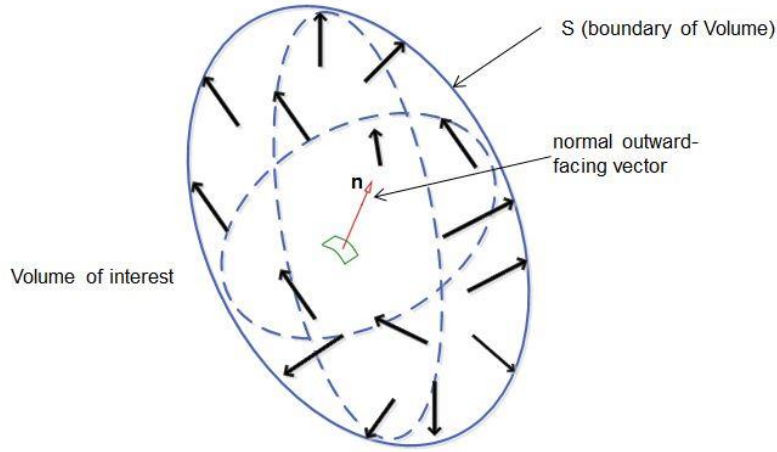


Figure 2-11. Divergence theorem in the region of interest

$$\iiint_V \nabla \cdot F dv = \oint_S F \cdot n ds \quad (2-20)$$

Therefore, by using Divergence Theorem and Eq. (2-19) the Maxwell stress tensor in two and three dimensions will be given by:

$$\iint_S \vec{F} ds = \oint_L T \cdot \vec{n} ds \quad (2-21)$$

Where:

$$T = \begin{bmatrix} \frac{\varepsilon}{2}(E_x^2 - E_y^2) & \varepsilon E_x E_y \\ \varepsilon E_x E_y & \frac{\varepsilon}{2}(E_y^2 - E_x^2) \end{bmatrix} \quad (2-22)$$

And in three-dimensions by:

$$\iiint_V \vec{F} dV = \oiint_S \vec{T} \cdot \vec{n} ds \quad (2-23)$$

Where:

$$T = \begin{bmatrix} \frac{\varepsilon}{2}(E_x^2 - E_y^2 - E_z^2) & \varepsilon E_x E_y E_z & \varepsilon E_x E_y E_z \\ \varepsilon E_x E_y E_z & \frac{\varepsilon}{2}(E_y^2 - E_x^2 - E_z^2) & \varepsilon E_x E_y E_z \\ \varepsilon E_x E_y E_z & \varepsilon E_x E_y E_z & \frac{\varepsilon}{2}(E_z^2 - E_x^2 - E_y^2) \end{bmatrix} \quad (2-24)$$

#### 2.2.2.8 Theoretical electroadhesive force calculation in two dimensions (2D) and three dimensions

There is always a very thin layer of vacuum or air between an electroadhesive pad and the substrate, which varies along the electroadhesive pad length. However, the thickness is assumed to be constant (a few micrometres). This simplification makes it possible to calculate the attractive force between the electroadhesive pad and the substrate analytically and numerically. Figure (2-12) shows an electroadhesive system with a constant vacuum or air layer schematically.

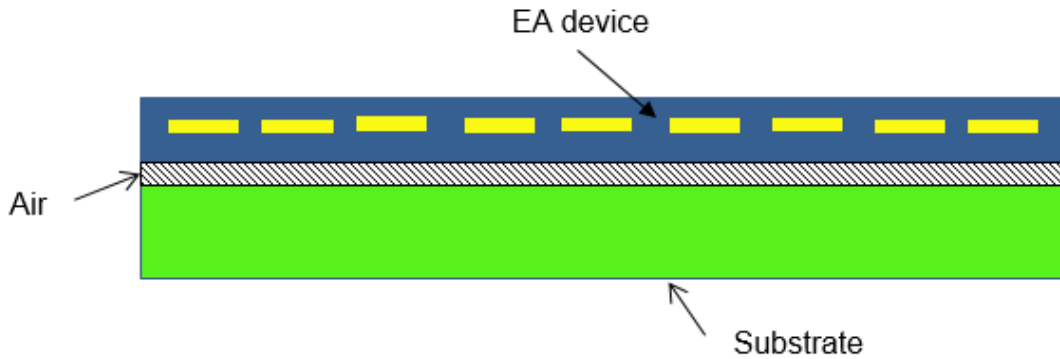


Figure 2-12. Simplification of contact interface for electroadhesion system

Slightly above and below the interface between air or vacuum, and substrate, is considered as the region of interest (see figure 2-13 and 2-14).

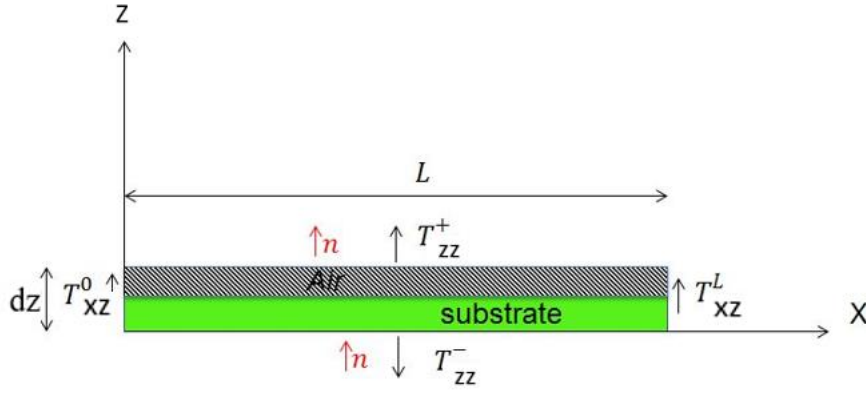


Figure 2-13. Electroadhesive force calculation in 2D

Therefore, the electroadhesive force in the z-direction could be calculated using:

$$\begin{aligned}
 F_z &= \iint_s \vec{F}_z ds = \oint_L T \cdot \vec{n} ds \\
 &= \int_0^L T_{zz}^+ dx - \int_0^L T_{zz}^- dx + \int_0^{dy} T_{xz}^L dy - \int_0^{dy} T_{xz}^0 dy \\
 F_z &= \int_0^L T_{zz}^+ dx - \int_0^L T_{zz}^- dx
 \end{aligned} \tag{2-25}$$

Similarly, for 3D electroadhesive forces in the z-direction, this is given by:

$$\begin{aligned}
 F_z &= \iiint_V \vec{F} dV = \oiint_S \vec{T} \cdot \vec{n} ds = \iint_{A_z} T_{zz}^+ dA - \iint_{A_z} T_{zz}^- dA + \iint_{A_x} T_{xz}^{L_1} dA - \\
 &\quad \iint_{A_x} T_{xz}^0 dA + \iint_{A_y} T_{yz}^{L_2} dA - \iint_{A_y} T_{yz}^0 dA \\
 F_z &= \iint_{A_z} T_{zz}^+ dA - \iint_{A_z} T_{zz}^- dA
 \end{aligned} \tag{2-26}$$

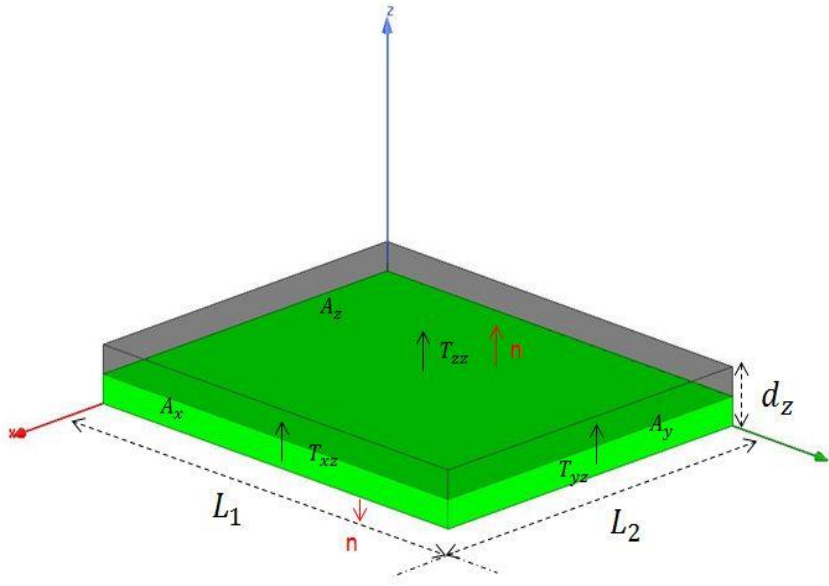


Figure 2-14. Electroadhesive force calculation in 3D

#### 2.2.2.9 Analytical approaches to calculating Electroadhesive force

2.2.2.9.1 i: Solving partial differential equation (PDE) in the domain of interest using the separation of variables method

Much research has been carried out to theoretically calculate the attractive electroadhesive force using the separation of variables method to solve the PDE governing electroadhesion (Laplace's equation) (Liu et al., 2013; Woo & Higuchi, 2010; Cao et al., 2016; Mao, Qin & Zhang, 2016) Assumptions that must be considered are listed below:

i): Assumptions:

- Electrodes are perfect conductors
- Dielectric materials are linear, isotropic, and homogenous (LIH)
- Power supplier is dual polarity DC voltage
- Electric field is almost identical in z-direction by neglecting the marginal part of the pad (2D)
- Dielectrics must not have free charge density

- Relative permittivity of dielectric layer, air and substrate should be equal to avoid any discontinuity in electric field distribution.

Table 2-4. Laplace's equation in Cartesian and Cylindrical coordinates and solution functions

Coordinates	Laplace's equation form	Solution function form	Ref
Cartesian	$\frac{\partial^2 \phi}{\partial x^2} + \frac{\partial^2 \phi}{\partial z^2} = 0$	$\phi_1 = \exp (\pm n\pi z/p) \cos (n\pi x/p)$ $\phi_2 = \cosh (\pm n\pi z/p) \cos (n\pi x/p)$ $\phi_3 = a + bz$	Liu et al., 2013
Cylindrical	$\frac{\partial^2 \phi}{\partial r^2} + \frac{1}{r} \frac{\partial \phi}{\partial r} + \frac{\partial^2 \phi}{\partial z^2} = 0$	$\phi = (A_0 Z + B_0)(C_0 \ln r + D_0)$ $+ \sum_{n_k} [A_k \exp(n_k z)$ $+ b_k \exp(-n_k z)] [J_0(n_k r)$ $+ D_k Y_0(n_k r)]$	Mao, Qin & Zhang, 2016

*ii) Boundary conditions at the dielectric interface:*

Most electroadhesion systems consist of multilayer dielectrics, therefore for each interface (see figure 2-15) there are two types of boundary condition (BC): normal and tangential. These two BCs in Cartesian coordinates can be written as:

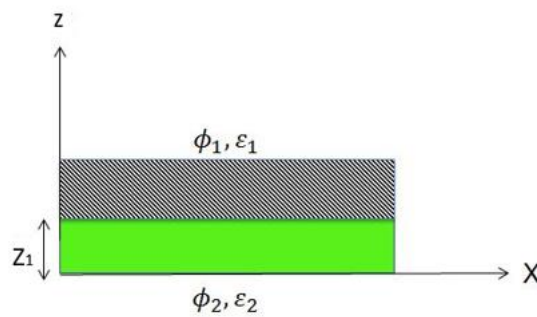


Figure 2-15. Definition of boundary conditions in Cartesian coordinates

$$\phi_1(x, z) = \phi_2(x, z) \quad \text{at } Z=z_1 \quad (2-27)$$

$$\epsilon_1 \frac{\partial \phi_1(x, z)}{\partial z} = \epsilon_2 \frac{\partial \phi_2(x, z)}{\partial z} \quad \text{at } Z=z_I \quad (2-28)$$

After calculating the potential distribution in the system, the electric field and attractive force can be given by  $\vec{E} = -\nabla\phi$ , Eq. (2-25) respectively.

2.2.2.9.2 ii: - Calculating electroadhesive force using Conformal Mapping and total capacity of a system (hypothesis).

It is worth mentioning that the only difference between assumptions in this case and the previous one is that the relative permittivity varies between dielectric layers. Since the governing equation for electroadhesion is Laplace's equation, therefore, by neglecting the thickness of electrodes, a suitable conformal mapping function can be found to transfer each point of the complex geometry of interest to a conventional domain that allows the PDE to be easily solved.

**Schwarz–Christoffel Transformation:**

The Schwarz–Christoffel Transformation is an appropriate function (see figure 2-16) which can map an interdigitated electroadhesive 2D pad domain of interest (figure 2-17) to a rectangle domain with boundary conditions that can be expressed mathematically. It is written as follows:

$$W = A \int A(z - x_1)^{\alpha_1/\pi-1} A(z - x_2)^{\alpha_2/\pi-1} \dots A(z - x_n)^{\alpha_n/\pi-1} dz + B \quad (2-29)$$

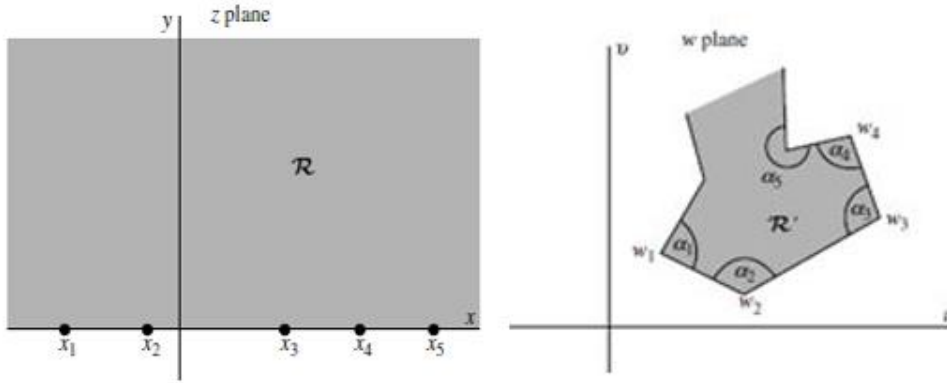


Figure 2-16. Schwarz-Christoffel transformation

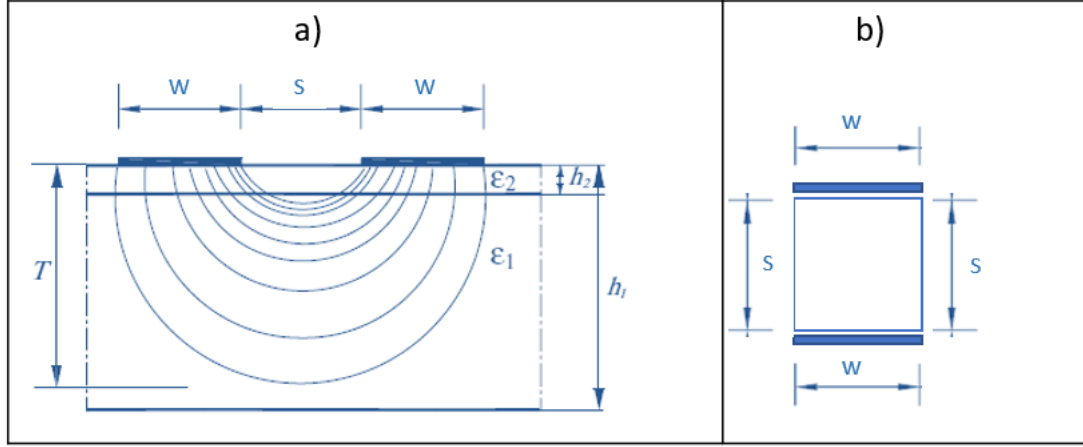


Figure 2-17. a) Coplanar capacitance domain for theoretical calculation using total capacity of system (Nassr et al., 2008) and b) mapped domain

Therefore, the total capacity of a system is calculated (Nassr, Ahmed & El-Dakhakhni, 2008) by the following Eq.:

$$C = \varepsilon_0 \varepsilon_{eff} \frac{K(K'_0)}{K(K_0)} \quad (2-30)$$

Where:

$\varepsilon_0$  is permittivity of free space

$\varepsilon_{eff}$  is effective permittivity of the system, and is calculated by:

$$\varepsilon_{eff} = 1 + (\varepsilon_1 - 1)q_1 + (\varepsilon_2 - \varepsilon_1)q_2 \quad (2-31)$$

$$q_i = \frac{1}{2} \frac{k(K'_i)K(K_0)}{k(K_i)K(K'_0)}; \quad i = 1, 2, \quad (2-32)$$

Where  $K_{(k)}$  is the complete elliptic integral of the first kind and the other parameters are calculated as follows:

$$K_0 = \frac{g}{W + S/2} K'_0 = \sqrt{1 - K_0^2} \quad (2-33)$$

$$K_i = \frac{\tanh(\frac{\pi g}{2h_i})}{\tanh(\frac{\pi(s+g)}{2h_i})}; \quad i = 1,2, \quad (2-34)$$

$$K'_i = \sqrt{1 - K_i^2}; \quad i = 1,2, \quad (2-35)$$

And finally, the electroadhesive force can be given as:

$$F = \frac{1}{2} \frac{C U^2}{\epsilon_0 S} \quad (2-36)$$

### 2.2.3 Parameters Influencing Electroadhesion

Many theoretical, experimental and numerical investigations (Ruffatto et al., 2014; Guo, Tailor, Bamber, 2015; Guo et al., 2016 a; Qin et al., 2007; Mao et al., 2016; Cao et al., 2016; Asano, Hatakeyama & Yatsuzuka, 2002; Koh, Chetty & Ponnambalam, 2011; Mao, Qin & Wang, 2014; Guo, Bamber & Hovell, 2016 b) have been carried out to find those parameters which influence the obtainable electroadhesive force, and they reported that applied voltage, electrical properties and pattern of electrodes, electrical properties of the dielectric layer, electrical properties of the substrate and the thickness of the air or vacuum layer between the dielectric and the substrate all affect the obtainable electroadhesive force which was listed below in more detail:

1- Magnitude of applied voltage (range of experimental tests up to now: 1-5 kV)

2- Electrode parameters including:

- a) Electrical conductivity of electrodes (usually copper with electrical conductivity of  $5.96 \times 10^7$  Siemens per meter (S/m) at 20 °C)
- b) Pattern of electrodes which includes shape of electrodes, width of electrodes, length of electrodes and space between adjacent electrodes

3-Dielectric parameters including:

- a) Relative permittivity of dielectric (which could vary with ambient temperature and relative humidity), (range of experimental tests up to now: 2-4)
- b) Volume resistivity of dielectric (range of experimental tests up to now:  $10^{16}$ - $10^{17}$  ( $\Omega \cdot \text{cm}$ ))
- c) Dielectric strength (range of experimental tests up to now: 150-200V/ $\mu\text{m}$ )



d) Thickness of dielectric (range of experimental tests up to now: 10-150  $\mu\text{m}$ )

e) Surface roughness of dielectric

4-Substrate parameters including:

a) Electrical conductivity (considered to be conductive or insulating material)

b) Relative permittivity of insulating substrate (range of experimental tests up to now: 2-5)

c) Surface roughness of substrate

5- Thickness of air or vacuum layer between dielectric and substrate

## 2.3 History of Electroadhesion Research

In this section, some of the most important research and development strategies followed are explained in more detail.

### 2.3.1 Empirical relation for EA force

Suggested empirical correlation (Monkman, Hesse, Steinmann et al., 2007 and Mao et al., 2014) of generated EA forces gives a good approximation of the relationships between parameters that have a profound effect on the obtainable attractive force; however, this correlation neglect some of the parameters which have been shown that influence obtainable EA force such as electrodes shape, the relative permittivity of the substrate. The correlation shows a quadratic relationship between applied voltage and obtainable EA force. The relation also shows that the obtainable EA force is inversely proportional to the dielectric thickness; therefore, decreasing dielectric thickness as much as possible in practice is desirable.

$$F \propto \frac{A\epsilon_r V^2}{d^2} \quad (2-37)$$

### 2.3.2 Effect of Electrode Thickness on EA Force Generation

Guo et al. (2016 a) numerically investigated the influence of electrode thickness and reported that electrode thickness does not have a marked effect on electroadhesive force (see figure 2-18) and could thus be neglected.

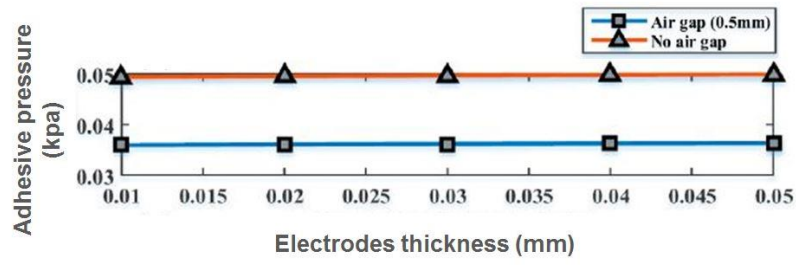


Figure 2-18. Independency of electroadhesive force to electrode's thickness (Guo et al., 2016 a)

### 2.3.3 Effect of air layer thickness and electrical properties of dielectric layer and substrate on EA force

Parametric analysis carried out by Mao et al. (2016) numerically and theoretically proved that the thickness of the air layer between a dielectric and a substrate could influence the obtainable force (see figure 2-19). They also reported that the obtainable force is proportional to both the dielectric and the substrate relative permittivities (see figure 2-20). The reported trends are in good agreement with the result (see figure 2-21) of the research carried out by Akherat, Karimi, Alizadehyazdi et al. (2019); however, there is the optimal relative permittivity of the dielectric layer for bi-layer EA devices according to the research findings (see figure 2-22) by Akherat et al. (2019).

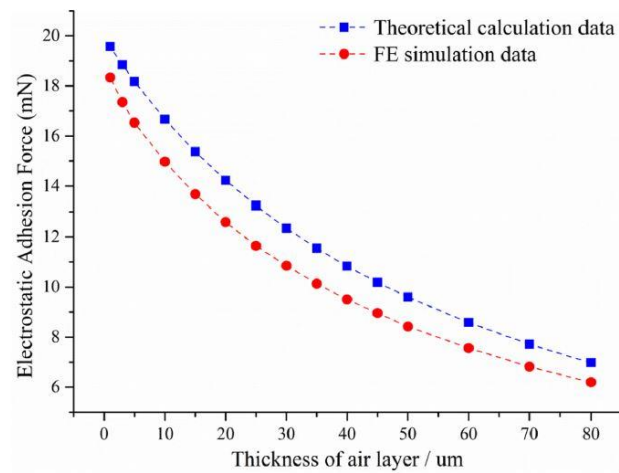


Figure 2-19. Thickness of air layer effect on electroadhesive force (Mao et al., 2016)

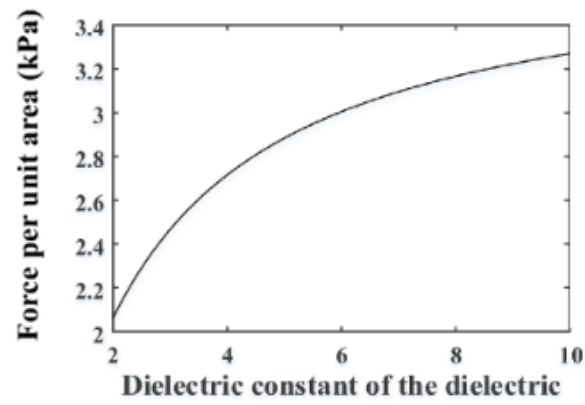


Figure 2-20. Effect of relative permittivity of dielectric layer on EA force (Guo et al., 2016 a)

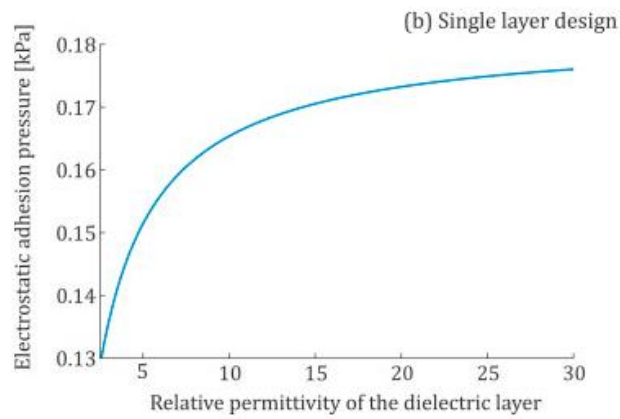


Figure 2-21. Effect of relative permittivity of dielectric layer on EA force (Akherat et al., 2019)

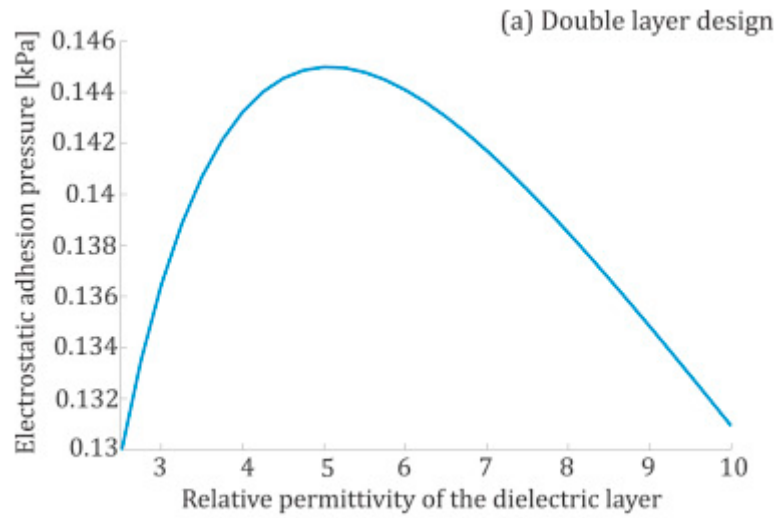


Figure 2-22. Optimal relative permittivity of a dielectric layer for bi-layer EA devices (Akherat et al., 2019)

### 2.3.4 Optimal electrode width and spacing for uni and bi-layer EA device

Experimental findings and numerical analysis explained in more detail below show that the optimal value of electrode width and spacing for uni-layer and bilayer is different. While there is an optimal electrode width and spacing value for bilayer EA devices, there is only an optimal electrode width value for uni-layer EA devices.

#### 2.3.4.1 Optimal electrodes width and spacing for uni-layer EA device

Guo et al. (2016 a) showed (see figure 2-23) that EA force is inversely proportional to the space between electrodes, and the shorter the distance between electrodes, the greater the EA force is generated; however, in practice, the dielectric strength of materials used for fabricating EA devices imposes limitations of the minimum space between electrodes avoiding a dielectric breakdown. Their finding also shows optimal electrode width to maximize obtainable EA force (see figure 2-24).

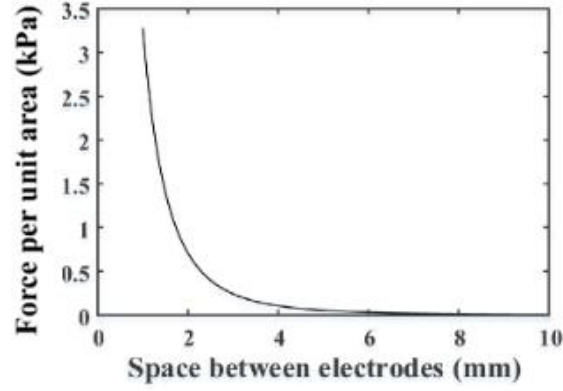


Figure 2-23. Effect of electrodes spacing on EA force (Guo et al., 2016 a)

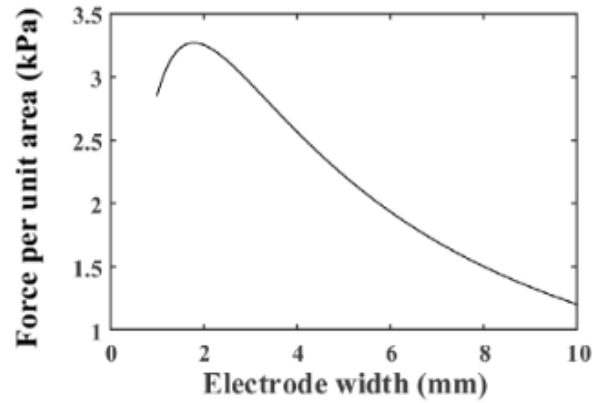


Figure 2-24. Optimal electrode's width for uni-layer EA devices (Guo et al., 2016 a)

#### 2.3.4.2 Optimal Electrode width and spacing of bi-layer EA devices

Dadkhah et al. (2019) investigated the relationship between optimum electrode width and spacing and a gap between EA device and substrates with different relative permittivity. The results showed (see figure 2-25) that optimum electrode width and spacing depend on the gap and substrate relative permittivity.

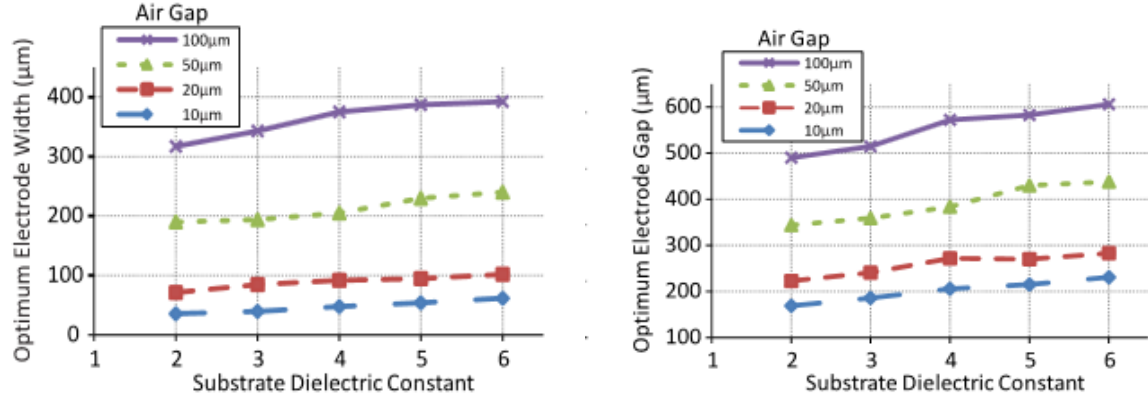


Figure 2-25. Optimal electrode widths for bi-layer EA devices (Dadkhah et al., 2019)

### 2.3.5 Effect of electrodes pattern on obtainable EA force

Topology optimization offers a significant development in engineering designs, and electroadhesion was no exception. Researchers started to find optimal topology of electrodes by try and error (testing different electrode patterns) and followed their investigations with the help of numerical analysis and mathematically sensible optimization criteria such as average intensity of electric field of a system (see figure 2-26) and total capacitance of a system (see figure 2-27).

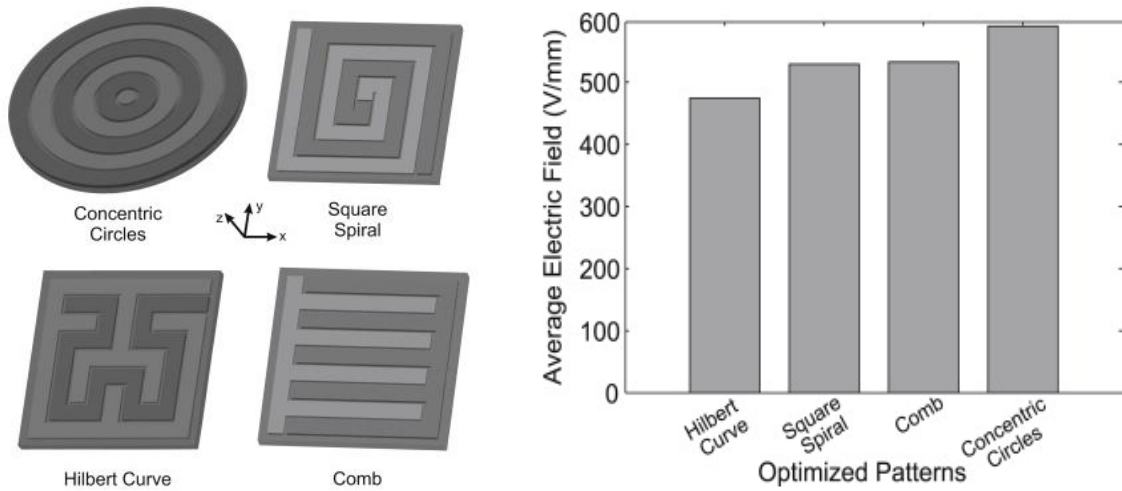


Figure 2-26. Optimization of electrodes pattern considering average intensity of electric field of a system (Ruffato et al., 2014)

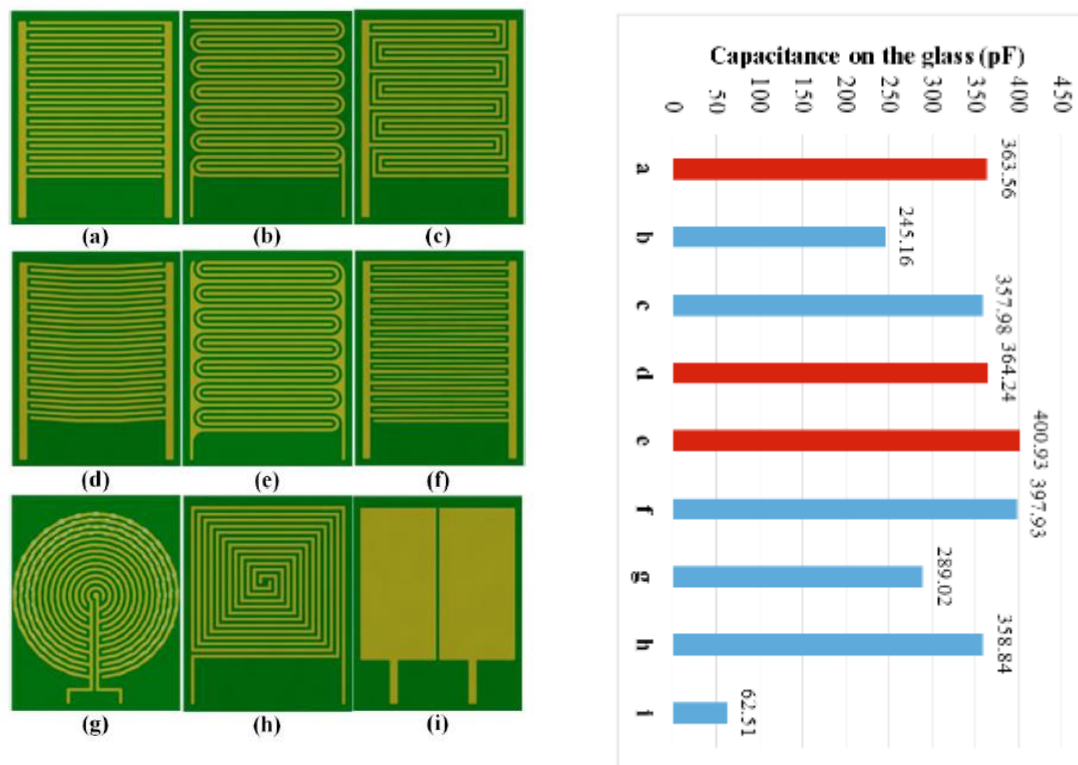


Figure 2-27. Optimization of electrodes pattern considering total capacitance of a system (Guo et al., 2016 b)

### 2.3.6 Effect of Surface texture on obtainable EA force

Guo et al. (2016 c) conducted an experimental investigation to find the relationship between surface texture and obtainable EA force. Findings indicate that EA force is inversely proportional to the interfacial surface's  $S_q$  (root mean square height). Figure (2-28) depicts the relationship between  $S_q$  and obtainable EA force.

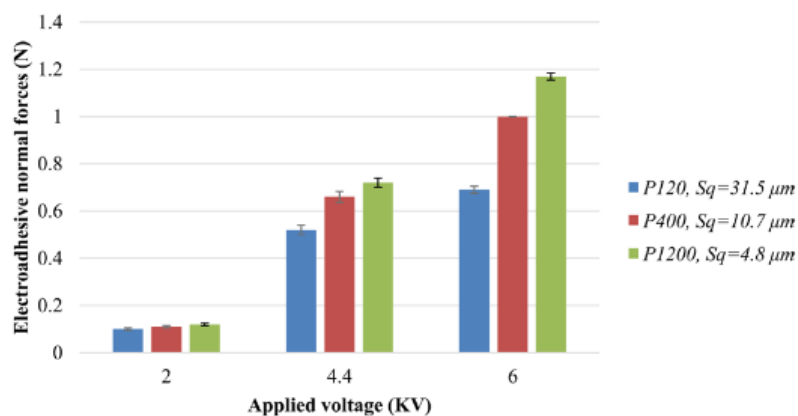


Figure 2-28. Relationship between EA force and surface texture (Guo et al., 2016 c)

### 2.3.7 Instability of EA devices performance

Guo et al. (2016 a) have tested an EA device over a period of 5 days and results showed (see figure 2-29) that the obtainable EA force is unstable. They suggested that possibly environmental conditions such as relative humidity result in this variability in EA performance.

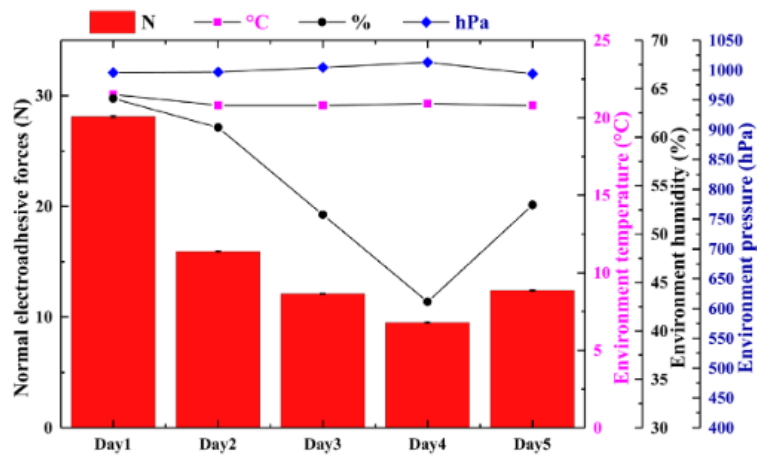


Figure 2-29. Instability of EA devices performance (Guo et al., 2016 a)

Table (2-3) summarizes some of the research that has been carried out to investigate parameters that influence electroadhesion and different criteria applied to optimize EA pad design.



Table 2-5. Summary of electroadhesion investigations and optimizations

Pattern of electrodes	Evaluation method	V <sub>DC</sub> (kV)	Effective area (mm <sup>2</sup> )	Dielectric material/ ε <sub>d</sub>	t <sub>d</sub>	Substrate(c onductive/ non- conductive)	ε <sub>s</sub>	Optimization method	Optimization criteria	Optimization parameters	EA Performance range	Ref
Interdigital	Theoretical	1 - 6	Periodic BC	2 – 10	0.2-1 mm	Non-con	2-10	Matlab function fminsearchbnd	$F = \frac{1}{2} \frac{C_e^2 U^2}{\epsilon_0 S}$	With/Space =1.8	0-3.5 kPa	Guo et al., 2016 a
Interdigital	Numerical	1 - 6	Periodic BC	2 – 10	0.2-1 mm	Non-con	2-10	Parametric FEA	Calculated force	Depending on substrate thickness	0-0.06 kPa	
Interdigital	Experimental	2	170-230	Polyester	23 μm	Toughened glass	NM	Parametric	measured force	Width/Space =1.9	0-0.08 kPa	
Interdigital	Experimental	2	170-230	Polyester	23 μm	Aluminium	NM	Parametric	measured force	With/Space as large as possible	0-0.035 kPa	
Interdigital	Numerical	5	40.8mm×L (constant number of electrodes )	3	150μ m	Glass	5	Gradient descent algorithm	Average electric field strength for total node	W <sub>1</sub> ...,W <sub>9(mm)</sub> = 1.6, 4.8, 4.6, 4.7, 4.6, 4.7, 4.6, 4.8, 1.6	average electric field =500(V/m m)	Ruffatto et al., 2014
Concentric circle	Numerical	5	π(22.8) <sup>2</sup>	3	150μ m	Glass	5	Gradient descent algorithm	Average electric field strength for total node	W <sub>1</sub> ...,W <sub>5(mm)</sub> = 6.8, 5.9, 5.3 4.6, 1.2	average electric field =600(V/m m)	

Pattern of electrodes	Evaluation method	V <sub>DC</sub> (kV)	Effective area (mm <sup>2</sup> )	Dielectric material/ $\epsilon_a$	t <sub>d</sub>	Substrate(c onductive/ non- conductive)	$\epsilon_s$	Optimization method	Optimization criteria	Optimization parameters	EA Performance range	Ref
Square spiral	Numerical	5	NM	3	150 $\mu$ m	Glass	5	Gradient descent algorithm	Average electric field strength for total node	W(CST)=3.6	Average electric field =500(V/m m)	
Hilbert pattern	Numerical	5	NM	3	150 $\mu$ m	Glass	5	Gradient descent algorithm	Average electric field strength for total node	W(CST)=3.6	Average electric field =450(V/m m)	
Interdigital	Experimental	5	40.8mm×L (Constant number of electrodes)	3.3	150 $\mu$ m	Dry wall, Cedar and Tile	NM	Gradient descent algorithm	Average electric field strength for total node	W <sub>1</sub> ..., W <sub>9(mm)</sub> = 1.6, 4.8, 4.6, 4.7, 4.6, 4.7, 4.6, 4.8, 1.6	Shear pre unit area 1.8-10 kPa	Ruffatto et al., 2014
Concentric circle	Experimental	5	$\pi(22.8)^2$	3.3	150 $\mu$ m	Dry wall, Cedar and Tile	NM	Gradient descent algorithm	Average electric field strength for total node	W <sub>1</sub> ..., W <sub>5(mm)</sub> = 6.8, 5.9, 5.3 4.6, 1.2	Shear pre unit area 3.8-11.8 kPa	
Square spiral	Experimental	5	NM	3.3	150 $\mu$ m	Dry wall, Cedar and Tile	NM	Gradient descent algorithm	Average electric field strength for total node	W(CST)=3.6	Shear pre unit area 2.2-10 kPa	
Hilbert pattern	Experimental	5	NM	3.3	150 $\mu$ m	Dry wall, Cedar and Tile	NM	Gradient descent algorithm	Average electric field strength for total node	W(CST)=3.6	Shear pre unit area 2.8-8 kPa	

Pattern of electrodes	Evaluation method	V <sub>DC</sub> (kV)	Effective area (mm <sup>2</sup> )	Dielectric material/ $\epsilon_d$	t <sub>d</sub>	Substrate (conductive/ non-conductive)	$\epsilon_s$	Optimization method	Optimization criteria	Optimization parameters	EA Performance range	Ref
Concentric circle	Theoretical and Numerical	0.5-4.5	$\pi(6)^2$	3.5	10-130 $\mu\text{m}$	non-con	6.4	Parametric	Calculated force	N/A	300 mN	Mao et al., 2016
Interdigital	Theoretical and Numerical	1-2	Periodic BC	2-10	15-55 $\mu\text{m}$	non-con	2-10	Parametric	Calculated force	N/A	Shear force 2.5-12 N	Qin et al., 2007
Interdigital	Experimental	3	360×360	Polyimide	25 $\mu\text{m}$	wall board and glass	Not	N/A	N/A	N/A	Shear force 1-40 N	
Different patterns	Numerical	6	150×180	Polyimide/10	0.5mm	Glass	4.2	Numerical calculation	Total capacity	Electrodes pattern	Capacitance range 62-400 pf	Guo et al., 2016 b

Average electric field strength for total node ( $E_{ave}$ ) is calculated by following  $E_{ave} = \frac{1}{p \times q \times r} \sum_{i=1}^p \sum_{j=1}^q \sum_{k=1}^r E_{i,j,k}$  where p, q and r are total number of nodes in x, y and z direction respectively.  $t_d$  is thickness of dielectric.  $\epsilon_d$  and  $\epsilon_s$  are relative permittivity of dielectric and substrate respectively and w is width of electrodes.

## ***Chapter 3* Dielectric materials**

As mentioned in the previous chapter, the relative permittivity of the dielectric layer and the substrate play an essential role in generated EA force; therefore, in this chapter, the electrical properties of many possible dielectric materials, including solids, liquid and gaseous dielectrics which potentially can be used for EA devices are reviewed.

### **3.1 Dielectric definition**

A dielectric material is a more or less insulating material (with high resistivity) which means that no current will flow through the material when a voltage is applied due to having an energy gap of 3eV or more (Gupta & Gupta, 2015). When external electric fields are applied to dielectric materials, the electron clouds of constituent atoms move slightly away from their normal positions and result in electrical energy storage. The capability of a dielectric material to store energy compared to a vacuum is called the relative permittivity ( $\epsilon_r$ ).

### **3.2 Classification of Dielectric Materials**

Dielectric materials may be classified by considering the state of material (solid, liquid and gaseous material); the maximum working temperature, and the material's availability (natural or synthetic materials).

### **3.3 Dielectric Properties**

Factors that need to be considered to choose adequate dielectric materials for every application are:

- i. Relative permittivity
- ii. Dielectric strength
- iii. Dielectric loss tangent ( $\tan \delta$ ) (only for AC voltage applications)
- iv. Surface and volume resistivity
- v. Relative permittivity temperature stability

### 3.4 Classification of dielectric materials based on relative permittivities and applications

#### 3.4.1 Low relative permittivity materials for interlayer dielectrics

The key drivers for the growth of this type of dielectric are to improve electronic circuit performance (Nalwa, 1999) in terms of speed, power consumption, and signal to noise ratio.

Table 3-1. Relative permittivity of low dielectric materials for interlayer dielectrics (Nalwa, 1999)

Compound	Melting point °C	$\epsilon_r$
SiO <sub>2</sub>	No issue	3.8
F-SiO <sub>2</sub>	No issue	$\approx 3.5$
Polystyrene	Tg $\approx 95$	2.6
Sesquisiloxane	>250	2.7
Poly(phenylene oxide)	170-190	2.6
Polyethylene	135	2.3
Polypropylene	170	2.3
Parylene	350	2.4-2.6
Teflon	325	1.9

#### 3.4.2 Low relative permittivity glasses and glass-ceramics for electronic packaging applications

Electronic packaging, here, is referred to as controlling and designing an environment which surrounds an electronic device by means of glass or glass-ceramic, and is optimized for following functions (Nalwa, 1999):

- i. Transferring generated heat from the chip
- ii. Distributing power efficiently
- iii. Providing protection system from corrosive environments
- iv. Transporting generated signal efficiently

Table 3-2. Relative permittivity of low relative permittivity glasses and glass-ceramic (Nalwa, 1999)

Material	Relative permittivity at 1 MHz	Coefficient of thermal expansion ( $10^{-7}/^{\circ}\text{C}$ )
<b>Glasses</b>		
SiO <sub>2</sub> (fused silica)	3.8	50
B <sub>2</sub> O <sub>3</sub> -SiO <sub>2</sub> -Al <sub>2</sub> O <sub>3</sub> -Na <sub>2</sub> O	4.1	32
<b>Glass+(ceramics)</b>		
PbO-B <sub>2</sub> O <sub>3</sub> -SiO <sub>2</sub> +(Al <sub>2</sub> O <sub>3</sub> )	7.5	42
MgO-Al <sub>2</sub> O <sub>3</sub> -SiO <sub>2</sub> -B <sub>2</sub> O <sub>3</sub> +(Al <sub>2</sub> O <sub>3</sub> )	4.5	30
B <sub>2</sub> O <sub>3</sub> -SiO <sub>2</sub> +(Al <sub>2</sub> O <sub>3</sub> )	5.6	45
2MgO·2Al <sub>2</sub> O <sub>3</sub> ·5SiO <sub>2</sub> +(Al <sub>2</sub> O <sub>3</sub> )	5.5	30
CaO-Al <sub>2</sub> O <sub>3</sub> -SiO <sub>2</sub> -B <sub>2</sub> O <sub>3</sub> -SiO <sub>2</sub> +(Al <sub>2</sub> O <sub>3</sub> )	7.7	55
Li <sub>2</sub> O-SiO <sub>2</sub> -MgO-Al <sub>2</sub> O <sub>3</sub> +(Al <sub>2</sub> O <sub>3</sub> )	7.3	59
Li <sub>2</sub> O- Al <sub>2</sub> O <sub>3</sub> - SiO <sub>2</sub> +(Al <sub>2</sub> O <sub>3</sub> )	7.8	30
<b>Glass-Ceramics</b>		
MgO-Al <sub>2</sub> O <sub>3</sub> -SiO <sub>2</sub> -B <sub>2</sub> O <sub>3</sub> +P <sub>2</sub> O <sub>5</sub>	5.0	30
Li <sub>2</sub> O- Al <sub>2</sub> O <sub>3</sub> - SiO <sub>2</sub> -B <sub>2</sub> O <sub>3</sub>	6.5	12
MgO-Al <sub>2</sub> O <sub>3</sub> -SiO <sub>2</sub> -B <sub>2</sub> O <sub>3</sub> containing ZnO, P <sub>2</sub> O <sub>5</sub> , TiO <sub>2</sub> , CaO, ZrO <sub>2</sub> , and Y <sub>2</sub> O <sub>3</sub>	5.0-5.7	16-37

Ceramic dielectrics are usually classified by their relative permittivities into three different categories as follows:

- i. Low permittivity ( $\epsilon_r < 15$ )
- ii. Medium permittivity ( $15 < \epsilon_r < 500$ )
- iii. High permittivity ( $\epsilon_r > 500$ )

#### 3.4.3.1 Low -permittivity ceramic dielectrics

Low -permittivity ceramic dielectrics are often natural mineral compounds (silicates and aluminosilicates) and are generally used as an insulator, therefore their mechanical properties may be important (Nalwa, 1999). Their applications are listed below:

- i. As a small capacitor for high frequency AC systems

- ii. As a large capacitor for high rate of heat dissipation

Table 3-3. Relative permittivity of low relative permittivity ceramic dielectrics (Nalwa, 1999)

Material	$\epsilon_r$	$\tan \delta / 10^{-4}$ at 1 MHz	at 1000°C	20- $\lambda / \text{Wm}^{-1}\text{k}^{-1}$ at 25°C
'Low-loss' steatite	6.1	7	8.9	3
Cordierite	5.7	80	2.9	2
Forsterite	6.4	2	10.7	3
96 Al <sub>2</sub> O <sub>3</sub>	9.7	3	8.2	35
99.5 BeO	6.8	2	8.8	250
AlN	8.8	5-10	4.5	100
Glass	4-15	2-22	0.8-9	0.5-2.0

### 3.4.3.2 Medium-permittivity ceramic dielectrics

Ceramic dielectrics with relative permittivity ranging between 15-100 and low dissipation factors are in this category. The most common compound of these dielectrics is titanium dioxide, TiO<sub>2</sub>. Between three phases of titania, rutile is the only stable phase above 800°C and is an important dielectric in this class.

Three main applications of medium-permittivity dielectrics are as follows:

- i. High-power transmitter capacitors for the frequency range 0.5–50MHz
- ii. Stable capacitors for general electronic use
- iii. Microwave resonant devices

### 3.4.3.3 High-permittivity ceramic dielectrics

This class of ceramic dielectrics is based on ferroelectric materials and compared to lower-permittivity dielectrics, shows more sensitivity to operating temperature, strength of electric field and frequency.

#### 3.4.3.3.1 Barium Titanate

Barium titanate (BaTiO<sub>3</sub>) with the perovskite structure (ABO<sub>3</sub>) is a well-known ferroelectric material which has received much attention since 1943 due to having high relative permittivity. BaTiO<sub>3</sub>, at room temperature, has a Tetragonal structure and could appear in Rhombohedral, Orthorhombic and Cubic structures at different temperature.



The relative permittivity of BaTiO<sub>3</sub> also strongly depends on grain size. Kinoshita & Yamaji (1976) investigated grain size (1.1 $\mu$ m to 53 $\mu$ m) effects on the relative permittivity of all possible BaTiO<sub>3</sub> phases and reported that only in the cubic phase that BaTiO<sub>3</sub> shows paraelectric behaviour, with the relative permittivity not dependant on grain size. Figure (3-1) shows the grain size dependency of BaTiO<sub>3</sub> relative permittivity for a range of temperatures. The peaks in relative permittivity correspond to phase transition points from cubic to tetragonal at above 100°C; tetragonal to orthorhombic at above 0°C; and orthorhombic to rhombohedral below -50°C.

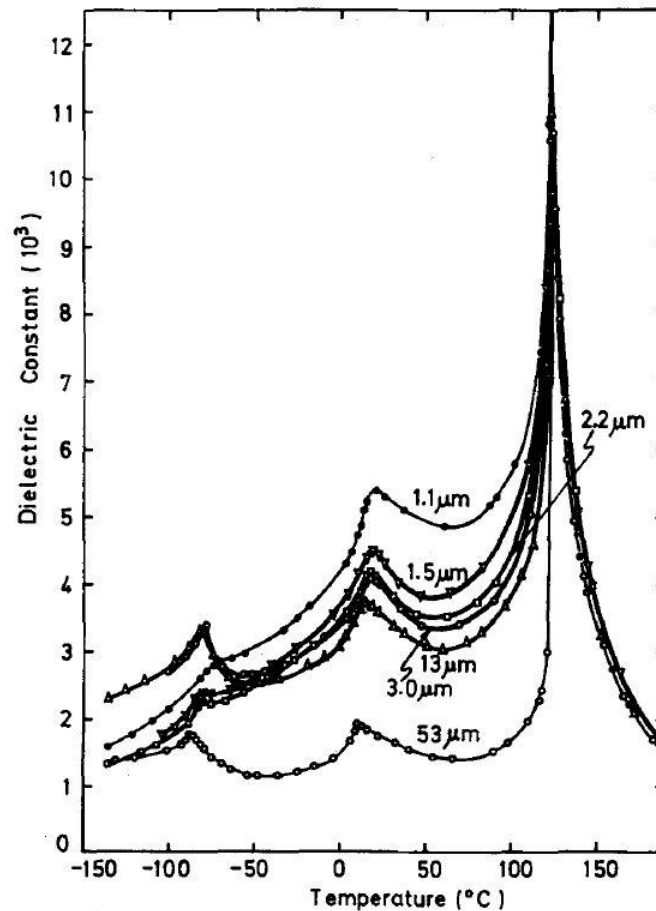


Figure 3-1. Grain size dependency of BaTiO<sub>3</sub> relative permittivity (Kinoshita & Yamaji, 1976)

Arlt, Hennings & De With (1985) measured the relative permittivity of BaTiO<sub>3</sub> with different grain sizes and reported that at room temperature, the relative permittivity of BaTiO<sub>3</sub> has a maximum at a grain size of about 1 $\mu$ m. Huan, Wang & Fang (2014) prepared BaTiO<sub>3</sub> with different grain sizes, ranging from 0.29 $\mu$ m to 8.61 $\mu$ m, and reported that for a grain size less than 1 $\mu$ m, the relative permittivity of BaTiO<sub>3</sub> decreases with decreasing grain size. Figure (3-2) shows the relative permittivity versus temperature curves of different grain size of BaTiO<sub>3</sub> at 1 kHz.

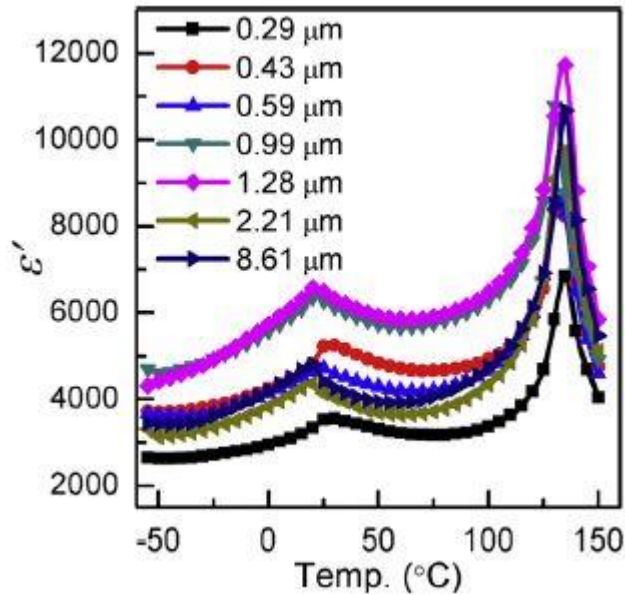


Figure 3-2. Grain size dependency of BaTiO<sub>3</sub> relative permittivity (Huan, Wang & Fang, 2014)

The A and B sites of BaTiO<sub>3</sub> have been modified independently and simultaneously with isovalent and heterovalent substitutions, to answer the needs of different applications, therefore these materials potentially could be suitable options for electroadhesion applications as dielectric materials. Following are some of the dielectric property investigations which have been carried out.

#### 3.4.3.3.2 Strontium Doped Barium Titanate (BST)

Ba<sub>(1-x)</sub>Sr<sub>x</sub>TiO<sub>3</sub> has received great attention, because not only doping BT by Sr improves relative permittivity of the composition (see figure 3-3) but also Curie temperature could be controlled by varying the strontium concentration (Tagantsev, Sherman & Astafiev, 2003). Curie point, also called Curie temperature, is a temperature at which magnetic materials undergo a sharp change in their magnetic properties. In this case relative permittivity of a dielectric undergoes a sharp decrease at temperatures above the Curie point.

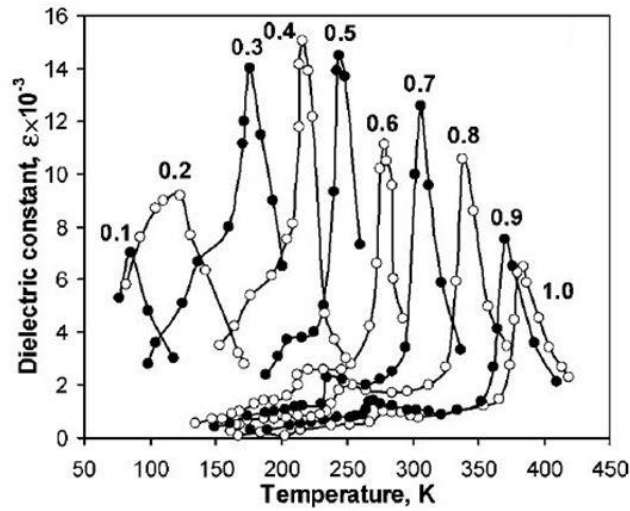


Figure 3-3. Relative permittivity of BT doped with different concentration (varies between 0 and 1) of strontium (Tagantsev et al., 2003).

Sr, La and Pb which modify A sites and Zr, Sn and Hf which modify B sites of BT are called Curie point shifters. Table (3-4) shows the effect of adding those materials on changing the Curie temperature of BT (Gupta & Gupta, 2015).

Table 3-4. Effect of different dopant materials on Curie temperature of BT (Gupta & Gupta, 2015)

Base titanate	+	Cure point shifter	Rate of change in Curie temperature (dT/dx)	Solid solubility (%)
BaTiO <sub>3</sub>	+	SrTiO <sub>3</sub>	-3.7°C	-
BaTiO <sub>3</sub>	+	LaTiO <sub>3</sub>	-18°C	15%
BaTiO <sub>3</sub>	+	PbTiO <sub>3</sub>	3.7°C	-
BaTiO <sub>3</sub>	+	BaZrO <sub>3</sub>	-5.3°C	100%
BaTiO <sub>3</sub>	+	BaSnO <sub>3</sub>	-8°C	100%
BaTiO <sub>3</sub>	+	BaHfO <sub>3</sub>	-5°C	100%

#### 3.4.3.3.3 Lanthanum Doped Barium Titanate

Ba<sub>(1-x)</sub>La<sub>2x/3</sub>TiO<sub>3</sub> ceramic is a non-stoichiometric perovskite type solid solutions and has been widely used as a dielectric material in multilayer ceramic capacitors with Ni internal electrode (Ni-MLcc). Increasing La content results in a phase transition from tetragonal to cubic, and

changes in grain size.  $\text{Ba}_{(1-x)}\text{La}_{2x/3}\text{TiO}_3$  ( $0.00 < x < 0.10$ ) was investigated by Ganguly, Rout & Sinha (2013). Figure (3-4) shows the relative permittivity of lanthanum doped barium titanate.

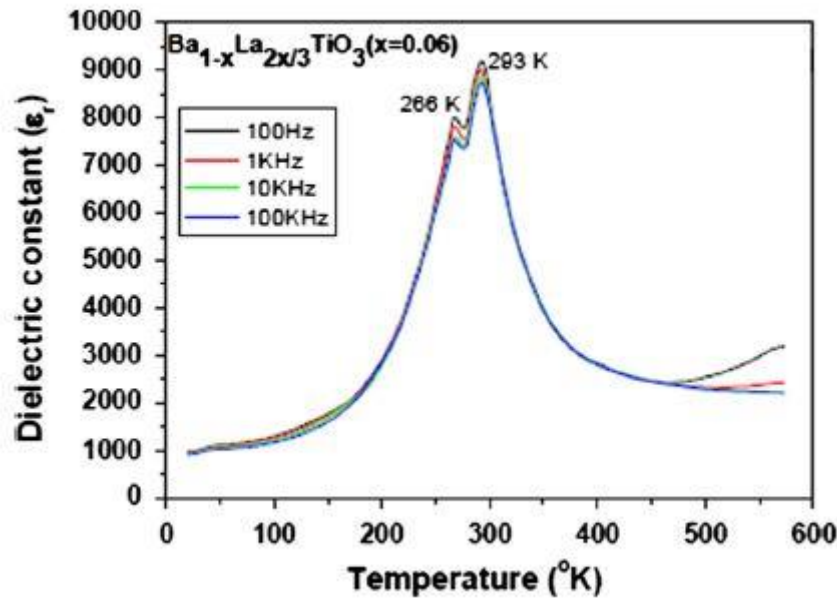


Figure 3-4. Relative permittivity of lanthanum doped barium titanate versus temperature (Ganguly et al., 2013)

#### 3.4.3.3.4 Lead doped barium titanate

Lead doped barium titanate ( $\text{Ba}_{(1-x)}\text{Pb}_x\text{TiO}_3$ ), where  $x$  ranged between 0.025 and 0.75, was investigated by Vold, Biederman & Rossetti (2001). They reported that  $\text{Pb}^{2+}$  incorporated into the BT perovskite structure if the dopant is less than 20%. Pb-doped Barium titanate has many applications including transducers, actuators, hydrophones and infrared sensors. Sareecha, Shah & Maqsood (2017, p. 42) fabricated  $\text{Ba}_{(1-x)}\text{Pb}_x\text{TiO}_3$ , with  $x$  varying between 0 and 0.1, and showed that by increasing Pb molar fraction, the Curie point shifted to higher temperatures and also relative permittivity was promoted. Figure (3-5) shows the effect of Pb molar fraction on relative permittivity of  $\text{Ba}_{(1-x)}\text{Pb}_x\text{TiO}_3$ .

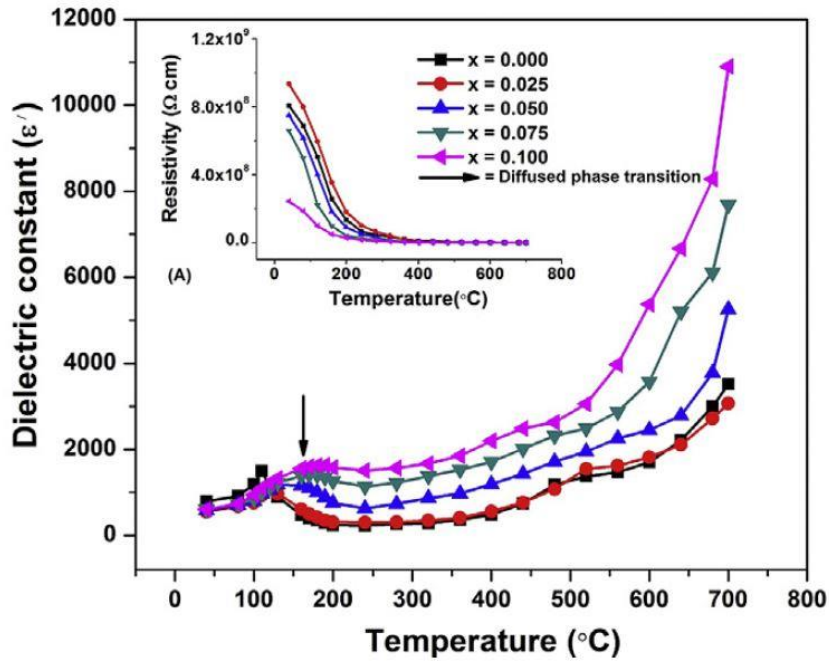


Figure 3-5. Relative permittivity of doped BT with different concentration of lead (Vold et al., 2001)

#### 3.4.3.3.5 Zirconium doped barium titanate

Finding environmentally- friendly materials with comparable electrical properties to replace Lead barium zirconate (PBZ) and lead zirconate titanate (PZT) has led researchers to focus on lead free ceramics. Zirconium doped barium titanate ( $\text{BaZr}_x\text{Ti}_{(1-x)}\text{O}_3$ ) is B-site modification of BT and was investigated by Sun, Li & Zheng (2015) with different zirconate contents (see figure 3-6).

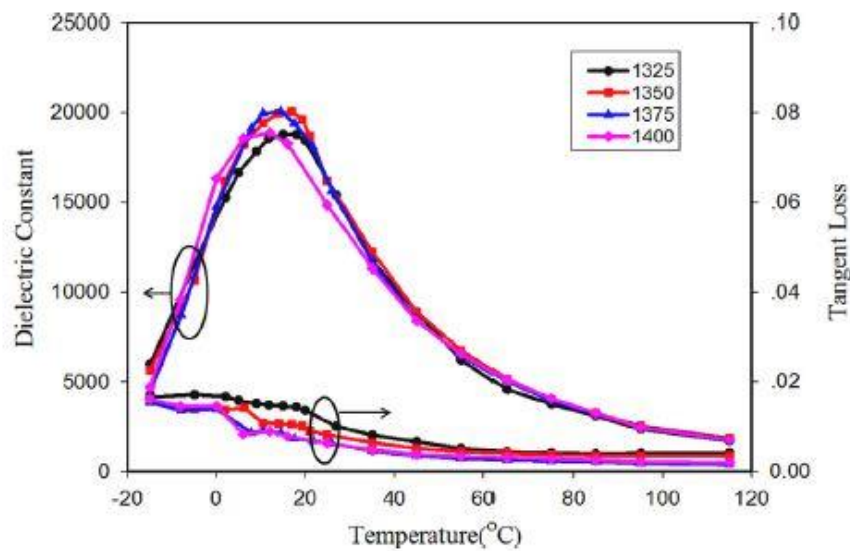


Figure 3-6. Dielectric properties of zirconium doped barium titanate with sintering temperature between 1325°C and 1400°C(Sun, Li & Zheng, 2015)

#### 3.4.3.3.6 Tin doped barium titanate ( $\text{BaSn}_x\text{Ti}_{(1-x)}\text{O}_3$ , BTS)

Tin (Sn) is classified as a Curie point shifter to a lower temperature and modifies the B-site of barium titanate. Wei & Yao (2007) synthesized BTS with different Sn concentrations using a solid state synthesis route and measured dielectric properties (see figure 3-7) and reported that the highest relative permittivity belongs to  $\text{BaSn}_{0.1}\text{Ti}_{0.9}\text{O}_3$ .

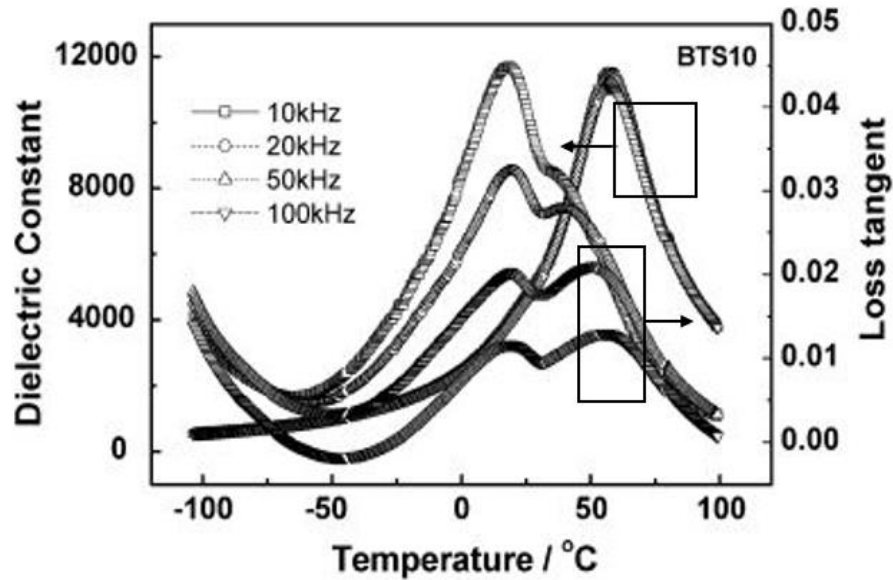


Figure 3-7. Relative permittivity of tin doped barium titanate versus temperature (Wei & Yao, 2007)

#### 3.4.3.3.7 Rare earth (Dy, Tb and Eu) doped barium titanate

2.0% molar Dy, Tb and Eu doped barium titanate and their dielectric properties were investigated by Li, and Yao (2012).  $\text{Dy}^{3+}$  and  $\text{Tb}^{3+}$  ions simultaneously modified the A site and B site of the perovskite structure of BT while  $\text{Eu}^{3+}$  only was substituted in the A site. Figure (3-8) shows the relative permittivity of rare earth doped BT.

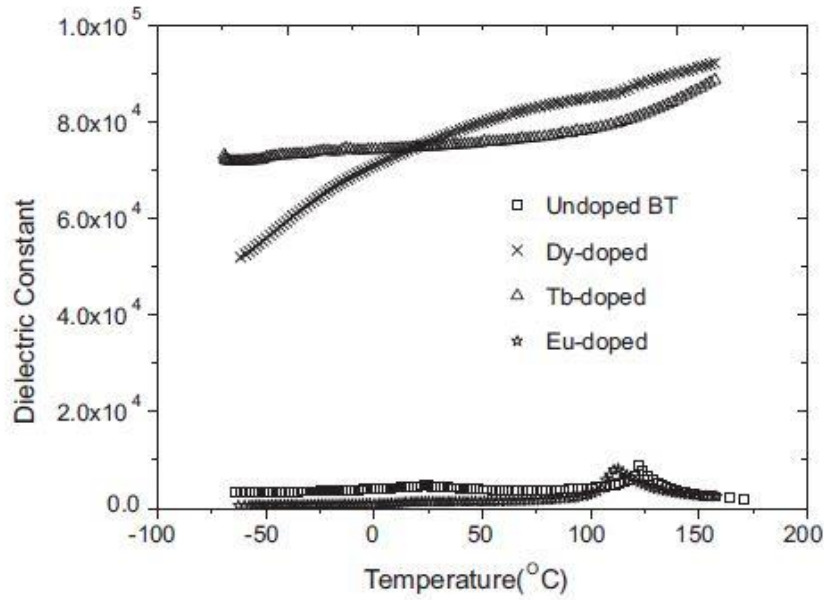


Figure 3-8. Relative permittivity of rare earth doped Barium titanate versus temperature (Li, and Yao, 2012)

#### 3.4.3.4 Co-doped Barium titanate

##### 3.4.3.4.1 La/Mn co-doped BaTiO<sub>3</sub>

One possible co-doping scenario of barium titanate is to modify the A site ( $\text{Ba}^{2+}$ ) by a donor and B site ( $\text{Ti}^{4+}$ ) by an acceptor which generally leads to a uniform microstructure and high relative permittivity at room temperature. Paunovic, Mitic & Marjanovic (2016) investigated the microstructure and dielectric properties of La/Mn co-doped BaTiO<sub>3</sub> ceramics with various La<sub>2</sub>O<sub>3</sub> content (from 0.3% to 1.0%) and constant MnO<sub>2</sub> content (0.01%). Figure (3-9) shows the effect of La/Mn co-doped on the relative permittivity of BT.

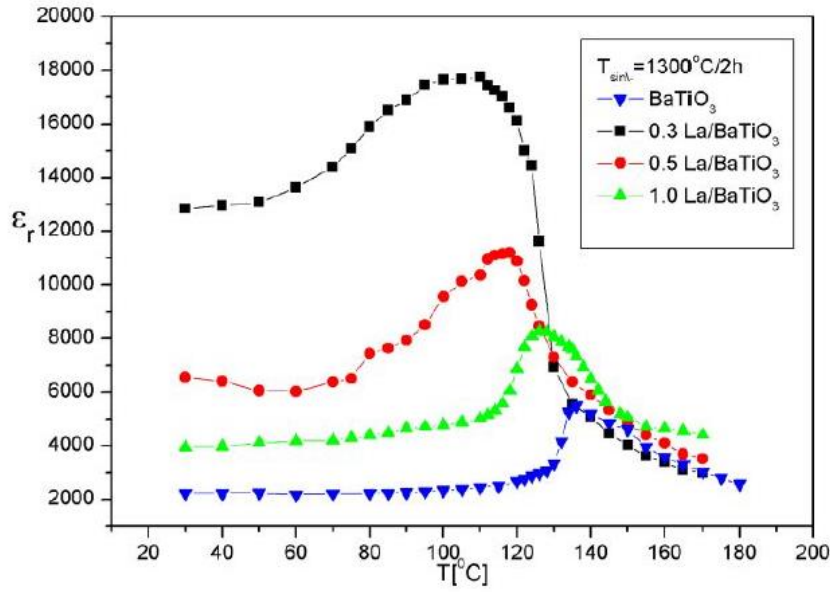


Figure 3-9. Relative permittivity of BT doped with different La concentration versus temperature (Paunovic et al., 2016)

#### 3.4.3.4.2 Modification of barium zirconate titanate ( $\text{BaZr}_{0.15}\text{Ti}_{0.85}\text{O}_3$ ) with donor dopants

Qi, Liu, Tian & Zou (2012) studied doped Barium zirconate titanate with donor dopants (La, Ce, Nd, Sm, Eu, Dy, Yb and Y) and reported that for some of dopants not only a large enhancement of the dielectric permittivity is achieved but also a remarkable shift of Curie temperature occurred. Figure (3-10) shows rare earth co-doped BZT relative permittivity versus temperature.

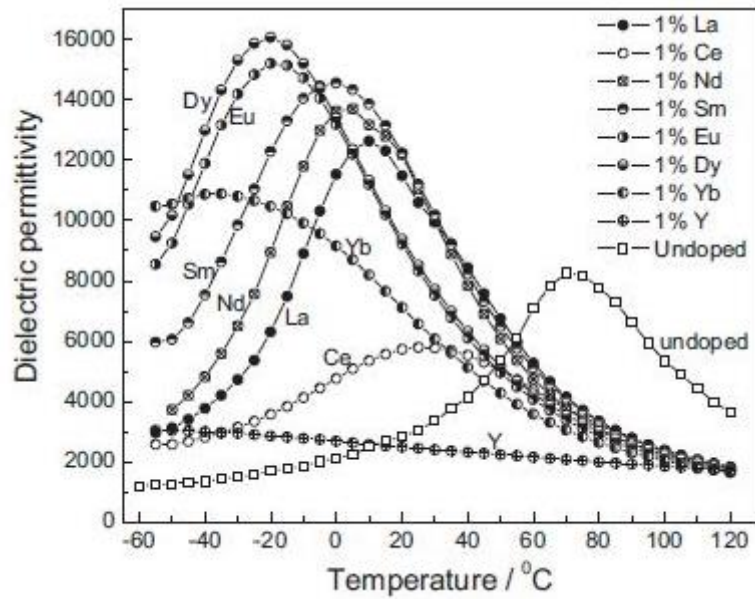


Figure 3-10. Relative permittivity of BT doped with 1% of different rare earth oxide (Qi et al., 2012)



Some other types of co-doped Barium titanate are listed in table (3-5).

Table 3-5. Room temperature relative permittivity of co-doped BT with different oxides

Material	A site dopant ratio	B site dopant ratio	$\epsilon_r$ at 20°C	Reference
$Ba_{(1-x)}Eu_xTi_{(1-y)}Dy_yO_3$	0.06	0.06	5900	Lu, Cui & Liu (2016, p. 14364).
$Ba_{(1-x)}Gd_xTi_{(1-y)}Dy_yO_3$	0.06	0.06	5700	
$Ba_{(1-x)}Tb_xTi_{(1-y)}Dy_yO_3$	0.06	0.06	2000	
$Ba_{(1-x)}Pb_xTi_{(1-y)}Sn_yO_3$	x = 0.05, 0.10, 0.30	y = 0.05, 0.10, 0.30	2000	Bak, Kajtoch & Ptaszek (2016, p.905)
Dy/Mn doped $BaTiO_3$	predominately $Dy_2O_3$ 0.1 to 5.0%	Mn 0.05%	5100	Paunovic, Mitic & Prijic (2014, p. 4277)
Sm/Mn doped $BaTiO_3$	$Sm_2O_3$ 0.1 to 2.0 at%.	Mn 0.05%	6800	Paunović, Živković & Mitić, (2010, p.69)
$Ba(Y_{0.5}Nb_{0.5})_xTi_{(1-x)}O_3$	N/A	0.5X x = 0.02, 0.04 and 0.06,	6500	Cao, Li & Ismail (2012, p.41503)

### 3.4.3.5 $ACu_3Ti_4O_{12}$ ceramic families

Materials with relative permittivities higher than 1000 were traditionally based on ferroelectric materials. Their relative permittivities strongly depend on temperature, while  $ACu_3Ti_4O_{12}$  ceramic families are a novel approach that has proven that they can meet the industrial demands of high relative permittivity with good temperature stability. Kum-onsa, Thongbai and Putasaeng (2015) studied the dielectric properties of  $Na_{1/3}Ca_{1/3}Bi_{1/3}Cu_3Ti_4O_{12}$  and showed that these materials have good stability for a wide range of temperatures (-75°C to 200°C)(see figure 3-11).

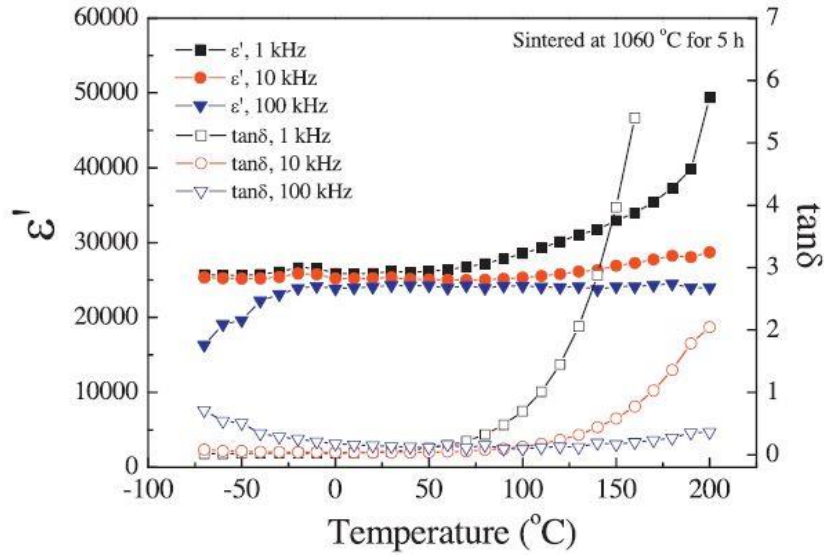


Figure 3-11. Relative permittivity temperature stability of  $\text{Na}_{1/3}\text{Ca}_{1/3}\text{Bi}_{1/3}\text{Cu}_3\text{Ti}_4\text{O}_{12}$  (Kum-onsa ,Thongbai & Putasaeng, 2015)

#### 3.4.3.5.1 Copper Calcium Titanate ( $\text{CaCu}_3\text{Ti}_4\text{O}_{12}$ , CCTO)

CCTO has a pseudo-cubic perovskite structure (space group:  $\text{Im}\bar{3}$ ) and belongs to the family of  $\text{ACu}_3\text{TiO}_{12}$ . CCTO has recently received great attention due to its high relative permittivity ( $\epsilon_r=10^5$ ) and phase transition stability over a wide range of temperatures (100–400°K) (Ahmadipour, Ain & Ahmad, 2016).

#### 3.4.3.5.2 Doping CCTO

Recently, many doping methods have been carried out to alter the dielectric properties of CCTO, and some of them have successfully improved relative permittivity by more than one order of magnitude. Table (3-6) shows dielectric properties of some of these doped CCTO (Ahmadipour et al., 2016).

Table 3-6. List of relative permittivity of doped CCTO reported (Ahmadipour et al., 2016)

Material	Concentration	$\epsilon_r$ ( $10^3$ Hz)	$\tan \delta$ ( $10^2$ – $10^4$ Hz)	Grain size
Al <sup>3+</sup>	0.3	16,000	~0.1	~5 $\mu\text{m}$
	0.06	70,000	<0.06	47 $\mu\text{m}$
Nb <sup>5+</sup>	0.1	400,000	<0.2	7 $\mu\text{m}$
	0.2	420,000	$2 \leq x \leq 0.4$	7 $\mu\text{m}$
Sb <sup>5+</sup>	0.05	24,000	$1.5 \leq x \leq 0.2$	20 $\mu\text{m}$
	0.025	20,000	$1 \leq x \leq 0.2$	30 $\mu\text{m}$
Zn <sup>2+</sup>	0.2	$12,500 \leq x \leq 2500$	$1.27 \leq x \leq 0.1$	1 $\mu\text{m}$
	0.05	15,000	0.029	~1 $\mu\text{m}$
Pr <sup>3+</sup> /Pr <sup>4+</sup>	0.2	4500	$0.4 \leq x \leq 0.1$	5 $\mu\text{m}$
	0.05	3500	$0.15 \leq x \leq 0.1$	4 $\mu\text{m}$
Sr <sup>2+</sup>	0.2	14,348	$0.7 \leq x \leq 0.08$	–
	0.1	14,369	$0.08 \leq x \leq 0.04$	–
Fe <sup>3+</sup>	0.2	100	$9.6 \leq x \leq 1$	~120 $\mu\text{m}$
	0.03	433	$5 \leq x \leq 1$	–
Ni <sup>2+</sup>	0.02	2500	0.15	4 $\mu\text{m}$
	0.2	10,000	~0.6	–
Y <sup>3+</sup>	0.02	2700	0.06	200 nm
	0.1	75,000	<0.2	93 $\mu\text{m}$
B <sup>3+</sup>	0.03	50,000	<0.1	12 $\mu\text{m}$
	0.01	~50,000	$0.16 \leq x \leq 0.09$	10 $\mu\text{m}$
Te <sup>2+</sup>	0.02	20,000	$0.1 \leq x \leq 0.05$	3.23 $\mu\text{m}$
	0.01	25,500	$0.12 \leq x \leq 0.05$	2.51 $\mu\text{m}$
Co <sup>2+</sup> /Co <sup>3+</sup>	0.4	9500	$1.3 \leq x \leq 0.5$	5 $\mu\text{m}$
	0.2	70,000	$\leq 0.6$	~5 $\mu\text{m}$
Zr <sup>4+</sup>	0.1	33,000	$1.6 \leq x \leq 0.2$	~10 $\mu\text{m}$
	0.05	15,000	$2.4 \leq x \leq 0.2$	5 $\mu\text{m}$
Ga <sup>3+</sup>	0.05	38,011	~0.1	136 $\mu\text{m}$
	0.1	66,736	$0.15 \leq x \leq 0.1$	199 $\mu\text{m}$
La <sup>3+</sup>	0.05	8000	$0.6 \leq x \leq 0.3$	–
	0.2	11,000	~0.2	2 $\mu\text{m}$
Mg <sup>2+</sup>	0.05	10,000	~0.2	10.5 $\mu\text{m}$
	0.1	5000	~0.2	~6 $\mu\text{m}$
Sm <sup>3+</sup>	0.005	10,000	$0.5 \leq x \leq 0.03$	–
	0.01	1200	$0.1 \leq x \leq 0.05$	–
Mn <sup>3+</sup> /Mn <sup>4+</sup>	0.06	45	–	–
	0.01	22,500	~0.5	–
Sc <sup>3+</sup>	0.08	80,000	$1.1 \leq x \leq 0.1$	30 $\mu\text{m}$
	0.2	30,000	$3 \leq x \leq 0.3$	10 $\mu\text{m}$
Ba <sup>2+</sup>	0.05	8000	~0.2	5.79 $\mu\text{m}$
	0.2	1500	$0.27 \leq x \leq 0.23$	~1 $\mu\text{m}$

### 3.5 Relative permittivity of Polymer-Ceramic composites

Some theoretical relationships have been developed to calculate the relative permittivity of a mixture of polymer ceramic composites, including Logarithmic theory, Smith theory, Maxwell Garnett theory and Effective Medium Theory EMT (Yunxiang, Zhang, Liu et al., 2011) and (Choi, Sekhar, Jo et al., 2016)

Logarithmic Theory:

$$\ln \varepsilon_{eff} = \beta \ln \varepsilon_c + (1 - \beta) \ln \varepsilon_p \quad (3-1)$$

Smith Theory:

$$\varepsilon_{eff} = \frac{\varepsilon_p (1 - \beta) + \varepsilon_c \beta \left[ (3\varepsilon_p) / (\varepsilon_c + 2\varepsilon_p) \right] \times \left[ 1 + \left( (3\beta(\varepsilon_f - \varepsilon_m)) / (\varepsilon_c + 2\varepsilon_p) \right) \right]}{(1 - \beta) + \beta \left[ (3\varepsilon_p) / (\varepsilon_f + 2\varepsilon_p) \right] \times \left[ 1 + \left( (3\beta(\varepsilon_c - \varepsilon_p)) / (\varepsilon_c + 2\varepsilon_p) \right) \right]} \quad (3-2)$$

Maxwell Garnett Theory:

$$\frac{\varepsilon_{eff} - \varepsilon_p}{\varepsilon_{eff} + 2\varepsilon_p} = \beta \frac{\varepsilon_c - \varepsilon_p}{\varepsilon_c + 2\varepsilon_p} \quad (3-3)$$

Effective Medium Theory (EMT) Theory:

$$\varepsilon_{eff} = \varepsilon_p \left[ 1 + \frac{\beta(\varepsilon_c - \varepsilon_p)}{\varepsilon_p + n(1 - \beta)(\varepsilon_c - \varepsilon_p)} \right] \quad (3-4)$$

Where  $\varepsilon_c$  is relative permittivity of ceramic,  $\varepsilon_p$  is relative permittivity of polymer,  $\beta$  is volume fraction and  $n (=1/\eta)$  is the morphology factor dependent on the shape of the ellipsoidal particles and their orientation in relation to composite film surface. Yunxiang et al. (2011) fabricated PTFE/CaTiO<sub>3</sub> polymer ceramic composites and measured relative permittivity of the composite. Figure (3-12) shows the relative permittivity of composite with various volume fraction of ceramic powders. Experimental measurements are in good agreement with some of the theoretical calculations. Choi et al. (2016) showed that relative permittivity of composites are also depends on particle size of the ceramic powder and the smaller the particles size are the greater the relative permittivity are (see figure3-13).

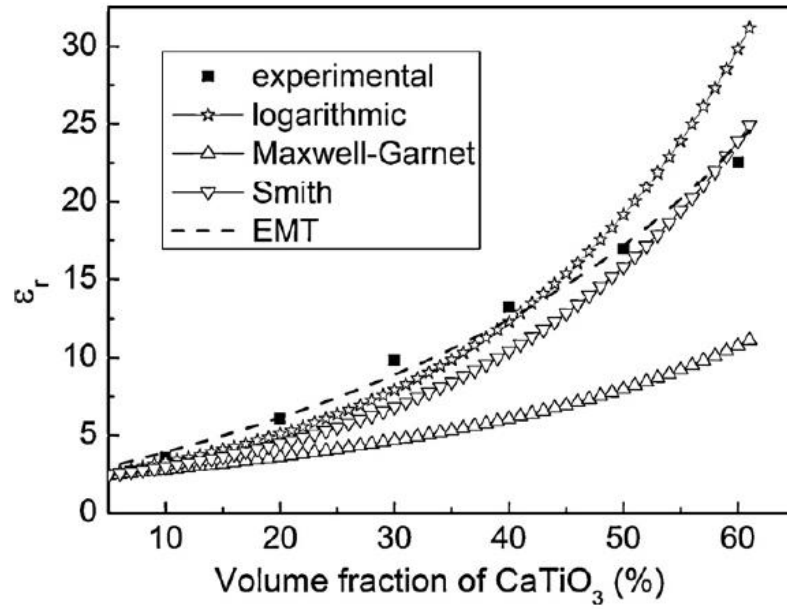


Figure 3-12. Comparison of theoretical and experimental of relative permittivity of PTEF/ $\text{CaTiO}_3$  (Yunxiang et al., 2011)

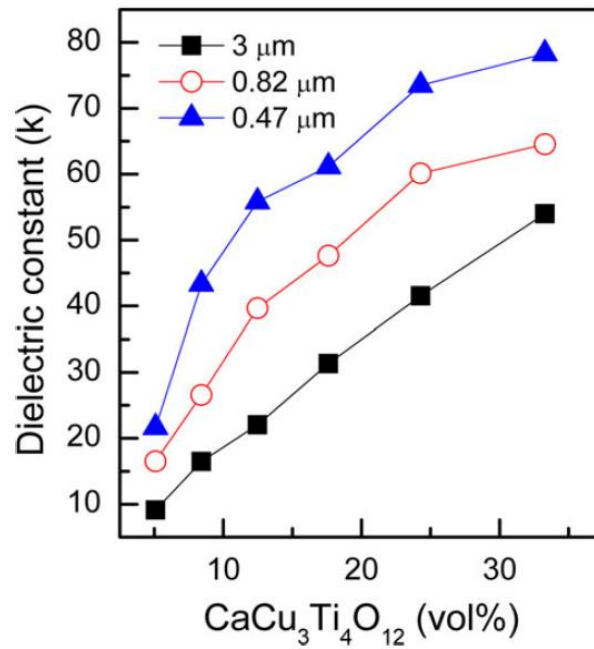


Figure 3-13. Ceramic particle size effect on relative permittivity of UV polymer /CCTO composite (Choi et al., 2016)

### 3.6 Liquid dielectrics

Liquid dielectrics are commonly used in high voltage power apertures such as transformers, circuit breakers and power cables (Arora & Mosch, 2011). Liquid dielectrics are classified into mineral, synthetic and vegetable oils. Table (3-7) shows some dielectric oils commonly used in industrial applications (Mahanta & Laskar, 2017).

Table 3-7. List of some liquid dielectric and their applications (Mahanta and Laskar, 2017).

Mineral insulating oil	Paraffinic oils	Nonring long-chained structure
	Naphthenic oils	Saturated ring structure
	Aromatic oils	Nonsaturated ring structure
Synthetic insulating oil	Polyalphaolefins	Manufactured by polymerization of hydrocarbon molecules
	Polyglycols	Produced by oxidation of ethylene and propylene
	Synthetic ester oils	Produced by reaction of acids and alcohols with water
Vegetable insulating oil	Soybean oil	Vegetable oils are nontoxic, biodegradable, low inflammable, have a higher breakdown voltage, high flash point, high acidity number, high viscosity and pour point
	Coconut oil	
	Cottonseed oil	
	Rapeseed oils	

### 3.7 Gaseous dielectrics

Gaseous dielectrics usually have low relative permittivity which are not desirable for EA devices but on the other hand some of those have very high voltage breakdown as a result, it is worth considering the for EA applications. Voltage breakdown in gaseous dielectrics can be estimated using Paschen's law. According to Paschen's law the voltage breakdown is given by (Gallot-Lavallée, 2013):

$$V_{BD} = \frac{Bpd}{\ln(Apd) - \ln\left(\ln\left(1 + \frac{1}{\gamma}\right)\right)} \quad (3-5)$$

Whereas  $V_{BD}$  is voltage breakdown of a gas,  $p$  is the pressure of the gas under test,  $d$  is the distance between electrodes,  $\gamma$  is the secondary-electron-emission coefficient and  $A$  is the saturation ionization in the gas.

In practice actual breakdown voltage is less than voltage calculated by Paschen's law (see Figure 3-14).

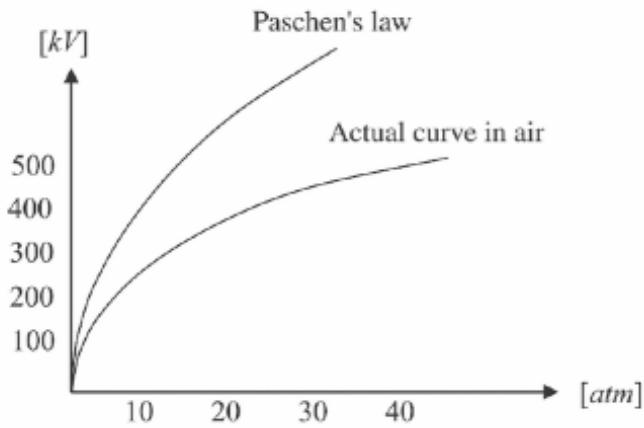


Figure 3-14. Comparison of actual critical voltage and critical voltage yielded by Paschen's law in air (Gallot-Lavallée, 2013)

Vacuum, in practice usually used for insulating voltage where the electric field can be reached up to 30 MV/m and by increasing pressure to 3000 kPa, a greater field up to 1000 MV/m is achievable (Gallot-Lavallée, 2013).

Sulphur hexafluoride ( $\text{SF}_6$ ) has excellent insulation performance about 75 kV for 25 mm gap (Tang et al., 2018) and is also widely used as an insulating gas for high voltage instrument such as Gas insulated switchgear (GIS) and gas circuit breaker (GCB).  $\text{SF}_6$  is not environment friendly and considered as greenhouse gas, therefore there have been lots of research to find alternatives (Woo, Jeong, Seo et al., 2012; Xiao, Zhang, Tang et al., 2018 and Onal, 2018).

Table 3-8. comparison of the physical and environmental properties of common dielectric gases (Xiao et al., 2018)

Gas	Electric strength relative to $\text{SF}_6$	Boiling point/ $^{\circ}\text{C}$	Atmospheric lifetime/years	GWP
$\text{SF}_6$	1	-63	3200	23900
$\text{N}_2$	0.36	-196	0	0
$\text{CO}_2$	0.30	-78.5	$\infty$	1
Air	0.30	-183	$\infty$	$\approx 0$
$\text{C}_2\text{F}_6$	0.78 ~ 0.79	-78	10000	9200
$\text{C}_3\text{F}_8$	0.96 ~ 0.97	-37	2600	7000
c- $\text{C}_4\text{F}_8$	1.25, 1.31	-6	3200	8700
$\text{CF}_3\text{I}$	1.23	-22.5	0.005	1 ~ 5
$\text{C}_4\text{F}_7\text{N}$	2.74	-4.8	35	2700

## *Chapter 4*

### **UV-curable polymer technology**

A possible approach to improve the electrical properties of dielectric layers of EA devices is to use polymer electroceramic composites to achieve dielectrics with higher relative permittivities, as shown in the previous chapter. Cold coating processes for dielectric deposition are also desirable to avoid copper oxidation; therefore, it was decided to study UV curing technology for dielectric deposition. Surface finishes of UV coating are glossy, which minimises surface roughness and, as a result, increases EA forces. This chapter describes free radical polymerisation in more detail, including a selection guide of monomers, oligomers and photoinitiators for pigmented UV-curable inks.

#### **4.1 UV curing**

Radiation curing is the solidification process of functional monomers and oligomers to form a cross-linked polymer network. This process is induced by photons (UV curing) or electron beam (EB curing) and happens in order magnitude of fractions of a second (Endruweit, Johnson, and Long, 2006). UV curing has several benefits over conventional curing by the application of heat, including no shrinkage, surface gloss, low to zero volatile organic compounds (VOCs), very rapid drying, low heat generation and, most importantly, since UV coating does not contain elements that oxidize or evaporate the thickness of the cured layer is equal to the thickness of an applied layer, therefore, UV coating is considered a controllable process in terms of the thickness of coating layer (Glöckner, 2009). These advantages result in the widespread modern use of UV coatings in applications such as adhesives and sealants, all printing technologies, including offset printing, inkjet, silkscreen, varnish, lacquer and electronics (electrically conductive UV-curable ink, patent number: US7,569,160 B2), stereolithography (SLA) 3D printing. Therefore, there has been rapid commercial growth in UV-curable coatings (see Figure 4-1).



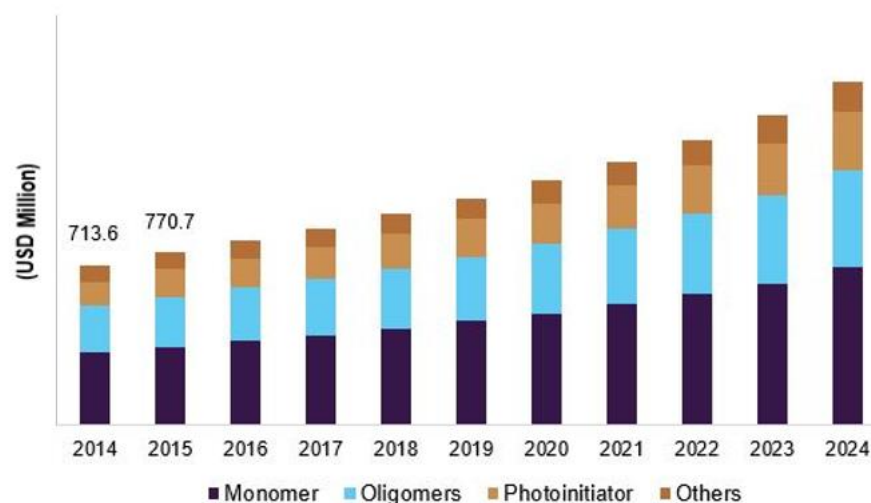


Figure 4-1. Market growth of UV ink and coating compositions (Marketandmarket website)

Low heat generation during the UV curing process makes it a strong option for electroadhesion applications, particularly for dielectric layers which are applied on top of the copper electrodes and can avoid any possible oxidation which can dramatically affect EA pad performance.

## 4.2 Free radical polymerization reaction sequence

First, a photoinitiator absorbs a photon of light ( $h\nu$ ), and an electrically excited species ( $R^{\cdot}$ ) are produced by the promotion of an electron to a higher energy orbital that readily decomposes to radicals. This reaction is called photolysis; then, in the initiation step, the reaction between monomer or oligomer with radicals involves breaking of a carbon-carbon double bond and formation of carbon-carbon single bond, initiating polymerization; this step is followed by the addition of other monomer or oligomer units, results in growing polymer chain in the propagation step. Propagation process repetition yields a polymer chain (see figure 4-2).

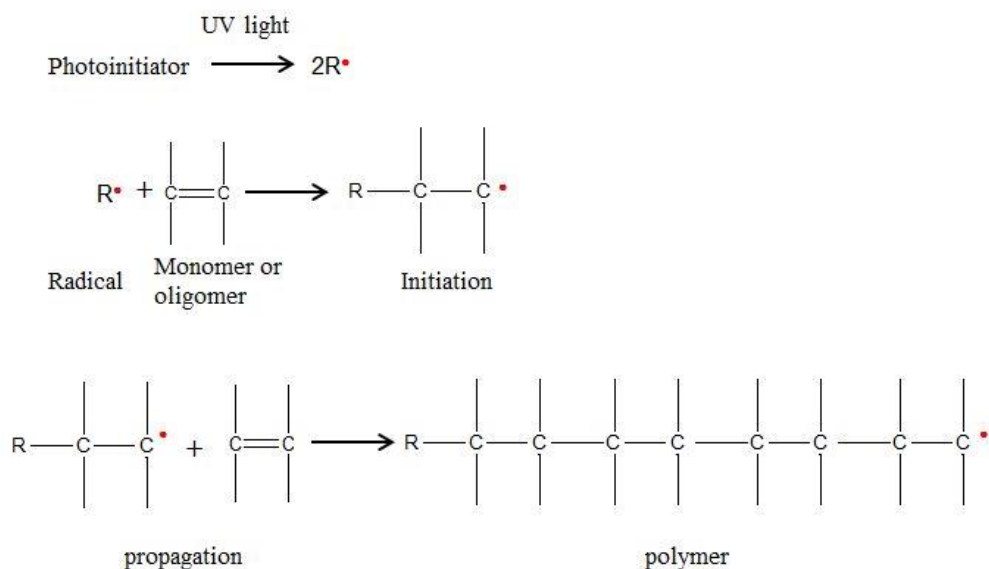


Figure 4-2. Reaction sequence of free radical polymerisation (Heath and Cooper ,2013)

### 4.3 UV curing ink components

UV curing inks consist of monomers, oligomers, and photoinitiators, and for pigmented inks, a dispersing agent and defoamer are usually required. In some special applications, an adhesion promoter may be used to improve bonding between the coating and the substrate. Unsaturated acrylate monomers and oligomers are the dominant chemistry for UV curing due to their higher reactivity than unsaturated methacrylate, allyl, or vinyl. Table 4-1 shows the chemical structure of UV curing polymers.

Table 4-1. Chemical structure of typical UV polymers

Monomer or Oligomer	Chemical structure
Acrylate	$\text{R}-\text{O}-\overset{\text{O}}{\parallel}{\text{C}}-\text{CH}=\text{CH}_2$
Methacrylate	$\text{R}-\text{O}-\overset{\text{O}}{\parallel}{\text{C}}-\underset{\text{CH}_3}{\text{C}}=\text{CH}_2$
Allyl	$\text{R}-\text{CH}_2-\text{CH}=\text{CH}_2$
Vinyl	$\text{R}-\text{CH}=\text{CH}_2$

#### 4.3.1 Monomers

The main purpose of using monomers in UV ink formulations is to lower the viscosity of the ink, however, it also has effects on mechanical properties of the cured ink such as surface tension, tensile strength, adhesion as well as curing rate, which should be considered

in the selection of suitable monomer in the ink formulation (Wei, Huang, and Wang, 2014). Based on the viscosity of the ink suitable for a particular application, the volumetric percentages of monomers in the ink are chosen. Monomers are classified based on their functionalities. In polymer chemistry the functionality of a monomer refers to as the number of polymerizable groups and affects the formation and the degree of crosslinking of polymers. A monofunctional molecule possesses one function, a difunctional two, a trifunctional three and so on. Monomers, based on their functionalities, are used for following purposes:

- a) Monofunctional monomers, the main application of this type of monomer is to lower the viscosity of UV ink or adhesion and to reduce cross-linking. As a result of cross-link reduction, volumetric shrinkage is reduced, and flexibility of cured film is increased.
- b) Multifunctional monomers: like monofunctional monomers, their major application is viscosity reduction, but also, they can cooperate in properties like hardness, adhesion, and chemical resistance of cured file.

As an example, table 4-2 and 4-3 show typical formulations of UV curing coatings and the effect of some of the prominent monomers on the chemical and mechanical properties of the aliphatic urethane acrylate oligomer with the commercial name of Bomar BR-7432GB provided by DYMAX company and cured films respectively. The flexibility of the cured film depends on the functionality of monomers, and generally speaking, coatings formulated by monofunctional monomers are more flexible than difunctional. Also, coatings formulated by difunctional monomers are more flexible than trifunctional monomers.

Table 4-2. Effect of typical monomers on lowering viscosity of the oligomer (DYMAX's material data sheets)

Test formulation name		I30	I50	TM50	TP50	H50
Aliphatic Urethane Acrylate (oligomer)	100	70	50	50	50	50
Isobornyl Acrylate		30	50			
Trimethylolpropane Triacrylate				50		
Tripropylene glycol diacrylate (TPGDA)					50	
1,6-Hexanediol diacrylate (HDDA)						50
Photoinitiator (Omnirad 481)		2	2	2	2	2
Viscosity,cp(25°C)	200000	59000	6400	31000	6400	2700

Table 4-3. Effect of typical monomers on mechanical properties of cured films (DYMAX's material data sheets)

Cured mechanical properties					
Property	I30	I50	TM50	TP50	H50
Tensile strength. psi	2000	2100	1400	1900	1900
Elongation, %	340	180	3	30	12
Elastic Modulus, ksi	0.7	2.1	72	10	25
Durometer Hardness	84A	43D	79D	57D	60D
MEK Double Rubs(#)	>200	110	>200	130	100

### Typical monomers of UV ink and coating

Typical monomers used for UV inks and coatings, their physical properties and chemical structure, as well as their applications are introduced in the following:

#### a) Isobornyl Acrylate (IBOA)

IBOA is a monofunctional monomer with chemical structure shown in Figure 4-3. Physical properties of IBOA are demonstrated in table 4-4 shows that IBOA is a good candidate for lowering viscosity of wide range of oligomers and minimizing crosslinking, therefore, it is recommended for paints and coatings that require some level of flexibility (Allnex and IGM's material data sheets). UV/EB curable formulated products containing IBOA are characterized by:

- Good flexibility
- Increased T<sub>g</sub> (glass transition temperature, the temperature at which amorphous polymer experience transition from rigid state to more flexible state), thermal resistance (thermal resistance is defined as the ratio of the temperature difference between the two faces of a material to the rate of heat flow per unit area.)
- Low shrinkage
- Improved water resistance

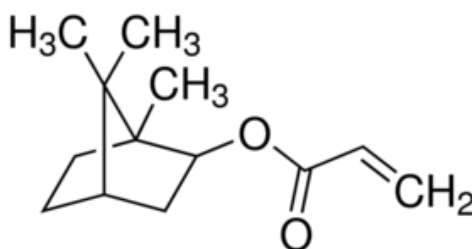


Figure 4-3. Chemical structure of IBOA

## Applications of IBOA

Typical applications of IBOA are adhesives, automotive coatings, metal, glass and plastic coatings, paint and coatings-solvent borne, plastics and other flexible substrates, coatings, polymer concrete and UV cure coatings.

Table 4-4. Physical properties of IBOA (Allnex and IGM's material data sheets)

Density, g/ml at 25°C	0.97
Flash point, Setaflash, °C	>100
Molecular weight (g/mol)	208
Melting point, °C	<-35
Viscosity	7.6 cps@ 28 °C

## b) Tripropylene Glycol Diacrylate (TPGDA)

TPGDA is a difunctional acrylic monomer with low viscosity ranging between  $10 \times 10^{-3}$  and  $15 \times 10^{-3}$  Pa.s, and low volatile is a good candidate for fast curing UV-polymer matrix. The cured film has moderate flexibility. Its mechanical properties and chemical structure can be seen in table 4-5 and Figure 4-4, respectively. The typical applications of this monomer are in clear coatings, pigmented systems, and overprint varnishes.

Table 4-5. Physical properties of TPGDA (Allnex and IGM's material data sheets)

Density, g/ml at 25°C	1.03
Flash point, Setaflash, °C	>100
Molecular weight (g/mol)	300
Young's modulus, (MPa)	1550
Viscosity	10-15 cps@ 28 °C

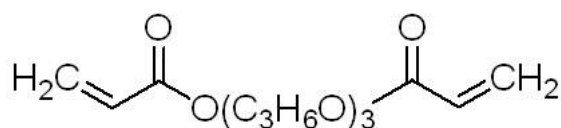


Figure 4-4. Chemical structure of TPGDA

## c) 1,6-Hexanediol diacrylate (HDDA)

HDDA is a difunctional acrylic monomer with very low viscosity (see table 4-6) and is a good candidate for water resistant applications and a low cross-link density which improves the elasticity of the coating layer and adhesive bonding. Figure 4-5 illustrates the chemical structure of this monomer.

Table 4-6. Physical properties of HDDA (Allnex and IGM's material data sheets)

Density, g/ml at 25°C	0.97
Flash point, Setaflash, °C	>100
Molecular weight (g/mol)	208
Melting point, °C	<-35
Viscosity	7.6 cps@ 28 °C

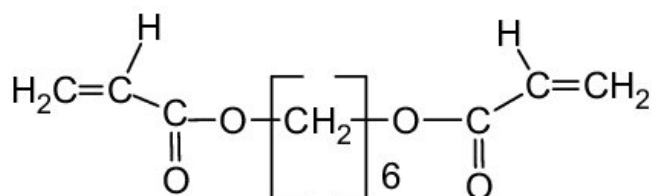


Figure 4-5. Chemical structure of HDDA

## Applications of HDDA

HDDA has a wide variety of applications, including Wood coatings, PVC coatings, plastic coatings, metal coatings, offset printing inks, flexographic printing, screen printing, and varnish.

### d) Trimethylolpropane Triacrylate (TMPTA)

TMPTA is a trifunctional acrylic monomer with high cross link density which improve hardness of coating layer and has a wide range of applications listed below:

- 1- Furniture and Floor coatings on wooden substrates
- 2- Coatings for plastic substrates as in automotive applications
- 3- Overprint varnishes for publications and packaging items.
- 4- Offset, Screen, Flexo and Inkjet printing inks for a variety of substrates including paper, plastic, metal and glass
- 5- 3D printing stereolithography

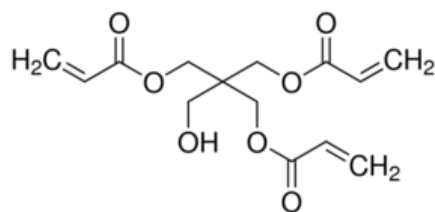


Figure 4-6. Chemical structure of TMPTA

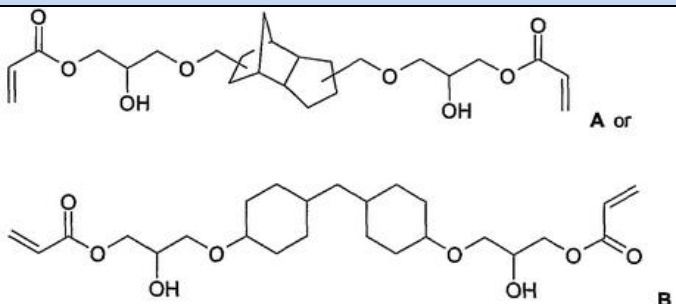
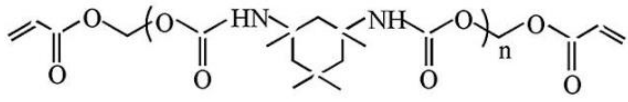
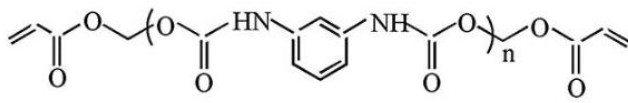
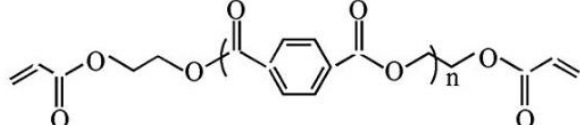
Table 4-7. Physical properties of TMPTA (Allnex and IGM's material data sheets)

Density, g/ml at 25°C	1.1
Flash point, Setaflash, °C	>100
Molecular weight (g/mol)	296
Viscosity	5-8 cps@ 28 °C

#### 4.3.2 Oligomers

Oligomers provide the vehicle for UV ink and coating; unlike monomers, they have already been partially polymerized (Todd, 1994). Most commercialized UV oligomers are based on polyester, polyether, and epoxy resins. Table 3-8 shows their chemical structure of commonly used oligomers in formulating inks and coating. The acrylate oligomers used in UV/EB radical polymerization are typically viscous liquids ranging from a few thousand to greater than  $10^3$  Pa.s in viscosity at 25°C. They also typically possess two to six acrylate groups per molecule and range in molecular weight from approximately 500 to 20,000. Oligomers affect the chemical properties of UV ink and coating and mechanical properties of the cured film. Table 3-9 summarises their performance and applications.

Table 4-8. Typical UV oligomers and their chemical structure

Chemical name	Chemical structure	Reference
Epoxy acrylate	 <p>A or B</p>	Patent number: WO2004056930A1
Aliphatic urethane acrylate		Maurya, Kurmvanshi, Mohanty et al. (2018)
Aromatic urethane acrylate		
Polyester acrylate		

#### 4.3.3 Photoinitiators (PIs)

Depending on applications, many PIs with different absorptions band have been developed to meet market needs. Choosing the right PI or PIs and the right concentration for coating formulation is challenging, and many parameters need to be considered, including thickness of coating, available UV source, clear or pigmented coating, Oxygen inhibition, and desirable curing speed (Green, 2010 and Gruber, 1992).

##### Type I and II PIs

There are two types of PIs for free radical polymerisation. PIs of type I are compounds that photo dissociate under UV/vis- irradiation. An example of chemical reactions that occurs when this type of PIS irradiates by UV light is demonstrated in figure 4-7. Typical PIs of this type widely used in industrial applications are TPO, TPO-L and 1173 (Green, 2010).



Table 4-9. Typical UV oligomers and their applications (Allnex and IGM's material data sheets)

Oligomer Type	Performance Effects	Applications
Epoxy acrylate	Increase reactivity, hardness, chemical resistance ; decrease cost	Oligomer of choice for coatings; used to lower cost in inks
Aliphatic urethane acrylate	Increase flexibility, toughness, weathering; multi-functional increase reactivity, hardness, chemical resistance; decrease yellowing	Oligomer of choice for coatings; used to lower cost in inks
Aromatic urethane acrylate	Increase flexibility, toughness; multifunctional increase reactivity, hardness, chemical resistance; decrease cost	Increase flexibility or hardness; not weatherable
Polyester acrylate	Increase wetting; decrease viscosity	For pigment wetting, adhesion; stereolithography ink
Acrylic acrylate	Increase adhesion, weathering	Increase adhesion

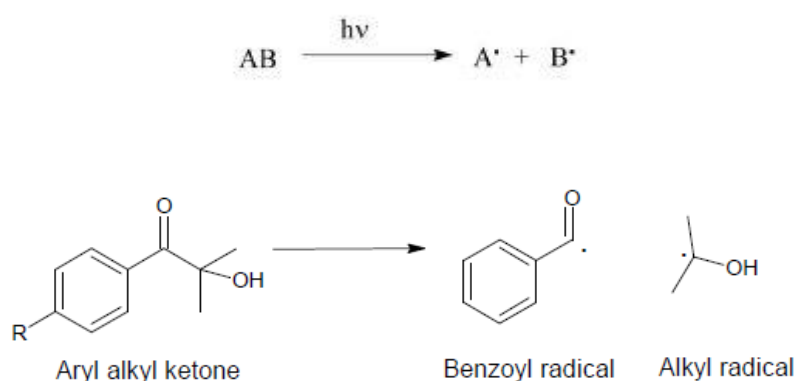


Figure 4-7. Chemical reactions of PI type I

**a) (2,4,6-Trimethylbenzoyl) diphenyl phosphine oxide (TPO)**

TPO absorbs UV light at longer wavelengths making it particularly suitable for curing white pigmented formulations and thick films. TPO can be used as the sole initiator or in combination with other PIS. Its chemical structure and absorption spectrum are illustrated in figure 4-8 and 4.9.

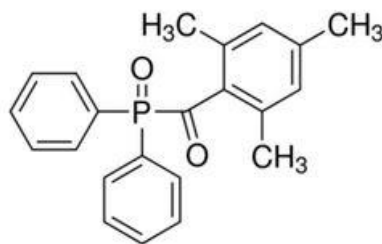


Figure 4-8. Chemical structure of TPO

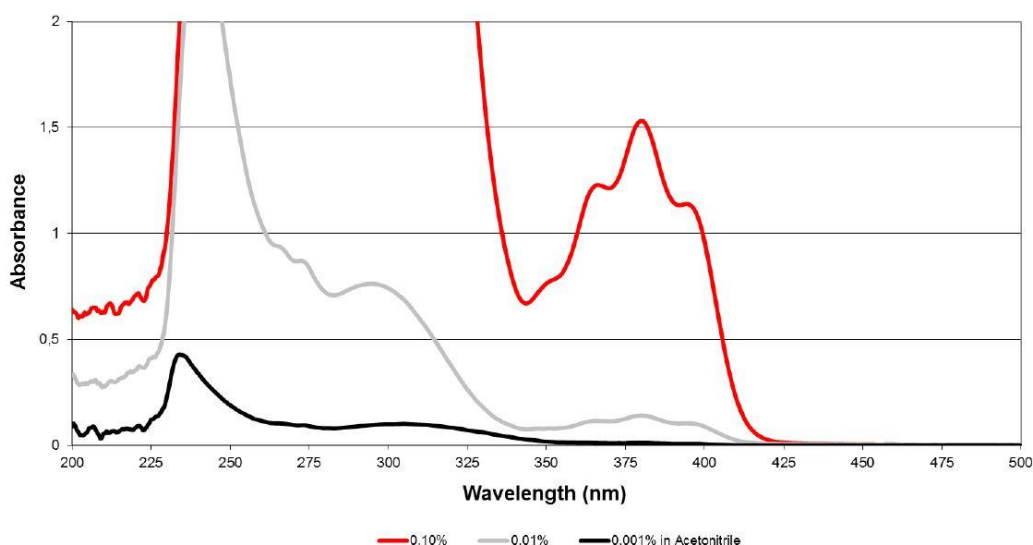


Figure 4-9. Absorption spectrum of TPO (IGM's material data sheets)

#### b) Ethyl(2,4,6-Trimethylbenzoyl)-phenyl phosphinate (TPO-L)

TPO-L (see Figure 4-10) is a liquid photoinitiator, making it easy to incorporate into formulations. It is compatible with most oligomers and monomers used in the UV cure industry. It is also useful for blending with other photoinitiators. This PI is suitable to produce formulations which, on curing, exhibit low yellowing and low odour. TPO-L absorbs the long wave region of the UV spectrum (see figure 4-11). It is particularly suitable for use in pigmented systems like  $\text{TiO}_2$  and thick film layers (IGM's material data sheets).

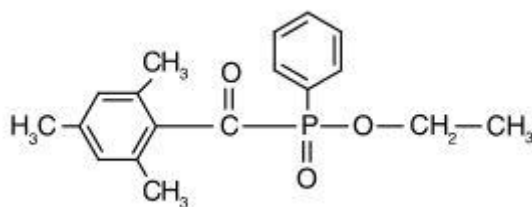


Figure 4-10. Chemical structure of TPO-L

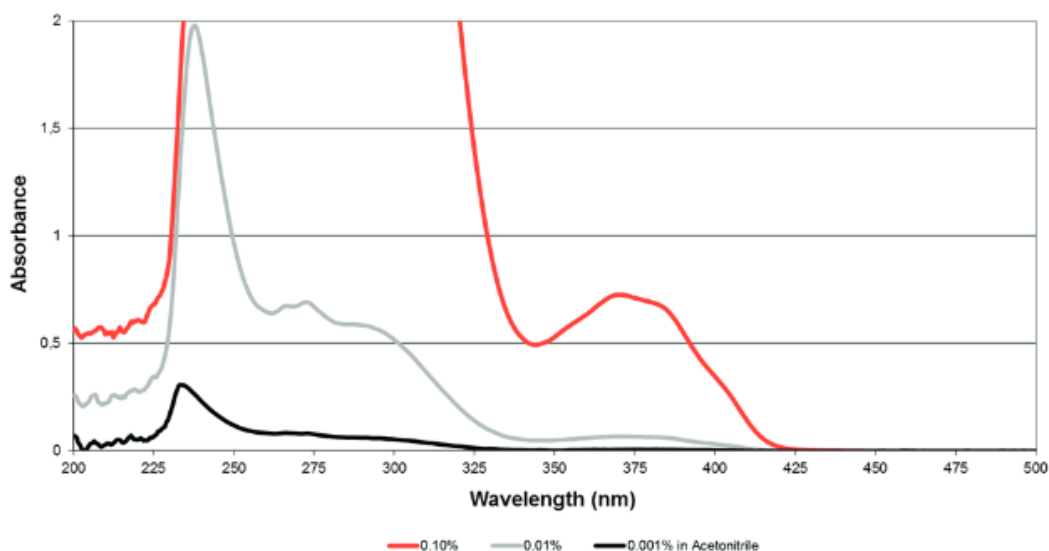


Figure 4-11. Absorption spectrum of TPO-L (IGM's material data sheets)

**c) 2-Hydroxy-2-methyl-1-phenylpropanone (industrial name:1173)**

PI 1173 (see Figure 4-12) is liquid and widely used for clear coating and varnishes, particularly low viscosity coating (Weber and Turro, 2003 and IGM's material data sheets). This PI increases speed and surface cure, usually used with a combination of other PIS, responsible for surface cure due to low wavelength absorption. Its absorption spectrum is illustrated in figure 4-13.

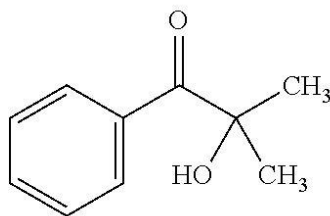


Figure 4-12. Chemical structure of 1173

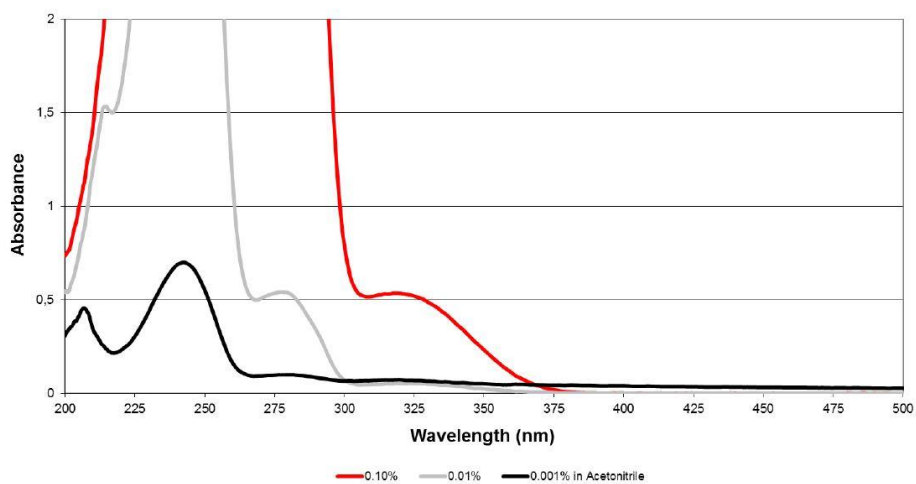


Figure 4-13. Absorption spectrum of 1173 (IGM's material data sheets)

PIs of type II are benzophenone, 2-isopropyl thioxanthene-9-one (ITX), and other compounds capable in the excited state to abstract hydrogen or electron from a donor (see Figure 4-14), which is usually amine and produce radicals (Green, 2010). ITX absorbs in the long wave region (see figure 4-15)

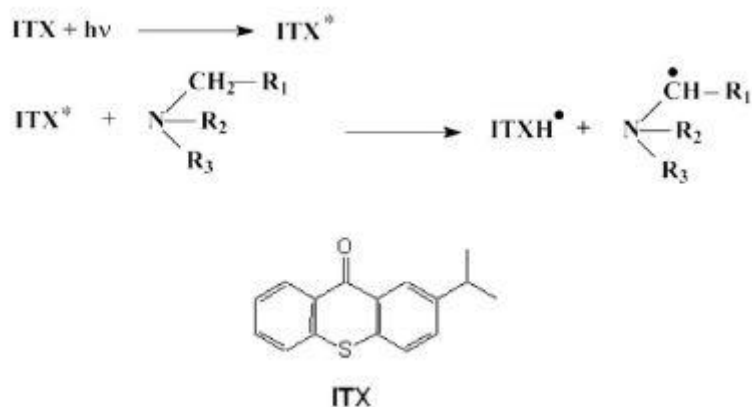


Figure 4-14. Chemical structure of ITX and reactions in presence of UV light

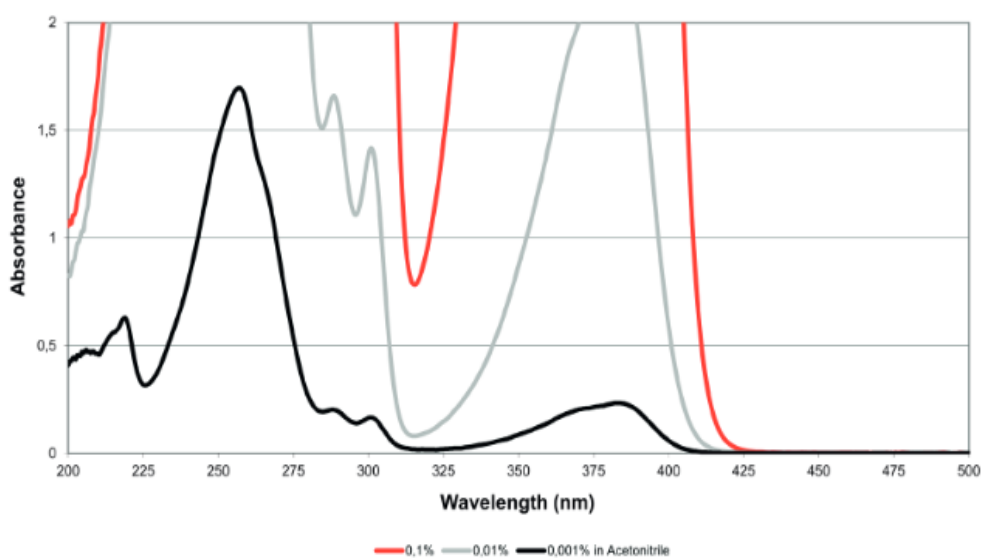


Figure 4-15. Absorption spectrum of ITX (IGM's material data sheets)

#### 4.4 The effect of pigments on the UV curing process

Pigments absorb discrete parts of the visible spectrum, and the remaining light is then reflected, conveying colour. Pigments also absorb light in the UV spectrum, particularly shorter wavelengths. This has an adverse effect on the curing process in that UV absorption by the pigment, sometimes loaded at 20% of the formulation weight, will leave little UV energy available for the PI, which may be loaded at only 2%. In the worst case, a UV light will not be able to penetrate to any depth due to pigment absorption, and curing will take place only at the surface. The transmission spectrum of a pigment will show a low UV absorption. This is also known as the “pigment window,” where light is more readily transmitted and where the absorption of a PI will be least affected by pigment

screening and is likely to be most efficient. To maximize the UV reactivity of a formulation, PI that has high absorption in the “transmission window” of each pigment should be chosen. The wavelengths of the pigment “window” vary with the colour and pigment type (Green, 2010, Shukla, Bajpai, Singh, et al., 2004, and Segurola, Allen, Edge et al., 1999), but in general, they are:

Magenta: 300–400 nm

Yellow: 290–370 nm

Cyan: 370–400 nm

Green: low transmission throughout UV

Black: low transmission throughout UV

Titanium dioxide white: >380 nm

#### **4.4.1 Dispersing agent**

Dispersing agents, based on their chemical structure, are classified to following groups groups:

##### **1) Polymeric dispersant**

Polymeric dispersants need two requirements to be able to perform suitable particle dispersion. They should be strongly absorbed into the particle surface and, as a result, possess a type of anchoring group, and they must contain polymeric chains to give steric stabilization (Yossif, Kandile, Abdelaziz et al., 2017).

##### **2) Surfactants**

surfactants are low molecular weight dispersing agents and provide particle dispersion in liquid media by lowering interfacial tension between the pigment and the resin solution (Myers, 2005).

#### **4.4.1.1 Dispersing process**

Van der Waals and liquid bridge forces hold pigment particles together (Lin, 2003), and to have well distributed particles into liquid media, these attraction forces must be overcome. The pigment dispersion in liquid media includes three following processes (Pal & Fleming III, 2006): pigment wetting, grinding stage and stabilization of pigment suspension. The wetting step replaces all the air between the pigment particles with resin solution. Pigment agglomerates, in the grinding stage, are broken up and uniformly distributed in liquid media. Stabilization prevents pigment agglomeration due to repulsive forces that do not let particles approach close enough and are attracted by van der Waals forces. A suitable dispersant must perform all functions to ensure pigment stabilization in the resin solution.

#### ***4.4.1.2 Dispersion Machinery***

The two most common dispersing machinery used in laboratories and industrial scale are high shear mixers and bead mills (see figures 4-16 and 4-17). Although these types of machinery are different, they are designed to maximise the efficiency of imparting mechanical energy to pigment particles (Agbo, Jakpa, Sarkodie et al., 2018). Dispersing forces provided by these types of machinery are the shear force, the impact force, and the attrition forces.



Figure 4-16. High shear mixer used for dispersing pigments (Dispermat LC75)



Figure 4-17. Industrial bead mills used for dispersing pigments

### **4.4.2 UV and Electron beam exposure devices**

#### ***4.4.2.1 Medium pressure mercury (MPM) lamps***

UV inks can be cured using UV light emitting device or high energy electrons or electron beam. UV curing uses UV energy or visible light to convert a liquid formulation of inks

into a solid film. UV light emitted by MPM lamps is classified to three regions according to their wavelength UV C between 220nm and 280nm, UV B between 280nm and 313nm and UV A between 360 nm and 404nm. UV C is absorbed by oligomers presented in ink and cannot contribute on depth cure, however, it plays important role on surface cure, particularly for thin film. UV B has better penetration characteristic; therefore, it is useful for both surface cure and depth cure. UV A and visible light emitted by a MPM is essential for depth cure and visible light with wavelength higher than 550nm have no effect on UV curing process (Fouassier and Lalevée , 2012 and Green, 2010).

### Doped MPM

Metal halides are added to MPM to modify the relative power of the lamp at particular wavelengths and produce a doped lamp. The most common metals are Helium, Iron and Gallium. Figure 4-18, 4-19 and 4-20 show their spectrums (Fouassier and Lalevée , 2012 and Green, 2010).

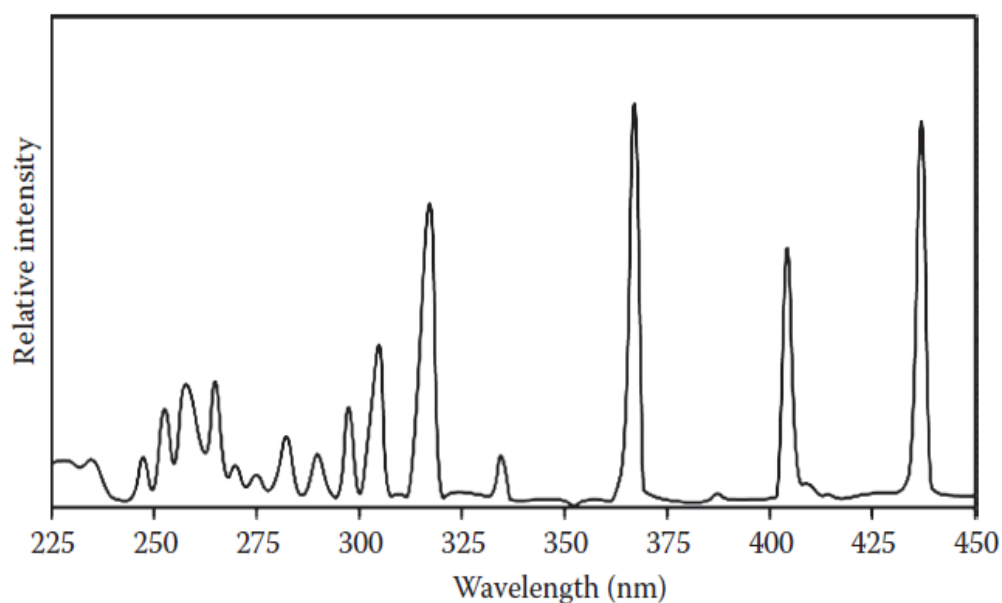


Figure 4-18. He standard UV lamp, 15 % UV-C 8 % UV-B 7 % UV-A 5 % UV-VIS 15 % VIS (Green, 2010)



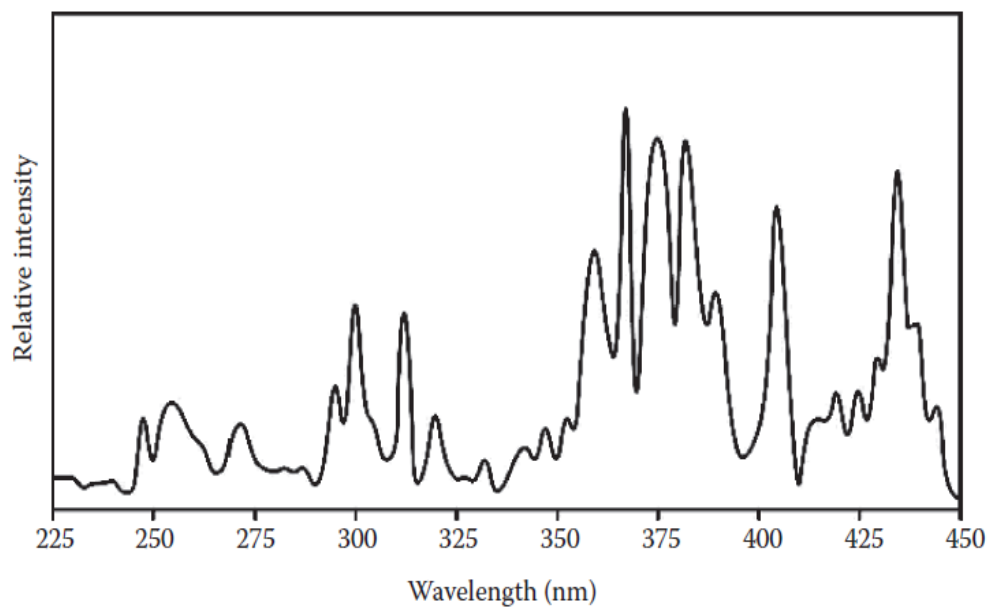


Figure 4-19. Fe doped UV lamp, 7 % UV-C 5 % UV-B 17 % UV-A 6 % UV-VIS 16 % VIS (Green, 2010)

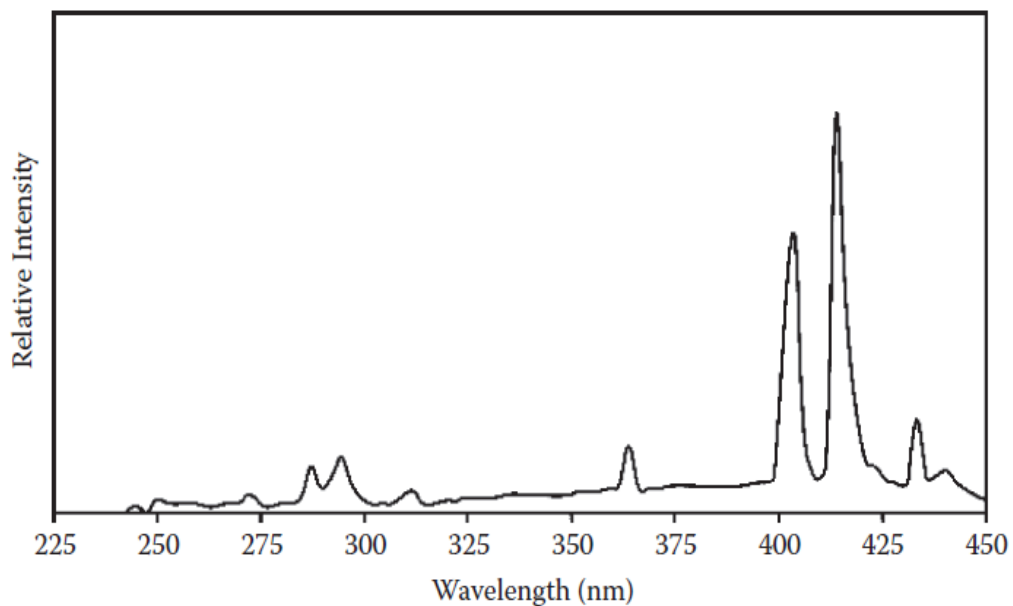


Figure 4-20. Gallium doped UV lamp, 7 % UV-C 8 % UV-B 5 % UV-A 17 % UV-VIS 24 % VIS (Green, 2010)

#### 4.4.2.2 Light emitting diodes (LED)

Using LED lamps for curing is difficult compared to standard medium pressure UV lamps as the spectrum of the light they emit is very narrow (see Figure 4-21), and for pigmented UV ink, it even becomes more challenging. LEDs have advantages over UV lamps, including lower energy consumption and instant start. With advances in LED technology, the combination of LEDs which emit a single peak at 365, 385, 395 and 405 nm gives more flexibility to formulate UV ink which can be fully cured by these LEDs. Figure 4.22 shows industrial LED used in the curing process of inkjet printing (Fouassier and Lalevée, 2012 and Green, 2010).

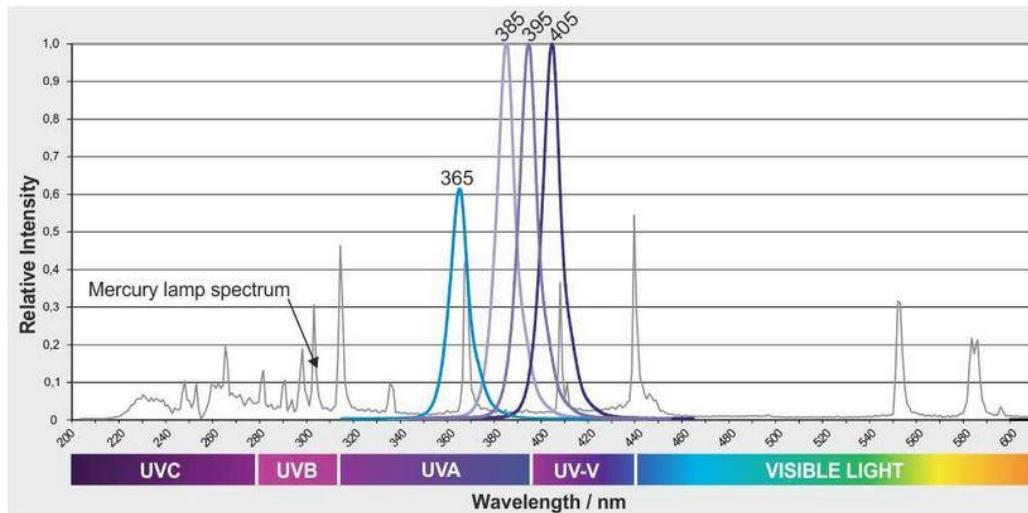


Figure 4-21. Comparison of LED's and standard UV lamp spectrums (Photoelcuring website)

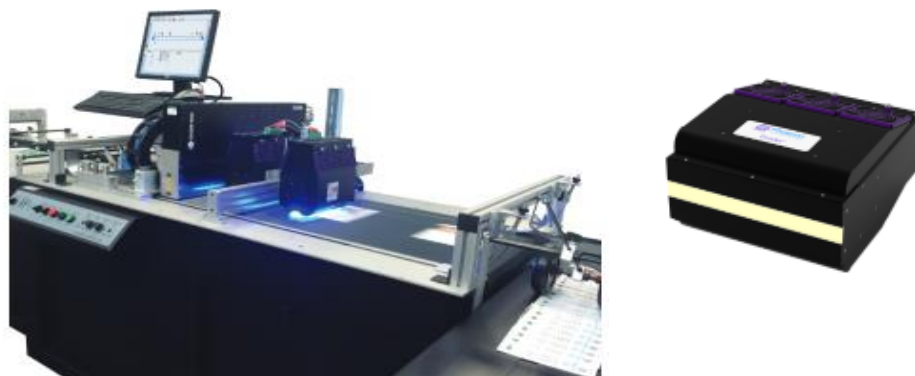


Figure 4-22. Phoseon's FireJet FJ200 for the K600i ink jet printer ( $12\text{W}/\text{cm}^2$  @ 365nm and  $8\text{W}/\text{cm}^2$  @ 385/395/405nm, Phoseon website)

#### **4.4.2.3 Electron beam (EB) curing**

EB curing is the absorption of accelerated electrons with typical energies of 80keV, and 180 keV, which can provide energy for the initiation of chain cross linking or curing process by decomposition of the photosensitive polymer. EB curing has many advantages over UV curing, such as curing thicker film, being more efficient for pigmented ink and reducing the cost of ink formulation as in EB curing; PIs are not needed. However, the upfront cost of EB curing is still the main barrier to using this technology. Figure 4-23 shows a typical commercial device used for EB curing.



Figure 4-23. EB Lab machine from 80 to 200 keV, format A4 up to 30m/min (Sartomer website)

## *Chapter 5*

# **Synthesis of ceramic dielectric materials and UV-electroceramic inks**

In this chapter, the methods were carried out to fabricate electroceramics, and UV-electroceramic inks are explained in more detail. Generally speaking, adding electroceramics to polymers results in increasing relative permittivity of the resulting composite materials, in theory. Some experimental findings provided in chapter 2 underpin this theory; therefore, it was decided to add suitable electroceramics to UV curable polymers as pigments to improve the electrical properties of the dielectric layers of EA devices.

### **5.1 Synthesis of electroceramics**

Generally speaking, ceramic properties are not only controlled by the chemical composition but also by the fabrication process, which can influence the crystalline structure, grain size and porosity of the final product. Synthesis of ceramic dielectrics has been carried out using many different procedures, including solid state reactions, hydrothermal, sol-gel and others. All methods have their advantages and drawbacks regarding energy consumption, time, difficulties in controlling critical features, and undesirable secondary phases in the final product. Among these methods, solid state reaction has been used more than others due to simplicity; however, undesirable secondary phases and high energy consumption are the most common problems of this method.

### **5.2 Solid state reactions**

This research was started by preparing ceramic dielectrics using conventional solid state reactions. The first step is to prepare stoichiometric amounts of precursors, which are in the form of oxide/carbonate, and then, in order to reduce particle size and mix powders well, a wet milling technique (acetone or propanol milling liquid and yttrium stabilized zirconium oxide grinding balls) is used for 24 hours. The next step is to dry the suspension

in an oven at 100 °C for 24 hours and grind them with the agate mortar. The prepared powder is then calcined at a suitable temperature for an appropriate period to remove volatile impurities by controlling the heating rate. The second milling step with the same procedure is done, and the suspension is dried again. The powders are compacted into disk-shaped pellets with 10mm diameter using a manual hydraulic press and pellet die at  $125 \times 10^6$  (Pa) pressure. Finally, the pellets are sintered for a certain period with a controlled heating rate (see Figure 5-1).

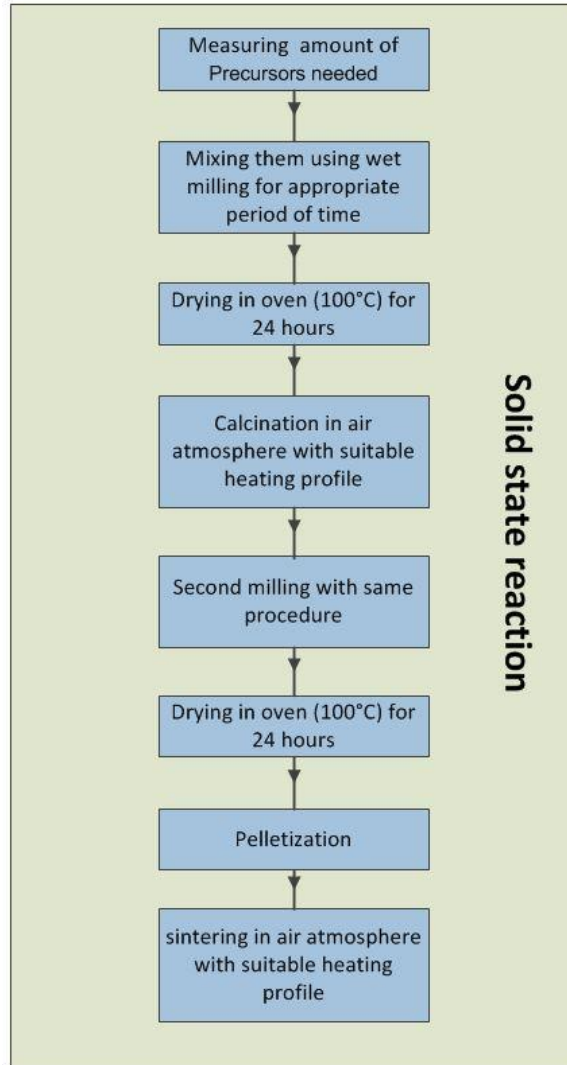


Figure 5-1. Flowchart of conventional solid-state reaction

## 5.3 Testing and Analysing Techniques and Instruments

### 5.3.1 X-Ray diffraction analysis

Crystal structure of calcined powders and sintered pellets, in terms of peak positions depending on atomic size and type of structure, can be measured using X-ray diffraction and compared with references to prove the formation of planned ceramic phases. The

room temperature X-ray diffractometer that has been used here is a PaNalytical X'pert Pro MPDl, and the X-ray source is Cu-K $\alpha$  with a wavelength ( $\lambda$ ) equals to 1.5405 Å.

### **5.3.2 Raman spectroscopy analysis**

Raman spectroscopy can measure vibrational frequencies or wavenumber of Raman-active modes in ceramics. The results can give complementary information that helps prove the formation of planned materials. The Raman spectrometer used in this study is a DXR2 Raman Microscope, Thermo Fisher Scientific, with a visible laser wavelength of 532 nm.

### **5.3.3 Scanning electron microscopy**

As mentioned in the previous chapter, research has proved that the relative permittivity of ceramic dielectrics like BaTiO<sub>3</sub> (Huan, Wang & Fang, 2014, and Kinoshita & Yamaji, 1976), doped BaTiO<sub>3</sub> (Zhang, Zhai & Shen, 2013) and CaCu<sub>3</sub>Ti<sub>4</sub>O<sub>12</sub> (Ahmadipour et al., 2016) depend on the grain size of the prepared ceramic samples; therefore, microstructure and grain size of ceramics are investigated using scanning electron microscopy (SEM). The instrument which is used in this research is Nova Nano SEM.

### **5.3.4 Electrical property measurement**

In order to measure the dielectric properties of ceramics, both surfaces of the prepared sintered pellets are coated with gold. Then the relative permittivity measurement is carried out using an LCR meter (Agilent 4285A, Agilent Technologies Japan, Ltd).

## **5.4 Preparation of BaTiO<sub>3</sub>**

BaTiO<sub>3</sub> was prepared using the conventional solid state route mentioned earlier. Stoichiometric amounts of BaCO<sub>3</sub> (Sigma-Aldrich, 99.98%) and TiO<sub>2</sub> (Sigma-Aldrich, 99%) were selected (Felgner, Müller & Langhammer, 2004) and were weighed out and mixed and dried for 24 hours and calcined at 1100°C, 1200°C and 1250°C for 3 hours and also at 1200°C for 5 hours. Heating rates for all samples were 5°C/min. XRD results show (figure4-2) that a low level of a secondary phase (Ba<sub>2</sub>TiO<sub>4</sub>) was formed for all samples, which were held for 3 hours at the calcination temperature.

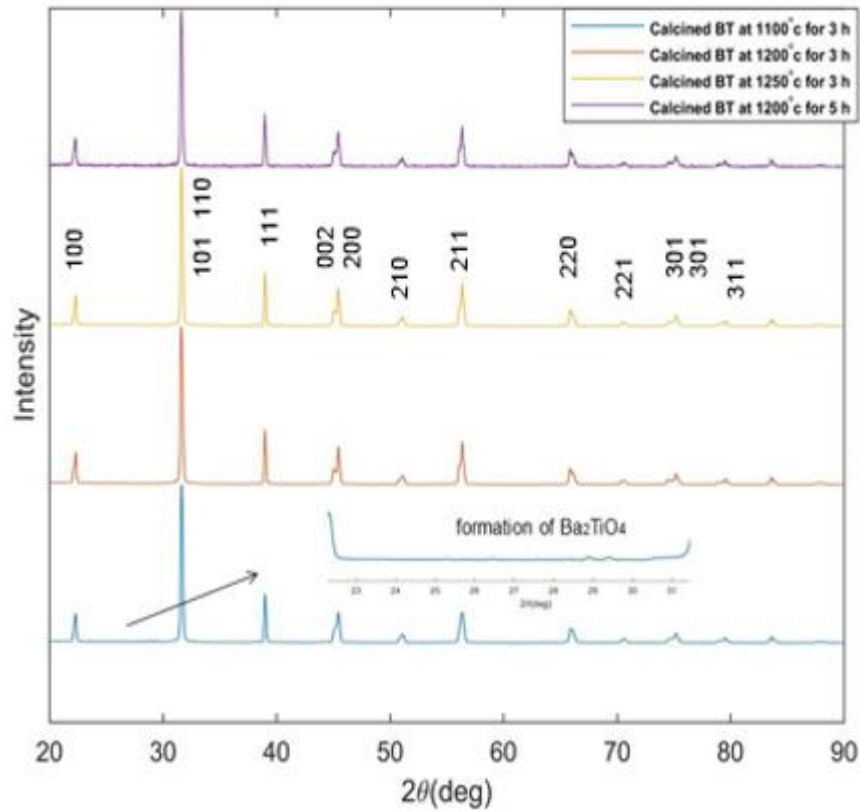
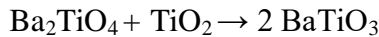
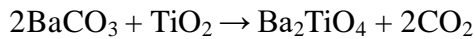


Figure 5-2. X-Ray diffractograms of BT powder calcined at different temperature

Many researchers (Brzozowski & Castro, 2000; Othman, Hassan & Abdelal, 2014; Felgner et al., 2004) have studied the formation of  $\text{BaTiO}_3$  using solid state reactions and have suggested that many reactions may take place. All suggested that  $\text{Ba}_2\text{TiO}_4$  is formed during this process. One of them is the following reactions:



Therefore, the formation of  $\text{Ba}_2\text{TiO}_4$  seems inevitable using solid state reactions; however, it is reported that by increasing the calcination temperature or time duration, pure  $\text{BaTiO}_3$  is achievable, therefore  $1200^\circ\text{C}$  and 5 hours is suggested. The calcined powder is crushed and mixed for 24 hours using the wet milling procedure mentioned earlier and dried for 24 hours. Pressed pellets were prepared and sintered for 5 hours at  $1200^\circ\text{C}$  using a  $5^\circ\text{C}/\text{min}$  heating rate. X-ray diffraction was carried out (see figure 5-3). Peak splitting at  $\theta=45^\circ$  and  $66^\circ$  prove that the tetragonal phase of  $\text{BaTiO}_3$  is formed.

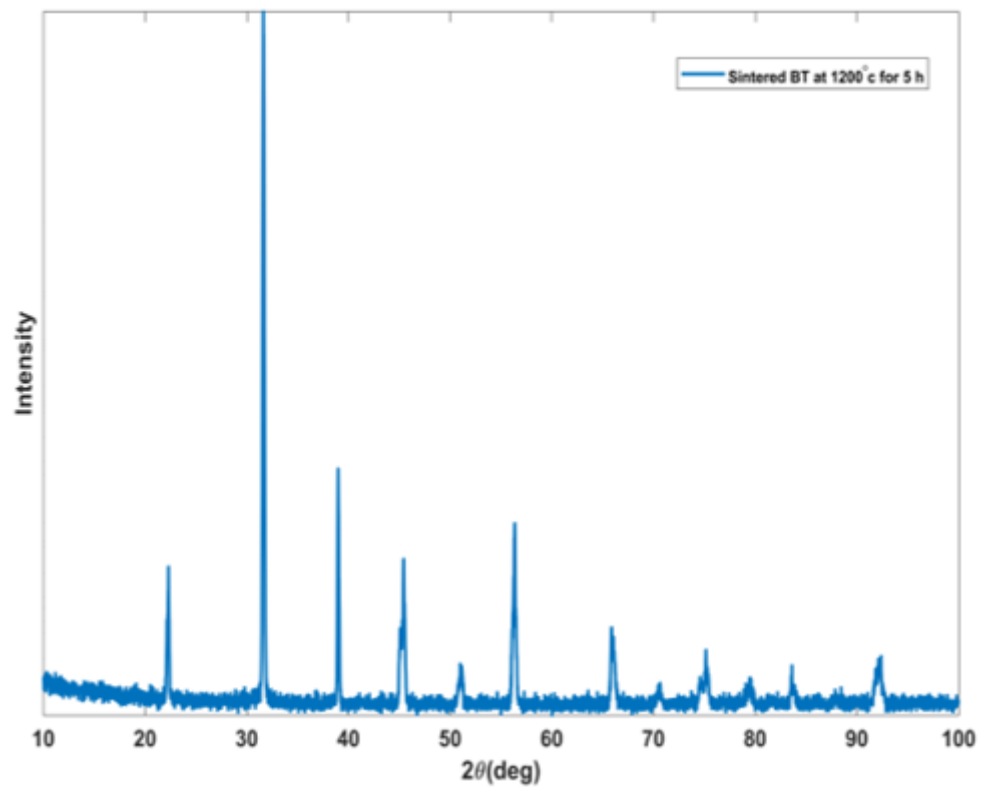


Figure 5-3. Room temperature X-Ray diffraction pattern of sintered BT at 1200°C

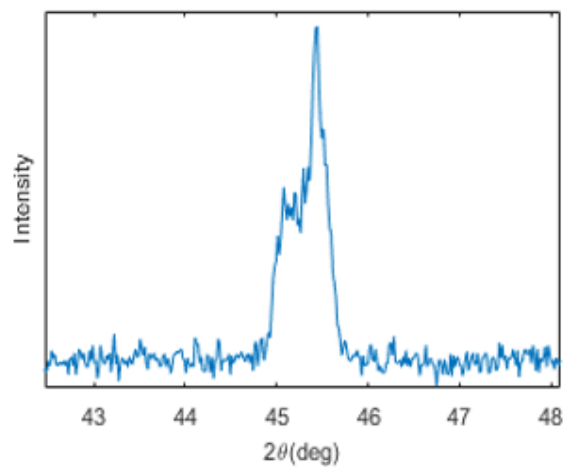


Figure 5-4. Peak splitting of tetragonal BT at 45 ° $2\theta$



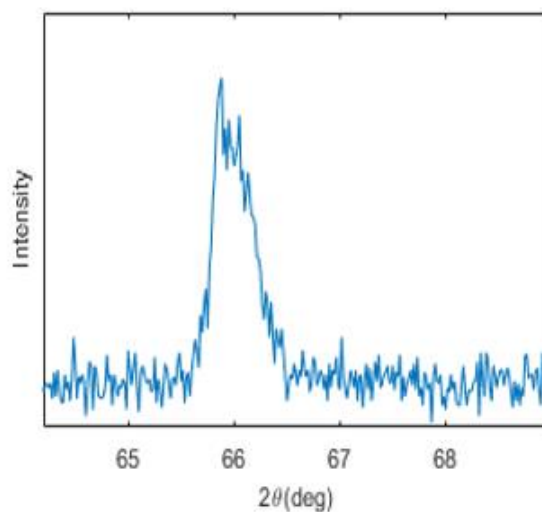


Figure 5-5. Peak splitting of tetragonal BT at 66 °2θ

In the tetragonal structure of  $\text{BaTiO}_3$   $\text{Ti}^{+4}$  and  $\text{O}^{2-}$  are slightly shifted from the centre of the cubic (see figure 5-6) therefore, a vibrational mode with wavenumber around  $305\text{ cm}^{-1}$  becomes Raman-active while in Raman spectroscopy of the cubic structure of  $\text{BaTiO}_3$  this peak does not appear (Hayashi, Nakamura & Ebina, 2013); therefore, Raman spectroscopy of the prepared sample (see figure 5-7) proved that the tetragonal structure of  $\text{BaTiO}_3$  was formed.

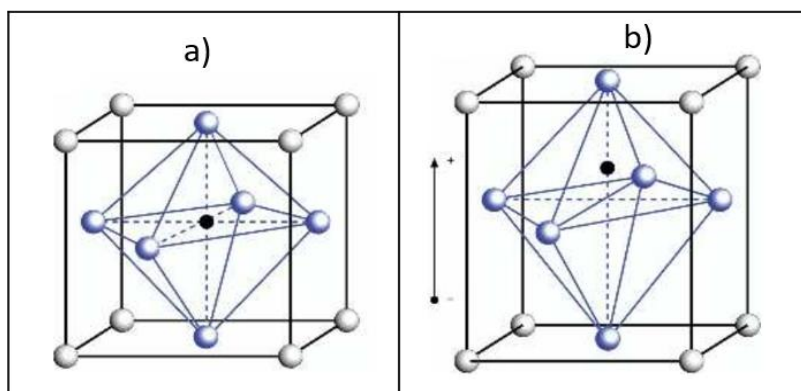


Figure 5-6. Comparison of a) cubic and b) tetragonal structure of  $\text{BaTiO}_3$

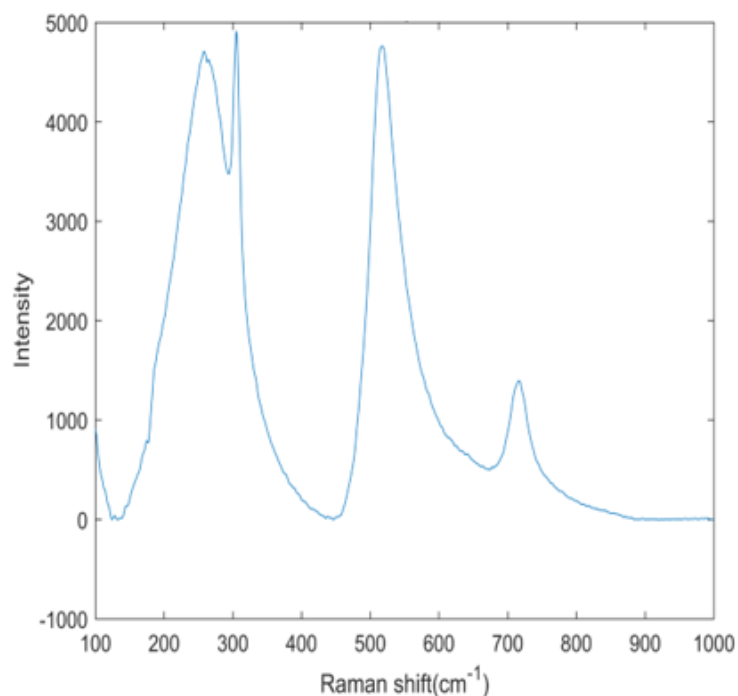


Figure 5-7. Raman spectrum of barium titanate at room temperature

One surface of the sintered pellets was coated with carbon, and the other side was stuck to the sample holder using a carbon adhesive disc. The average grain size of the sample could be estimated using images recorded by the SEM microscope (see figure 5-8). As mentioned earlier, grain size influences the dielectric properties of ceramics; therefore, the average grain size needs to be reported.

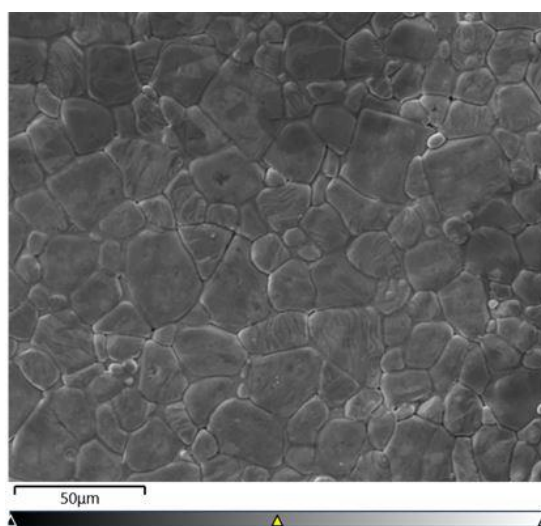


Figure 5-8. SEM image of prepared BaTiO<sub>3</sub>

## 5.5 Dielectric properties measurement

To make both sides of the prepared sample conductive, sintered pellets of BaTiO<sub>3</sub> were coated with gold and dielectric properties were measured using the LCR meter. Figure (5-9) shows the relative permittivity of prepared BaTiO<sub>3</sub> versus frequency at room temperature.

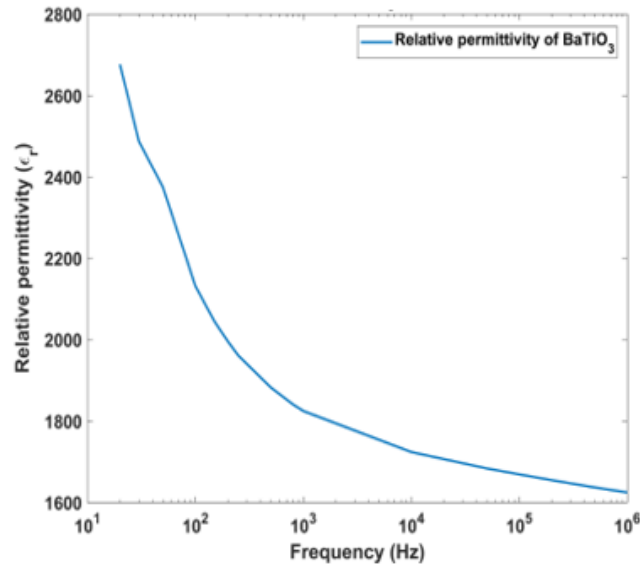


Figure 5-9. Room temperature relative permittivity of BT versus frequency

## 5.6 Preparation of Ba<sub>0.65</sub>Sr<sub>0.35</sub>TiO<sub>3</sub>

According to figure (3-3), the relative permittivity of Ba<sub>(1-x)</sub>Sr<sub>x</sub>TiO<sub>3</sub> at room temperature reaches a maximum for x ranging between 0.6 and 0.7. Therefore among all possible doping concentrations, Ba<sub>0.65</sub>Sr<sub>0.35</sub>TiO<sub>3</sub> was selected as the best potential option for dielectric materials for electroadhesion applications.

Stoichiometric amounts of BaCO<sub>3</sub> (Sigma-Aldrich, 99.98%), TiO<sub>2</sub> (Sigma-Aldrich, 99%) and SrCO<sub>3</sub> (Sigma-Aldrich, 99.98%) were weighed out and mixed and dried using the same procedure of previous fabrication. The powder was calcined at 1250°C for 5 hours. XRD analysis confirmed that BST was formed (see figure 5-10). Doping Barium titanate by 0.36 concentration of strontium resulted in a transition from tetragonal to cubic crystal structure; therefore, peak splitting did not occur at  $2\theta=45^\circ$  for (002) and (200) reflection and at  $2\theta=65^\circ$  for (202) and (220) reflections (see figure 5-11). The calcined powder is crushed and mixed for 24 hours using the wet milling procedure mentioned earlier and dried for 24 hours. Pressed pellets were prepared and sintered for 5 hours at 1200°C using the same heating rate.

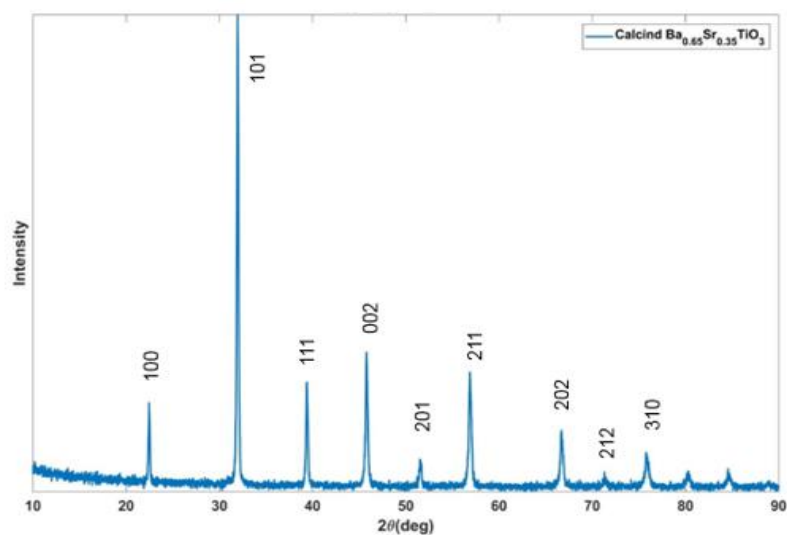


Figure 5-10. Room temperature X-ray diffraction pattern of BST

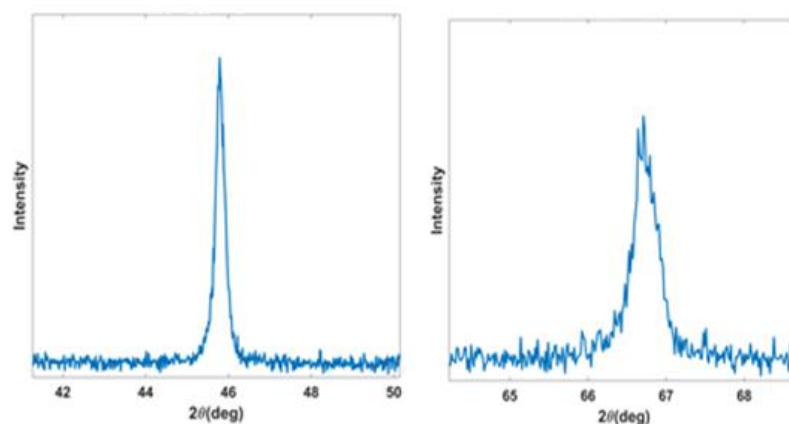


Figure 5-11. Peak merging at  $45^\circ 2\theta$  and  $66^\circ 2\theta$  due to cubic structure of BST

Raman spectroscopy of  $\text{Ba}_{0.65}\text{Sr}_{0.35}\text{TiO}_3$  (see figure 4-12) reveals that the peak at  $305\text{ cm}^{-1}$  disappears because of the phase transition from tetragonal BT to cubic BST.

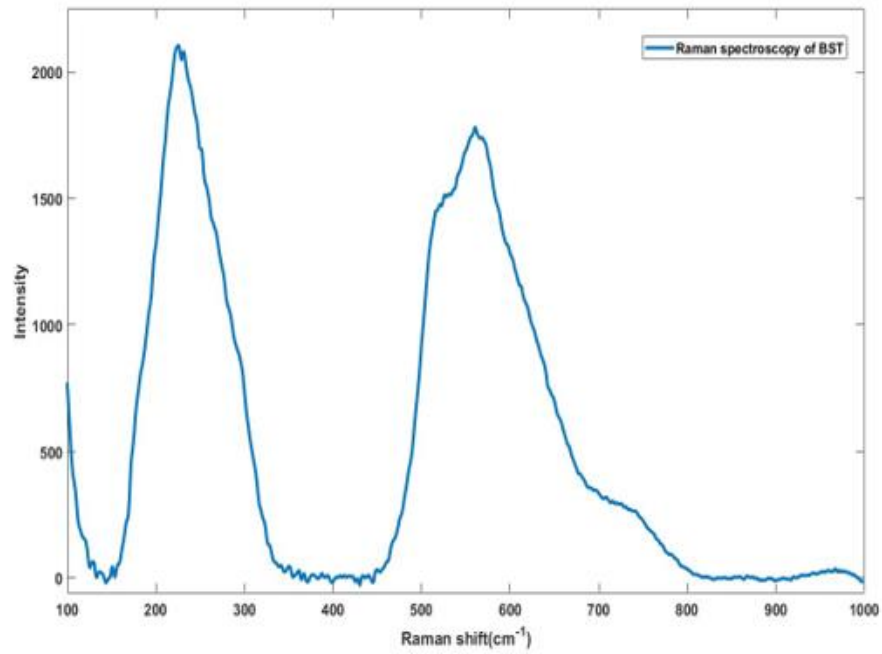


Figure 5-12. Room temperature Raman spectroscopy of BST

The relative permittivity of the prepared BST was measured using the same procedure, and as can be seen in figure (4-13), the relative permittivity of BST increased by approximately one order of magnitude compared to BT in the range of frequencies measured.

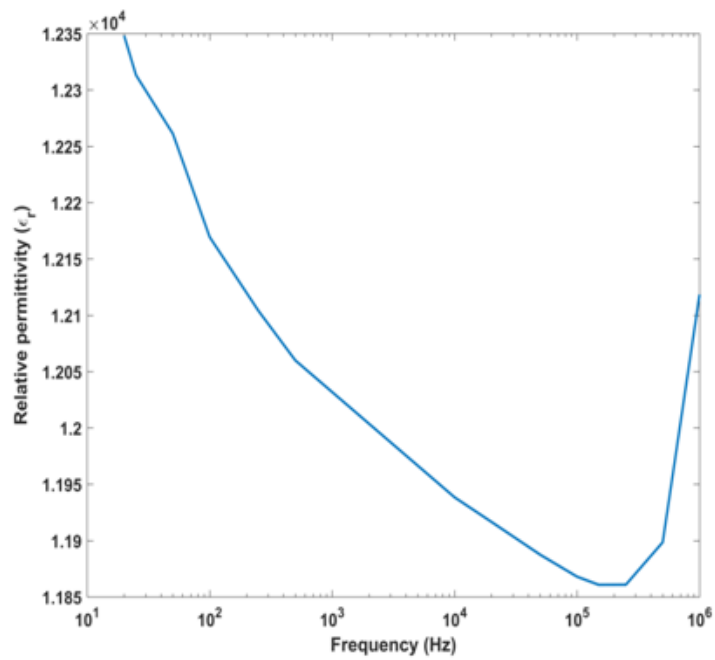


Figure 5-13. Room temperature relative permittivity of BST versus frequency

## 5.7 Preparation of $\text{CaCu}_3\text{Ti}_4\text{O}_{12}$

CCTO has received much attention (Ahmadipour et al., 2016, Tang, Wu, Huang et al., 2017) as a dielectric material due to its gigantic relative permittivity. Figure 5-14 depicts its cubic pseudo-perovskite chemical structure of CCTO. One of the possible solid-state reactions that can result in the formation of CCTO is to use  $\text{CaCO}_3$ ,  $\text{CuO}$  and  $\text{TiO}_2$  as starting materials. The chemical reaction involved is shown below; therefore, stoichiometric amounts of  $\text{CaCO}_3$  (Sigma-Aldrich, 99.98%),  $\text{TiO}_2$  (Sigma-Aldrich, 99%) and  $\text{CuO}$  (Sigma-Aldrich, 99.98%) were weighed out and mixed and dried using the same procedure explained previously and Powder was calcined and sintered at  $1100^\circ\text{C}$  for 8 hours. X-ray diffraction pattern (see figure 5-15) has proved the formation of CCTO with minor secondary phase of  $\text{CaTiO}_3$ .

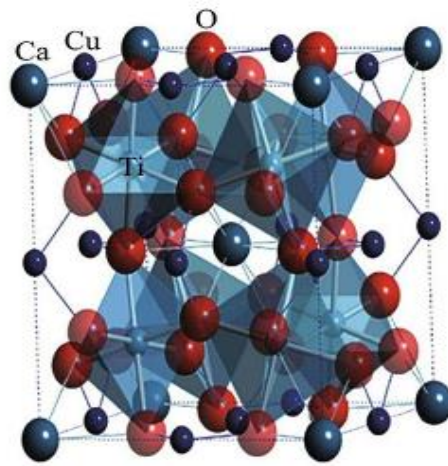
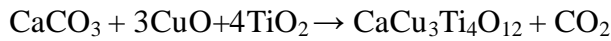


Figure 5-14. Structure of the cubic pseudo-perovskite ( $\text{Im}\bar{3}$ )  $\text{CaCu}_3\text{Ti}_4\text{O}_{12}$

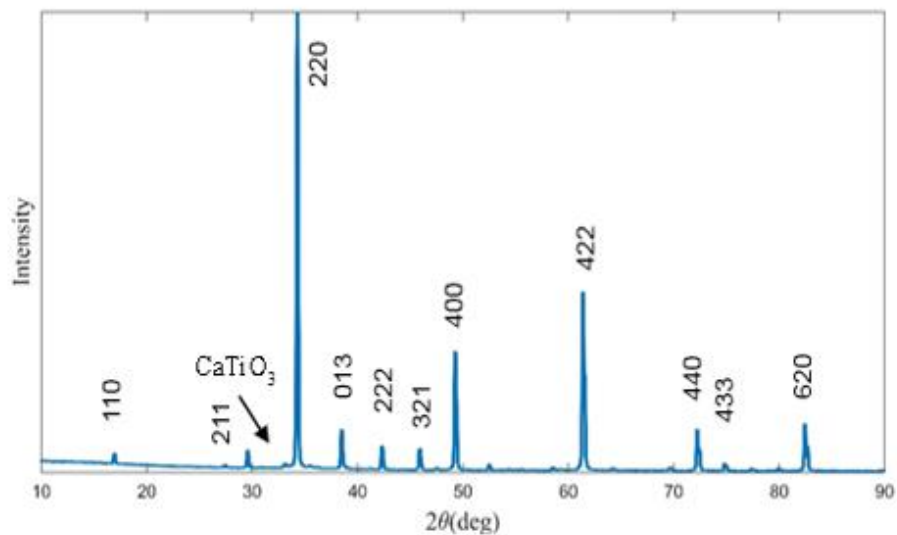


Figure 5-15. Room temperature X-ray diffraction pattern of CCTO

## 5.8 Relative permittivity measurement of CCTO

Sintered pallets were gold coated (see figure 4-16), and relative permittivity was measured with respect to the frequency ranging from 20Hz to 1MHz by the LCR meter with specifications explained above see figure 4-17 Results are in agreement with previous studies (Ahmadipour et al., 2016 and Tang et al.,2017).

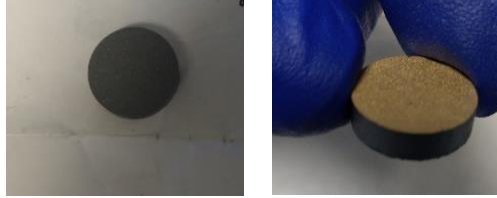


Figure 5-16. A CCTO sample prepared for relative permittivity measurement

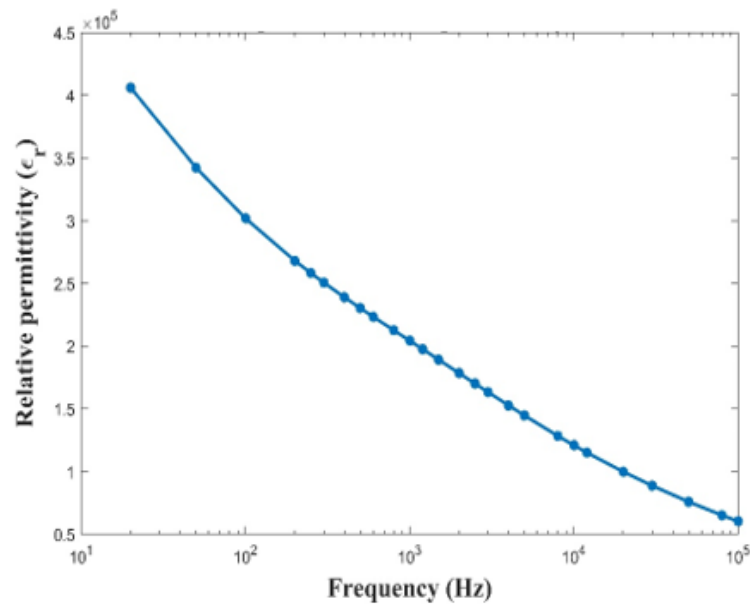


Figure 5-17. Room temperature relative permittivity of CCTO versus frequency

## 5.9 UV curing electroceramic pigmented dielectric preparation

This section explains the procedure of preparing UV curing electroceramic pigment used as a dielectric layer of EA devices in more detail.

Aliphatic urethane diacrylate oligomer (EBECRYL 284) diluted with 12% of 1,6 hexanediol diacrylate monomer prepared by Allnex company was used as the benchmark ink. An extra 1,6 hexanediol diacrylate monomer might be used to control the viscosity of the final ink formulation. BYK-2009 dispersing agent was added and mixed using Dispermat LC75 E high shear mixer (see figure 5-18). The high shear mixer speed was

controlled to be 12000 rpm/min during the whole ink preparation process, and then the pigments (BT or CCTO) were added gradually to the solution to perform the best dispersion. Finally, BYK 1799 defoamer was added to the mixture. The chemical compositions of each ink used in this research are listed in table 5-1, 5-2 and 5-3.



Figure 5-18. Dispermat LC75 E high shear mixer used for dispersing electroceramic particles

Table 5-1. Composition of UV-BaTiO<sub>3</sub> ink

Composition type	Composition name	Density (g/cm <sup>3</sup> )	Composition percentage	Volume (cm <sup>3</sup> )	Mass (g)
Oligomer	EBECRYL 284	1.18	56.50%	48.025	56.6695
Monomer	HDDA	1.0219	0	0	0
Pigment	BaTiO <sub>3</sub>	6.02	30%	25.5	153.51
Dispersing agent	BYK-2009	1.02	5%	4.25	4.335
Photoinitiator	2022	1.1	8%	6.8	7.48
Defoamer	1799	0.99	0.50%	0.425	0.42075
Total	-	-	100%	85	222.4153



Table 5-2. Composition of UV-CCTO ink

Composition type	Composition name	Density (g/cm <sup>3</sup> )	Composition percentage	Volume (cm <sup>3</sup> )	Mass (g)
Oligomer	EBECRYL 284	1.18	56.50%	48.025	56.6695
Monomer	HDDA	1.0219	0	0	0
Pigment	CCTO	4.8	30%	25.5	122.4
Dispersing agent	BYK-2009	1.02	5%	4.25	4.335
Photoinitiator	2022	1.1	8%	6.8	7.48
Defoamer	1799	0.99	0.50%	0.425	0.42075
Total	-	-	100%	85	191.3053

Table 5-3. Composition of UV ink without pigment

Composition type	Composition name	Density (gr/cm <sup>3</sup> )	Composition percentage	Volume (cm <sup>3</sup> )	Mass (gr)
Oligomer	EBECRYL 284	1.18	76.50%	65.025	76.7295
Monomer	HDDA	1.0219	15.5%	13.175	13.4635
Photoinitiator	2022	1.1	8%	6.8	7.48
Total	-	-	100%	85	97.673

## 5.10 Viscosity measurement

Screen printing inks are non-Newtonian fluids (Kapur, Abbott, Dolden et al., 2013) and have shear thickening (Dilatant) behaviour; the viscosity of fluid increases with the rate of shear strain due to thick suspensions of particles in inks. In order to make sure that formulated inks have the same fluid behaviour under shear stress, their viscosities are compared with some mass product screen printing inks. Two thermal cured inks with the lowest and highest viscosity were chosen to find the range of ink viscosity for screen printing. Mass products UV cured ink were also tested for reference. Results show (see figure 5-19) that formulated inks have suitable viscosity for screen printing.

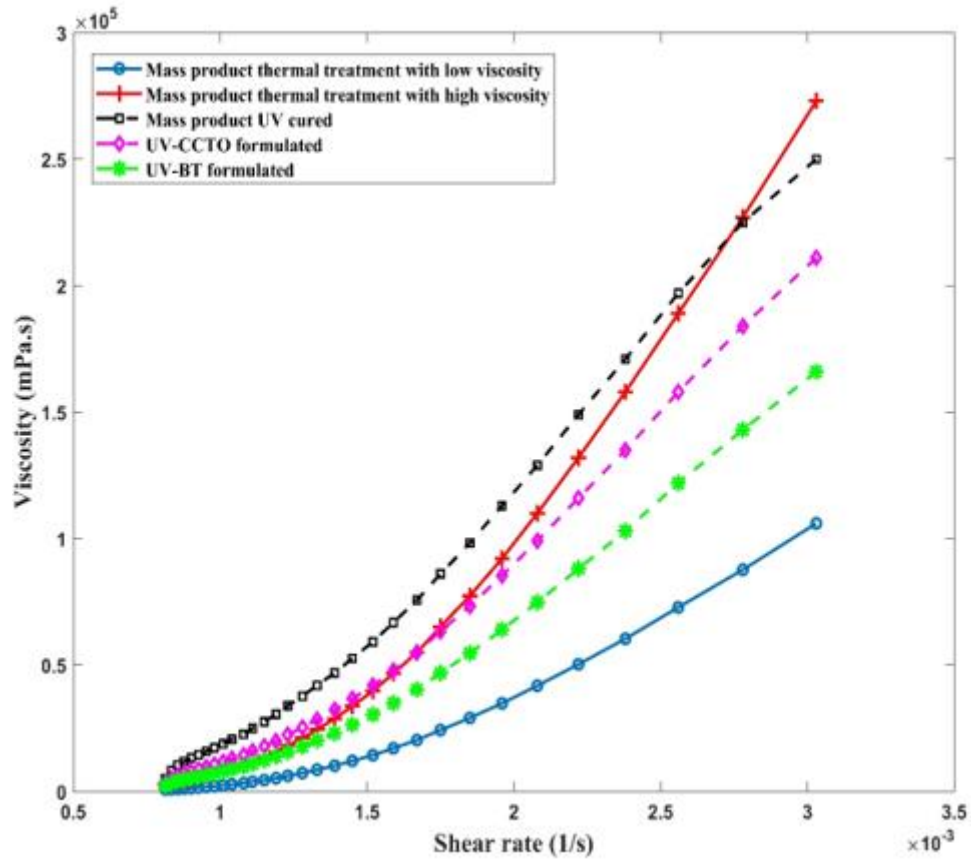


Figure 5-19. Viscosity of mass product screen printing inks and formulated inks versus shear rate

## 5.11 SEM image

### 5.11.1 Sample preparation for SEM analysis

The next step was to ensure that ceramics powders were distributed uniformly in the inks. XRF sample cups were modified to fabricate cylindrical cured samples of the inks. A hollow circular cylinder of polycarbonate was made with an internal radius of 5 mm. The external radius value was chosen to be fitted inside the XRF sample cup. A polypropylene film covered the bottom and internal surface of the hole (see Figure 5-20). The inks were poured into the hole, and the samples were put in the sample holder of the XRF instrument and exposed to an electron beam generated by the XRF instrument (see Figure 5-21); as a result, the inks were cured. Figure 5-22 shows a cured sample of BT-UV composite used for SEM analysis and dielectric measurement. Images created by the backscattered technique with different magnifications (see Figure 5-23) show the quality of dispersion of electroceramic particles in the cured ink.

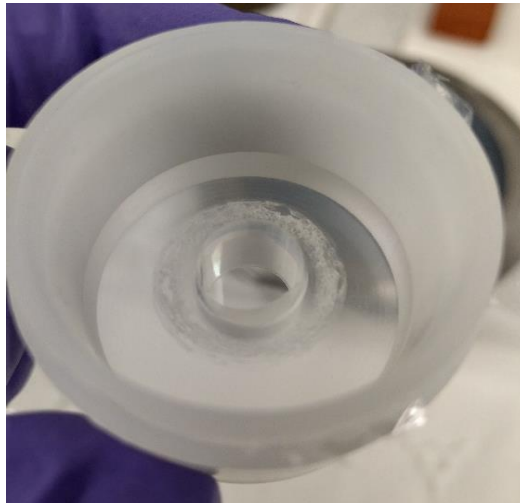


Figure 5-20. Modified XRF cup to prepare cured ink sample

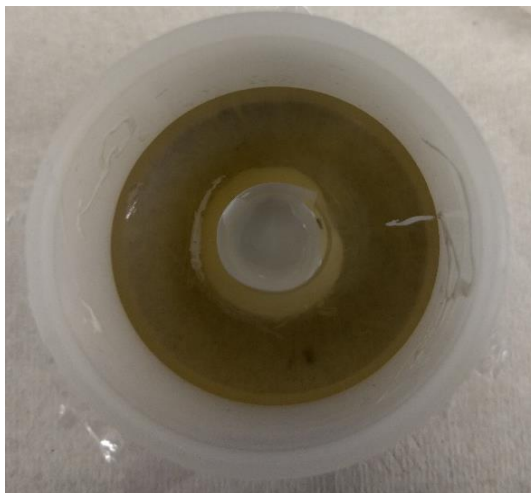


Figure 5-21. Cured UV ink sample by electron beam radiated from XRF

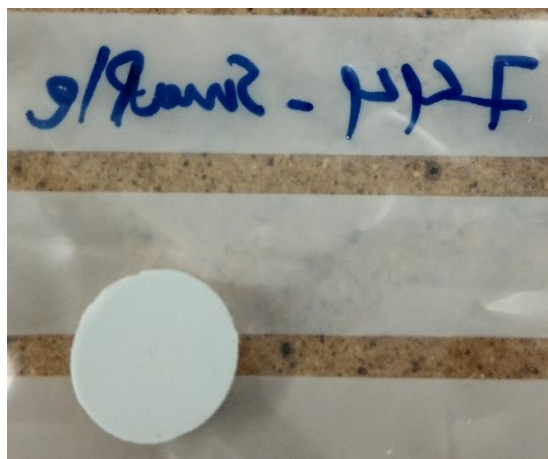
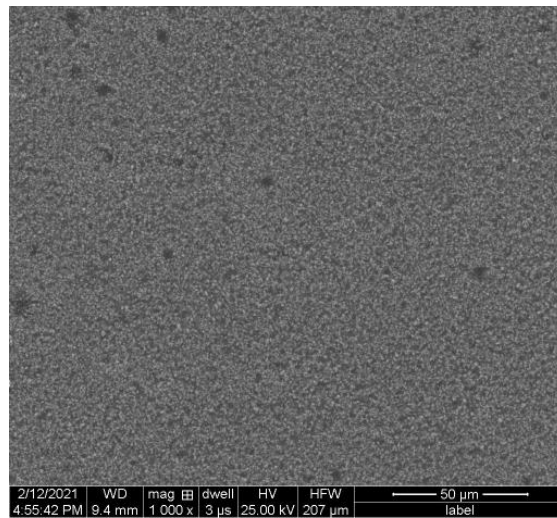
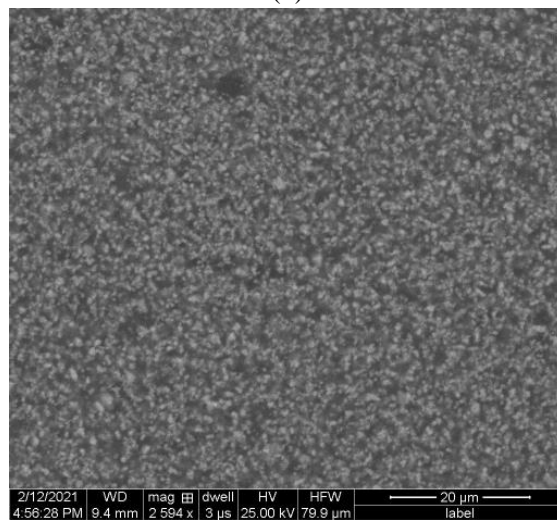


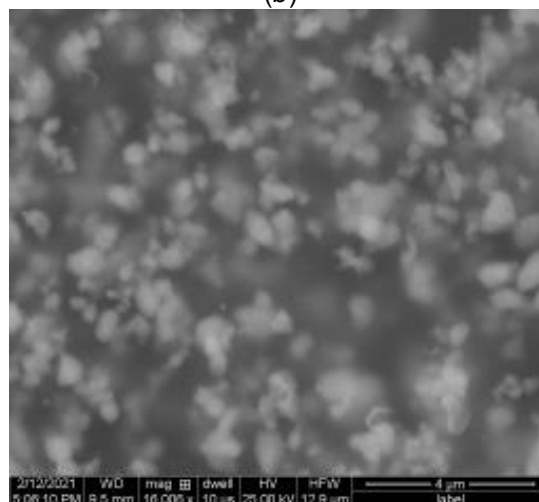
Figure 5-22. Cylindrical sample of cured ink (mixture of  $\text{BaTiO}_3$ - UV polymers)



(a)



(b)



(c)

Figure 5-23. SEM image of cured ink (BT-UV polymer) with scale of (a) 50 μm, (b) 20 μm and (c) 4 μm

## 5.12 Dielectric measurement

The same procedure (see section 5-11-1) was followed to prepare a cylindrical sample of UV cured inks with and without electroceramic pigment to compare their relative permittivities. Figure 5-24 compared relative permittivities of samples for a range of frequencies.

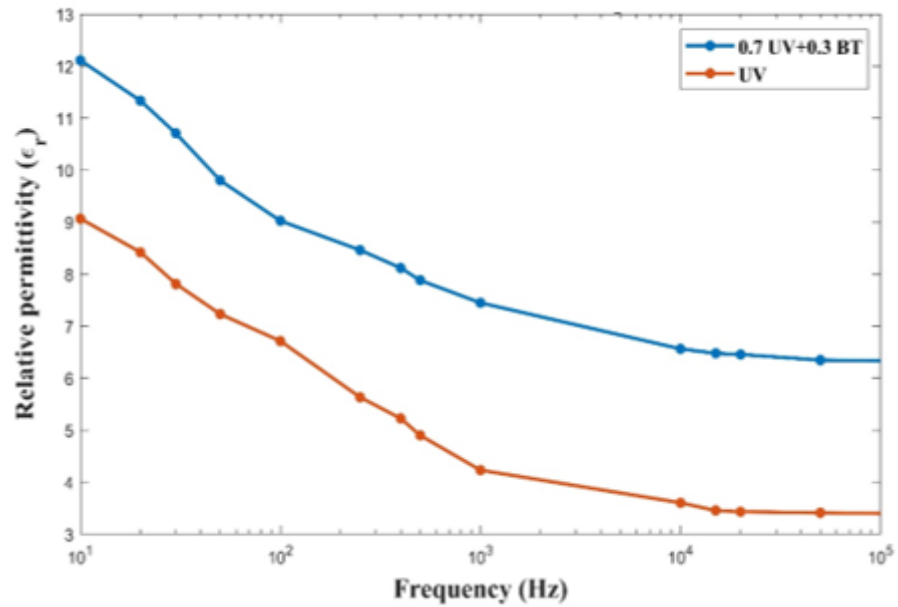


Figure 5-24. Comparison of room temperature relative permittivity of cured UV polymer and BT-UV composite versus frequency

## *Chapter 6*

# **EA fabrication and testing procedure**

### **6.1 EA device history and fabrication methods**

EA devices can be made either by printing mask on prefabricated material and etching techniques or using conductive ink and printing EA electrodes on suitable dielectric materials.

#### **6.1.1 Photo-masking process and etching technique**

In this method, a limited number of available prefabricated copper clads have to be chosen, and electrode shapes are printed on the copper side of the pad; the ink printed may or may not need treatment to be etching-resistant (Guo et al., 2016 b). Thermal printhead and solid ink technology provide a masking layer that does not need treatment. This technology is discontinued, and the alternative is UV curing inkjet printers (method followed in this research) with a piezoelectric printhead and a UV lamp. In this method, printing and treatment are synchronized. This technology has become prominent in the printing industry, and nowadays, UV flat bead printers can print in most materials. Photo-masking technique is cheaper than the other method; however, the guaranteed tolerance may not be achieved since chemical processing is involved (Dadkhah et al., 2019). Also, the etching time is another drawback, and overall, this is not an environmentally friendly process compared to conductive inkjet printing.

##### **6.1.1.1 Rigid EA devices**

FR-4 and FR-5 copper clads can be potentially used to fabricate rigid EA devices. FR-4 is Epoxy resin and glass fibre fabric, whereas FR-5 is made of Epoxy resin thermostable

glass fibre fabric; therefore, the glass transition temperature and operating temperature of RF-5 is slightly (about 30°C) higher than RF-4. Copper clads are also available on a single side and double side with different thicknesses of copper layers (between 1/8 and 4 oz or 3.1 and 117.5  $\mu\text{m}$ ).

#### 6.1.1.2 Flexible EA devices

Flexible EA devices can be fabricated using copper-clad laminate. Copper-clad laminates include copper foil bonded to various polymer composite films such as polyester and polyimide (Guo et al., 2016 b and Dadkhah et al., 2019). This material system is designed for multilayer flexible and rigid-flexible applications. Two methods are used to fabricate copper-clad laminates, Electrodeposited (ED) and Rolled-annealed (RA). Generally speaking, RA laminates are more recommended than ED in fabricating flexible ones and rigid-flexible circuit boards due to less surface roughness. DuPont is a pioneer in fabricating this type of material and offers a variety of products shown in table 6-1.

Table 6-1. Properties of mass product flexible copper-clad laminates

Product Name	relative permittivity	Dielectric strength	Loss Tangant	Volume resistivity	Copper Thickness	Dielectric thickness
Pyrulux AP	3.4(1MHz), 3.2(10 GHz)	200(V/ $\mu\text{m}$ )	0.0021MHz), 0.003(10 GHz)	$>10^{17}(\Omega.\text{cm})$	18, 35( $\mu\text{m}$ )	25, 50,75,100,125 and 150( $\mu\text{m}$ )
Pyrulux TAS	3.4(1MHz), 3.2(10 GHz)	Not Available	0.0031MHz), 0.0045(10 GHz)	$>10^{16}(\Omega.\text{cm})$	12( $\mu\text{m}$ )	12, 25, 45( $\mu\text{m}$ )
Pyrulux TA (double sided)	3.2(10 GHz)	Not Available	0.003(10 GHz)	$>10^{16}(\Omega.\text{cm})$	12, 18( $\mu\text{m}$ )	25,38,50( $\mu\text{m}$ )

#### 6.1.2 Conductive inkjet printing

Conductive inks can be fabricated using conductive polymers (Yang, Stoeckel, Ruoko, et al., 2021) or inks with highly loaded conductive particles such as Carbon, Silver and Copper with micro or Nano size particles (Tao, Wang and Tai, 2013, Zhang, Zhu, Li, Zhao et al., 2014 and Islam, Khair, Ahmed et al., 2019). Generally speaking, conductive inks based on metal particles have shown better conductivity. Typically, the conductivity of 105 S/m is obtainable using silver particle based ink compared to  $59 \times 10^7$  S/m for bulk copper. Lessing, Glavan, Walker et al., 2014, fabricated EA devices using Silver based ink with the resistivity of  $13 \pm 1 \Omega$  and reproducible width and spacing of 0.5mm.



Figure 6-1. Fabricated EA device using conductive ink jet printer (Lessing et al., 2014)

## 6.2 Dielectric layer of EA devices

The electrical properties of a dielectric layer that need to be considered while designing an EA device are relative permittivity and dielectric breakdown voltage. Physical properties like surface roughness should also be considered when choosing the dielectric layer. Numerical investigations of the influence of relative permittivity on uni-layer EA devices showed that the higher the relative permittivity, the higher the EA force can be generated (explained in more detail in chapter 2); however, the improvement of EA force for relative permittivity higher than 20 is negligible. Bi-layer EA devices, based on their design, have an optimum value of relative permittivity of a dielectric layer (Akherat, Karimi, Alizadehyazdi et al., 2019). Dielectric breakdown of dielectric layer plays an essential role in obtainable EA force. Investigation (Akherat et al., 2019) shows that uni-layer EA devices having dielectric layers with higher dielectric strength enable a designer to decrease the spacing between electrodes or increase applied voltage and, as a result, increase obtainable EA force, therefore choosing the best materials for dielectric layers is very important in designing EA devices with better performance. In most cases of studies of electroadhesion, a combination of prefabricated materials and industrial adhesives has been used, which adds complexity to reach a suitable conclusion, and there is a lack of systematic experimental investigation of electrical properties of dielectric layers on obtainable EA forces, which have been considered to address in this research.

## 6.3 Uni-layer and Bi layer electrodes

In terms of electrode positions, EA devices can be fabricated by two different methods, uni-layer (see figure 6-2) and bi-layer structures. In uni-layer structures, the positive and negative electrodes are in the same plane, whereas in bi-layer structures (see Figures 6-3



and 6-4), there is a dielectric layer between positive and negative electrodes; therefore, this give the flexibility to design more complex EA devices as well as the risk of shorts decreases moreover the effective gap of second layer is wider and therefore etching process or printing electrodes are more controllable.



Figure 6-2. Schematic of Uni layer EA devices

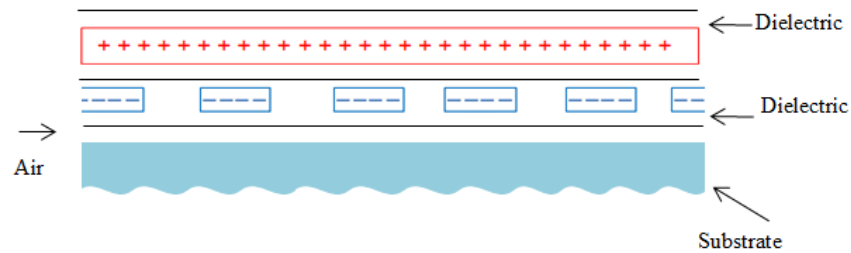


Figure 6-3. Schematic of bi-layer EA devices

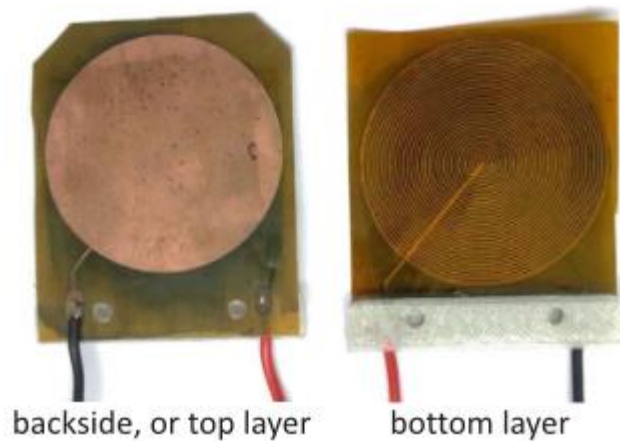


Figure 6-4. Fabricated bi-layer EA devices (Dadkhah et al., 2019)

## 6.4 EA device preparation

### 6.4.1 EA devices with bare electrodes

In this research, a photo-masking process and etching technique were used to fabricate both rigid and flexible EA devices. A Canon Arizona 2280 XT, UV curing flatbed printer was used to prepare photo-masking of electrode patterns (see figures 6-5 and 6-6) designed in AUTOCAD in actual size. The geometry accuracy of the printer is shown in table 5-1. FR4 single sided copper clads  $18" \times 12" \times 1.6\text{mm}$  1oz and copper/polyester films were used to fabricate rigid and flexible devices, respectively (see figures 6-5 and 5-6). After printing photo masks, the copper clads were etched to remove unprotected areas (see figure 6-7 a), and then the copper clads were washed carefully to remove all solutions; finally, the photo mask protection layers were removed using Acetone (see figure 6-7 b). After this step, EA devices with bare electrodes were ready to test. Names were chosen for patterns according to figure 6-8.



Figure 6-5. Printing photo-mask on rigid copper clads using the UV flatbed printer

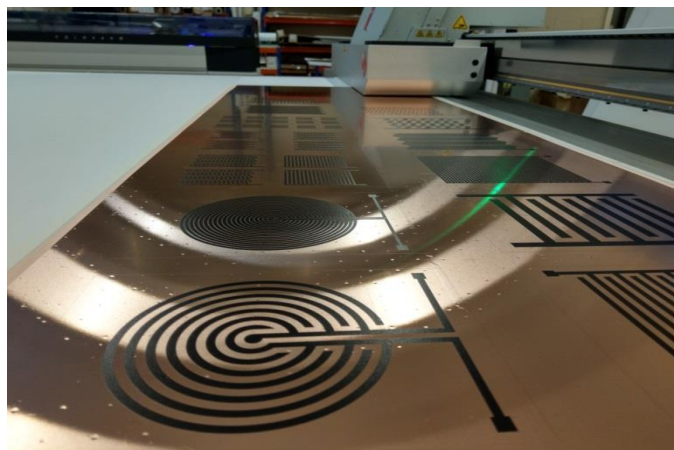


Figure 6-6. Printing photo-mask on flexible copper-clad laminate using the UV flatbed

Table 6-2. Geometric accuracy of the UV flatbed printer

Line width	$\pm 0.8$ mm max error, measures over 2.5m
Line length	$\pm 1.0$ mm max error, measures over 3.08m
Line straightness/width	0.7 mm max error, measures over 2.5m
Line straightness/length	0.7 mm max error, measures over 3.08m
Diagonal error	$\pm 1.0$ mm max error, measures over $3.08 \times 2.5 \text{m}^2$

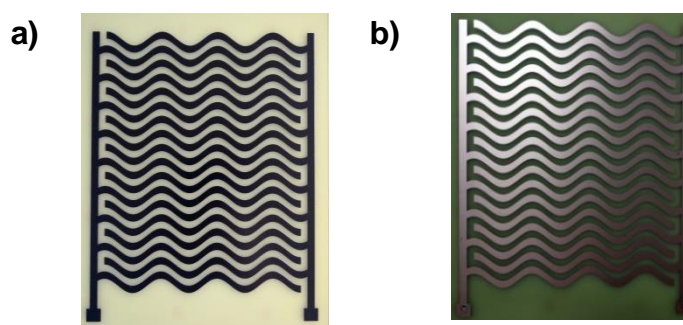


Figure 6-7 a) rigid copper clad after etching and b) rigid copper clad after washing with acetone

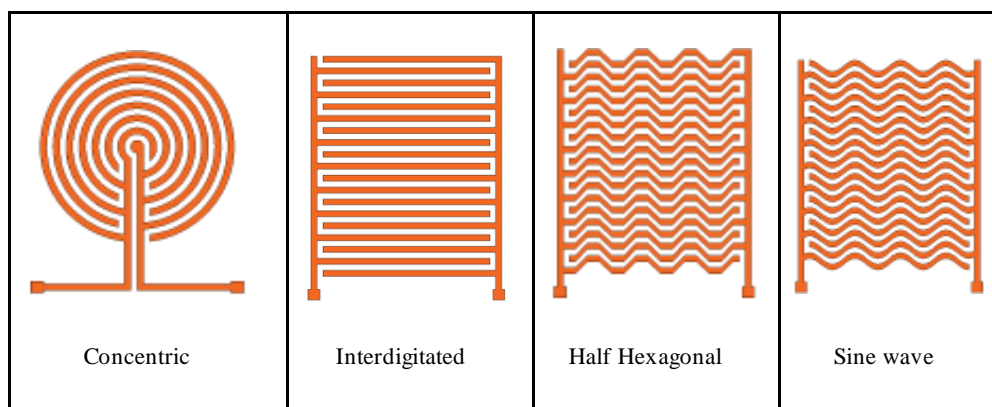


Figure 6-8. Electrode patterns

#### 6.4.2 Rigid and Flexible EA devices coated with prefabricated UV- $\text{TiO}_2$ dielectric layer

EA devices with bare electrodes fabricated using the same procedure explained in the previous section, and then 2-pass printing ( $10\mu\text{m}$  thickness each) of mass product white UV ink with  $\text{TiO}_2$  pigment was used to coat EA devices using the same flatbed printer (see figure 6-9).

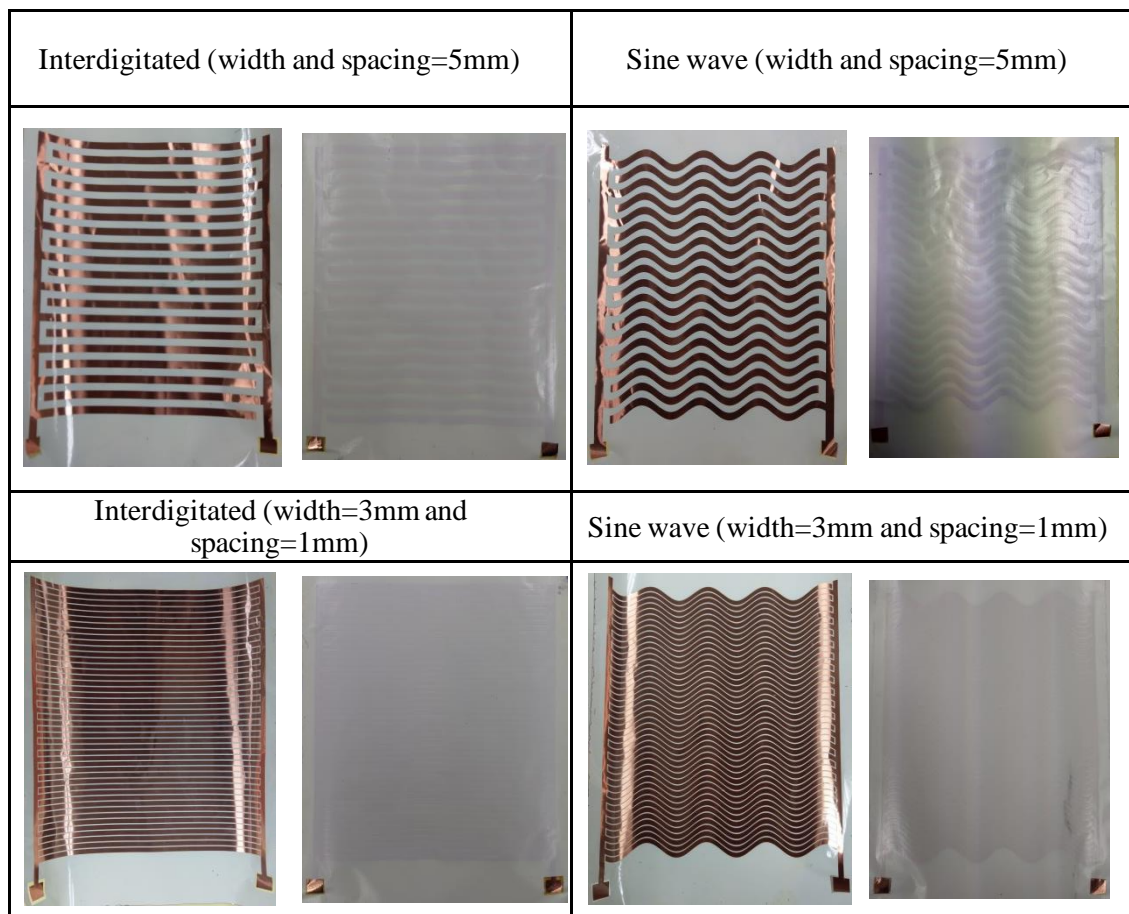


Figure 6-9. Flexible EA device with UV- $\text{TiO}_2$  dielectric layer

#### 6.4.3 Rigid EA device coated with fabricated UV (without pigment) and UV-electroceramic dielectric layer (BT and CCTO)

The formulated UV-electroceramic inks were used as a dielectric layer for this type of EA device. The procedure was, first, to fill the gap between electrodes of EA devices with bare electrodes by inks and cure the inks by the hired Fe doped medium pressure Mercury UV lamp (see Figure 6-10) in the designed safety box and then for the purpose of constancy of the dielectric layer the following two layers of the coating were applied using prepared silk screen (see Figure 6-11). The schematic of the two last layers applied

using the screen printing technique is shown in figure 6-12. To avoid complexity, this type of EA device is fabricated only using the interdigitated pattern of electrodes with 5mm electrode width and spacing. Figure 6-13 shows EA devices fabricated by this procedure using UV ink (without pigment or clear coating) and electroceramic pigmented inks.



Figure 6-10. Fe doped medium pressure mercury UV lamp



Figure 6-11. Prepared silk screen for UV-electroceramic coating

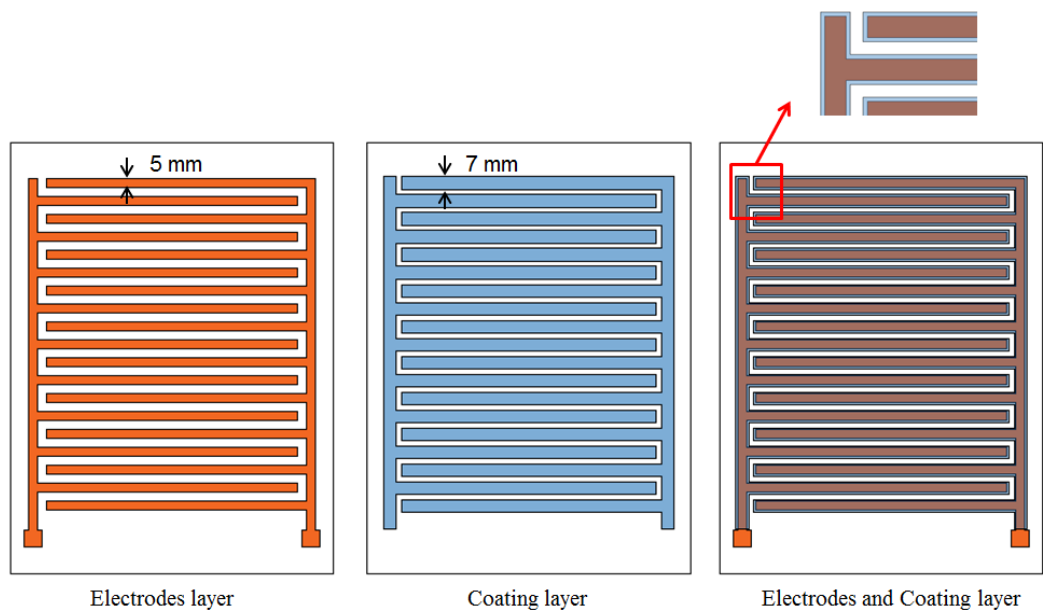
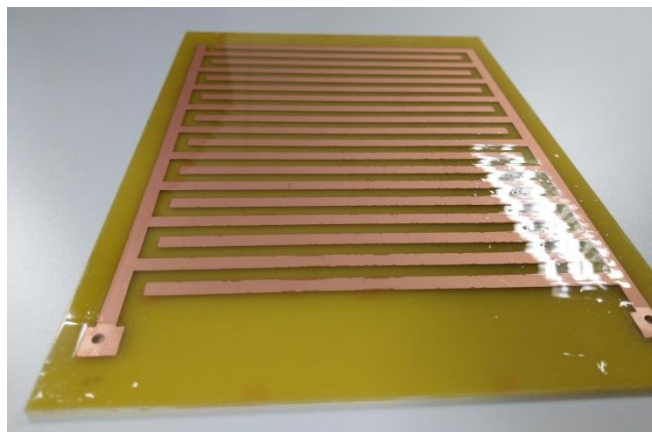


Figure 6-12. Schematic of coating layer applied by screen printing technique



Interdigitated EA device  
with clear UV coating



Interdigitated EA device  
with BT-UV coating  
With 30% volumetric  
ratio of BT



Interdigitated EA device  
with CCTO-UV coating  
With 30% volumetric  
ratio of CCTO



Figure 6-13. Interdigitated EA device coated by formulated inks (with and without pigment)

#### 6.4.4 Rigid EA device with high voltage oil dielectric layer

NYTRO10XN Industrial high voltage oil was used to fill the gaps between electrodes and then EA devices were covered by 10  $\mu\text{m}$  polyester film (see Figure 6-14).

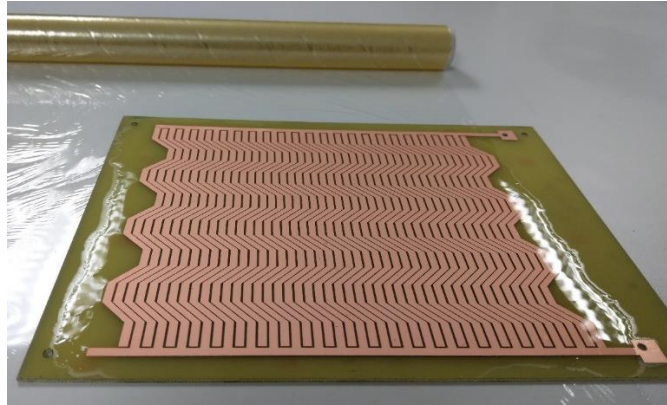


Figure 6-14. An EA device with high voltage oil as dielectric layer

### 6.5 History of EA force measurement

Two methods have been used to evaluate EA devices' performance: the direct method (see figure 6-15) and the indirect method (see figure 6-16). In the direct method, the normal force generated by EA devices has been measured (Guo et al., 2016 a). In the indirect method, the shear force generated because of normal EA force has been evaluated (Dadkhah et al., 2018). The experimental configurations, either for direct or indirect measurement tests, should generally include a mechanism to control the movement of EA devices, A force sensor (6-DOF force-torque sensor) and a high DC power supply. Figure 6-17 shows two examples of experimental apparatus used to evaluate EA devices' performance (Guo et al., 2016 a; Dadkhah et al., 2018).

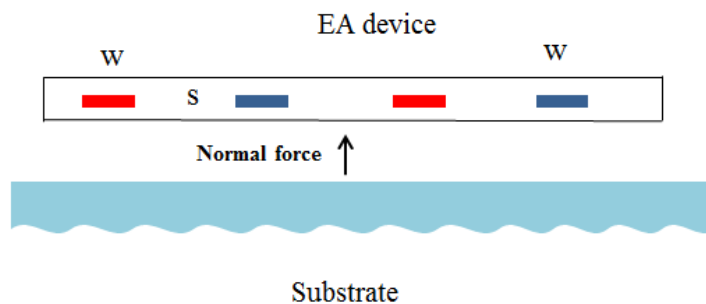


Figure 6-15. Schematic of direct method to measure normal force obtained by EA devices



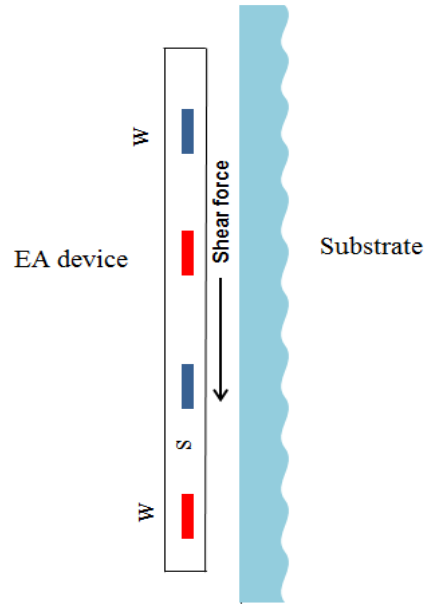


Figure 6-16. Schematic of indirect method to measure shear force obtained by EA devices

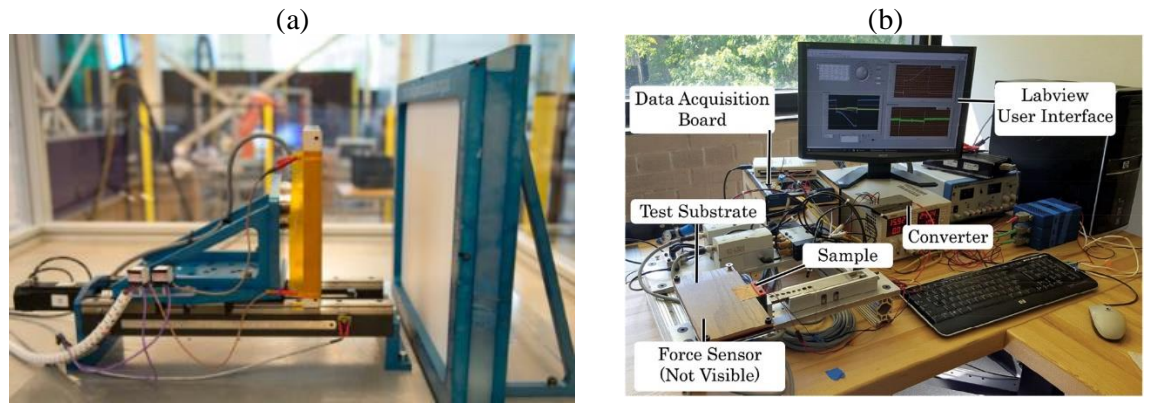


Figure 6-17. Experimental apparatus used to measure a) normal force (Guo et al., 2016 a) and b) shear force (Dadkhah et al., 2018) obtained by EA devices

## 6.6 The experimental setup and procedure of tests

The experimental setup used for this research includes DENSO Robot VP-6242(6-axis type), ATI Six-Axis Force/Torque sensor model Gamma, a high DC power supply, a USB DAQ device, and a laptop. All experiments were carried out in the Faraday cage. The force sensor was mounted to the end effector of the Denso robot using a 3D printed interface. The pad holder was assembled to the other side of the force sensor, and EA devices were fixed to the pad holder. The high DC power supplier was connected to the EA devices by test leads to supply DC voltage for tests. The substrate was assembled to

the substrate holder, and the holder was fixed to the table. Figure 6-18 shows more detail of the experimental setup.

### 6.6.1 Repeatability of the instrument

The accuracy of each instrument was used is listed below:

- Denso robot repeatability accuracy:  $\pm 0.02$  mm consistency in production (Denso robot data sheet)
- DC power supply repeatability:  $\pm 0.01$  kV
- ATI Six -Axis Force sensor with below specification:

Calibration ranges ( $\pm$ ):

$F_x$	$F_y$	$F_z$	$T_x$	$T_y$	$T_z$
32 N	32 N	100 N	2.5 N.m	2.5 N.m	2.5 N.m

Measurement uncertainty (95% confidence level, percent of full-scale load):

$F_x$	$F_y$	$F_z$	$T_x$	$T_y$	$T_z$
0.75%	0.75%	0.75%	1.0%	1.0%	1.0%

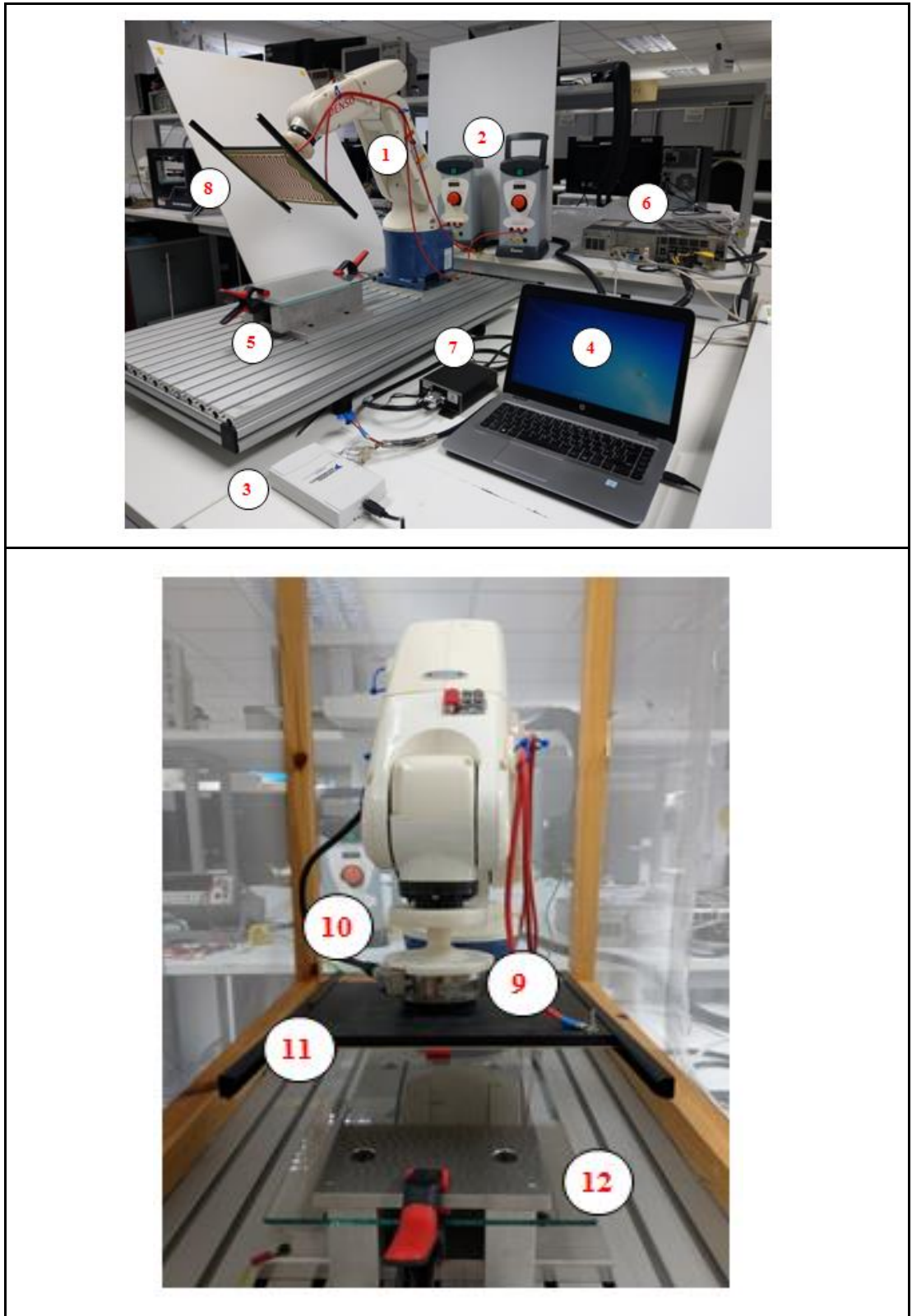
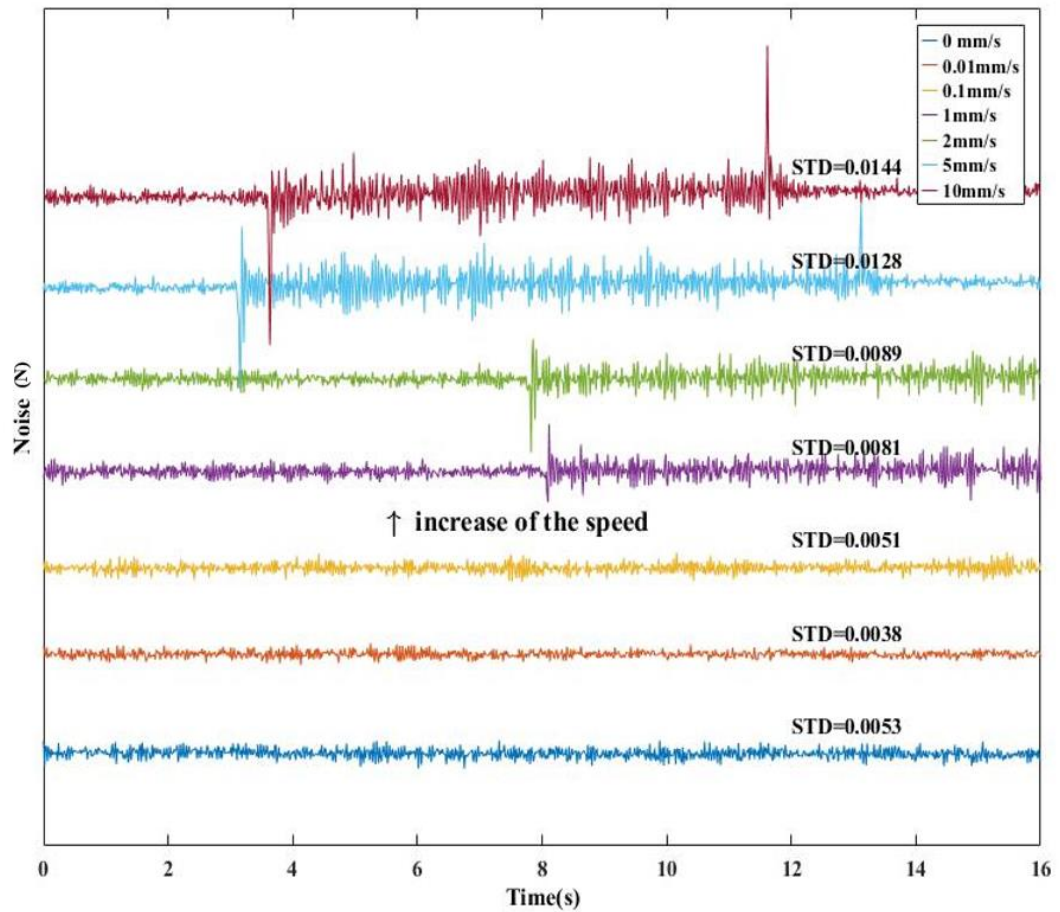


Figure 6-18. Experimental configuration including : (1) Denso robot, (2) DC power suppliers, (3) usb DAQ device, (4) Laptop (5) Substrate holder (6) Robot main controller, (7) interface power supply box of the sensor, (8) EA device, (9) Force sensor, (10) Interface between the robot end effector and the force sensor, (11) Pad holder (12) Substrate

### 6.6.2 Denso Robot speed and its effect on data recorded by the force sensor

To find the optimum speed of the robot, which minimizes the effect of the movement on the EA force measurements, the sensor, the pad holder and one of the rigid pads were mounted to the Denso robot. The robot moved with various speed (0.01 mm/s, 0.1mm/s, 1mm/s, 2 mm/s, 5mm/s and 10mm/s) in the z direction while the sensor was recording the force. The results showed (Figure 6-19) that speeds less than 1 mm/s had no effect on the data recorded by the sensor.



### 6.6.3 Applied voltage measurement before tests

A high DC voltage probe testec TT-HVP40 and multimeter Agilent 34405A (see Figure 6-20) were used to measure applied voltage before each test to make sure about all connections and also to check if EA devices received the voltage the power supply generates.

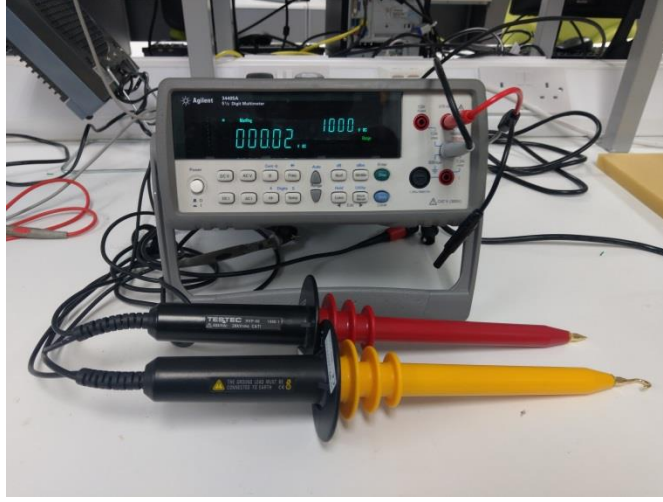


Figure 6-20. High DC voltage probe test TT-HVP40 and multimeter Agilent 34405A

#### 6.6.4 Testing EA device without charge

Each EA device was tested without charge (applied voltage) to ensure that the force generated during the test was purely a result of applying voltage, and EA force was only measured. In the beginning, an EA device is 10mm away from the substrate and moves toward the substrate at the speed of 10 $\mu$ m/s until an EA device pushes the substrate. As a result, a negative force was generated, indicating a perfect connection between the EA device and substrate. The negative force generated will be called preload force then the robot moves away at the same speed to reach its initial position. Figure 6-21 shows the force (a) and the filtered force (b) recorded by the sensor.

#### 6.6.5 Filtering signal recorded by the sensor

A Butterworth filter was used to remove the noise of the signal received from the sensor. This filter has a maximum flat pass band or smoothest frequency response for a given order without including peaks. The response of this filter is given by

$$\left| \frac{V_{out}}{V_{in}} \right|^2 = \frac{1}{1 + \left( \frac{f}{f_c} \right)^{2n}} \quad (6-1)$$

Where  $f$  is the frequency at which the signal is recorded,  $f_c$  is the cut-off frequency,  $V_{in}$  is the input signal,  $V_{out}$  is the output signal, and  $n$  is the order of the filter. The sample rate of the data recorded by the force sensor was 1000 Hz, and the cut-off frequency of 48Hz was found by try and error to be the most efficient for signal processing.

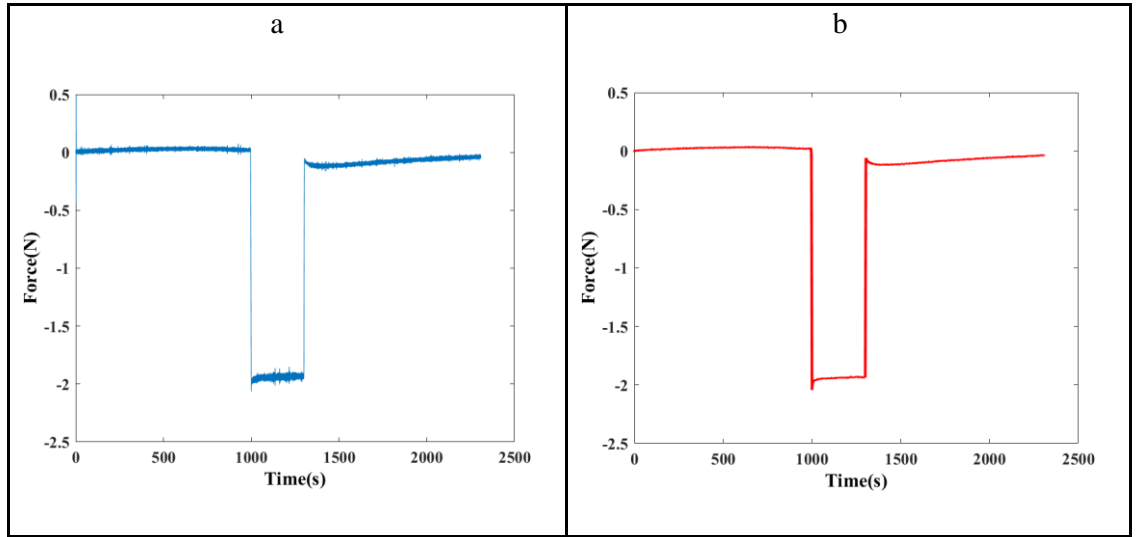


Figure 6-21. Signal recorded by the force sensor a) before filtering and b) after filtering

## 6.7 Test procedure

In this study, the normal force obtained by EA devices was chosen to record to evaluate EA device performance instead of shear force to avoid the complexity of friction due to surface roughness. The initial position of the EA device was set to be 10mm away from the substrate, and both substrate and pad were in the x-y plane (here, z is parallel to the direction of the gravity). The power supply was switched on for 5 min, and then the robot moved toward the substrate at the speed of  $10 \mu\text{m/s}$  (only in z direction) and reached the point that the force direction was reversed, indicating the perfect connection between EA devices and the substrate after holding EA devices in this position for 5 min, the robot moved only in z direction to relocate the EA device to its initial position. The force is continuously recorded in during the whole cycle using the z direction of the sensor. The cycle is repeated 3 times for each test, and 3 EA devices with exactly the same design were tested to check the reproducibility of the results.

## *Chapter 7*

# **Numerical Analysis**

### **7.1 Introduction**

#### **7.1.1 Finite element method**

The finite element method (FEM) is a well-known numerical procedure for solving complicated partial differential equations (PDE), which cannot be solved using classical analytical methods due to the complexity of either PDE or the geometry of interest. The FEM can be used to approximate the solutions to a wide variety of physical problems, including solids, fluids, porous media, or electromagnetic environments. Commercial and open-source software have now been developed that can simulate weakly or strongly coupled physical problems such as acoustic-structure interactions (Łapka, 2018), fluid-structure interactions (Chen, Christensen, 2017) and saturated porous media. The procedure for FEM analysis is to divide the geometry of interest into very small elements using different meshing techniques and to solve PDEs approximately within each element. Those PDEs that need to be solved in electrostatic field analysis are the Laplace and Poisson equations (Woo and Higuchi, 2010). Researchers have shown that FEM is an effective method for electrostatic field analysis in two-dimensional (2D), axisymmetric and three-dimensional (3D) regions of interest with multiple dielectric media (Mao, Qin and Zhang, 2016, Liu et al., 2013 and Guo et al., 2016 b).

#### **7.1.2 FEM procedure for high voltage field problems**

**1-** The region of interest is subdivided into finite elements. Different methods can be used for this purpose. The simplest 2D element from a mathematical point of view is the linear triangular element (see figure 7-1), which has only three nodes and is numbered in the anti-clockwise direction around the element.



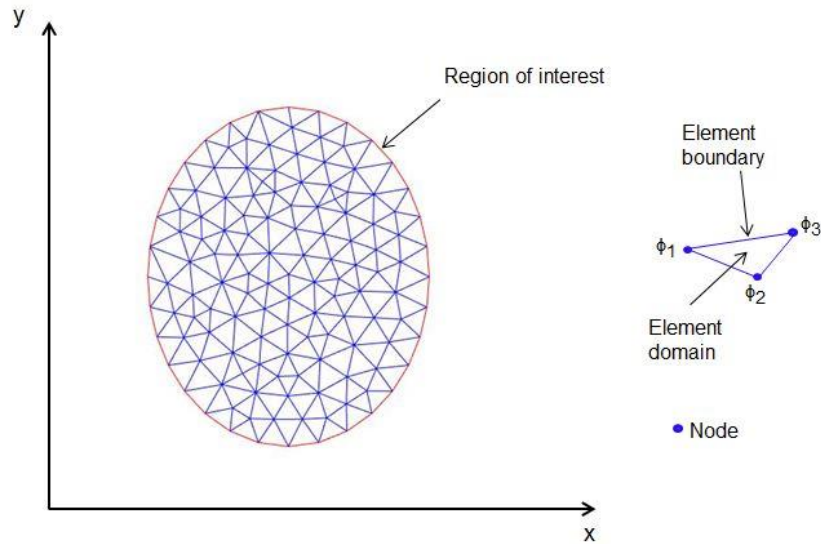


Figure 7-1. Subdividing region of interest into finite elements

**2-** Interpolation models (see figure 7-2) are used to estimate the field variables (electric potential) over the elements. Electric potential ( $\phi$ ) is assumed to be varying linearly within an element, therefore:

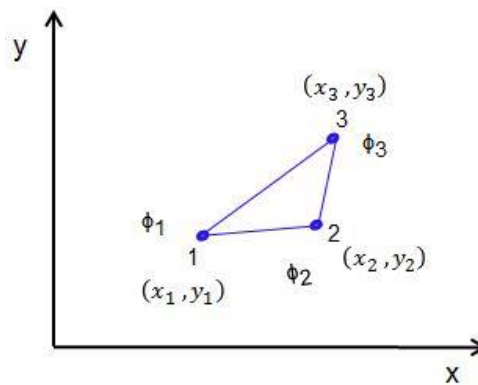


Figure 7-2. Linear interpolation of electric potential in an element

$$\phi = \alpha_1 + \alpha_2 x + \alpha_3 y \quad (7-1)$$

**3-** Relationships between unknown field variables and other physical parameters for each node are used to form the matrix equation for the finite element. Physical parameters which need to be calculated in electrostatic field analysis is the electric field intensity and will be given by:



$$E_x = -\frac{\partial \phi}{\partial x} = -\alpha_2 \quad \text{and} \quad E_y = -\frac{\partial \phi}{\partial y} = -\alpha_3 \quad (7-2)$$

As a result of using a linear variable for electric potential and linear triangular elements, the electric field is constant throughout the element; therefore, this type of element is also called a constant stress element (CST).

**4-** All the element equations are assembled to form a global equation system, and boundary conditions are considered for nodes connected to the surface of interest.

**5-** The global equation system is solved in the loop until finding a potential function  $\phi(x,y)$  which minimizes the potential energy equation. This function satisfies equilibrium and is the actual potential distribution in the region of interest. The potential energy equation in a 2D electric field is given by:

$$u_{total} = \iint_A \frac{1}{2} \epsilon_0 \epsilon_r |\vec{E}|^2 \cdot l \cdot dA \quad (7-3)$$

$$\text{or, } u_{total} = \iint_A \frac{1}{2} \epsilon_0 \epsilon_r |\nabla \phi|^2 \cdot l \cdot dA \quad (7-4)$$

Where:

E = electric field intensity

$\phi$  = electric potential

l = length normal to the area A (usually considered as unity for 2D field)

$\epsilon_0$  = permittivity of free space

$\epsilon_r$  = relative permittivity of dielectric

### 7.1.3 Numerical Assumptions

There are several assumptions needed to take in to account to be able simulating Electrodehesion using commercialised FEA codes like ANSYS Maxwell, Abacus and COMSOL. These assumptions include:

**(1)** Electrodes are perfect electrical conductors.

(2) Dielectric materials are linear, isotropic, and homogenous (LIH), which in reality it is not the case. Linear dielectric materials are materials for which there is a linear relationship between their polarisation and the intensity of the electric field. Isotropic, in this context, means that their relative permittivities are not dependent upon a direction and homogenous means that their relative permittivities do not depend on coordinate:

$$\epsilon_x = \epsilon_y = \epsilon_z$$

(3) The power supply is a dual-polarity DC voltage.

(4) In 2D simulations, the electric field is constant in the y-direction, neglecting the marginal part of the EA pad (thus representing the central part of the electrode).

(5) Dielectrics do not have free charge density.

(6) EA pads are considered to be fully charged and the generated force is not time dependent. It was noted (Bamber et al., 2016) that measured the electric potential distribution of an interdigitated EA pad with 230 mm × 190 mm effective area and their results showed that it took roughly 5 minutes for that pad to become fully charged.

(7) To simplify simulations and achieve mesh independent results, the effect of the backing plate is neglected, and we assumed that electrodes are embedded precisely in the middle of a dielectric layer.

## 7.2 Hardware specifications for simulations

Electroadhesion simulations using ANSYS MAXWELL are memory-bound, which means the time needed to complete a simulation is mostly dependent upon the amount of memory required to hold data; hence, it needs a “fat node” setup. Therefore, all simulations were performed on an 8-core Intel(r) Xeon(r) CPU E5-1620 v4 @ 3.50GHz workstation with 256 GB RAM. The simulation time for 2D parametric simulations with a particular electrode width and spacing was approximately 80 minutes, and for a 3D simulation was approximately 50 hours.

## 7.3 Simulation procedure in ANSYS Maxwell

ANSYS MAXWELL has been used to simulate electrostatic problems before (Yu, Han, Wang et al., 2019, Nassr, Ahmed, El-Dakhakhni, 2008 and Tajdari, Fua'ad bin Rahmat and Thuku, 2012). The simulation procedure includes three main steps: pre-processing, processing, and post-processing. In the pre-processing step, first, the domain of interest is created, including the electrode pattern, a dielectric layer, air layer and substrate, and then the electrical properties of each material are added (electrodes are pure copper with perfect electrical conductivity, the relative permittivity of dielectric, air and substrate) and finally, boundary conditions (B.C) are specified as follows:

(i) Potential difference for electrodes (Dirichlet boundary condition).

(ii) Interfacial boundary conditions between two layers with different relative permittivity (see figure 7-3): electric potential and tangential orientation of the electric field are equal at the interface see Eq. (7-5, 7-6) and normal orientation of the electric field is varying according to Eq. (7-7).

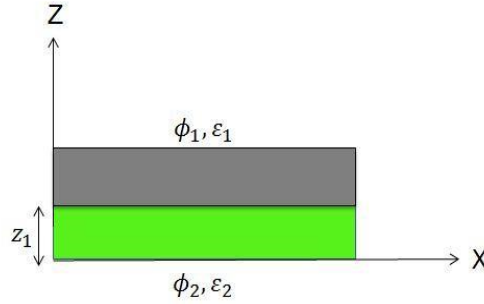


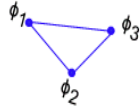
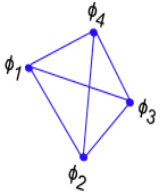
Figure 7-3. Definition of boundary conditions in Cartesian coordinates

Table 7-1. Types of B.C used for 2D and 3D simulation

2DB.C	3DB.C		
$\phi_1(x, z) = \phi_2(x, z)$	$\phi_1(x, y, z) = \phi_2(x, y, z)$	at line/plane $Z=z_1$	(7-5)
$\frac{\partial \phi_1(x, z)}{\partial x} = \frac{\partial \phi_2(x, z)}{\partial x}$	$\frac{\partial \phi_1(x, y, z)}{\partial x} = \frac{\partial \phi_2(x, y, z)}{\partial x}$ $\frac{\partial \phi_1(x, y, z)}{\partial y} = \frac{\partial \phi_2(x, y, z)}{\partial y}$	at line/plane $Z=z_1$	(7-6)
$\epsilon_1 \frac{\partial \phi_1(x, z)}{\partial z} = \epsilon_2 \frac{\partial \phi_2(x, z)}{\partial z}$	$\epsilon_1 \frac{\partial \phi_1(x, y, z)}{\partial z} = \epsilon_2 \frac{\partial \phi_2(x, y, z)}{\partial z}$	at line/plane $Z=z_1$	(7-7)

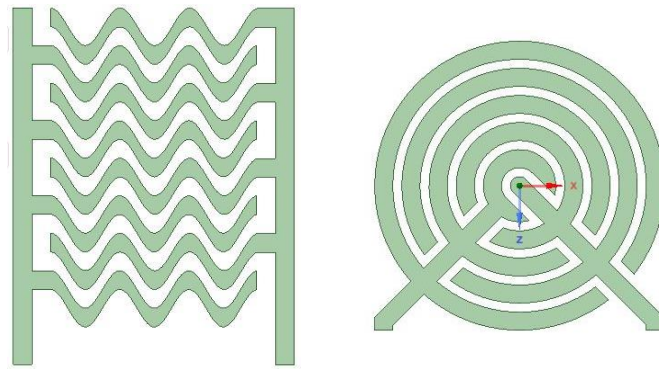
Where  $\phi$  is electric potential and  $\epsilon_1$ , and  $\epsilon_2$  are the relative permittivities of two different layers. In the processing step, the region of interest is discretised to triangular elements for 2D simulations and tetrahedral elements for 3D simulations, and it is assumed that electric potential varies linearly within each element and that also electric field in all directions is constant within each element (see table 7-2).

Table 7-2. Types of elements available in ANSYS Maxwell, discretisation methods and calculation of potential energy

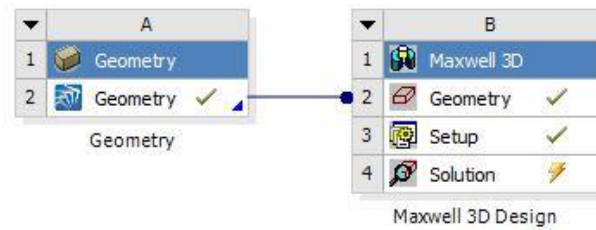
	Type of element	shape of element	Potential distribution at the corners of element	Electric field in element	Potential energy in element
2D	Triangular		$\phi_i = \alpha_1 + \alpha_2 x_i + \alpha_3 y_i$	$E_x = -\frac{\partial \phi}{\partial x} = -\alpha_2$ $E_y = -\frac{\partial \phi}{\partial y} = -\alpha_3$	$u_\theta = \frac{1}{2} \varepsilon_0 \varepsilon_r V (\alpha_2^2 + \alpha_3^2)$
3D	Tetrahedral		$\phi_i = \alpha_1 + \alpha_2 x_i + \alpha_3 y_i + \alpha_4 z_i$	$E_x = -\frac{\partial \phi}{\partial x} = -\alpha_2$ $E_y = -\frac{\partial \phi}{\partial y} = -\alpha_3$ $E_z = -\frac{\partial \phi}{\partial z} = -\alpha_4$	$u_\theta = \frac{1}{2} \varepsilon_0 \varepsilon_r V (\alpha_2^2 + \alpha_3^2 + \alpha_4^2)$

## 7.4 Simulation procedure in ANSYS MAXWELL

In the processing, first, the geometry of an EA device is designed or exported from different software. Here, for complex geometries concentric or sine shape electrodes, the patterns were first designed in ANSYS workbench using Space Claim, and then the geometries were linked to ANSYS MAXWELL(see figures 7-4a and 7-4b).and it was followed by generating the initial mesh (triangle elements for 2D and tetrahedral elements for 3D ) and then based on simulation type (electrostatic, electromagnetic, eddy current and transient) the electric field is solved in a loop until total error energy Eq. (7-4) meets the convergence criteria. In post-processing, the user can create a report including a contour of an equipotential or electric field or use an advanced ANSYS Maxwell calculator to measure parameters like Maxwell stress distribution and electroadhesive force. Figure (7-5) shows all steps of pre-processing and processing by ANSYS Maxwell.



(a)



(b)

Figure 7-4. (a) Creating complex geometries in Space Claim, (b) Linking geometries created in Space Claim to ANSYS Maxwell

## 7.5 Maxwell stress distribution and electroadhesive force calculation in ANSYS MAXWELL

ANSYS MAXWELL has a field calculator (see figure 7-6), which can be used to define new quantities and extend the software's capabilities beyond the calculation or plotting of the main field quantities (such as  $E$ ,  $D$ , etc.) in the post-processing step. The Field Calculator can also be used to perform line, surface, and volume integration of quantities over specified geometric entities.

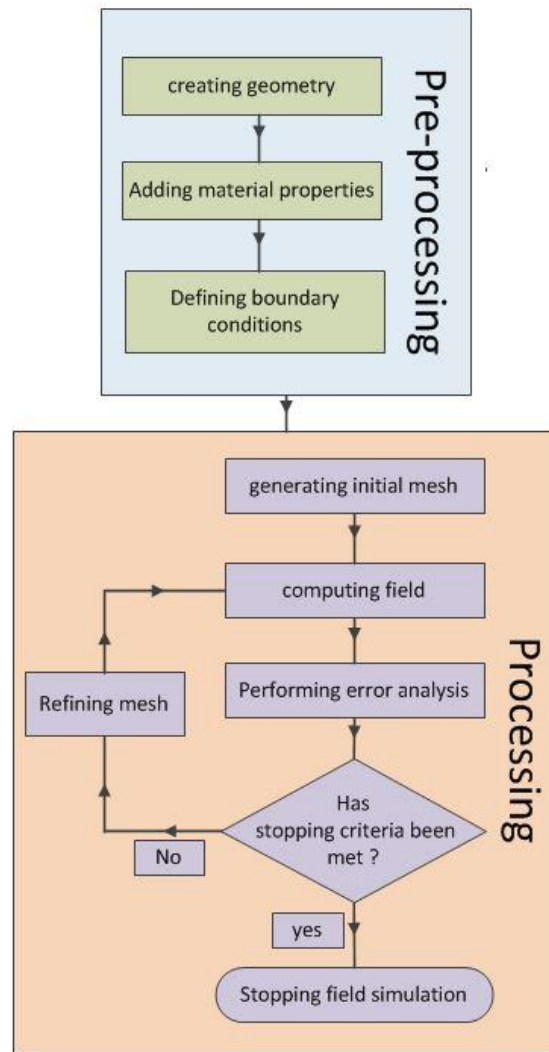


Figure 7-5. Pre-processing and processing steps of FEA in ANSYS Maxwell

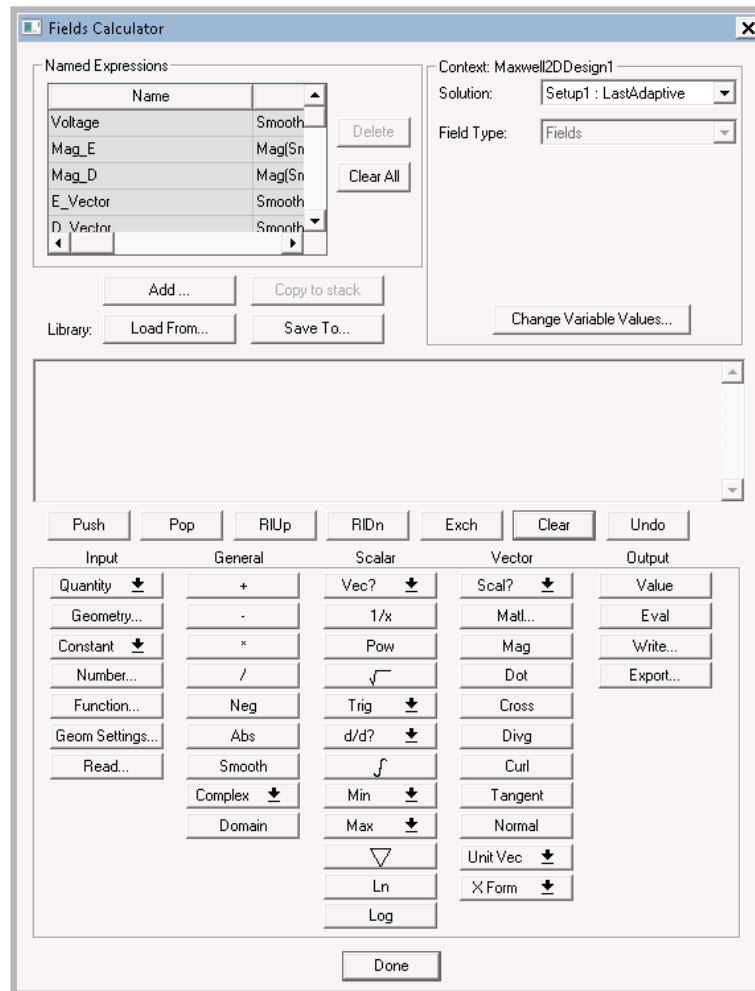


Figure 7-6. ANSYS MAXWELL field calculator

## 7.6 Maxwell stress calculation procedure in ANSYS MAXWELL

Following the sequence of calculator commands given below, Maxwell stress distribution on a line in 2D simulation and on the surface in 3D simulation can be calculated.

1. Quantity (D)
2. Geometry (selecting the line or the surface of interest)
3. Unit Vector (creates the normal unit vector corresponding to the surface of interest)
4. Dot Product
5. Quantity (E)
6. (Multiply)
7. Geometry (selecting the line or the surface of interest)
8. Unit Vector (creating the normal unit vector corresponding to the surface of interest)

9. Number Scalar (0.5)
10. Multiply
11. Constant ( $\epsilon_0$ )
12. multiply
13. Quantity (E)
14. Push
15. Dot product
16. Multiply
17. Minus)
18. Geometry (selecting the line or the surface of interest)
19. Unit Vector (creating the normal unit vector corresponding to the surface of interest)
20. Dot product

After calculating the Maxwell stress, the EA force can be calculated by performing a line or surface integral.

## 7.7 Parametric simulations

### 7.7.1 The relationship between EA force and applied voltage

2D parametric simulations were carried out to find the relationship between obtainable EA force and applied voltage (figure 7-10 shows the schematic of computational domain), and results show that EA force (see Figure 7-7) and Maxwell stress (EA pressure) distribution (see Figure 7-8) are proportional to the applied voltage square.

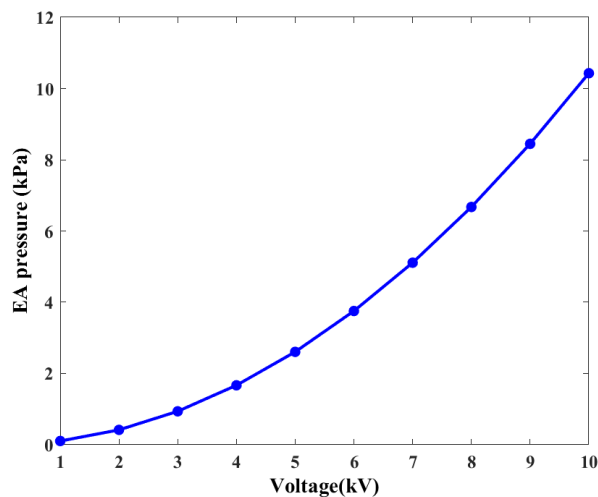


Figure 7-7. 2D modelled EA pressure of interdigitated pattern with electrode width and spacing of 0.5 mm



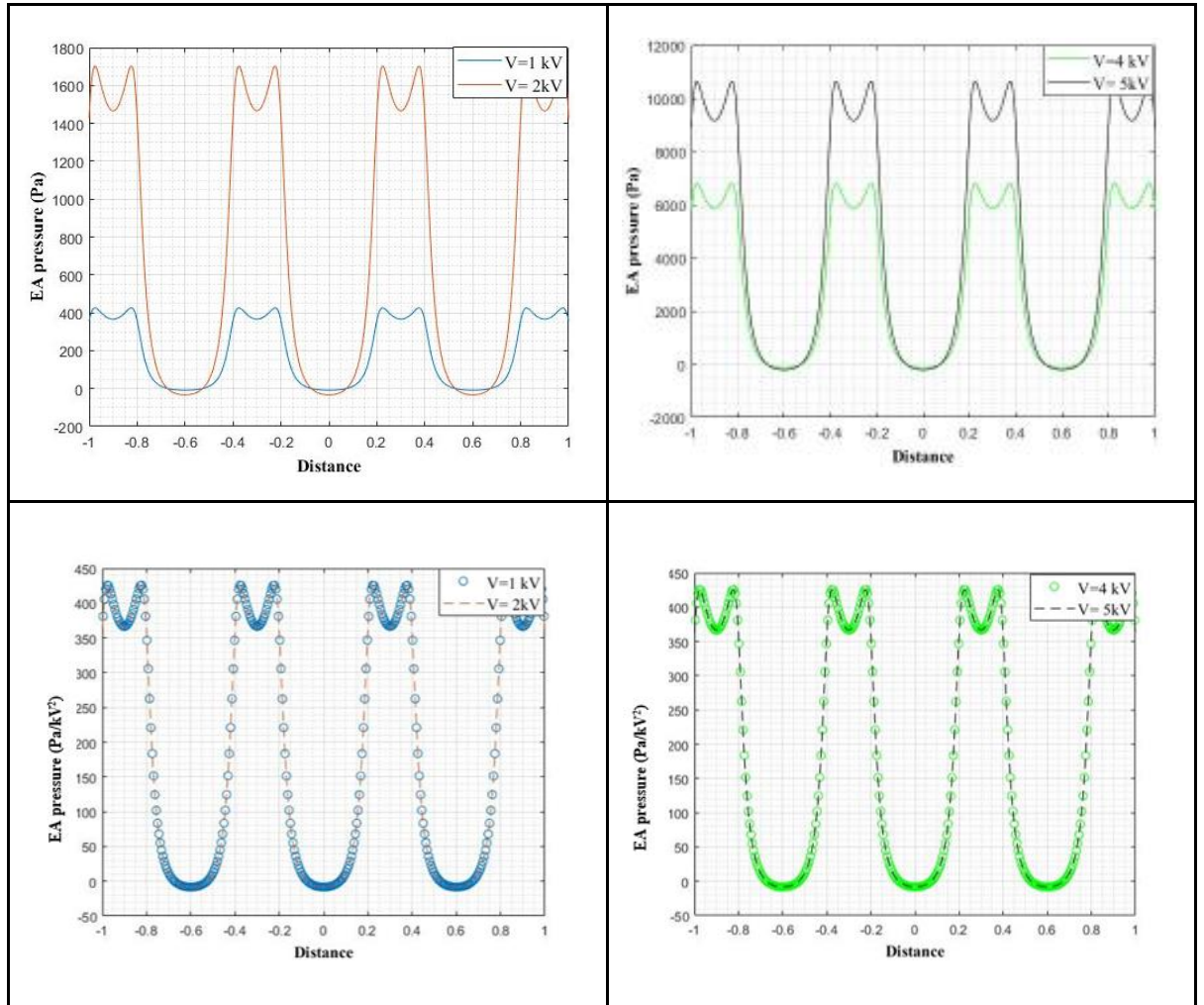


Figure 7-8. 2D modelled EA pressure distribution of interdigitated pattern with electrode width of 0.4 mm and spacing of 0.2 mm

### 7.7.2 The relationship between EA force and relative permittivity of the dielectric layer

The numerical analysis shows that obtainable EA force can be increased by increasing the relative permittivity of the dielectric layer (see figure 7-9). The result for wider range of relative permittivity is provided in section 8.2.2.

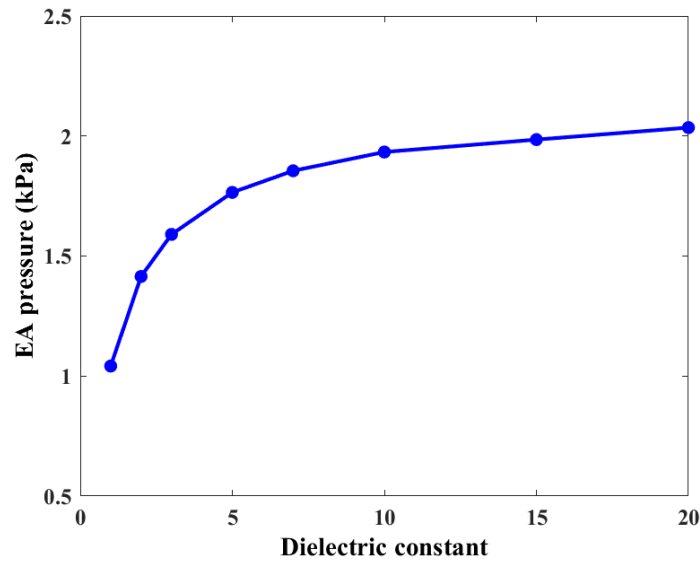


Figure 7-9. The relationship between EA force and relative permittivity of dielectric layer

### 7.7.3 Parametric simulation to find optimal value of electrodes width and spacing

2D interdigitated EA devices were simulations using the parametric electrode width and spacing values. The parametric geometry of interest was designed (see Figure 7-10), and in order to investigate the effects of electrode widths and spacings on the Maxwell stress tensor distribution and obtainable EA force, other parameters were kept constant, and only the electrode widths and space between electrodes allowed to vary and to minimise the marginal effect of 2D simulation, only 3.6 mm in the middle of the EA device was considered as effective area (see figure 7-10). Table 6-3 shows details of the parameters used for the 2D simulations. Figure 7-10 shows the Maxwell stress distribution on the line slightly above the interface of the air and substrate layers. According to the Maxwell stress equation Eq. (2-22), the maximum Maxwell stress is expected to occur where the cross-product of electric field and electric field gradient reaches its maximum. Results show (see Figure 7-11) that by increasing the width of electrodes, the intensity of the Maxwell distribution decreases, but the peaks become wider and also, as the effective area was kept constant, the number of peaks decreased. Therefore, there is an optimum electrode width needed to maximise the total attractive force generated for a specified effective area of an EA pad (see Figure 7-12). As can be seen from figure 7-12, the smaller the spacing between electrodes, the higher the EA forces generated, although in reality, this will be limited by practical considerations such as the fabrication process. Figure 7-13 illustrates for each particular spacing between electrodes; there is an optimum electrode width. It must thus be noted that these values depend on the effective area, the dielectric thickness, the thickness of the air gap and the relative permittivity of the substrate, which we considered constant here. Also, on a practical basis, electrode spacing will have a minimum safe value to avoid arcing during use, and the minimum safe spacing will thus depend on the applied voltage, amongst other factors. Therefore, the dielectric breakdown voltages of constituent materials also need to be considered when designing

and building an EA pad. Dadkhah et al. (2018) suggested a bi-layer electrode design to avoid dielectric breakdown for smaller electrode spacings.

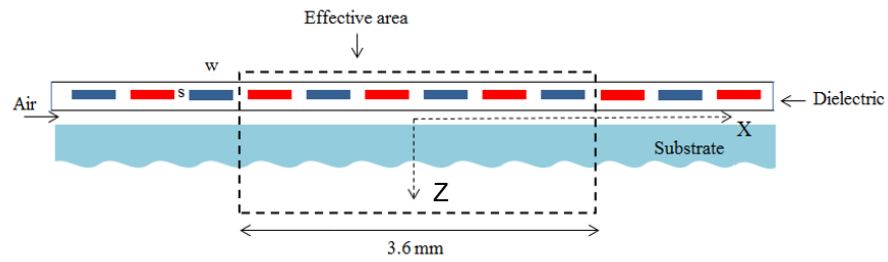


Figure 7-10. Schematic of simulated 2D interdigitated EA devices and its effective area

Table 7-3. Parameters used for 2D interdigitated electroadhesive pad simulation

Voltage	Dual polarity	$\pm 1$ kV
Electrodes	Copper (perfect conductor)	Electrical Resistivity ( $\rho$ ohm $\times$ m)=0
Electrodes width	Varied	0.2 mm to 2 mm
Electrodes thickness	0.5 mm	
Space between electrodes	Varied	1 mm to 4 mm
Dielectric	$\epsilon_r=1000$	
Dielectric thickness	1 mm	
Layer between dielectric and substrate	Air	$\epsilon_r=1$
Thickness of air layer	0.5 mm	
Substrate	Glass	$\epsilon_r=4.6$
Substrate thickness	30 mm	
Effective pad surface area	36.2 mm $\times$ 1 (dimensionless constant)	

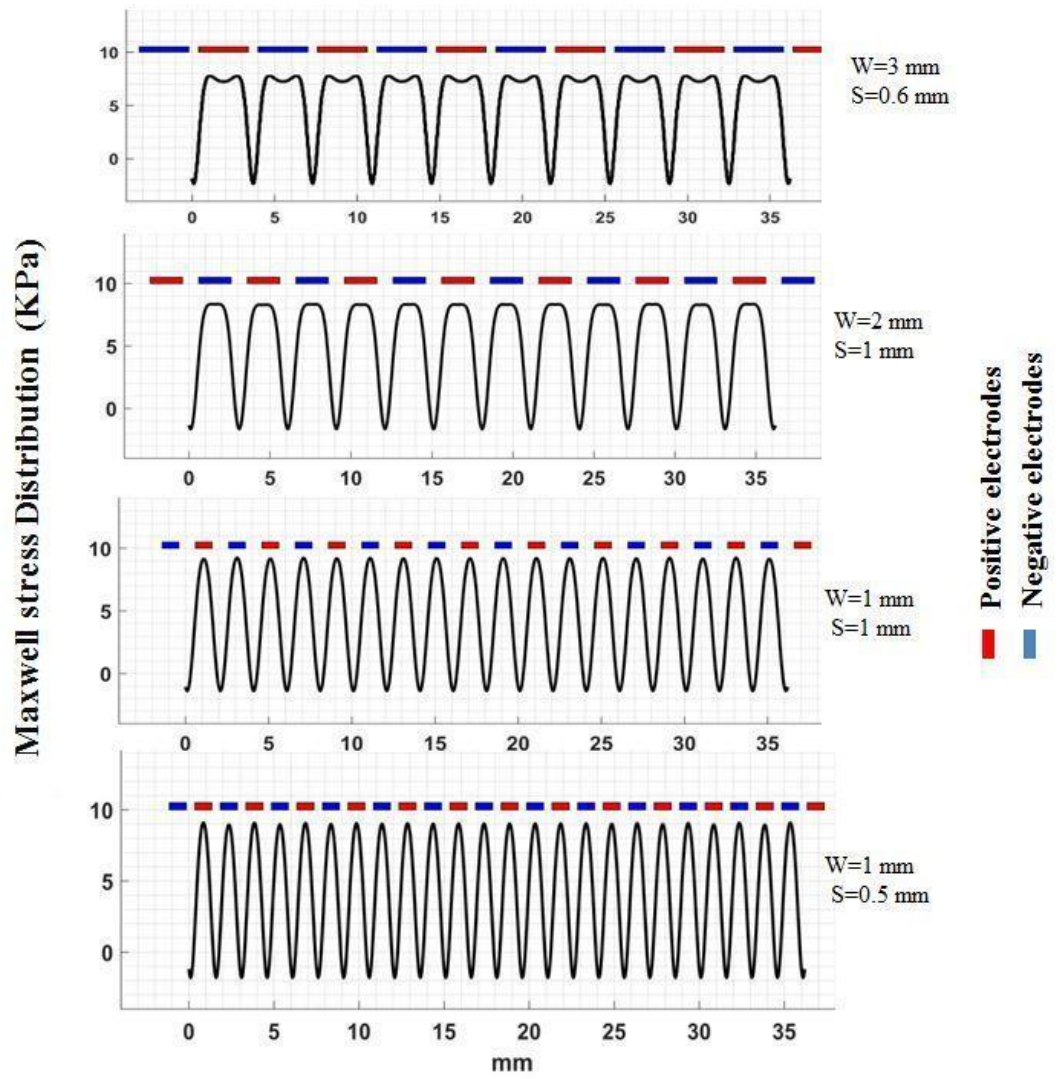


Figure 7-11. 2D Numerical investigation of the relationship between electrode parameters (width and spacing) and Maxwell stress distribution on nonconductive substrates

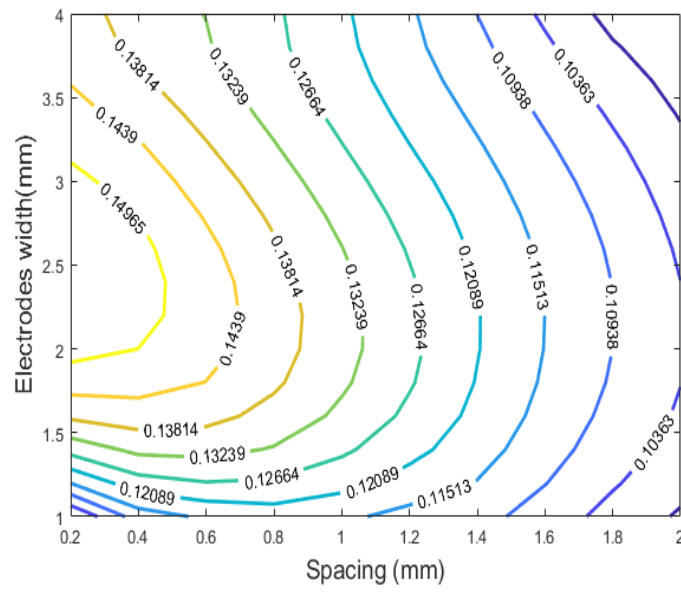


Figure 7-12. 2D Numerical investigation of the relationship between optimum electrode width and spacing to maximize obtainable EA force (N) on non-conductive substrates

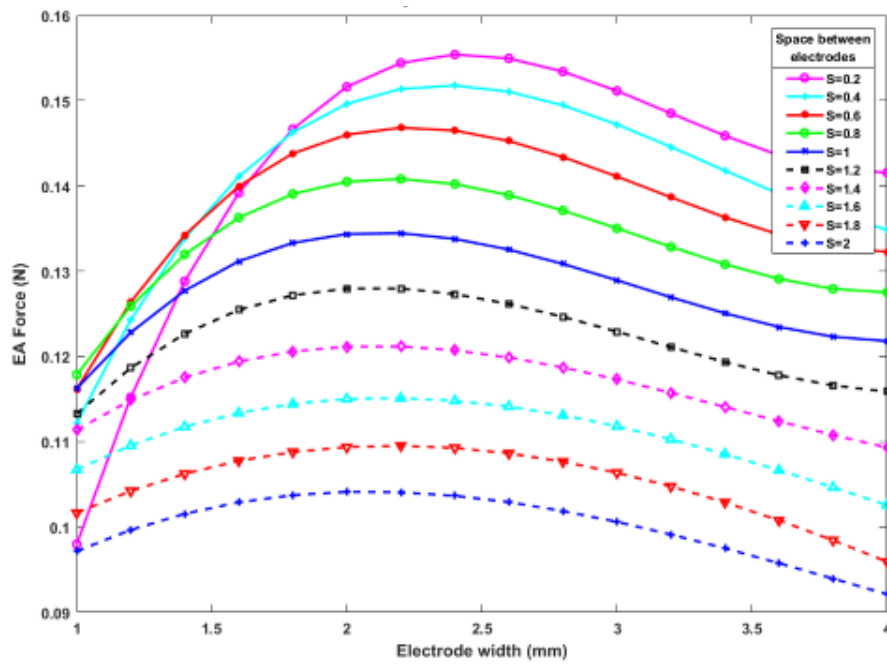


Figure 7-13. 2D Numerical investigation of EA force generated at various electrodes width and spacing on non-conductive substrates

#### 7.7.4 Optimizing EA device design with respect to dielectric layer thickness

##### 7.7.4.1 Integrating ANSYS MAXWELL and MATLAB to perform optimization for EA devices

Maximising the EA force is a nonlinear multidimensional, and constrained optimisation problem. The optimisation simulation can be performed using ANSYS MAXWELL alone. Optimisation algorithms available in ANSYS MAXWELL are Sequential nonlinear programming (gradient), Sequential mixed integer nonlinear programming (gradient discrete), Quasi newton gradient, Pattern search (search-based) and Genetic algorithm (random search). Optimisation also can be performed by Integrating ANSYS MAXWELL and MATLAB. In this study, MATLAB has been used as the optimiser, and the suggested MATLAB function for the nonlinear constraint problem is FMINCON (see appendix B).

##### 7.7.4.2 2D Optimisation simulation using ANSYS and MATLAB

In the previous section, simulations show that to maximise EA force, it needs to decrease the spacing between electrodes as much as possible while the other parameters that influence EA force were kept constant. In this section, it was tried to find the optimal electrodes' width for a range of thickness of the dielectric layer. Other parameters used for these simulations are shown in table 7-4. Results show (see figure 7-14) that the greater the dielectric layer thickness, the greater the electrodes' width needed to maximise obtainable EA force.

Table 7-4. Parameters used for 2D optimization simulations of interdigitated EA device

Voltage	Dual polarity	$\pm 2.5$ kV
Electrodes	Copper (perfect conductor)	Electrical Resistivity ( $\rho$ ohm $\times$ m)=0
Electrodes width	Varied	0.2 mm to 3 mm
Electrodes thickness	15 $\mu$ m	
Space between electrodes	0.2 mm	
Dielectric	$\epsilon_r=3.7$	
Dielectric thickness	Varied	30 $\mu$ m to 200 $\mu$ m
Layer between dielectric and substrate	Air	$\epsilon_r=1$
Thickness of air layer	10 $\mu$ m	
Substrate	Glass	$\epsilon_r=4.6$
Substrate thickness	1 mm	
Effective pad surface area	36.2 mm $\times$ 1 (dimensionless constant)	

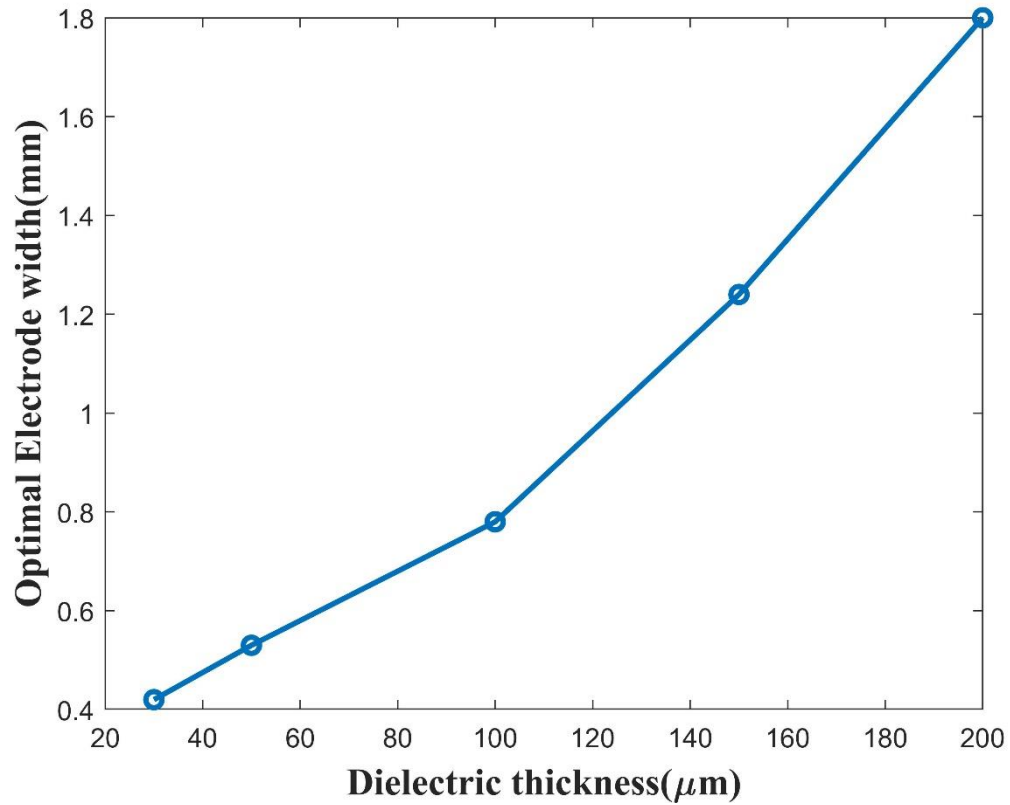


Figure 7-14. Optimal electrodes width versus dielectric thickness obtained by 2D numerical simulations of interdigitated EA device

## 7.8 Shape optimization

Shape optimisation of EA pads has been carried out by designing seven different shapes while other parameters, including effective area, electrode width, spacing between electrodes, and relative permittivities of both the dielectric layer and the substrate, were kept constant (see table 7-5). First, two representative EA pads, (i) interdigitated and (ii) concentric circles were simulated to understand the relationship between electrode geometries and the generated EA forces. Simulation of the interdigitated electrode showed that the maximum EA pressure occurs at the corners of electrodes due to the maximisation of electric field and electric field gradient in those areas. Therefore, it was attempted to increase the EA force by increasing the number of electrode corners at the next step. The results show that although the number of maximum local pressures increases, the total EA force for the whole interdigitated EA pad decreases. This means that electrode corners increase local pressures but negatively affect the area nearby, and the net effect on the whole EA pad is deleterious. Simulation of electrodes in concentric circles reveals that the curved shape of the electrodes results in homogeneous pressure distribution and increased electric field gradient, resulting in higher EA force generation compared with simple interdigitated EA pads, which is in agreement with previous findings (Ruffatto III et al., 2014). The next step was to decrease the sharpness of corners and use a half-hexagonal electrode shape. This was simulated, and the results show an

improvement in the obtainable EA force. Finally, a sinusoidal electrode shape was designed and simulated to combine both features. This provided the best performance among all designs studied here. Table 7-6 compares the obtainable attractive force and total capacity for different electrode structures, and Table 6-7 shows the effect of electrode shape on the electric field, electric field gradient and the Maxwell stress generated. It is noteworthy that 3D simulations of electroadhesion and particularly contour of the electric field indicate those parts of EA pads in which dielectric breakdown occurs first. As an example, in an interdigitated EA pad, dielectric breakdown occurs at the right angles of electrodes. Capacitances of the new electrode designs are also calculated, and results show that capacitance associated with sinusoidal and half-hexagonal shapes are higher than with other electrode geometries. A grid independence study for all of the simulations was carried out by applying 50% mesh refinement for each iteration to ensure that EA forces computed are independent of the number of elements. Table 6-8 shows statistical information on the last iteration of the 3D simulated interdigitated pad. Figure 6-15 shows convergence criteria (energy error and delta energy), force computed, and the number of elements for iterations.

Table 7-5. Parameters used for 3D interdigitated electroadhesive pad simulation

Voltage	Dual polarity	$\pm 1$ kV
Electrodes width	1 mm	
Electrodes thickness	0.5 mm	
Space between electrodes	1 mm	
Dielectric	$\epsilon_r=1000$	
Dielectric thickness	1 mm	
Layer between dielectric and substrate	Air	$\epsilon_r=1$
Thickness of air layer	0.5 mm	
Substrate	Glass	$\epsilon_r=4.6$
Substrate thickness	30 mm	
Effective pad surface area	357 cm <sup>2</sup>	



Table 7-6. The effect of electrodes design on obtainable attractive forces

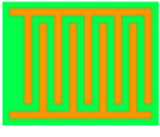
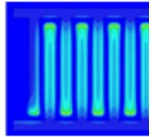
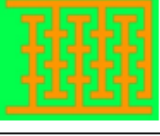
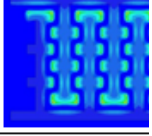

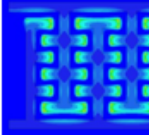
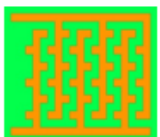
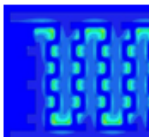

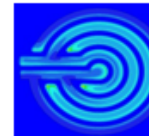

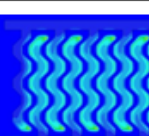
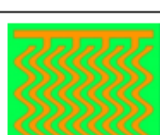
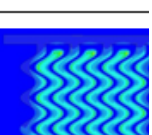
Pattern name	Shape of electrodes	Total area of electrodes( $\text{cm}^2$ )	Total EA force (mN)	Total Capacitance (pF)	Maxwell stress
Interdigitated		146	14.483	962.69	
Interdigitated with teeth (1)		143	10.189	755.13	
Interdigitated with teeth (2)		146	11.381	835.57	
Interdigitated with teeth (3)		143	9.5595	712.43	
Concentric circles		142.17	15.031	1009	
Half-hexagonal		146	17.847	1279.7	
Sinusoidal shape		134	21.222	1700.8	

Table 7-7. The effect of electrode shapes on generated electric field and Maxwell stress distribution


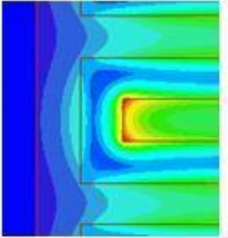
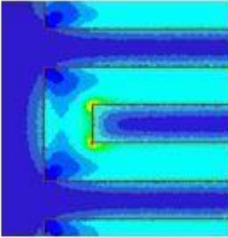
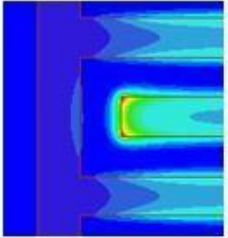
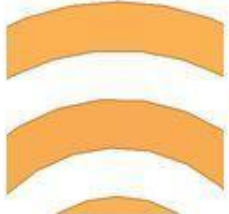
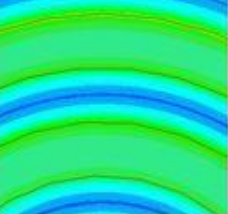
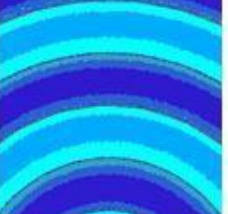
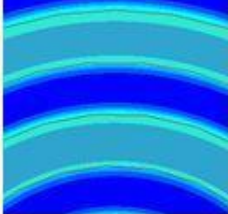
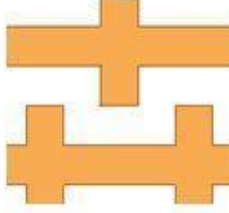
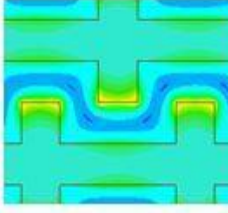
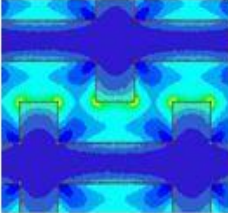
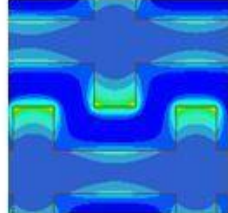

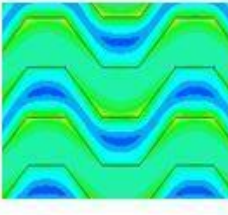
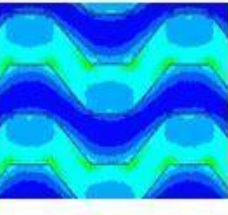
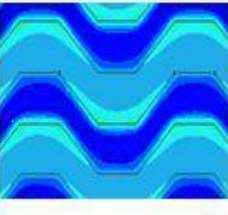
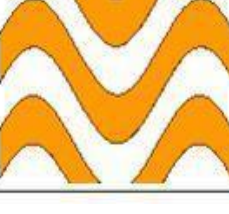
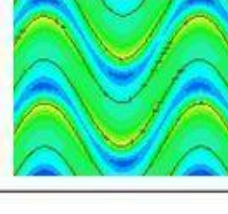
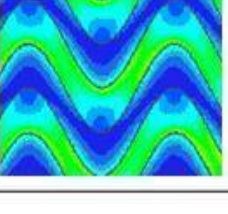
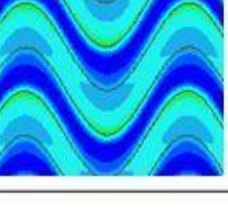
Electrodes shape	Magnitude of E- field	Gradient of E-field in Z direction	Maxwell stress
			
			
			
			
			

Table 7-8.Statistical information of the grids generated for the last iteration of 3D modelled of the interdigitated pad

3D Mesh Statistics				
Geometry Name	Number of elements	Min edge length (mm)	Max edge length (mm)	Mean elements volume(mm <sup>3</sup> )
Positive electrodes	1167164	0.00366118	0.174809	3.38E-06
Negative electrodes	1149252	0.00309745	0.161847	2.91E-06
Dielectric layer	14186716	0.00242048	0.148935	2.00E-06
Air	6409107	0.00682014	0.14254	2.79E-06
Substrate	3469347	0.0149766	0.677267	1.03E-04
Total number	26381586			

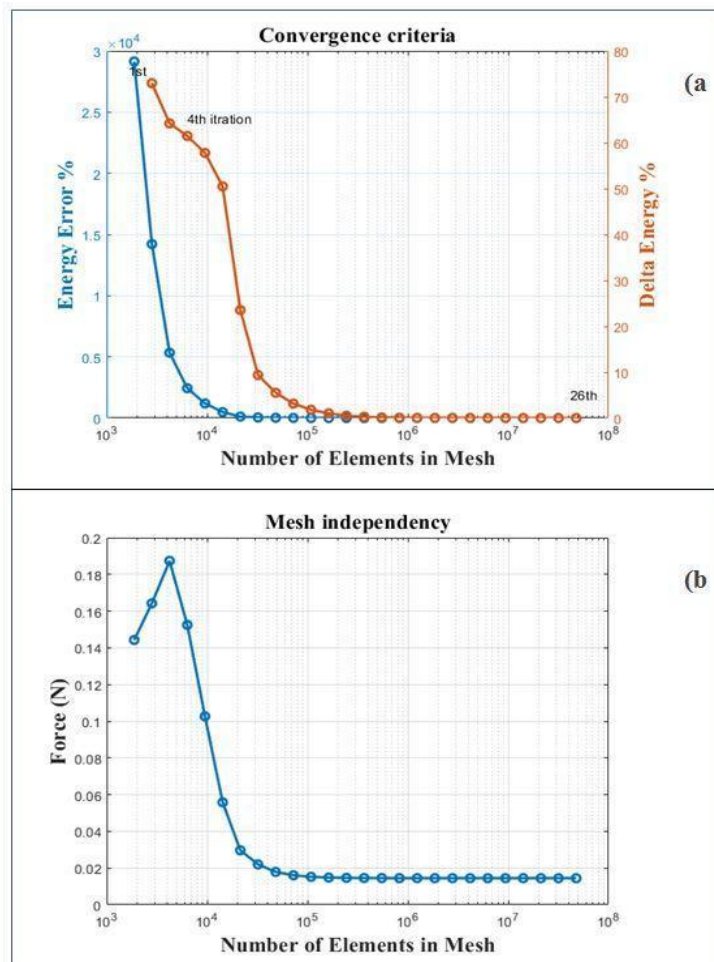


Figure 7-15. Energy error and delta energy b) mesh independency of interdigitated EA pad simulation

## 7.9 Comparison of obtainable EA force of bi-layer and uni layer EA devices

### 7.9.1 Bi-Layer EA devices simulation

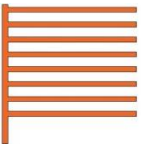

Bi-layer EA devices have several advantages over uni-layer devices, including the flexibility of designing more complex Devices; the spacing between electrodes can be greater as there are only electrodes with the same polarity in one of the electrodes' layers. Dadkhah, et al.(2018) showed by using bi-layers devices; obtainable EA force can be increased; therefore, in this section, some possible designs were simulated, and results were compared with uni layer with same properties (electrical properties of dielectric layer and substrate showed in table 7-9 ) to find the optimal bi-layer EA device design.

Table 7-9. Parameters used for 3D bi-layer EA devices simulation

Voltage	Dual polarity	$\pm 2.5$ kV
Electrodes thickness	15 $\mu$ m	
Dielectric	$\epsilon_r=3.7$	
Dielectric layers thickness	40 $\mu$ m	
Layer between dielectric and substrate	Air	$\epsilon_r=1$
Thickness of air layer	10 $\mu$ m	
Substrate	Glass	$\epsilon_r=4.6$
Substrate thickness	1 mm	

**Device 1:** Solid top and interdigitated bottom with 0.2mm electrodes width and 0.4mm spacing

Table 7-10. Device 1 characteristics

Bottom layer	Top layer	Effective area(mm <sup>2</sup> )	Total Electrodes area	Normal pressure (kPa)
		37.12	Top=28mm <sup>2</sup> Bottom=8.8mm <sup>2</sup>	7.61

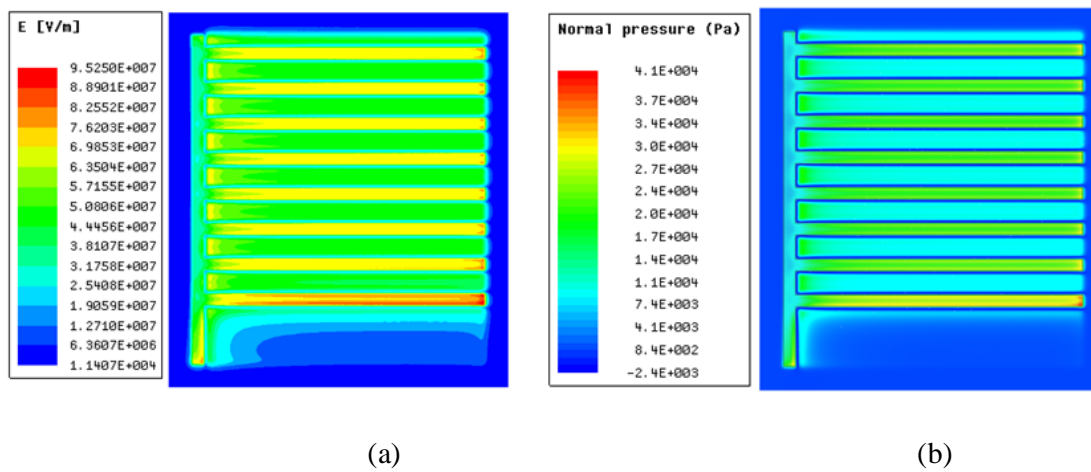
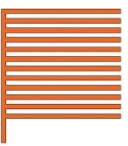



Figure 7-16. Contour of a) electric field, b) pressure obtained by Solid top and interdigitated bottom EA device (1)

**Device 2:** Solid top and interdigitated bottom with 0.2mm electrode width and 0.2mm spacing

Table 7-11. Device 2 characteristics

Bottom layer	Top layer	Effective area(mm <sup>2</sup> )	Total Electrodes area	Normal pressure (kPa)
		37.12	Top=28 mm <sup>2</sup> Bottom=12.64 mm <sup>2</sup>	6.31

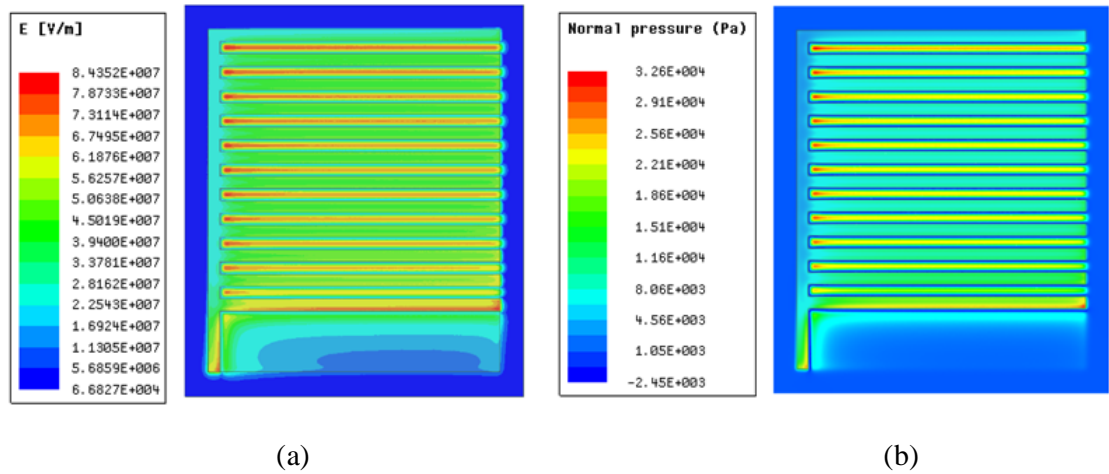
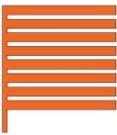



Figure 7-17. Contour of a) electric field, b) Pressure obtained by Solid top and interdigitated bottom EA device (2)

**Device 3.** Solid top and interdigitated bottom with 0.4mm electrodes width and 0.2mm spacing

Table 7-12. Device 3 characteristics

Bottom layer	Top layer	Effective area(mm <sup>2</sup> )	Total Electrodes area	Normal pressure (kPa)
		37.12	Bottom=16.48 mm <sup>2</sup> Top=28 mm <sup>2</sup>	4.31

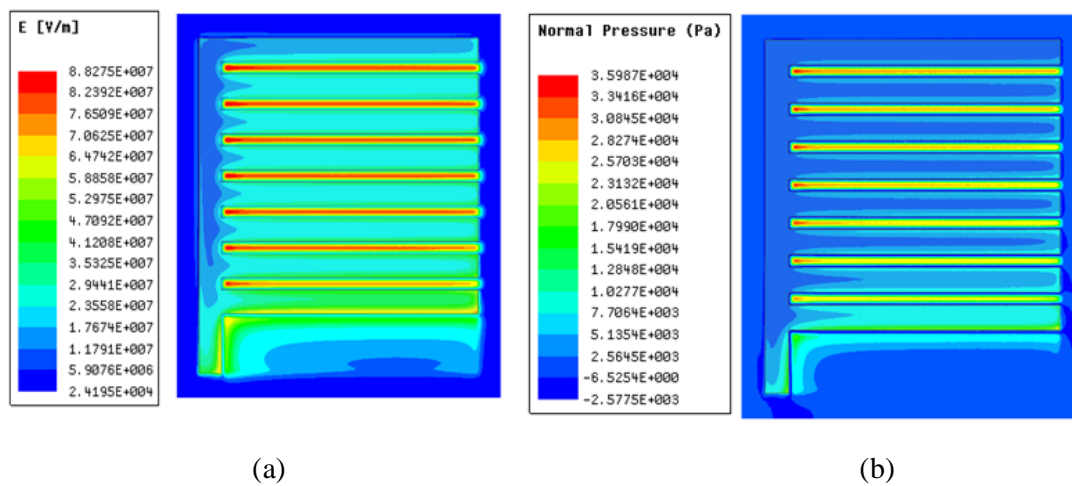




Figure 7-18. Contour of a) electric field, b) Pressure obtained by solid top and interdigitated bottom EA device (3)



**Device 4:** Solid top and concentric circles with 0.4mm electrode width and 0.2mm spacing

Table 7-13. Device 4 characteristics

Bottom layer	Top layer	Effective area(mm <sup>2</sup> )	Total Electrodes area (mm <sup>2</sup> )	Normal pressure (kPa)
		32.17	Top=24.63 Bottom=8.54	8.88

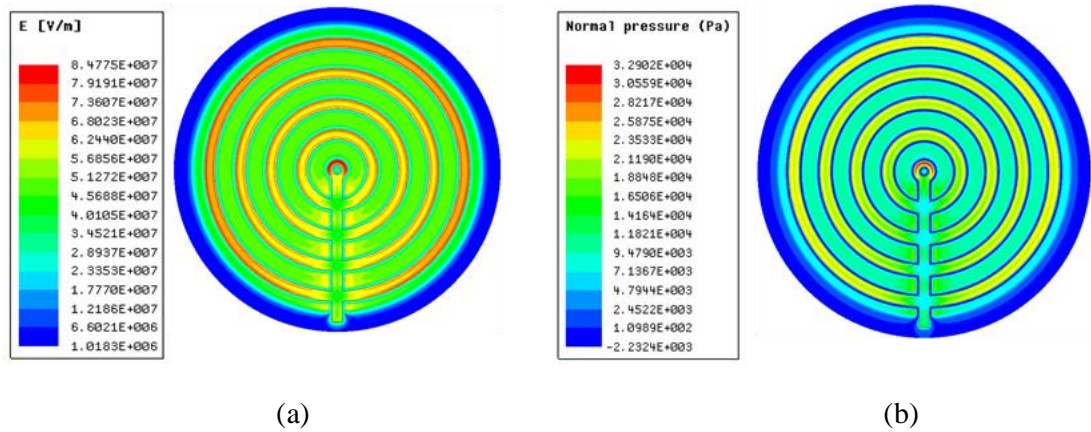
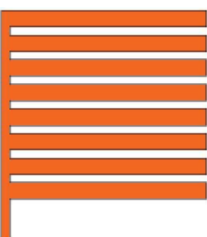
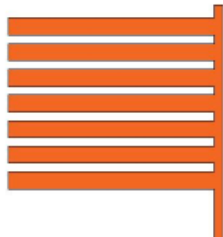


Figure 7-19. Contour of a) electric field, b) pressure obtained by solid top and concentric circles EA device

**Device 5.** Two partially overlapped interdigitated (0.4mm electrodes width and 0.2mm spacing)

Table 7-14. Device 5 characteristics

Bottom layer	Top layer	Effective area(mm <sup>2</sup> )	Total Electrodes area (mm <sup>2</sup> )	Normal pressure (kPa)
		32.17	Top=14.56 Bottom=16.48	4.38

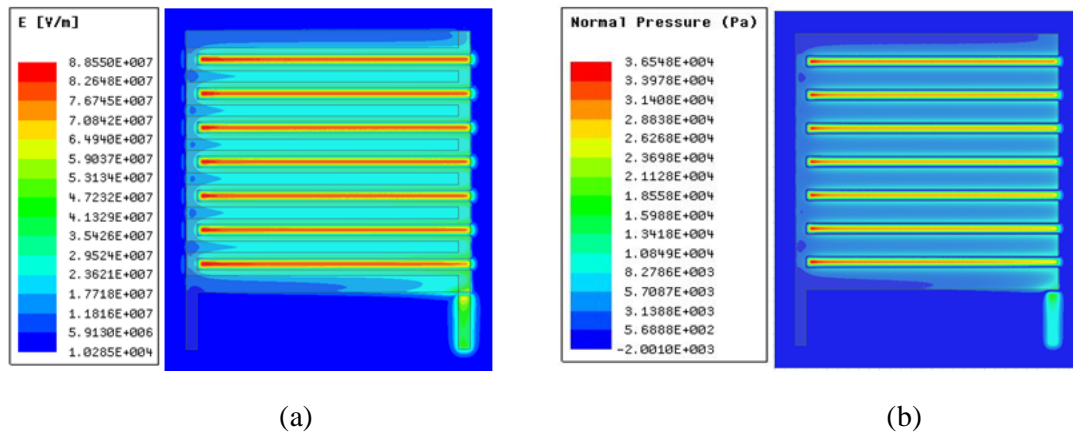


Figure 7-20. Contour of a) electric field, b) pressure obtained by two partially overlapped interdigitated EA device

**Device 6.** Two interdigitated with offset (0.4mm electrode width and 0.2mm spacing for top layer and 0.2mm electrode width and 0.4mm spacing for bottom layer)

Table 7-15. Device 6 characteristics

Bottom layer	Top layer	Effective area(mm <sup>2</sup> )	Total Electrodes area (mm <sup>2</sup> )	Normal pressure (kPa)
		32.17	<p>Top=16.48</p> <p>Bottom=8.8</p>	6.06



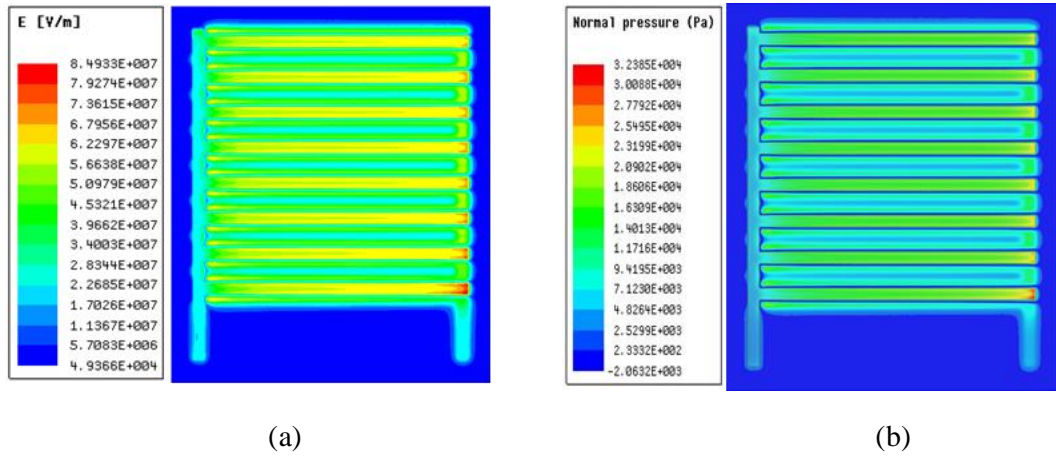


Figure 7-21. Contour of a) electric field, b) pressure obtained by two interdigitated electrodes with offset EA device

**Device 7.** Two orthogonal interdigitated (0.2mm electrode width and 0.2mm spacing)

Table 7-16. Device 7 characteristics

Bottom layer	Top layer	Effective area(mm <sup>2</sup> )	Total Electrodes area (mm <sup>2</sup> )	Normal pressure (kPa)
		32.17	Top=12.56 Bottom=12.64	4.37

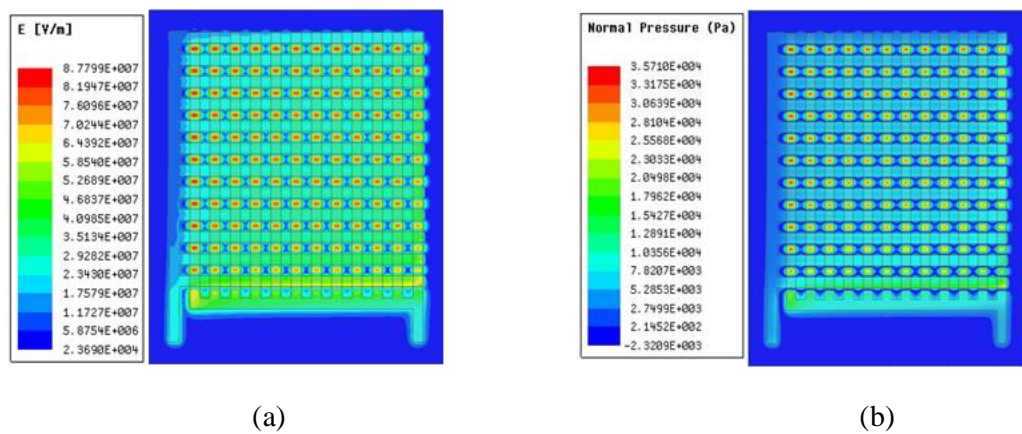


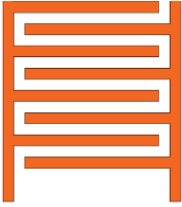
Figure 7-22. Contour of a) electric field, b) pressure obtained by two orthogonal interdigitated EA devices

### 7.9.2 Uni-Layer EA device simulation

In order to compare the results obtained for bi-layer devices, a uni-layer device with the same effective area was designed and simulated.

**Uni Layer Device:** Interdigitated with electrodes width of 0.4mm and spacing of 0.2mm

Table 7-17. Uni-layer device characteristics

Uni-layer interdigitated	Effective area(mm <sup>2</sup> )	Total Electrodes area	Normal pressure (kPa)
	37.12	2×8.64 mm <sup>2</sup>	1.13

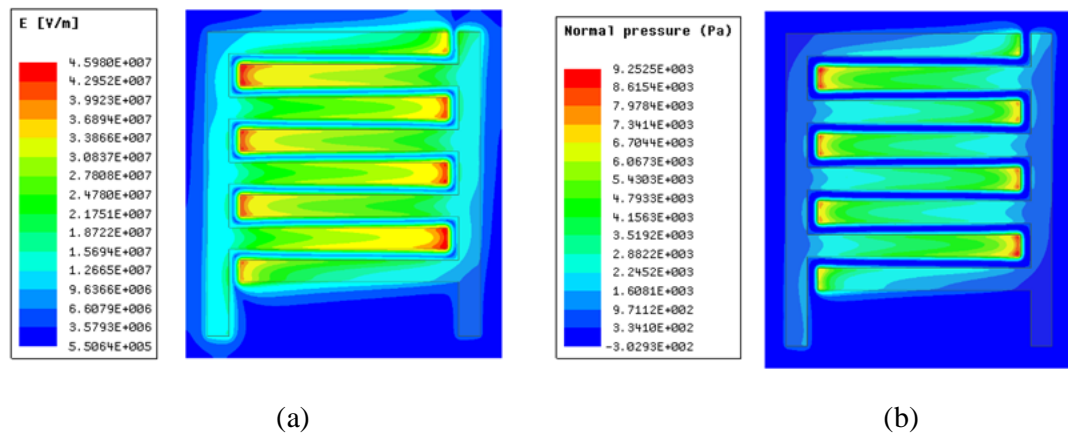


Figure 7-23. Contour of a) electric field, b) Pressure obtained by uni-layer interdigitated EA device

### 7.9.3 Comparison of obtainable EA force of bi-layer and uni-layer EA devices

Numerical simulations show that all bi-layer designs can produce greater force compared to the uni-layer EA device with the same effective area. Having a top solid layer of electrodes results in greater EA force than two interdigitated electrodes. Between top solid and bottom interdigitated electrodes, device (1) with 0.2mm electrodes width and 0.4mm, spacing generates a more significant force which is in agreement with Dadkhah et al. (2018) findings.

## Chapter 8

### Results and conclusions

In this chapter, first, the analytical approach and its limitation to calculate the EA force are explained, and then the results of the experimental tests performed are presented.

#### 8.1 Analytical Solution of an interdigitated EA device

Considering polarisation tensor as a scalar value and simplifying electroadhesion problem to a 2D problem, potential distribution in electroadhesion is governed by Poisson's equation. Assuming no free charge density and also neglecting marginal effect, electroadhesion problem has periodic boundary conditions in terms of the potential of electrodes (see figure 8-1), whereas the periodicity of Maxwell stress is half of the periodicity of potential, and it is due to the fact that Maxwell stress only depends on the magnitude of potential. Fourier transform of periodic part of Maxwell stress (see figure 8-2 and 8-3) of the same EA device obtained by numerical analysis also proves this phenomenon and shows that the fundamental frequency is  $\frac{2\pi}{w+s}$  where W is the width of electrodes and S is spacing between them.

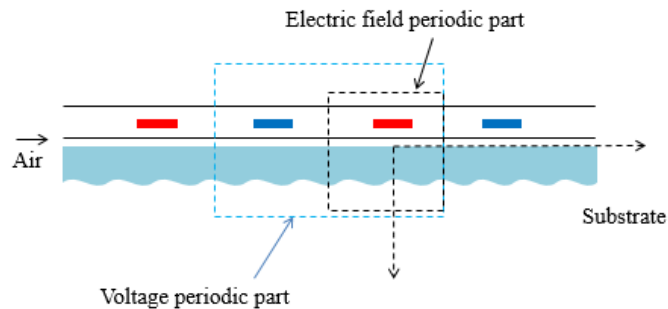


Figure 8-1. periodic part of voltage and electric field of 2D interdigitated EA device

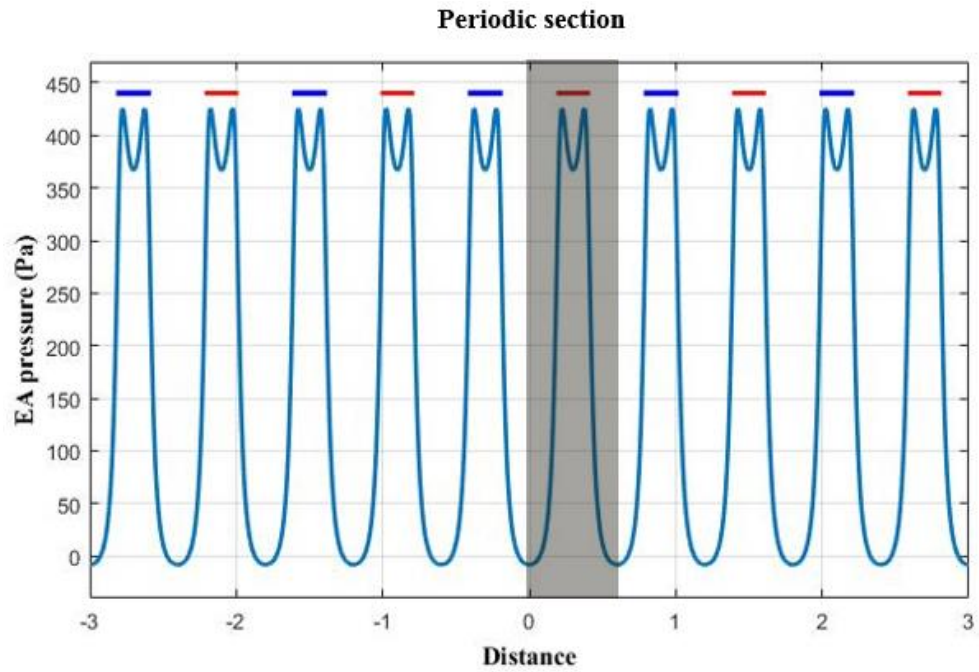


Figure 8-2. 2D Maxwell stress distribution of an EA device with electrode's with of 0.2mm and spacing of 0.4mm obtained by numerical simulation

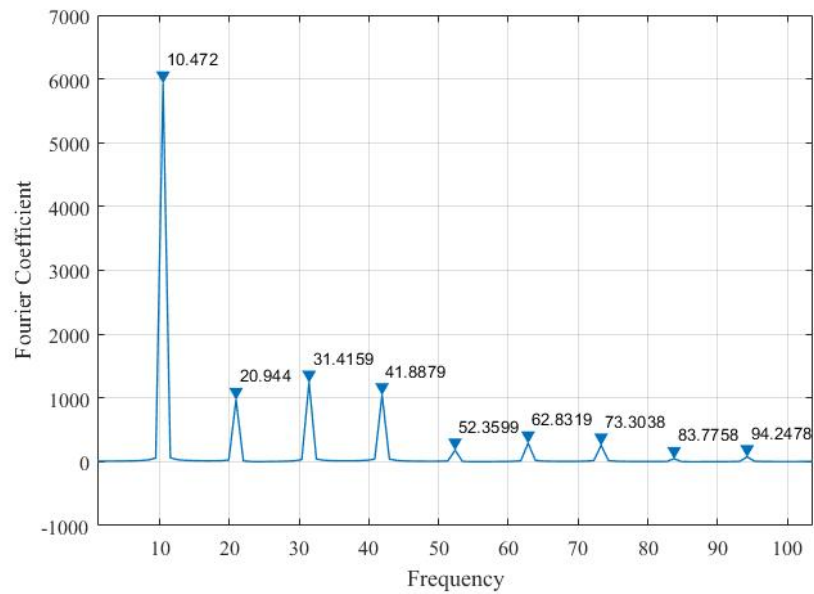


Figure 8-3. Fourier transform of periodic part of Maxwell stress of the same EA device

### 8.1.1 Boundary conditions of the EA problem

EA problem is a partial differential problem, and boundary conditions should be specified to solve this type of problem analytically. Below are the boundary conditions of this EA problem.

### 8.1.1.1 Boundary conditions at $y=0$

The boundary condition of an EA device at  $z=0$  is Dirichlet boundary condition and should be considered based on the periodicity of voltage (see figure 8-4).

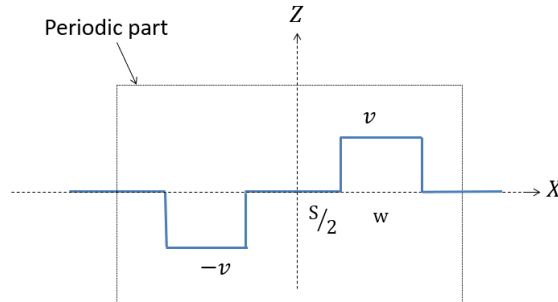


Figure 8-4. Dirichlet boundary condition at  $z=0$  of a interdigitated EA device

### 8.1.1.2 Boundary condition at $x=\pm(W+S)/2$

The boundary conditions of an EA device at  $x=\pm(W+S)/2$  are Neumann boundary condition and are illustrated in figure 8-5.

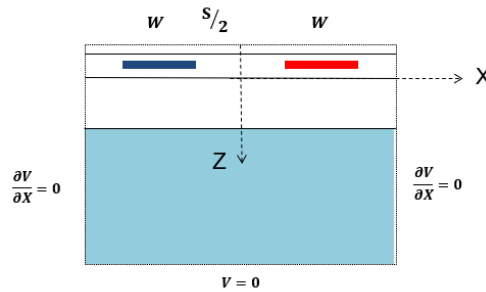
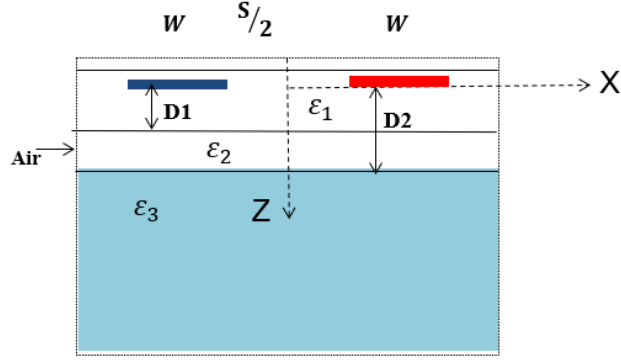


Figure 8-5. Neumann boundary conditions at  $x=\pm(W+S)/2$  of a interdigitated EA device

### 8.1.1.3 Boundary conditions at $Z=D_1$ and $Z=D_2$ (interface between materials, dielectric layer, Air and substrate)

There are different relationships between the x and y direction of the electric field at the interfaces between layers of materials involved in EA problems(see figure 8-6), expressed mathematically by Eq.(8-1) and (8-2).



$$z = D_1 \quad \left\{ \begin{array}{l} (1) E_{x,1} = E_{x,2} \\ (2) \varepsilon_1 E_{z,1} = \varepsilon_2 E_{z,2} \end{array} \right. \quad (8-1)$$

$$z = D_2 \quad \left\{ \begin{array}{l} (3) E_{x,2} = E_{x,3} \\ (4) \varepsilon_2 E_{z,2} = \varepsilon_3 E_{z,3} \end{array} \right. \quad (8-2)$$

And if  $\varepsilon_1 \neq \varepsilon_2 \neq \varepsilon_3$  which is in most scenarios it is the case, then the first and third boundary conditions impose discontinuity in electric field distribution, and EA force cannot be calculated analytically.

### 8.1.2 Analytical Solution for constant relative permittivity of system

For a system with constant relative permittivity, Laplace's equation can be solved using the separation of variation method:

$$U = X(x)Z(y) \quad (8-3)$$

whereas:

$$X(x) = \sum_{n=1}^{\infty} a_n \sin n\omega x \quad (8-4)$$

$$a_n = \frac{2v}{n\pi} \left( \sin \left( \frac{n\omega w}{2} \right) \right) \quad (8-5)$$

$$Z(yz) = e^{-n\omega y} \quad (8-6)$$

$$\omega = \frac{2\pi}{(w+s)} \quad (8-7)$$

Therefore, potential distribution is given by:

$$U = a_0 e^{-n\omega z} + \sum_{n=1}^{\infty} a_n e^{-n\omega z} \cos n\omega x \quad (8-8)$$

And electric field in x and y direction are given by following equations

$$E_x = \frac{\partial U}{\partial x} = \left( \sum_{n=1}^{\infty} -n\omega a_n e^{-n\omega z} \sin n\omega x \right) \quad (8-9)$$

$$E_z = \frac{\partial U}{\partial z} = \sum_{n=1}^{\infty} -n\omega a_n e^{-n\omega z} \cos n\omega x \quad (8-10)$$

and EA force is given by:

$$\iint_A \vec{F} dA = \oint_L \vec{T} \cdot \vec{n} ds \quad (8-11)$$

Whereas T is Maxwell stress and is given by

$$\vec{T} = \frac{\epsilon}{2} \begin{bmatrix} E_x^2 - E_z^2 & -2E_x E_z \\ -2E_x E_z & E_z^2 - E_x^2 \end{bmatrix} \quad (8-12)$$

And Maxwell stress in x and y directions is calculated by the dot product of Maxwell stress and unit vector in a 2D Cartesian coordinate system.

$$\vec{T} \cdot \vec{n} = \frac{\epsilon}{2} \begin{bmatrix} E_x^2 - E_z^2 & -2E_x E_z \\ -2E_x E_z & E_z^2 - E_x^2 \end{bmatrix} \begin{bmatrix} i \\ k \end{bmatrix} \quad (8-13)$$

or

$$\vec{T} \cdot \vec{n} = \frac{\epsilon}{2} (E_x^2 - E_z^2 - 2E_x E_z) i + \frac{\epsilon}{2} (E_z^2 - E_x^2 - 2E_x E_z) k \quad (8-14)$$

Whereas i, k are unit vectors in x and z direction respectively and therefore EA force is given by

$$F_z = \int \left( \frac{\varepsilon_3}{2} (E_z^2 - E_x^2 - 2E_y E_x) \right) dx \quad (8-15)$$

therefore, for the periodic part of EA device generated force is given by:

$$\begin{aligned} F_{periodic} &= \varepsilon \int_{-\frac{1}{2}(w+s)}^{\frac{1}{2}(w+s)} \left( \left( \sum_{n=1}^{\infty} -n\omega a_n e^{-n\omega z} \cos n\omega x \right) \left( \sum_{m=1}^{\infty} -m\omega a_m e^{-m\omega z} \cos m\omega x \right) \right. \\ &\quad - \left( \sum_{n=1}^{\infty} -n\omega a_n e^{-n\omega z} \sin n\omega x \right) \left( \sum_{m=1}^{\infty} -m\omega a_m e^{-m\omega z} \sin m\omega x \right) \\ &\quad \left. - 2 \left( \sum_{n=1}^{\infty} -n\omega a_n e^{-n\omega z} \cos n\omega x \right) \left( \sum_{m=1}^{\infty} -m\omega a_m e^{-m\omega z} \sin m\omega x \right) \right) dx \end{aligned} \quad (8-16)$$

The Eq.8-16 can be written in the following form

$$\begin{aligned} F_{periodic} &= \varepsilon \int_{-\frac{1}{2}(w+s)}^{\frac{1}{2}(w+s)} \left( \sum_{n=1}^{\infty} \sum_{m=1}^{\infty} nm\omega^2 a_n a_m e^{-n\omega z} e^{-m\omega z} \cos n\omega x \cos m\omega x \right. \\ &\quad - \sum_{n=1}^{\infty} \sum_{m=1}^{\infty} nm\omega^2 a_n a_m e^{-n\omega z} e^{-m\omega z} \sin n\omega x \sin m\omega x \\ &\quad \left. - 2 \sum_{n=1}^{\infty} \sum_{m=1}^{\infty} nm\omega^2 a_n a_m e^{-n\omega z} e^{-m\omega z} \cos n\omega x \sin m\omega x \right) dx \end{aligned} \quad (8-17)$$

And because of orthogonality of sine and cosine for  $m \neq n$

$$\begin{aligned} \int_{-\frac{1}{2}(w+s)}^{\frac{1}{2}(w+s)} (nm\omega^2 a_n a_m e^{-n\omega z} e^{-m\omega z} \sin n\omega x \sin m\omega x) dx &= 0 \\ \int_{-\frac{1}{2}(w+s)}^{\frac{1}{2}(w+s)} (nm\omega^2 a_n a_m e^{-n\omega z} e^{-m\omega z} \cos n\omega x \sin m\omega x) dx &= 0 \\ \int_{-\frac{1}{2}(w+s)}^{\frac{1}{2}(w+s)} (nm\omega^2 a_n a_m e^{-n\omega z} e^{-m\omega z} \cos n\omega x \cos m\omega x) dx &= 0 \end{aligned} \quad (8-18)$$

Therefore, the Eq. 8-17 reduced to the following



$$F_{periodic} = \varepsilon \int_{-\frac{1}{2}(w+s)}^{\frac{1}{2}(w+s)} \left( \left( \sum_{n=1}^{\infty} n^2 \omega^2 a_n^2 e^{-2n\omega z} \left( \left( \frac{\varepsilon_1}{\varepsilon_2} \right)^2 \cos^2 n\omega x - \sin^2 n\omega x - 2 \sin n\omega x \cos n\omega x \right) \right) \right) dx \quad (8-19)$$

and as

$$\begin{aligned} \cos^2 n\omega x &= \frac{1}{2}(1 + \cos 2n\omega x) \\ \sin^2 n\omega x &= \frac{1}{2}(1 - \cos 2n\omega x) \end{aligned} \quad (8-20)$$

Therefore, the first two integrals are equal to zero and the periodic force is given by

$$F_{periodic} = \varepsilon \int_{-\frac{1}{2}(w+s)}^{\frac{1}{2}(w+s)} \left( \sum_{n=1}^{\infty} -n^2 \omega^2 a_n^2 e^{-2n\omega z} (\sin 2n\omega x) \right) dx \quad (8-21)$$

Calculating the integral, EA force is given by the following

$$F_{periodic} = \varepsilon \sum_{n=1}^{\infty} n\omega a_n^2 e^{-2n\omega z} \quad (8-22)$$

And by substituting  $a_n$ , finally, EA force obtained by interdigitated EA device is given by

$$F = \varepsilon \frac{4v^2 A}{\pi(w+s)^2} \sum_{n=1}^{\infty} \frac{1}{n} e^{-2n\omega z} \left( \sin\left(\frac{n\omega w}{2}\right) \right)^2 \quad (8-23)$$

The summation can be replaced by  $\delta$  which is very sensitive to the distance between an EA device and a substrate as well as electrodes width and spacing between them. Figure 8-7 shows the value of  $\delta$  for a range of W and S at  $z=0$ , which is equivalent to neglecting the thickness of the dielectric layer and air between an EA device and substrate:

$$F = \varepsilon \frac{4v^2 A}{\pi(w+s)^2} \delta(W, S, z) \quad (8-24)$$

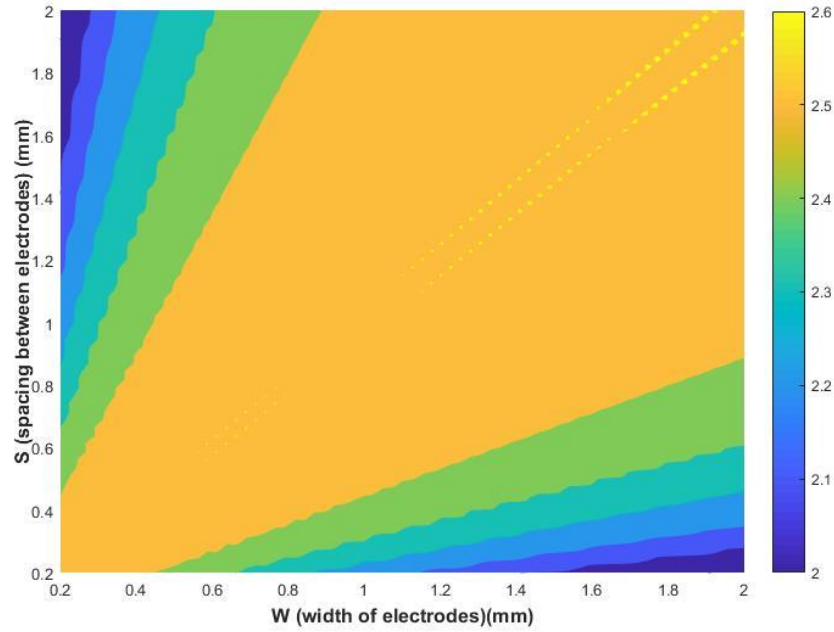


Figure 8-7. Contour of  $\delta$  at  $z=0$  for a range of  $W$  and  $S$

Neglecting the thickness of the dielectric layer and air between an EA device and substrate, the good approximation of EA force for a wide range of width and spacing is given by:

$$F = \varepsilon \frac{10 v^2 A}{\pi(W+S)^2} \quad (8-25)$$

## 8.2 Analytical solution of force obtained by EA device with concentric circles electrode pattern

Similar to interdigitated EA devices, some simplifications need to apply to have an analytical solution for concentric circles EA devices. In addition to the assumptions mentioned above, electrodes' pattern should be simplified according to the figure 8-8.

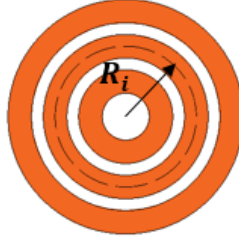


Figure 8-8. Simplified geometry of concentric EA device for analytical solution

$$F = \varepsilon \sum_{i=1}^m \frac{10R_i^2 v^2}{(W+S)^2} \sum_{n=1}^{\infty} \frac{1}{n} e^{-2n\omega z} \left( \sin\left(\frac{n\omega W}{2}\right) \right)^2 \quad (8-26)$$

And similarly the EA force with no dielectric layer and air is given by :

$$F = \sum_{i=1}^m \varepsilon \frac{25R_i^2 v^2}{(W+S)^2} \quad (8-27)$$

Where m is the number of electrodes, and  $R_i$  is the radius of circle in the middle of each electrode.

### 8.3 EA force and Total capacitance of the system

Following (Nassret al., 2008 and Mak and Hao, 2014) the total capacitance of a co-planar capacitor can be calculated using a conformal mapping (CM) technique. To prove this, the potential distribution of a 2D EA system with 16 electrodes was simulated (see figure 8-9). As can be seen, in the middle of the system, there are vertical equipotential lines with a value of zero between electrodes. Therefore, ignoring marginal effects, the total capacitance of the system can be approximated with acceptable accuracy using a conformal mapping technique. The capacitance of a periodical section (see Figure 8-10) of a dielectric layer and a substrate of an EA system are then given by:

$$C_p = \varepsilon_0 \varepsilon_r L \frac{K(k_r)}{K(k_r')} \quad (8-29)$$

where  $\varepsilon_r$  is relative permittivity of the dielectric layer or the substrate; L is length of electrodes; K is elliptic integral of the first kind; and  $k_r$  is given by:

$$k_r = \frac{\sinh\left(\frac{\pi W}{2h}\right)}{\sinh\left(\frac{\pi\left(\frac{W}{2} + S\right)}{2h}\right)} \sqrt{\frac{\sinh^2\left(\frac{\pi\left(\frac{3W}{2} + S\right)}{2h}\right) - \sinh^2\left(\frac{\pi\left(\frac{W}{2} + S\right)}{2h}\right)}{\sinh^2\left(\frac{\pi\left(\frac{3W}{2} + S\right)}{2h}\right) - \sinh^2\left(\frac{\pi W}{2h}\right)}} \quad (8-30)$$

where w is width of electrodes; s is space between electrodes; h is thickness of dielectric layer or substrate; and  $k'_r$  is given by:

$$k'_r = \sqrt{1 - k_r^2} \quad (8-30)$$

Finally, total capacitance of the system is given by:

$$C_{total} = (N - 1)C_{p_{dielectric\ layer}} + (N - 1)C_{p_{Substrate}} \quad (8-31)$$

As can be seen in figure 8-11, the smaller the spacing between electrodes and the smaller the width of the electrodes, the higher the total capacitance of the system. These results are in agreement with findings reported by Huang et al. (2017), whereas in section 7.7.3, it was shown that there is the optimal value of electrodes' width to maximise EA force. Therefore, it is concluded that there is no relationship between EA force and the total capacitance of an EA system.

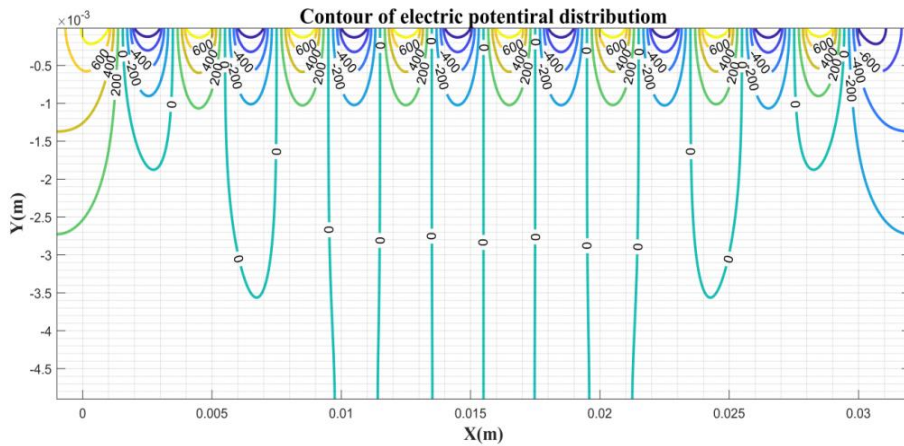


Figure 8-9. 2D Modelled potential distribution of coplanar capacitance with 16 electrodes

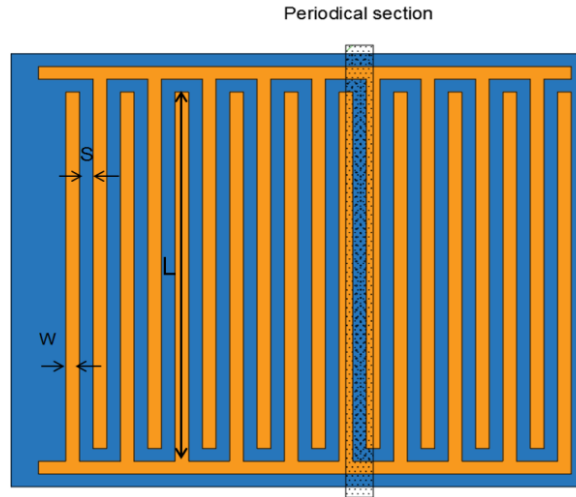


Figure 8-10. Schematic of coplanar capacitance showing simulated area and parameters

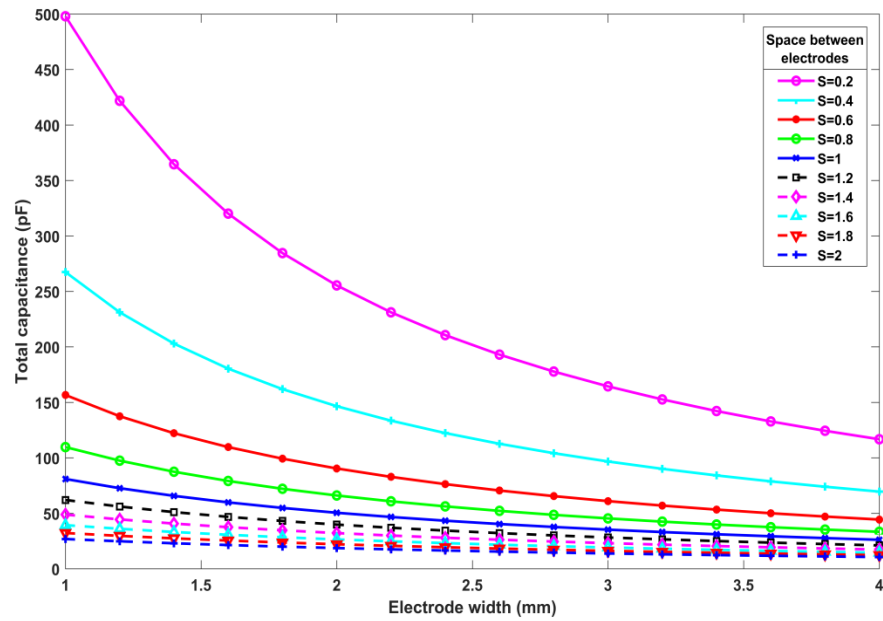


Figure 8-11. Relationship between capacitance of coplanar capacitor and electrode width and spacing

## 8.4 Experimental Results

### 8.4.1 Bare Electrodes

The EA devices with bare electrodes were tested as the benchmark. Their simplicity can help build up the theoretical relationship between EA force and parameters like electrodes' width, spacing, and distance between EA device and substrate.

#### 8.4.2 Considerations for testing EA devices with bare electrodes

Electrode widths and spacings should be carefully selected, and applied voltage should be gradually increased to avoid dielectric breakdown as tests were carried out in the air, and air has very low dielectric strength compared to other materials.

#### 8.4.3 Typical receded force obtained by rigid EA devices

As explained in section 7-6, the initial distance between EA devices and substrate was 10cm, and the robot arm started moving toward the substrate (sheet of glass); after having 5 min connection between an EA device and the substrate, the robot arm moved back to its initial position while the force obtained by an EA device had been recorded during whole steps. Figure 8-12 illustrates a typical obtained EA force during each test. As can be seen, there are two peaks of force in the graph, referred to as the reached force and the released force, respectively. A Butterworth filter explained in section 6.6.5 was used to filter the force recorded. Figure 8-13 compared the recorded force and filtered one.

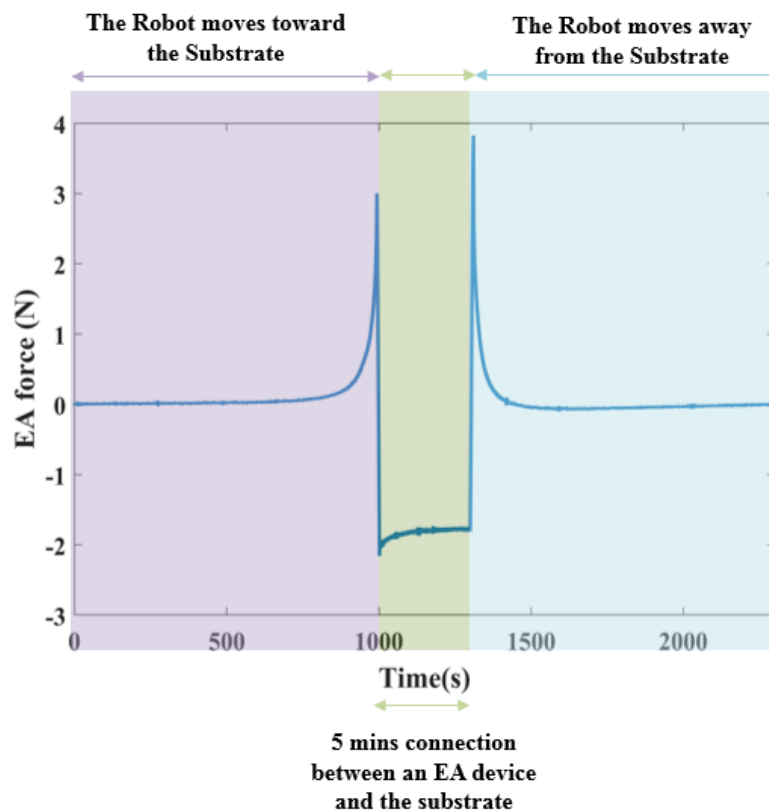


Figure 8-12. A Typical EA force recorded by the sensor during tests of EA devices with bare electrodes

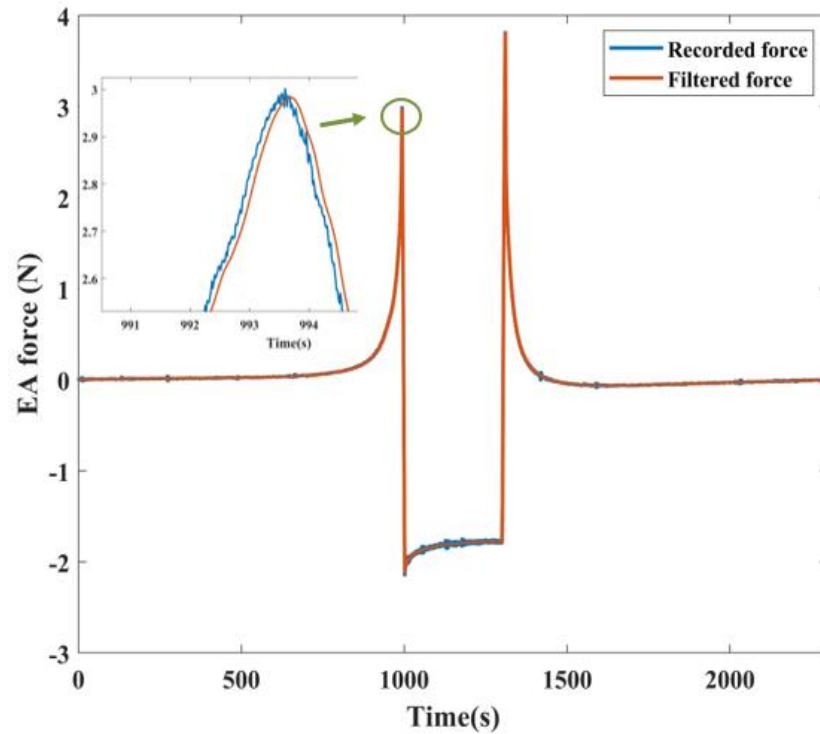


Figure 8-13. Compression between recorded EA force and filtered one

#### 8.4.4 Relationship between EA force and distance between EA device and substrate

Results showed (see figure 8.14) that there is an approximately exponential relationship between the obtained EA force and the distance between the EA devices and the substrate. Table 8-1 shows the fitting curve parameters and goodness-of-fit criteria for fitting an exponential function to the data. With  $R^2 > 0.95$ , it can reasonably be stated that the relationship is approximately exponential.

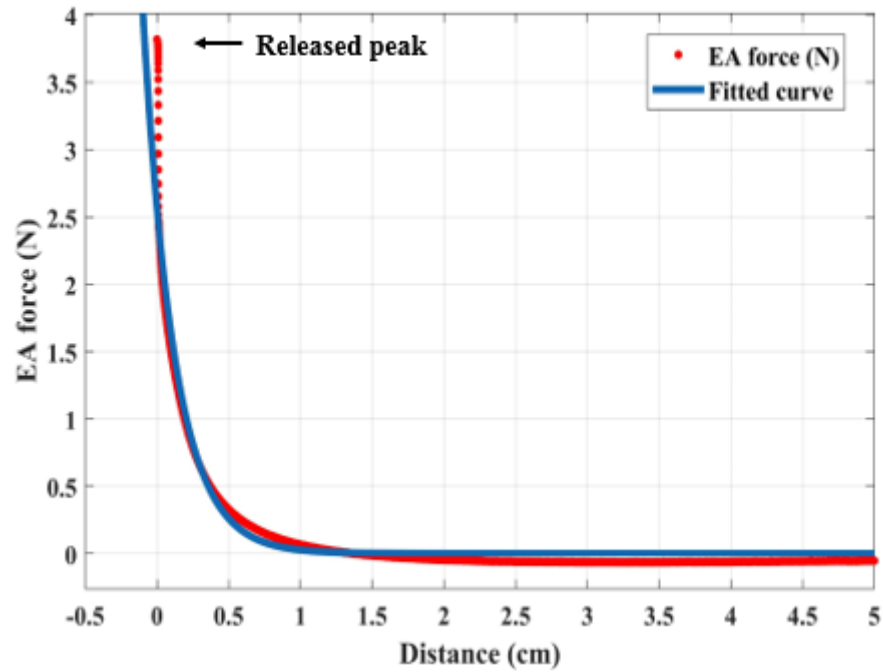


Figure 8-14. EA force obtained by interdigitated EA device (W & S=5) with bare electrodes versus distance

Table 8-1 Curve fitting parameters and it's goodness factors.of EA force versus distance

Equation type	Parameters of the equation		R-squared	RMSE
$a + e^{(bV)}$	a=2.564	b=-4.577	0.9515	0.06026

#### 8.4.5 Effect of spacing between electrodes on obtained EA force

Although the smaller the spacing between electrodes, the greater the force that will be obtained, having shorter spacing results in a more concentrated electric field generated by an EA device; therefore, as can be seen in figure 8.15, the EA device with larger spacing (10 cm) can generate greater force up to the certain point away from the substrate.



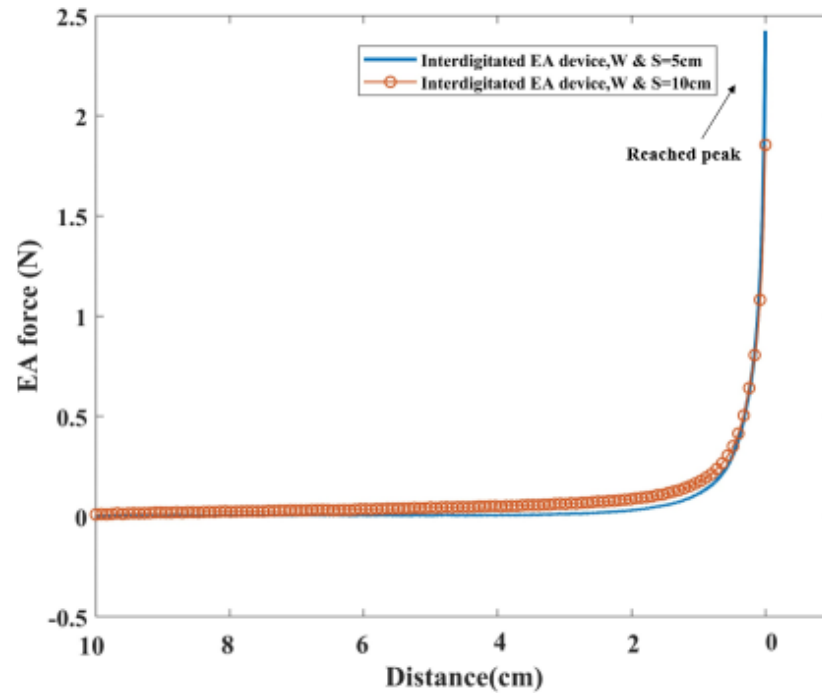


Figure 8-15. Comparison of generated EA forces of two interdigitated devices (W & S=5mm and W & S=10mm) with bare electrodes

#### 8.4.6 Effect of voltage on EA force obtained by rigid devices with bare electrodes

Numerical analysis (Section 7-7-1) and analytical solution (section 8-1) both indicate that the obtainable EA force is proportional to the square of the voltage; however, in practice, after certain values of voltage, the relationship is more likely to be linear (see figure 8-16), and it is believed that applied voltage is close to the voltage breakdown of materials used to fabricated EA device or the air layer trapped between devices and the substrate. In this case, it seems that the transition bound from square behaviour to liner behaviour is between 1 and 2 kV. Figure 8-16 shows the fitting curves out of this bound (see table 8-2 for curve fittings parameters and their goodness); however, more systematic experiments may help to clarify this issue. Figure 8-16 also depicts the maximum tolerance of the force obtained by interdigitated EA device (W & S=5mm) with bare electrodes. This is a typical tolerance for rigid EA devices with bare electrodes.

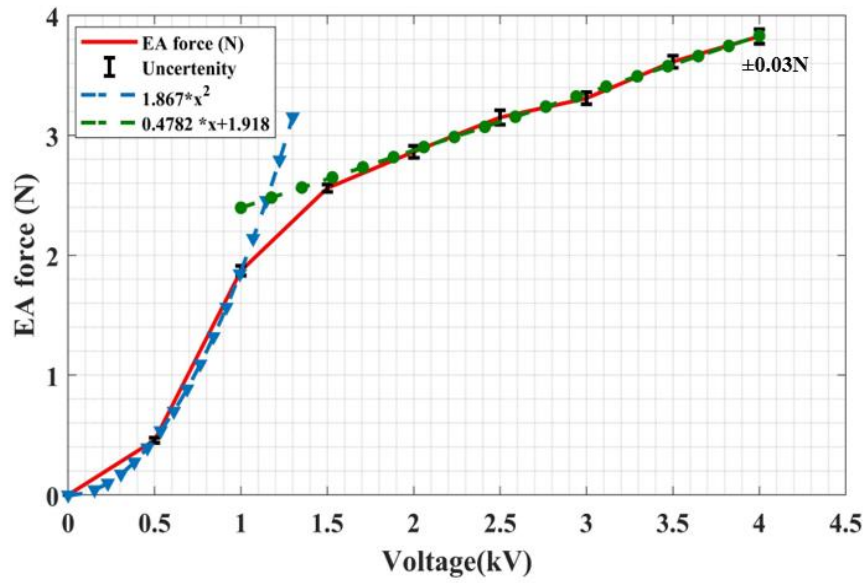


Figure 8-16. Obtained EA force of interdigitated device (W & S =5mm) with bare electrodes versus applied voltage

Table 8-2 Curve fitting parameters and goodness criteria of EA force versus applied voltage

Equation type	Parameters of the equation		R-squared	RMSE	Bound
$aV^2$	a=1.867		0.9999	0.007889	[0,1]
$bV + c$	b=0.4782	C=1.918	0.9934	0.03562	[2,4]

#### 8.4.7 Effect of electrodes pattern on obtainable EA force

Numerical analysis showed that the sine wave generated higher EA force between EA devices with the same effective area. Experiments carried out (see figure 8-17) show that the sine wave is the best-performing shape from the other tested shapes of electrodes.

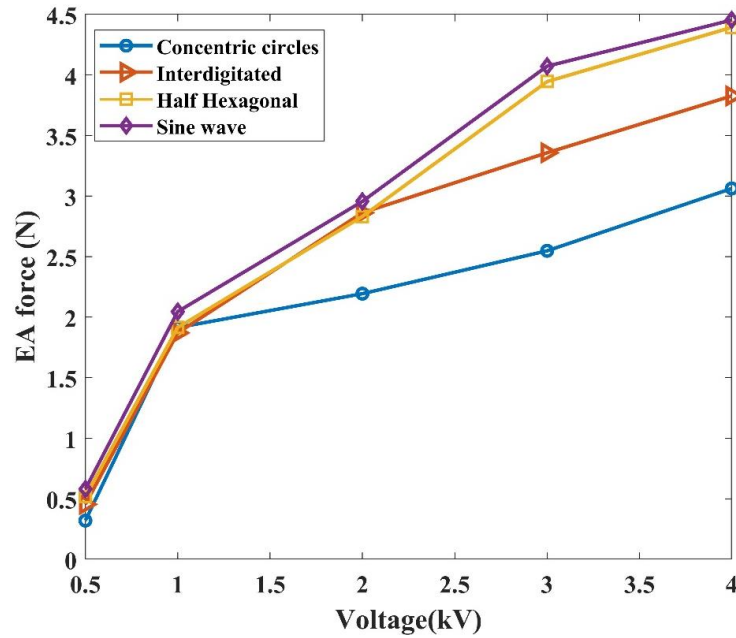


Figure 8-17. Comparison of generated EA forces by sine wave, half hexagonal, interdigitated and concentric circles devices (W & S=5mm) with bare electrodes

#### 8.4.8 Pros and cons of bare electrodes EA devices:

- 1) Simple fabrication method
- 2) Reproducible results
- 3) Limitation in applied voltage range or limitation in decreasing spacing between electrodes and as result lower obtainable EA force

### 8.5 Flexible EA devices

#### 8.5.1 Typical recorded force obtained by flexible EA devices

The same procedure explained in the previous section was used to record forces obtained by flexible EA devices. Figure 8-18 depicts a typical variation of EA force during experiments. As can be seen in this figure, the flexibility of devices imposed huge fluctuation during release and results are not usually reproducible; therefore, rigid devices were used for the rest of this study. The experiments show that, generally, flexible EA devices produce greater force than rigid devices with the same effective area. This is probably because flexible EA devices create a better connection with substrates.

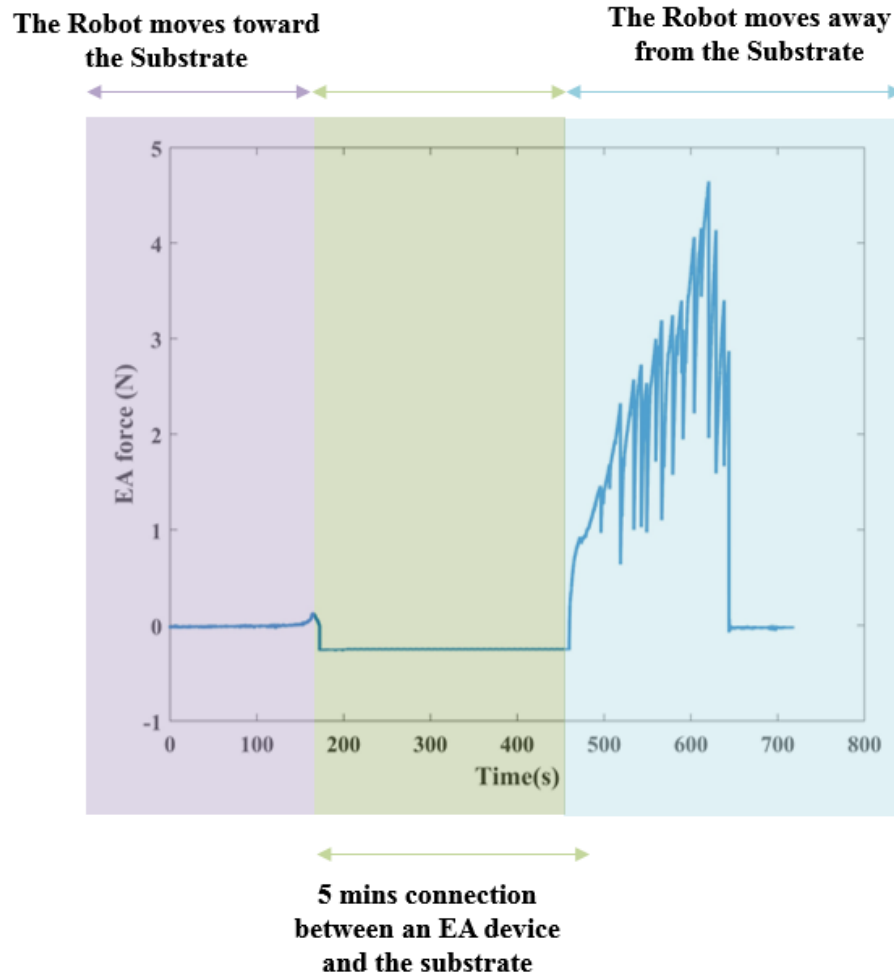


Figure 8-18. Variation of EA force obtained by a flexible and interdigitated device (W & S=5) with bare electrodes during test

### 8.5.2 Reproducibility of EA force obtained by flexible EA devices

Figure 8-19 shows the typical tolerance of EA force recorded for flexible EA devices. As can be seen, the order of magnitude of uncertainty is one decimal point greater than that of rigid devices.

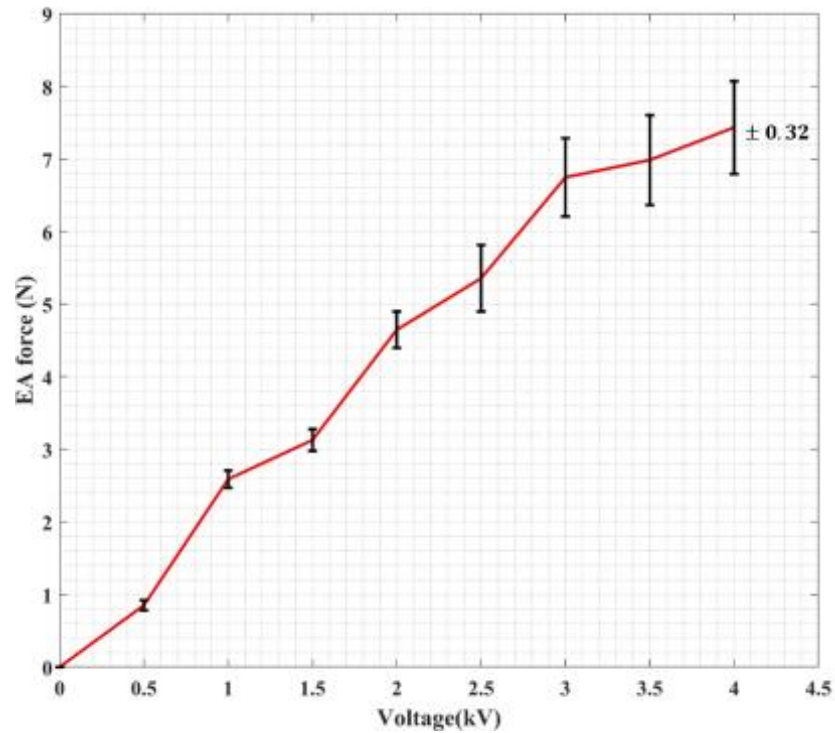


Figure 8-19. Uncertainty in recorded EA force obtained by flexible and interdigitated EA devices (W & S=5mm) with bare electrodes

## 8.6 EA device with liquid dielectric

### 8.6.1 Consideration in fabricating EA device the with high voltage dielectric oil

In the process of fabricating EA devices with liquid dielectric, the gap between the EA device and covering layer should be carefully filled with oil to avoid air bubbles trap because these could significantly decrease voltage breakdown of the oil and, as a result, limits the applicable voltage to feed the EA device.

### 8.6.2 Test procedure of EA devices with liquid dielectric

The only difference between the testing procedure of this type of EA device with the others is that the applied force during the connection between the EA device and the substrate was lower to avoid oil leakage. Figure 8-20 shows that the force recorded during connection is positive, unlike the other tests.

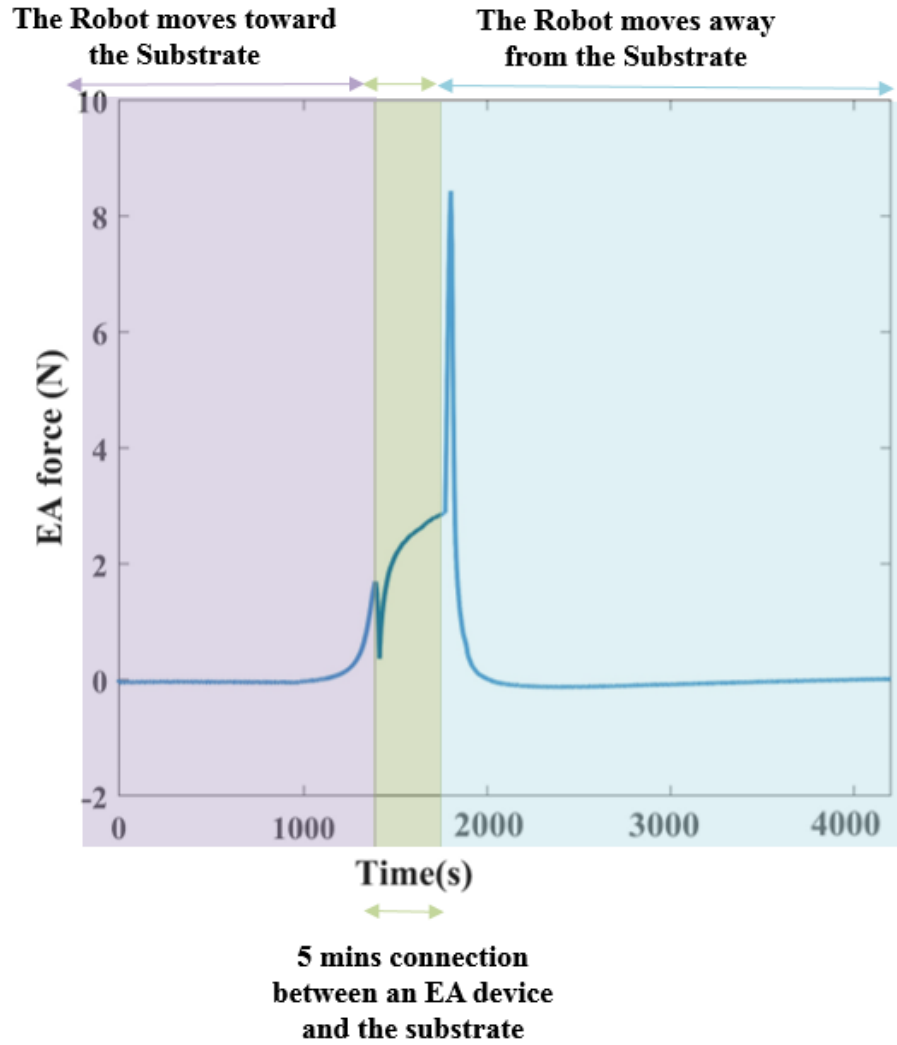


Figure 8-20. A Typical EA force obtained by an interdigitated device (in this case, W & S=5) with liquid dielectric during test

### 8.6.3 Stability in performance of EA devices with liquid dielectric

Instability in EA device performance was discussed in section 2.3.9. Findings showed that for a period of 5 days working, the obtainable EA force has decreased by approximately 2/3, and the researcher believed that it could not only be a result of a change in environment condition (humidity and temperature) and possibly residual electrical stress generated because of long-time operation can affect the EA performance. The EA devices with liquid dielectric show more stable performance than EA devices with a rigid dielectric layer in the long-time operation due to their intrinsic behaviour of releasing residual electrical stress after being subjected to a high DC voltage. The performance of an EA device with liquid dielectric was compared with EA devices with a rigid dielectric layer for a period of 4 days in figure 8-21.

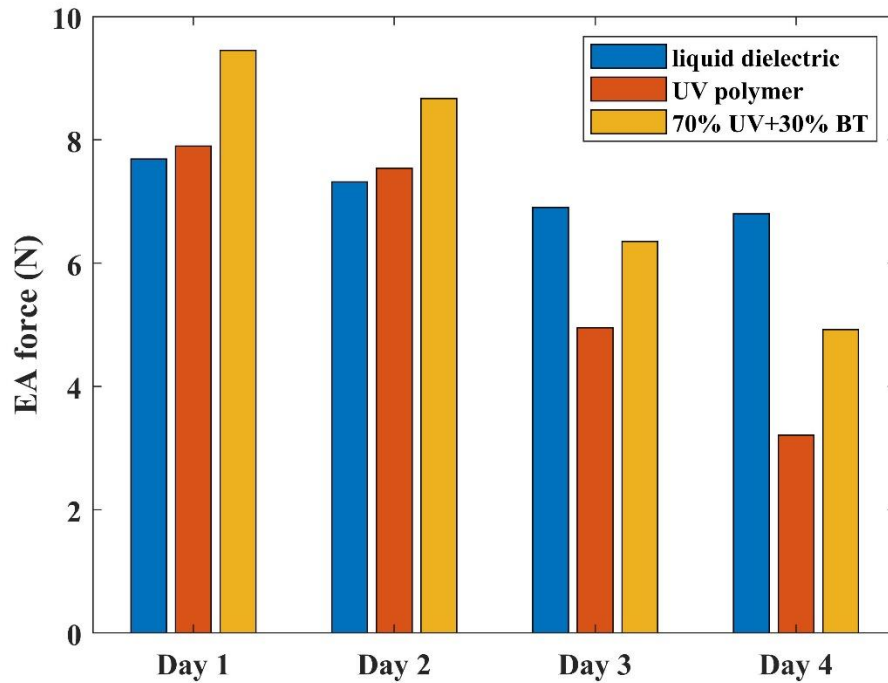


Figure 8-21. Comparison of stability in performance of interdigitated EA devices (W & S=5mm) with liquid and rigid dielectric layer

## 8.7 EA devices with UV polymer and electroceramic –UV polymer composites dielectric layer

### 8.7.1 Forces obtained by EA devices with polymer and composites dielectric layer

The same procedure (see section 8.4.3) was used to evaluate forces obtained by EA devices with polymer and composite dielectric layers. In section 5.3, it was shown that the relative permittivity of the polymer reinforced by electroceramics has improved. It is expected that devices coated by composites show better performance compared to devices coated purely by UV polymers. Figure 8-22 compares EA forces obtained by EA devices with different coating systems and bare electrodes of interdigitated EA devices with W and S=5mm and the same effective area. Results are in agreement with numerical findings explained in section 7.2.2, where it showed that increasing the relative permittivity of the dielectric layer up to a specific value is noticeable.

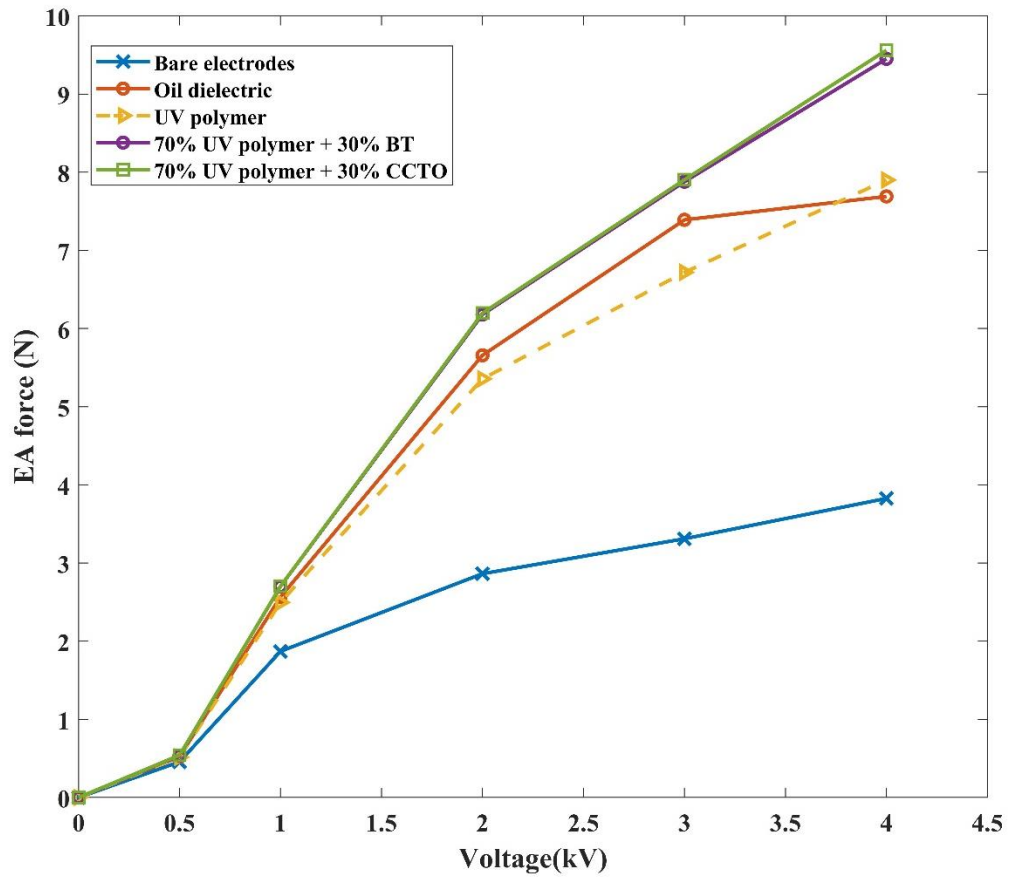


Figure 8-22. Comparison of EA forces obtained by rigid interdigitated EA devices (W& S=5mm) with different dielectric layer

### 8.7.2 Uncertainty in Forces obtained by EA devices with polymer and composites dielectric layer

A screen printing coating system was used to manufacture EA devices with polymer and composites dielectric layer, which is a relatively uncontrollable system; therefore, it was expected to see greater uncertainty in results (see figure 8-23) compared to EA devices with bare electrodes.



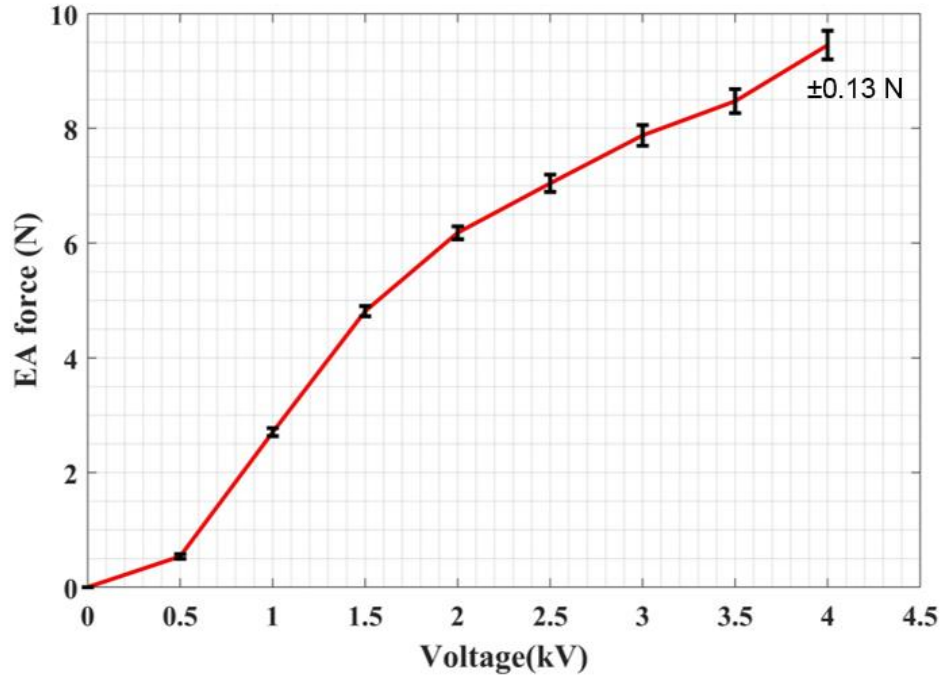


Figure 8-23. Comparison of EA forces obtained by rigid interdigitated EA devices (W& S=5mm) with different dielectric layer

## 8.8 Discussions

### 8.8.1 Analytical Solution

Persson and Guo (2019) offer the below analytical equation to calculate EA force for a interdigitated EA device

$$F(t) = \varepsilon_0 A (\varepsilon_1^2 - 1) q_0^2 e^{-2q_0 d} V^2(t) \quad 8-32$$

Whereas

$$q_0 = \frac{2\pi}{4a} \quad 8-33$$

And  $a$  is width of electrodes and spacings.

$\varepsilon_0$  and  $\varepsilon_1$  are relative permittivity of Air and a dielectric layer, respectively. In contrast, Eq. 8-23 was offered to calculate EA force in this study. It is only applicable when the relative permittivity of the dielectric layer and Air and the substrate are equal. Both equations indicate that EA force is proportional to the voltage square. However, in Eq. 8-32, they considered different relative permittivity for dielectric layer and Air, which the researcher believes that in this condition, the EA force does not have an analytical solution since having different relative permittivity imposes discontinuity in the electric field at the interface.

## **8.8.2 Numerical Analysis**

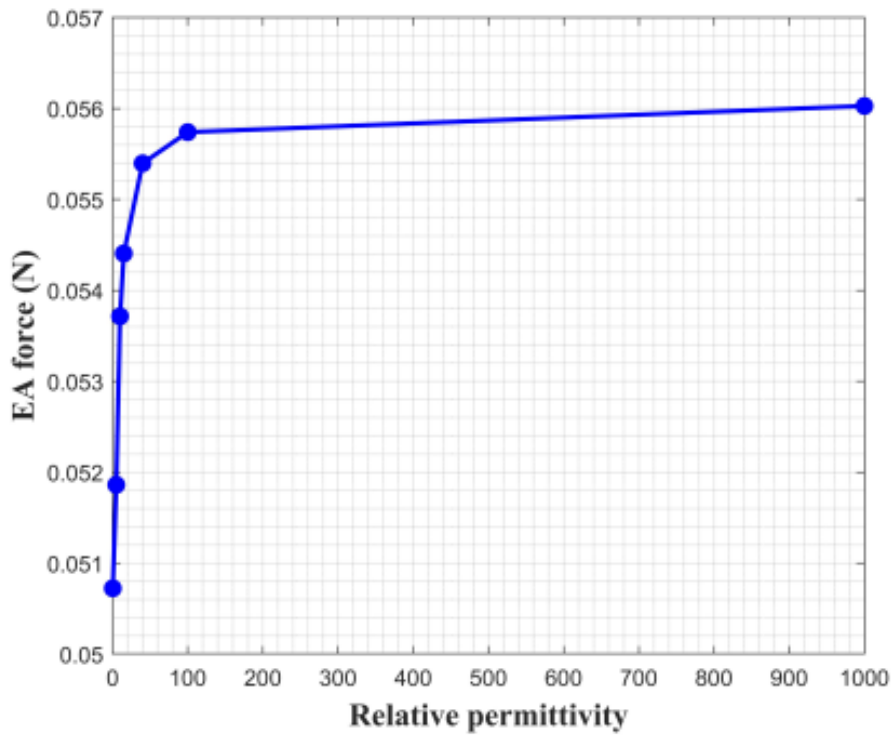
### **8.8.2.1 2D simulations results**

- 1) In this study, for the first time, convergence criteria (total energy error and EA force were considered for all 2D and 3D simulations.
- 2) In this study, for the first time, the influence of electrodes width and spacing of uni-layer interdigitated EA devices on pressure distribution (Maxwell stress) were demonstrated by 2D parametric simulations and similar to previous findings (Guo et al., 2016 b), it was concluded that there is optimal electrode width to maximise obtainable EA force. However, the optimal values are different, and it is because different parameters were used in this study compared to previous studies.

### **8.8.2.2 3D simulations results**

#### **8.8.2.2.1 Effect of relative permittivity of the dielectric layer on obtainable EA force**

3D simulations of an interdigitated EA device (see section 7-9-2 for more details) were carried out to investigate the effect of relative permittivity of a dielectric layer on obtainable EA force. Results show (see figure) that there is no noticeable EA force increase for relative permittivities greater than 20.



**Figure 8-24** EA force versus relative permittivity of dielectric layer of the modelled interdigitated EA device

#### 8.8.2.2.2 Effect of Pattern of electrodes on obtainable EA force of uni-layer devices

- 1) 3D simulations have shown that the pattern of electrodes can influence obtainable EA force and the sine wave pattern has a better performance compared to other designs that were tested.

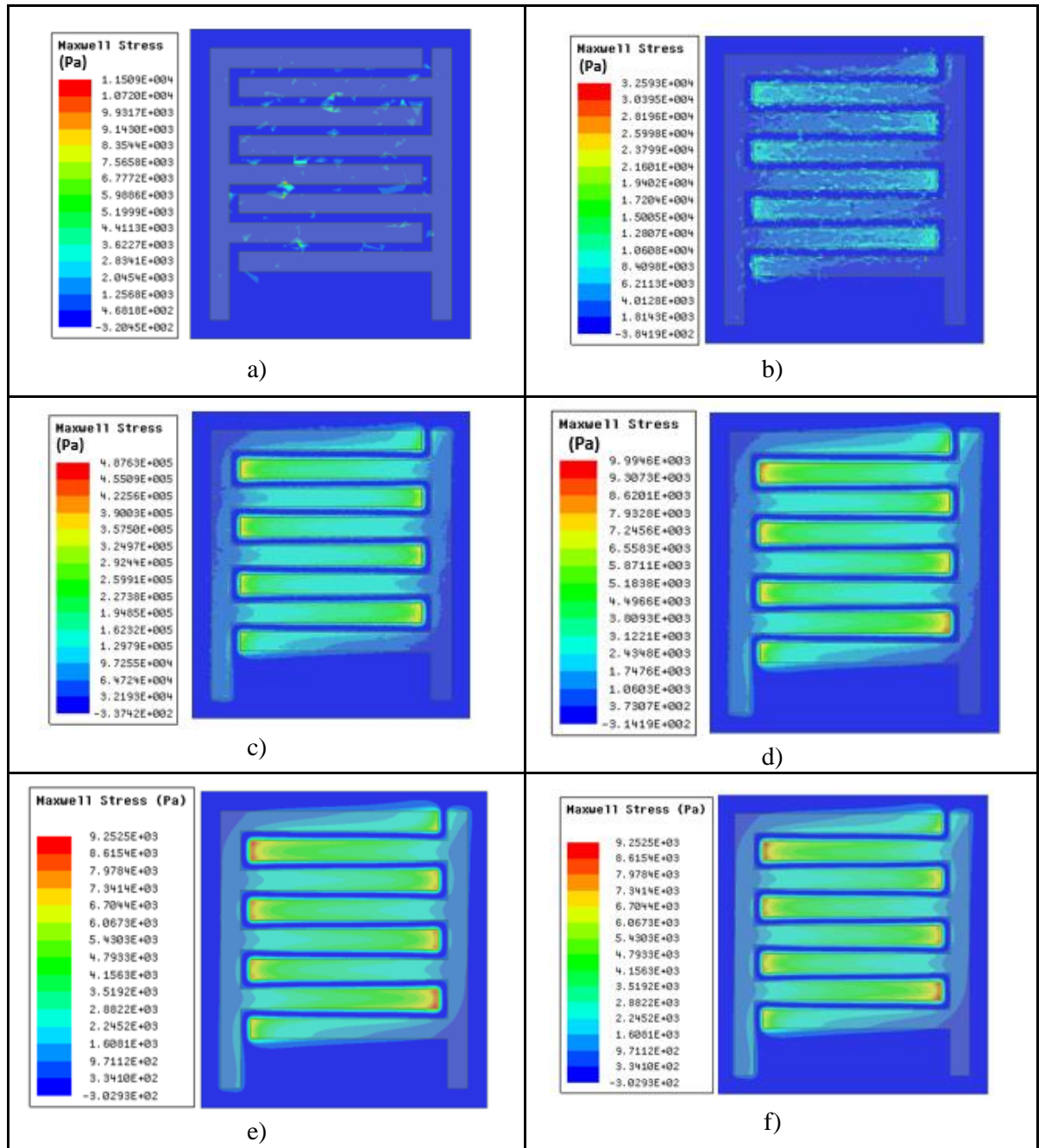
#### 8.8.2.2.3 Sensitivity of Maxwell stress (EA pressure) distribution to the number of elements

Table 8-3a and b compared the sensitivity of Maxwell stress and EA force obtained by 3D simulations of an interdigitated EA device (see section 7-9-2 for more details). The results show that Maxwell stress is more sensitive to the number of elements, which should be considered in reporting the EA pressure of 3D simulations. Figure 8-24 shows an example of low fidelity of EA pressure presented by Dadkhah et al. (2018).

Table 8-3a Comparison of Maxwell stress and obtainable EA force mesh independency

No of elements	EA force (N) / Error %	EA pressure distribution
11916	0.12178/140.23	Figure (a)
80331	0.053384/5.31	Figure (b)
540586	0.050879/0.37	Figure (c)
1402206	0.050766/0.14	Figure (d)
3637023	0.050723/0.06	Figure (e)
41020811	0.050693	Figure (f)

Table 8-4b Maxwell stress distribution versus number of elements



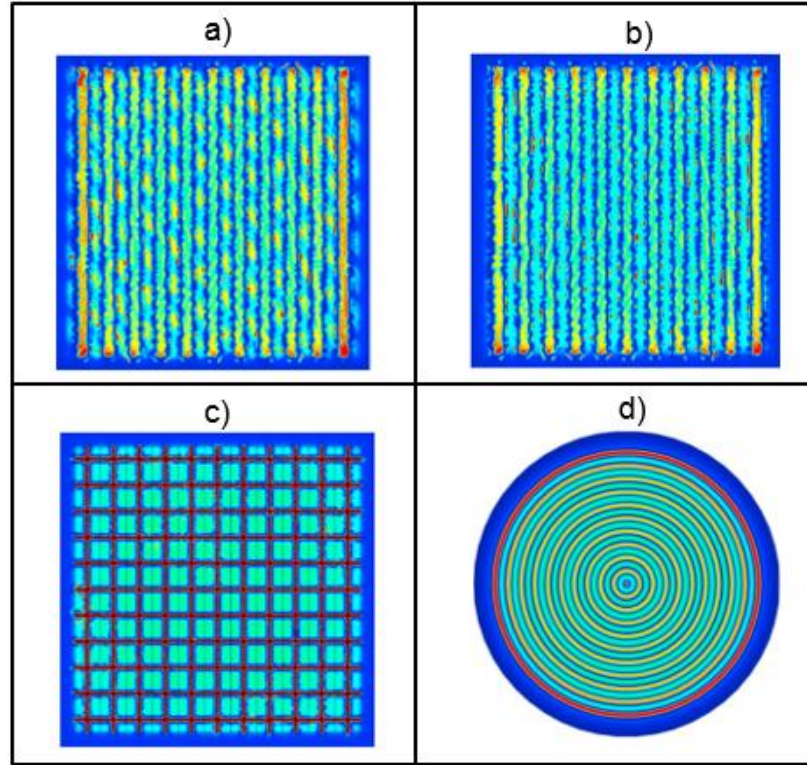


Figure 8-25 Pressure distribution of EA devices: (a) Parallel electrodes  $45^\circ$ , (b) offset electrodes, (c) Solid top electrode with bottom orthogonal electrodes, (d) Solid top electrode with concentric circles bottom electrode obtained by 3D simulations (Dadkhah et al. (2018))

### 8.8.2.3 *Bi layer EA devices*

Simulation of a bi-layer EA device with Top solid and bottom concentric circles electrodes (see section 7.9.1 for more details) shows that the normal pressure obtained by the EA device is 8.8 kPa which is in the same order of magnitude as experimental results of shear pressure obtained by a device with same specifications (bi-layer metalized) reported by Dadkhah et al. (2018) illustrated in figure 8-25.

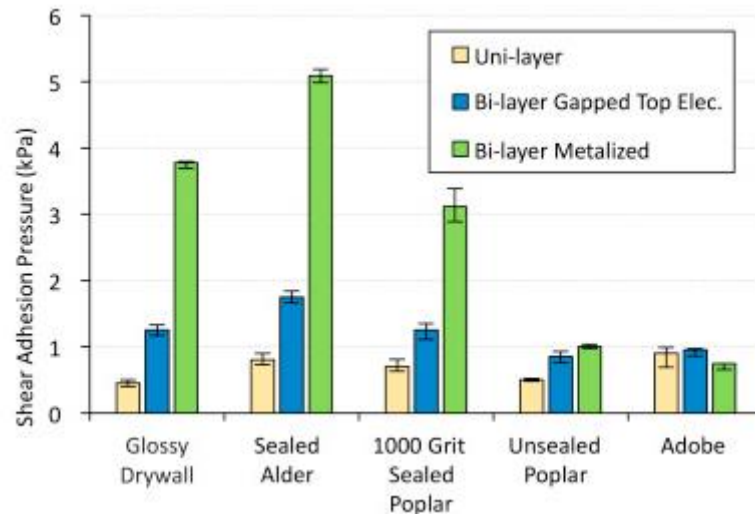


Figure 8-26. Shear pressure obtained by uni-layer and bi-layer EA devices of substrates with various materials (Dadkhah et al. 2018)

### 8.8.3 Relationship between EA force and total capacitance of the system

Guo et al. (2016 a) assumed that potential distribution near two adjacent electrodes with different polarity is according to the figure 8-24. The researcher believes that this is a wrong assumption, and therefore the rest of the calculations that were carried out based on this assumption are not acceptable. In this study (section 8-3), it was shown that there is no relationship between EA force and the total capacitance of the system; therefore, the total capacitance of the system cannot be used as a criterion to optimise obtainable EA force.

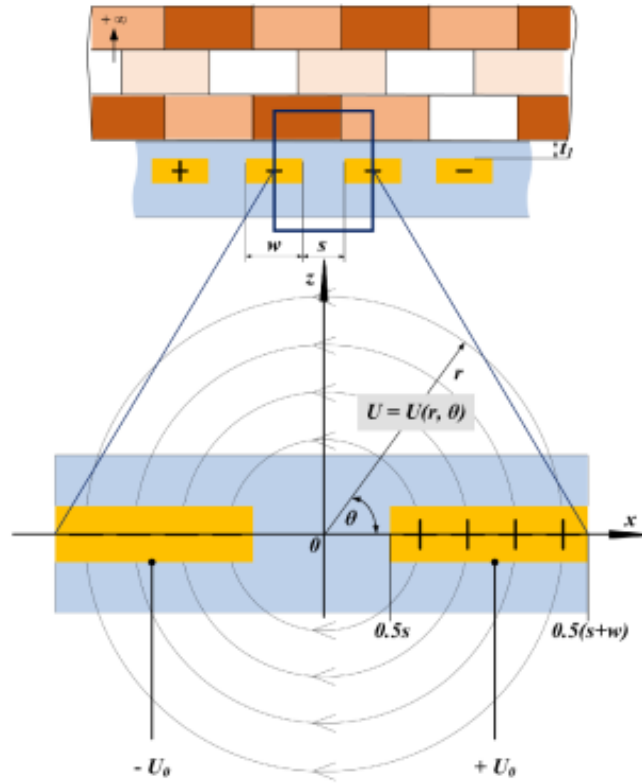


Figure 8-27 Electric potential distribution near two adjacent electrodes with different polarity (Guo et al., 2016 a)

## 8.8.4 Experimental Results

### 8.8.4.1 EA devices with bare electrodes

In this study, EA devices with bare electrodes were fabricated with a width and spacing of 10 cm, width and spacing of 5 cm and width of 3 cm and spacing of 1 cm. Although it was predicted by the Paschen curve of Air that voltage breakdown should be around 10 kV (see figure 8-25), it was noticed that EA devices with the spacing of 1 cm could not be charged. It was concluded that more systematic research needs to estimate the dielectric breakdown voltage of materials subjected to coplanar electrodes.

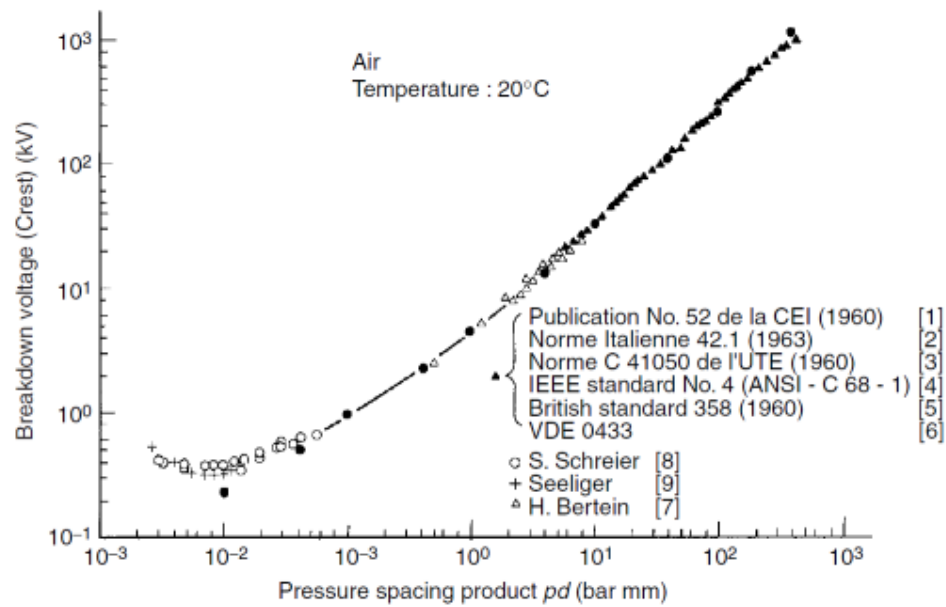


Figure 8-28. Paschen curve of Air at 20°C (Kuffel and Kuffel, 2000)

#### 8.8.4.2 EA devices with polymer and composite dielectric layer

In section 5-12, it was shown that the relative permittivity of Polymer could be increased using electroceramic particles. In this case, adding 30% (volume fraction) BT particles result in more than a 30% increase in relative permittivity of composites. Unfortunately, the researcher could not manage to calculate CCTO-UV polymer composite relative permittivity since the XRF device used for this purpose was broken for more than a year, but it was expected to achieve a composite with higher relative permittivity. The results show (see figure 8-22) that obtainable EA force can be increased using a dielectric layer with higher relative permittivity, and in higher applied voltage, this improvement is more noticeable (18.75% with 4 kV applied voltage).

#### 8.8.4.3 Optimal Electrode width and spacing

The limitation of having access to appropriate equipment does not allow the researcher to fabricate devices with optimal electrode width and spacing. However, it was managed to fabricate EA devices with 3 cm electrode width and 1 cm spacing which are helpful to show the trend that is expected from numerical analysis. Results of EA devices with dielectric oil show the effect of width and spacing on obtainable EA force.



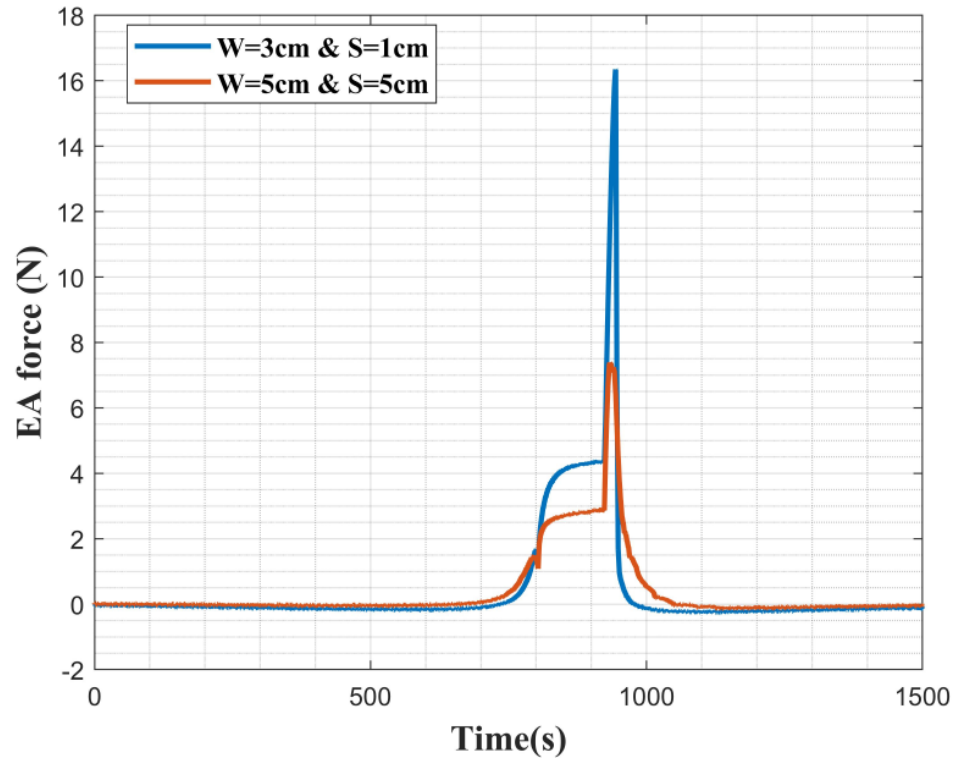


Figure 8-29. Comparison of obtained EA force of interdigitated EA devices (liquid dielectric layer) with W=3cm, S=1cm and W=5cm, S=5cm, applied voltage 3kV

## *Chapter 9*

# **Conclusions and further research**

### **9.1 Conclusion**

#### **9.1.1 Physics of Electroadhesion**

In this study, it was tried to improve understanding of the physics of electroadhesion by developing mathematical relationships between main parameters that influence the performance of EA devices, such as electrode width and spacing, the pattern of electrodes, and electrical properties of dielectric layer and substrate. Analytical solutions for obtainable EA force and its limitations were proposed. It was also shown that maximising the total capacitance of the EA system does not lead to maximising EA forces.

#### **9.1.2 Material development and coating procedure**

The main focus of this research was on developing new dielectric material for electroadhesion; therefore, extensive research was carried out about solid, liquid and gaseous dielectrics. Electroceramics including BT, BST and CCTO were fabricated using solid state reaction, and material tests were carried out to ensure the desirable phases were formed. Finally, the relative permittivities of the fabricated electroceramics were measured. Under investigation electroceramic particles were mixed (30% volume fraction) with UV curable polymers, and a suitable photoinitiator (2022) was added to prepare electroceramic UV polymer composites. The photoinitiator shows good performance in imitating polymer chains as well as pigmented inks fabricated for EA applications under exposure of UV light with a suitable range of wavelengths. Iron doped medium pressure mercury lamp was used for curing prepared composites as it creates a wide range of wavelengths of UV light that are required for both surface and deep curing. To measure the relative permittivity of formulated inks, a cylindrical sample of inks was

curd using electron beams exposed by XRF source provided for a liquid test. Adding 30% of total volume fraction of BT particles resulted in approximately 30% increase in relative permittivity of the composite. Viscosities of formulated inks were measured and compared with mass product screen printing inks to ensure that formulated inks are applicable for screen printing.

### **9.1.3 Experimental apparatus preparation and test procedure**

A suitable experimental configuration, including DENSO ROBOT arm, ATI Six-Axis Force/Torque sensor model Gamma and data acquisition hardware, were assembled to examine the performance of fabricated EA devices. The force sensor shows a good performance in recording a range of forces obtained by EA devices in this research. To record force obtained by EA devices minimum achievable speed (10 $\mu$ m/s) of the robot arm was used. The power supply was switched on for 5 min before the robot moved toward the substrate. After reaching the point that the force direction was reversed, EA devices were held in this position for 5 min, and then the robot moved to relocate the EA device to its initial position. The force is continuously recorded during the whole cycle. Following this procedure for rigid EA devices, reproducible results were produced.

### **9.1.4 Numerical analysis**

2 D numerical simulations were carried out to demonstrate the relationship between EA force and applied voltage for uni-layer EA devices and find optimal electrode width and spacing. The influence of electrode width and spacing on EA pressure distribution also was quantified and presented.

3D simulations were performed to show the influence of electrodes pattern on obtainable EA forces for uni-layer and bi-layer EA devices. For all simulations, convergence criteria were considered, and mesh independence analyses were carried out. The findings could be in good agreement with experimental results if the problem of voltage breakdown of the dielectric layer of EA devices is sorted. It was also shown that Maxwell stress (EA pressure) is very sensitive to the number of elements, and to achieve high fidelity simulations, the number of elements should be much more than the numbers needed to achieve mesh independence EA forces.

### **9.1.5 Experimental results**

#### ***9.1.5.1 EA devices with bare electrodes***

Experimental tests showed that EA devices with bare electrodes have reproducible performance, but the obtainable EA force is limited by voltage breakdown of Air; therefore, they may not be considered an option in practice.

#### ***9.1.5.2 Flexible EA devices***

Generally speaking, Flexible EA devices create a higher force compared to rigid EA, and probably this is due to the better connection this type of device can have with the substrate, but the flexibility of the devices should be carefully controlled to achieve reproducible performance.

#### ***9.1.5.3 EA devices with polymer and composite dielectric layer***

EA devices with composite dielectric layers created higher force than devices with polymer dielectric. This could result from improved relative permittivity of the dielectric layer and voltage breakdown. More systematic research can help distinguish which improvement in electrical properties is dominant.

#### ***9.1.5.4 EA devices with liquid dielectric layer***

Experimental tests show that although EA devices with liquid dielectric cannot create EA force higher than EA devices with a composite dielectric layer, they are more stable in long-term operation, which is worth considering for fabrication of new generation of EA devices.

### **9.2 Further research**

1. In this study, screen printing was used to fabricate dielectric layers, which is a relatively uncontrollable process, and guaranteed tolerance may not be achieved, and also it is time consuming process; therefore, it is suggested to reformulate electroceramic-UV ink prepared in this study to be able to use as an inkjet printing ink and combining this with conductive inkjet printing can give the flexibility of designing more complex EA devices with better performance (bi-layer EA devices). There are also other electroceramics that can be used to fabricate EA devices, particularly CCTO families, which have higher relative permittivities.
2. EA devices with liquid dielectric have shown promising results, particularly stabilising the EA device's long-term operating performance. Available Liquid dielectrics have low relative permittivity (less than 4). It is suggested to use electroceramics to improve the electrical properties of liquid dielectrics for EA applications.
3. The glass was used as a substrate in this study. It is suggested to test fabricated EA devices with a different substrate to evaluate their performance on other materials.

# References

- Ahmadipour, M., Ain, M. F., & Ahmad, Z. A. (2016). A Short Review on Copper Calcium Titanate (CCTO) Electroceramic: Synthesis, Dielectric Properties, Film Deposition, and Sensing Application. *Nano-Micro Letters*, 8(4). <https://doi.org/10.1007/s40820-016-0089-1>
- Arlt, G., Hennings, D., & de With, G. (1985). Dielectric properties of fine-grained barium titanate ceramics. *Journal of Applied Physics*, 58(4). <https://doi.org/10.1063/1.336051>
- Asano, K., Hatakeyama, F., & Yatsuzuka, K. (2002). Fundamental study of an electrostatic chuck for silicon wafer handling. *IEEE Transactions on Industry Applications*, 38(3). <https://doi.org/10.1109/TIA.2002.1003438>
- Bagheri, A., & Jin, J. (2019). Photopolymerization in 3D Printing. *ACS Applied Polymer Materials*, 1(4). <https://doi.org/10.1021/acsapm.8b00165>
- Bak, W., Kajtoch, C., Ptaszek, S., Lisińska-Czekaj, A., Czekaj, D., Zietek, D., ... Garbarz-Glos, B. (2016). Influence of Sn and Pb ions substitutions on dielectric properties of barium titanate. *Archives of Metallurgy and Materials*, 61(2A), 905–907. <https://doi.org/10.1515/amm-2016-0153>
- Bamber, T., Guo, J., Singh, J., Bigharaz, M., Petzing, J., Bingham, P. A., ... Jackson, M. (2017). Visualization methods for understanding the dynamic electroadhesion phenomenon. *Journal of Physics D: Applied Physics*, 50(20). <https://doi.org/10.1088/1361-6463/aa6be4>
- Brzozowski, E., & Castro, M. S. (2000). Synthesis of barium titanate improved by modifications in the kinetics of the solid state reaction. *Journal of the European Ceramic Society*, 20(14–15). [https://doi.org/10.1016/S0955-2219\(00\)00148-5](https://doi.org/10.1016/S0955-2219(00)00148-5)
- Cao, C., Sun, X., Fang, Y., Qin, Q.-H., Yu, A., & Feng, X.-Q. (2016). Theoretical model and design of electroadhesive pad with interdigitated electrodes. *Materials & Design*, 89. <https://doi.org/10.1016/j.matdes.2015.09.162>
- Cao, W. Q., Li, F. L., Ismail, M. M., & Xiong, G. (2012). Dielectric Properties of Y<sub>2</sub>O<sub>3</sub> and Nb<sub>2</sub>O<sub>5</sub> Co-Doped Barium Titanate Ceramics. *Japanese Journal of Applied Physics*, 51. <https://doi.org/10.1143/JJAP.51.041503>
- Chen, H., & Christensen, E. D. (2017). Development of a numerical model for fluid-structure interaction analysis of flow through and around an aquaculture net cage. *Ocean Engineering*, 142. <https://doi.org/10.1016/j.oceaneng.2017.07.033>
- Choi, H. R., Sekhar, K., Jo, A. R., & Cho, Y. S. (2016). Dielectric Characteristics of UV-Curable CaCu<sub>3</sub>Ti<sub>4</sub>O<sub>12</sub> Composite Thick Film Capacitors on Cu Foils. *International Journal of Applied Ceramic Technology*, 13(4). <https://doi.org/10.1111/ijac.12545>
- Correia, V., Mitra, K. Y., Castro, H., Rocha, J. G., Sowade, E., Baumann, R. R., & Lanceros-Mendez, S. (2018). Design and fabrication of multilayer inkjet-printed

passive components for printed electronics circuit development. *Journal of Manufacturing Processes*, 31. <https://doi.org/10.1016/j.jmapro.2017.11.016>

Dadkhah, M., Ruffatto, D., Zhao, Z., & Spenko, M. (2018). Increasing adhesion via a new electrode design and improved manufacturing in electrostatic/microstructured adhesives. *Journal of Electrostatics*, 91. <https://doi.org/10.1016/j.elstat.2017.12.005>

EB curing Sartomer

<https://www.sartomer.com/en/innovations/collaborative-partnerships/eb-curing-innovation-hub/>

(Accessed November 2021)

Endruweit, A., Johnson, M. S., & Long, A. C. (2006). Curing of composite components by ultraviolet radiation: A review. *Polymer Composites*, 27(2), 119–128. <https://doi.org/10.1002/pc.20166>

Felgner, K.-H., Müller, T., Langhammer, H. T., & Abicht, H.-P. (2004). On the formation of BaTiO<sub>3</sub> from BaCO<sub>3</sub> and TiO<sub>2</sub> by microwave and conventional heating. *Materials Letters*, 58(12–13). <https://doi.org/10.1016/j.matlet.2003.11.037>

Fouassier, J. P., & Lalevée, J. (2012). *Photoinitiators for Polymer Synthesis*. Weinheim, Germany: Wiley-VCH Verlag GmbH & Co. KGaA. <https://doi.org/10.1002/9783527648245>

Galembeck, F., & A. L. Burgo, T. (2017). Electrostatic Processes and Products. In *Chemical Electrostatics*. Cham: Springer International Publishing. [https://doi.org/10.1007/978-3-319-52374-3\\_13](https://doi.org/10.1007/978-3-319-52374-3_13)

Ganguly, M., Rout, S. K., Sinha, T. P., Sharma, S. K., Park, H. Y., Ahn, C. W., & Kim, I. W. (2013). Characterization and Rietveld Refinement of A-site deficient Lanthanum doped Barium Titanate. *Journal of Alloys and Compounds*, 579. <https://doi.org/10.1016/j.jallcom.2013.06.104>

Germann, J., Schubert, B., & Floreano, D. (2014). Stretchable electroadhesion for soft robots. In *2014 IEEE/RSJ International Conference on Intelligent Robots and Systems*. IEEE. <https://doi.org/10.1109/IROS.2014.6943115>

Gruber, H. F. (1992). Photoinitiators for free radical polymerization. *Progress in Polymer Science*, 17(6), 953–1044. [https://doi.org/10.1016/0079-6700\(92\)90006-K](https://doi.org/10.1016/0079-6700(92)90006-K)

Green, W. A. (2010). *Industrial photoinitiators: a technical guide*. CRC Press. <https://www.routledge.com/Industrial-Photoinitiators-A-Technical-Guide/Green/p/book/9781439827451>

Guo, J., Bamber, T., Chamberlain, M., Justham, L., & Jackson, M. (2016 a). Optimization and experimental verification of coplanar interdigital electroadhesives. *Journal of Physics D: Applied Physics*, 49(41). <https://doi.org/10.1088/0022-3727/49/41/415304>

Guo, J., Bamber, T., Hovell, T., Chamberlain, M., Justham, L., & Jackson, M. (2016 b). Geometric Optimisation of Electroadhesive Actuators Based on 3D Electrostatic Simulation and its Experimental Verification. *IFAC-PapersOnLine*, 49(21). <https://doi.org/10.1016/j.ifacol.2016.10.574>

Guo, J., Tailor, M., Bamber, T., Chamberlain, M., Justham, L., & Jackson, M. (2016 c). Investigation of relationship between interfacial electroadhesive force and surface texture. *Journal of Physics D: Applied Physics*, 49(3). <https://doi.org/10.1088/0022-3727/49/3/035303>

Hayashi, H., Nakamura, T., & Ebina, T. (2013). In-situ Raman spectroscopy of BaTiO<sub>3</sub> particles for tetragonal–cubic transformation. *Journal of Physics and Chemistry of Solids*, 74(7). <https://doi.org/10.1016/j.jpcs.2013.02.010>

Heath, D. E., & Cooper, S. L. (2013). Polymers. In *Biomaterials Science* (pp. 64–79). Elsevier. <https://doi.org/10.1016/B978-0-08-087780-8.00008-5>

HDDA Allnex data sheet

<https://allnex.com/en/product/9351fea1-0383-4674-853e-fbd5e45744b5/hdda>

(Accessed November 2021)

HDDA IGM resin data sheet

[https://www.igmlresins.com/en/product/photomer\\_4017](https://www.igmlresins.com/en/product/photomer_4017)

(Accessed November 2021)

Hu, Y., Zhang, Y., Liu, H., & Zhou, D. (2011). Microwave dielectric properties of PTFE/CaTiO<sub>3</sub> polymer ceramic composites. *Ceramics International*, 37(5). <https://doi.org/10.1016/j.ceramint.2011.01.039>

Huan, Y., Wang, X., Fang, J., & Li, L. (2014). Grain size effect on piezoelectric and ferroelectric properties of BaTiO<sub>3</sub> ceramics. *Journal of the European Ceramic Society*, 34(5). <https://doi.org/10.1016/j.jeurceramsoc.2013.11.030>

Huang, Y., Zhan, Z., & Bowler, N. (2017). Optimization of the coplanar interdigital capacitive sensor. <https://doi.org/10.1063/1.4974695>

IBOA Allnex data sheet

<https://allnex.com/en/product/7fdbd318-0b27-4c88-b1e8-4ae4a2bf5bae/iboa>

(Accessed November 2021)

IBOA IGM resin data sheet

[https://www.igmlresins.com/en/product/pureomer\\_4012](https://www.igmlresins.com/en/product/pureomer_4012)

(Accessed November 2021)

Islam, R., Khair, N., Ahmed, D. M., & Shahariar, H. (2019). Fabrication of low cost and scalable carbon-based conductive ink for E-textile applications. *Materials Today Communications*, 19. <https://doi.org/10.1016/j.mtcomm.2018.12.009>

Kapur, N., Abbott, S. J., Dolden, E. D., & Gaskell, P. H. (2013). Predicting the Behavior of Screen Printing. *IEEE Transactions on Components, Packaging and Manufacturing Technology*, 3(3), 508–515. <https://doi.org/10.1109/TCPMT.2012.2228743>

- Kim, E. K., & Willson, C. G. (2006). Thermal analysis for step and flash imprint lithography during UV curing process. *Microelectronic Engineering*, 83(2), 213–217. <https://doi.org/10.1016/j.mee.2005.08.007>
- Kim, S., Jiang, Y., Thompson Towell, K. L., Boutilier, M. S. H., Nayakanti, N., Cao, C., ... Hart, A. J. (2019). Soft nanocomposite electroadhesives for digital micro- and nanotransfer printing. *Science Advances*, 5(10). <https://doi.org/10.1126/sciadv.aax4790>
- Kinoshita, K., & Yamaji, A. (1976). Grain-size effects on dielectric properties in barium titanate ceramics. *Journal of Applied Physics*, 47(1). <https://doi.org/10.1063/1.322330>
- Koh, K. H., Kuppen Chetty, R. M., & Ponnambalam, S. G. (2011). Modeling and simulation of Electrostatic Adhesion for Wall Climbing Robot. In *2011 IEEE International Conference on Robotics and Biomimetics*. IEEE. <https://doi.org/10.1109/ROBIO.2011.6181590>
- Kum-onsa, P., Thongbai, P., Putasaeng, B., Yamwong, T., & Maensiri, S. (2015). Na<sub>1/3</sub>Ca<sub>1/3</sub>Bi<sub>1/3</sub>Cu<sub>3</sub>Ti<sub>4</sub>O<sub>12</sub>: A new giant dielectric perovskite ceramic in ACu<sub>3</sub>Ti<sub>4</sub>O<sub>12</sub> compounds. *Journal of the European Ceramic Society*, 35(5). <https://doi.org/10.1016/j.jeurceramsoc.2014.11.028>
- Łapka, W. (2018). Numerical study of acoustic-structure interaction of selected helicoidal resonator with flexible helicoidal profile. *Archives of Acoustics*, 43(1), 83-92. <https://doi.org/10.24425/118083>

LED Phoseon

<https://phoseon.com/industrial-curing/products/firejet/>

(Accessed November 2021)

LED wavelength

<https://www.photoelcuring.com/en/technologies/uv-led/emission-spectrum/>

(Accessed November 2021)

- Lessing, J., Glavan, A. C., Walker, S. B., Keplinger, C., Lewis, J. A., & Whitesides, G. M. (2014). Inkjet Printing of Conductive Inks with High Lateral Resolution on Omniphobic “R<sup>F</sup> Paper” for Paper-Based Electronics and MEMS. *Advanced Materials*, 26(27). <https://doi.org/10.1002/adma.201401053>
- Li, Y.-X., Yao, X., Wang, X.-S., & Hao, Y.-B. (2012). Studies of dielectric properties of rare earth (Dy, Tb, Eu) doped barium titanate sintered in pure nitrogen. *Ceramics International*, 38. <https://doi.org/10.1016/j.ceramint.2011.04.042>
- Lin, L. (2003). Mechanisms of pigment dispersion. *Pigment & Resin Technology*, 32(2). <https://doi.org/10.1108/03699420310464784>
- Liu, R., Chen, R., Shen, H., & Zhang, R. (2013). Wall Climbing Robot Using Electrostatic Adhesion Force Generated by Flexible Interdigital Electrodes. *International Journal*



- of Advanced Robotic Systems*, 10(1). <https://doi.org/10.5772/54634>
- Lu, D.-Y., Cui, S.-Z., Liu, Q.-L., & Sun, X.-Y. (2016). Dielectric properties and defect chemistry of barium titanate ceramics co-doped R and Dy ions ( R =Eu, Gd, Tb). *Ceramics International*, 42(13). <https://doi.org/10.1016/j.ceramint.2016.05.197>
- Mahanta, D. K., & Laskar, S. (2017). Electrical insulating liquid: A review. *Journal of Advanced Dielectrics*, 07(04). <https://doi.org/10.1142/S2010135X17300018>
- Mahmoudzadeh Akherat, S. M. J., Karimi, M. A., Alizadehyazdi, V., Asalzadeh, S., & Spenko, M. (2019). A tunable dielectric to improve electrostatic adhesion in electrostatic/microstructured adhesives. *Journal of Electrostatics*, 97. <https://doi.org/10.1016/j.elstat.2018.12.001>
- Mak, K., & Hao, J. (2014). Advance in the Analysis Models for Characterizing Multi-Layered Interdigital Capacitors. *International Journal of Advanced Applied Physics Research*, 1(1). <https://doi.org/10.15379/2408-977X.2014.01.01.1>
- Mao, J., Qin, L., Wang, Y., Liu, J., & Xue, L. (2014). Modeling and simulation of electrostatic attraction force for climbing robots on the conductive wall material. In *2014 IEEE International Conference on Mechatronics and Automation*. IEEE. <https://doi.org/10.1109/ICMA.2014.6885832>
- Mao, J., Qin, L., & Zhang, W. (2016). Modeling and Simulation of Electrostatic Adhesion Force in Concentric-Ring Electrode Structures of Multilayer Dielectrics. *The Journal of Adhesion*, 92(4). <https://doi.org/10.1080/00218464.2015.1030014>
- Maurya, S. D., Kurmvanshi, S. K., Mohanty, S., & Nayak, S. K. (2018). A Review on Acrylate-Terminated Urethane Oligomers and Polymers: Synthesis and Applications. *Polymer-Plastics Technology and Engineering*, 57(7). <https://doi.org/10.1080/03602559.2017.1332764>
- Melcher, J. R. (1981). Electromagnetic Force, Force Densities and Stress Tensor, Continuum electromechanics (pp. 7). Cambridge, MA: MIT press.
- Microrobot Inspectors, Electroadhesive wall Climbing Robots and more, 2009 [https://www.nasa.gov/pdf/626527main\\_3B-5\\_Pelrine.pdf](https://www.nasa.gov/pdf/626527main_3B-5_Pelrine.pdf) (Accessed November 2021)
- Monkman, G. J. (1992). Compliant robotic devices, and electroadhesion. *Robotica*, 10(2), 183-185. [doi:10.1017/S0263574700007608](https://doi.org/10.1017/S0263574700007608)
- Monkman, G. (2003). Electroadhesive microgrippers. *Industrial Robot: An International Journal*, 30(4). <https://doi.org/10.1108/01439910310479595>
- Monkman, G.J. (1997). An Analysis of Astrictive Prehension. *The International Journal of Robotics Research*, 16(1). <https://doi.org/10.1177/027836499701600101>
- Monkman, Gareth J., Hesse, S., Steinmann, R., & Schunk, H. (2006). *Robot Grippers*. Wiley. <https://doi.org/10.1002/9783527610280>
- Monkman, G. J., Taylor, P. M., & Farnworth, G. J. (1989). Principles of electroadhesion in clothing robotics. *International Journal of Clothing Science and Technology*. <https://www-emerald-com.hallam.idm.oclc.org/insight/content/doi/10.1108/eb002951/full/html>
- Nalwa, H. S. Handbook of Low and High Dielectric Constant Materials and Their

Applications, 1999. Two-volume Set.

- Nassr, A. A., Ahmed, W. H., & El-Dakhakhni, W. W. (2008). Coplanar capacitance sensors for detecting water intrusion in composite structures. *Measurement Science and Technology*, 19(7). <https://doi.org/10.1088/0957-0233/19/7/075702>
- Onal, E. (2018). Breakdown Mechanism of Different Sulphur Hexafluoride Gas Mixtures. *Advances in Materials Science and Engineering*, 2018. <https://doi.org/10.1155/2018/3206132>
- Othman, K. I., Hassan, A. A., Abdelal, O. A. A., Elshazly, E. S., Ali, E. -S., El-Raghy, S. M., & El-Houte, S. (2014). Formation Mechanism of Barium Titanate by Solid-State Reactions. *International Journal of Scientific & Engineering Research*, 5(7). Retrieved from <http://www.ijser.org>
- Pal, L., & Paul Fleming, D. D. (2006). *The Hilltop Review: A Journal of Western Michigan Graduate Research* (Vol. 2). Retrieved from <https://scholarworks.wmich.edu/hilltopreview/vol2/iss1/9><http://www.wmich.edu/gac/hilltop>
- Paunovic, V., Mitic, V. V., Prijic, Z., & Zivkovic, L. (2014). Microstructure and dielectric properties of Dy/Mn doped BaTiO<sub>3</sub> ceramics. *Ceramics International*, 40(3). <https://doi.org/10.1016/j.ceramint.2013.08.092>
- Paunovic, Vesna, Mitic, V., Marjanovic, M., & Kocic, L. (2016). Dielectric properties of La/Mn codoped barium titanate ceramics. *Facta Universitatis - Series: Electronics and Energetics*, 29(2). <https://doi.org/10.2298/FUEE1602285P>
- Paunovic, Vesna, Zivkovic, L., & Mitic, V. (2010). Influence of rare-earth additives (La, Sm and Dy) on the microstructure and dielectric properties of doped BaTiO<sub>3</sub> ceramics. *Science of Sintering*, 42(1). <https://doi.org/10.2298/SOS1001069P>
- Persson, B. N. J., & Guo, J. (2019). Electroadhesion for soft adhesive pads and robotics: theory and numerical results. *Soft Matter*, 15(40), 8032–8039. <https://doi.org/10.1039/C9SM01560D>

Photoinitiator TPO absorption spectrum

[https://www.igmresins.com/en/product/omnirad\\_tpo](https://www.igmresins.com/en/product/omnirad_tpo)

(Accessed November 2021)

Photoinitiator TPO-L absorption spectrum

[https://www.igmresins.com/en/product/omnirad\\_tpo\\_1](https://www.igmresins.com/en/product/omnirad_tpo_1)

(Accessed November 2021)

Photoinitiator 1173 absorption spectrum

[https://www.igmresins.com/en/product/omnirad\\_1173](https://www.igmresins.com/en/product/omnirad_1173)

(Accessed November 2021)

[https://www.igmresins.com/en/product/omnirad\\_itx](https://www.igmresins.com/en/product/omnirad_itx)

(Accessed November 2021)

Qi, J. Q., Liu, B. B., Tian, H. Y., Zou, H., Yue, Z. X., & Li, L. T. (2012). Dielectric properties of barium zirconate titanate (BZT) ceramics tailored by different donors for high voltage applications. *Solid State Sciences*, 14(10). <https://doi.org/10.1016/j.solidstatesciences.2012.08.009>

Qin, S., & McTeer, A. (2007). Wafer dependence of Johnsen–Rahbek type electrostatic chuck for semiconductor processes. *Journal of Applied Physics*, 102(6). <https://doi.org/10.1063/1.2778633>

Resistivity of various materials.  
<http://dileepmyphysics.com/resistivity-of-various-materials/>  
(Accessed November 2021)

Ruffatto, D., Shah, J., & Spenko, M. (2014). Increasing the adhesion force of electrostatic adhesives using optimized electrode geometry and a novel manufacturing process. *Journal of Electrostatics*, 72(2). <https://doi.org/10.1016/j.elstat.2014.01.001>

Sanches-Silva, A., Pastorelli, S., Cruz, J. M., Simoneau, C., Castanheira, I., & Paseiro-Losada, P. (2008). Development of an Analytical Method for the Determination of Photoinitiators Used for Food Packaging Materials with Potential to Migrate into Milk. *Journal of Dairy Science*, 91(3), 900–909. <https://doi.org/10.3168/jds.2007-0811>

Sareecha, N., Shah, W. A., Maqsood, A., Anis-ur-Rehman, M., & Latif Mirza, M. (2017). Fabrication and electrical investigations of Pb-doped BaTiO<sub>3</sub> ceramics. *Materials Chemistry and Physics*, 193. <https://doi.org/10.1016/j.matchemphys.2017.01.088>

Segurola, J., Allen, N. S., Edge, M., Parrondo, A., & Roberts, I. (1999). Photocuring activity of several commercial, near UV activated photoinitiators in clear and pigmented systems. *Journal of Coatings Technology*, 71(7), 61–67. <https://doi.org/10.1007/BF02698372>

Shukla, V., Bajpai, M., Singh, D. K., Singh, M., & Shukla, R. (2004). Review of basic chemistry of UV-curing technology. *Pigment & Resin Technology*, 33(5), 272–279. <https://doi.org/10.1108/03699420410560461>

Sun, Z., Li, L., Zheng, H., Yu, S., & Xu, D. (2015). Effects of sintering temperature on the microstructure and dielectric properties of BaZr<sub>0.2</sub>Ti<sub>0.8</sub>O<sub>3</sub> ceramics. *Ceramics International*, 41(9). <https://doi.org/10.1016/j.ceramint.2015.06.035>

Tagantsev, A. K., Sherman, V. O., Astafiev, K. F., Venkatesh, J., & Setter, N. (2003). Ferroelectric Materials for Microwave Tunable Applications. *Journal of Electroceramics*, 11(1/2). <https://doi.org/10.1023/B:JECR.0000015661.81386.e6>

Tajdari, T., bin Rahmat, M. F., & Thuku, I. T. (2012). Sensitivity characteristics of electrostatic sensor using finite element modeling. In *2012 IEEE International*

*Conference on Control System, Computing and Engineering*. IEEE.  
<https://doi.org/10.1109/ICCSCE.2012.6487140>

Tang, Z., Wu, K., Huang, Y., & Li, J. (2017). High Breakdown Field  $\text{CaCu}_3\text{Ti}_4\text{O}_{12}$  Ceramics: Roles of the Secondary Phase and of Sr Doping. *Energies*, 10(7).  
<https://doi.org/10.3390/en10071031>

Tao, Y., Tao, Y., Wang, B., Wang, L., & Tai, Y. (2013). A facile approach to a silver conductive ink with high performance for macroelectronics. *Nanoscale Research Letters*, 8(1). <https://doi.org/10.1186/1556-276X-8-296>

Teng, K. F. (1989). Theory of pseudoplastic screen inks in orifice printing. *IEEE Transactions on Components, Hybrids, and Manufacturing Technology*, 12(2), 254–258. <https://doi.org/10.1109/33.31431>

TMPTA Allnex data sheet

<https://allnex.com/en/product/4eec5188-e95c-4fb9-a2c4-01473b01e30a/tmpta>

(Accessed November 2021)

TMPTA IGM resin data sheet

[https://www.igmresins.com/en/product/photomer\\_4006](https://www.igmresins.com/en/product/photomer_4006)

(Accessed November 2021)

TPGDA Allnex data sheet

<https://allnex.com/en/product/6c601ab9-7135-44d1-b567-50b57e92bcef/tpgda>

(Accessed November 2021)

TPGDA IGM resin data sheet

[https://www.igmresins.com/en/product/photomer\\_4061](https://www.igmresins.com/en/product/photomer_4061)

(Accessed November 2021)

Vold, R. E., Biederman, R., Rossetti Jr., G. A., Sacco Jr., A., Sjodin, T., & Rzhevskii, A. (2001). Hydrothermal synthesis of lead doped barium titanate. *Journal of Materials Science*, 36(8). <https://doi.org/10.1023/A:1017582915853>

WO2004056930A1 Patent Number

<https://patents.google.com/patent/WO2004056930A1/en>

(Accessed June 2022)

Weber, M., & Turro, N. J. (2003). A Novel Approach for Measuring Absolute Rate Constants by Pulsed Electron Spin Resonance: Addition of Phosphinoyl and 2-Hydroxy-2-propyl Radicals to Several Alkenes. *The Journal of Physical Chemistry A*, 107(18), 3326–3334. <https://doi.org/10.1021/jp021790x>

- Wei, X., & Yao, X. (2007). Preparation, structure and dielectric property of barium stannate titanate ceramics. *Materials Science and Engineering: B*, 137(1–3). <https://doi.org/10.1016/j.mseb.2006.11.012>
- Woo, S.-Y., Jeong, D.-H., Seo, K.-B., & Kim, J.-H. (2012). A Study on Dielectric Strength and Insulation Property of SF<sub>6</sub> /N<sub>2</sub> Mixtures for GIS. *Journal of International Council on Electrical Engineering*, 2(1). <https://doi.org/10.5370/JICEE.2012.2.1.104>
- Woo, S. J., & Higuchi, T. (2010). Electric field and force modeling for electrostatic levitation of lossy dielectric plates. *Journal of Applied Physics*, 108(10). <https://doi.org/10.1063/1.3487938>
- Wu, S.-Y., Yang, C., Hsu, W., & Lin, L. (2015). 3D-printed microelectronics for integrated circuitry and passive wireless sensors. *Microsystems & Nanoengineering*, 1(1). <https://doi.org/10.1038/micronano.2015.13>
- Xiao, S., Zhang, X., Tang, J., & Liu, S. (2018). A review on SF<sub>6</sub> substitute gases and research status of CF<sub>3</sub>I gases. *Energy Reports*, 4. <https://doi.org/10.1016/j.egyr.2018.07.006>
- Yang, C.-Y., Stoeckel, M.-A., Ruoko, T.-P., Wu, H.-Y., Liu, X., Kolhe, N. B., ... Fabiano, S. (2021). A high-conductivity n-type polymeric ink for printed electronics. *Nature Communications*, 12(1). <https://doi.org/10.1038/s41467-021-22528-y>
- Yi, Q., Wei, X. F., Huang, B. Q., & Wang, Q. (2013). Effect of Monomer on Performance of UV-LED Inkjet Ink. *Applied Mechanics and Materials*, 469, 68–73. <https://doi.org/10.4028/www.scientific.net/AMM.469.68>
- Yossif, N. A., Kandile, N. G., Abdelaziz, M. A., & Negm, N. A. (2017). Preparation and characterization of polymeric dispersants based on vegetable oils for printing ink application. *Progress in Organic Coatings*, 111, 354–360. <https://doi.org/10.1016/j.porgcoat.2017.06.005>
- Yu, Y., Han, D., Wang, Y., Wang, F., Chen, X., Lyu, P., ... Li, Y. (2019). The simulation and application of three-dimensional electrostatic weighting field in MRPC detector. *Journal of Instrumentation*, 14(07). <https://doi.org/10.1088/1748-0221/14/07/P07020>
- Zhang, Q., Zhai, J., Shen, B., Zhang, H., & Yao, X. (2013). Grain size effects on dielectric properties of barium strontium titanate composite ceramics. *Materials Research Bulletin*, 48(3). <https://doi.org/10.1016/j.materresbull.2012.11.085>
- Zhang, Y., Zhu, P., Li, G., Zhao, T., Fu, X., Sun, R., ... Wong, C. (2014). Facile Preparation of Monodisperse, Impurity-Free, and Antioxidation Copper Nanoparticles on a Large Scale for Application in Conductive Ink. *ACS Applied Materials & Interfaces*, 6(1). <https://doi.org/10.1021/am404620y>

# Appendix A

## The ATI force sensor reproducibility test

A series of tests was carried out to check reproducibility and liner behaviour of the force sensor in the range of loads that was generated by EA devices.

### Reproducibility test procedure

First a number of M5 nuts ( $\sim 1$  gr), M6 nuts ( $\sim 2$  gr) and M10 nuts ( $\sim 10$  gr) were weighted out by a three precision scale, then each nut was put on (forward mode) the pad holder mounted on the sensor and also was taken (backward mode) in the same consequence.

Table A-1. weight of nuts

No	M5	M6	M10
1	0.987	2.05	10.325
2	0.989	2.059	10.511
3	1.002	2.071	10.532
4	1.015	2.042	10.426
5	0.999	2.048	10.641
6	1.005	2.064	10.418
7	0.988	2.044	10.344
8	1		10.611
9	1.018		10.456
10	0.982		10.355

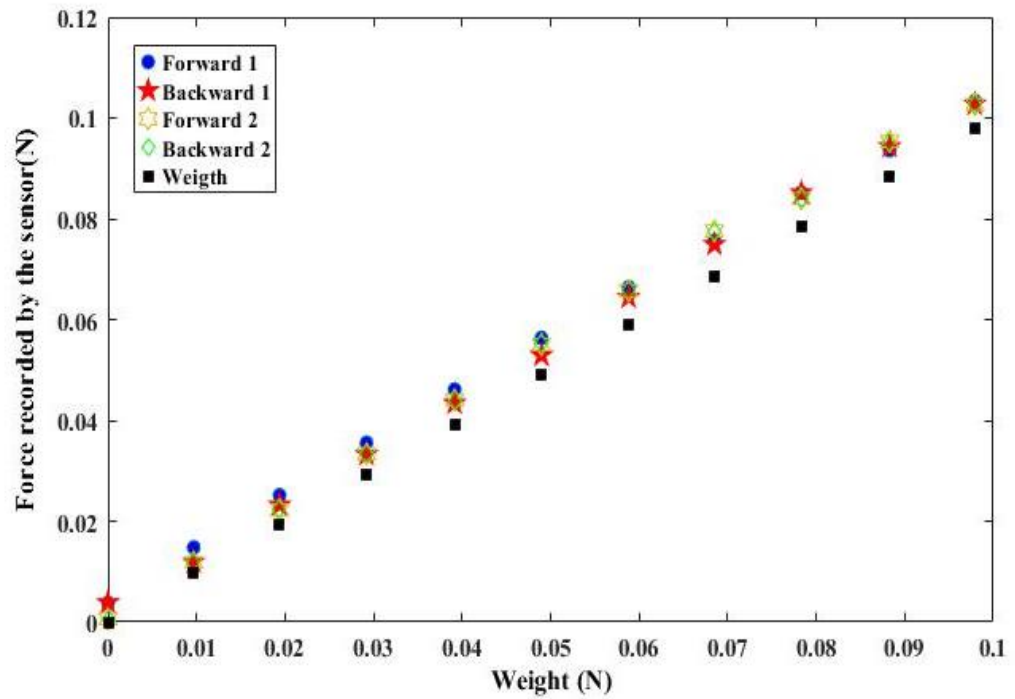


Figure A-1. Calibration test of the force sensor between 0 and 0.1 N

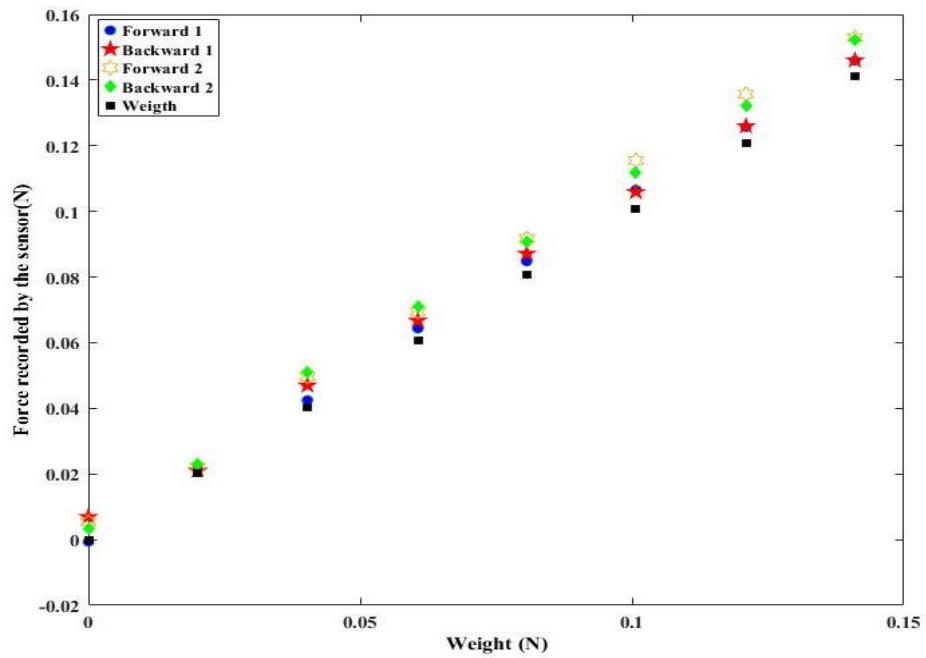


Figure A-2. Calibration test of the force sensor between 0 and 0.15 N

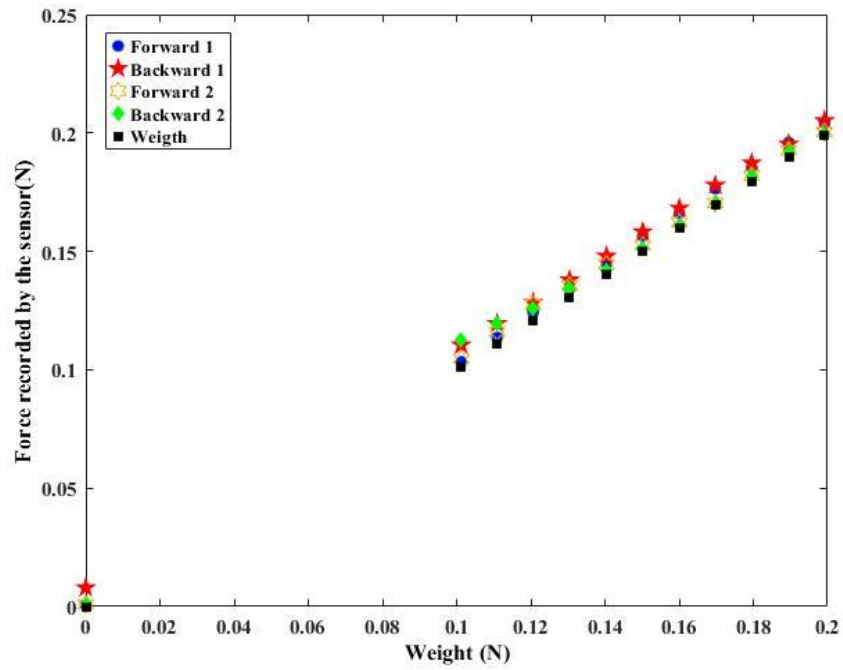


Figure A-3. Calibration test of the force sensor between 0.1 and 0.2 N

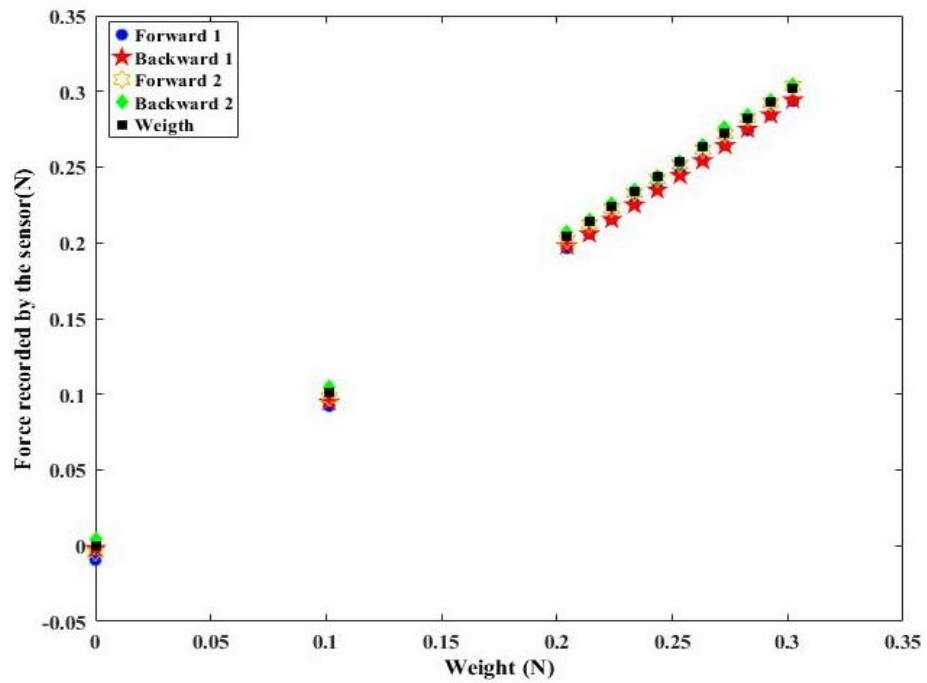


Figure A-4. Calibration test of the force sensor between 0.2 and 0.35 N



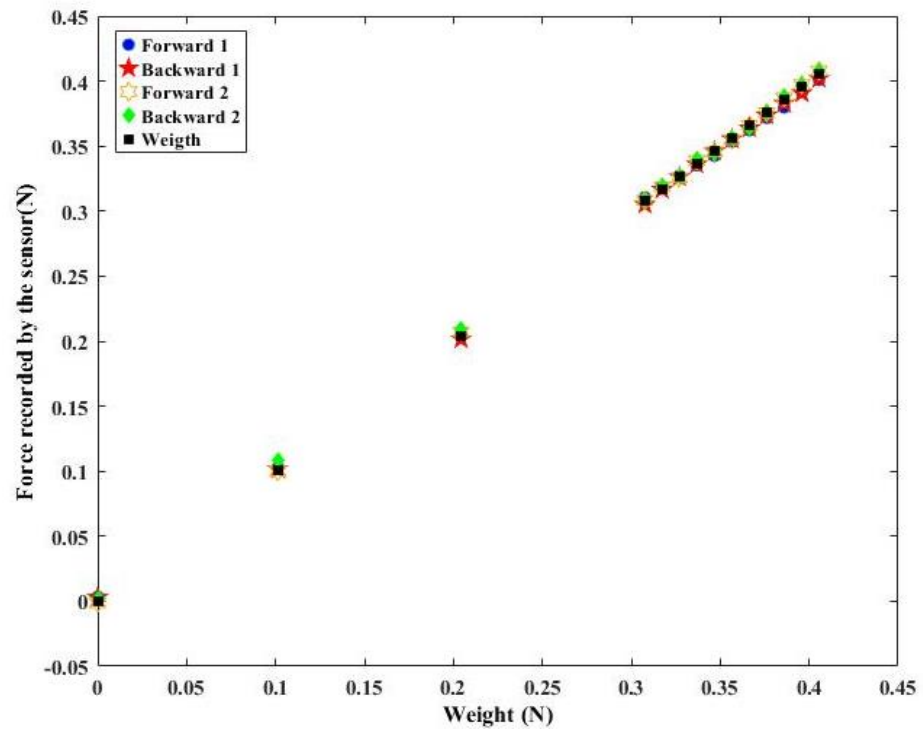


Figure A-5. Calibration test of the force sensor between 0.3 and 0.45 N

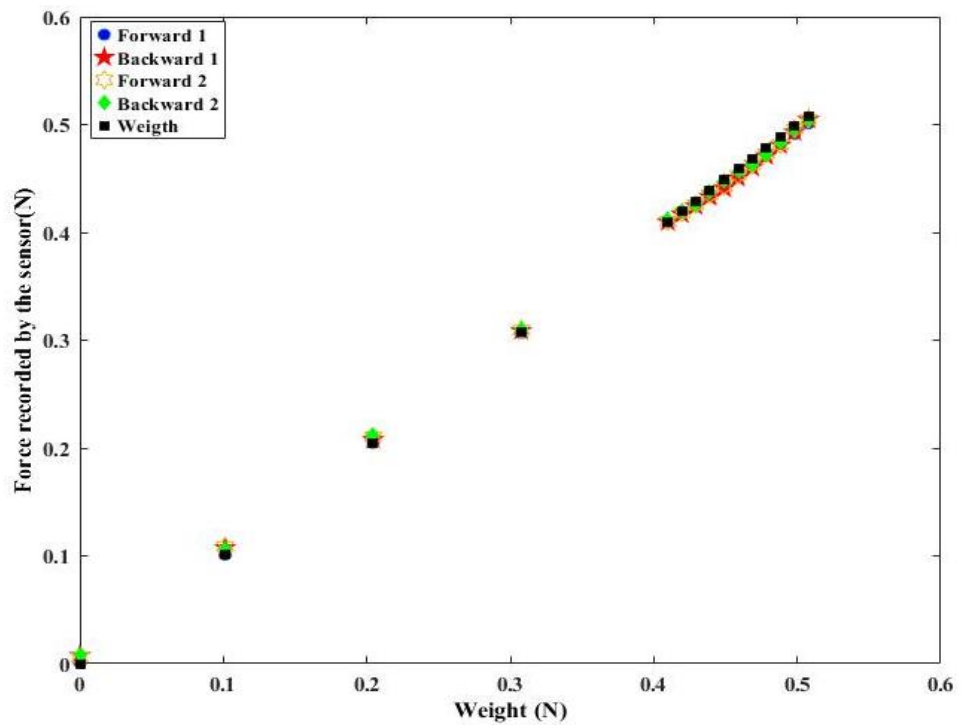


Figure A-6. Calibration test of the force sensor between 0.4 and 0.6 N

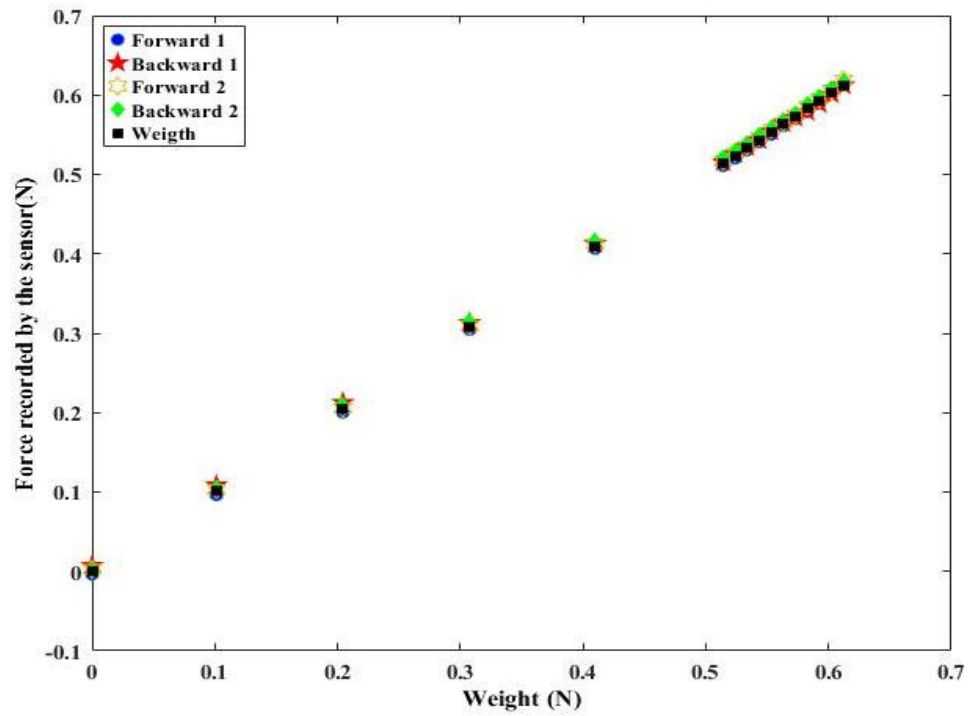


Figure A-7. Calibration test of the force sensor between 0.5 and 0.7 N

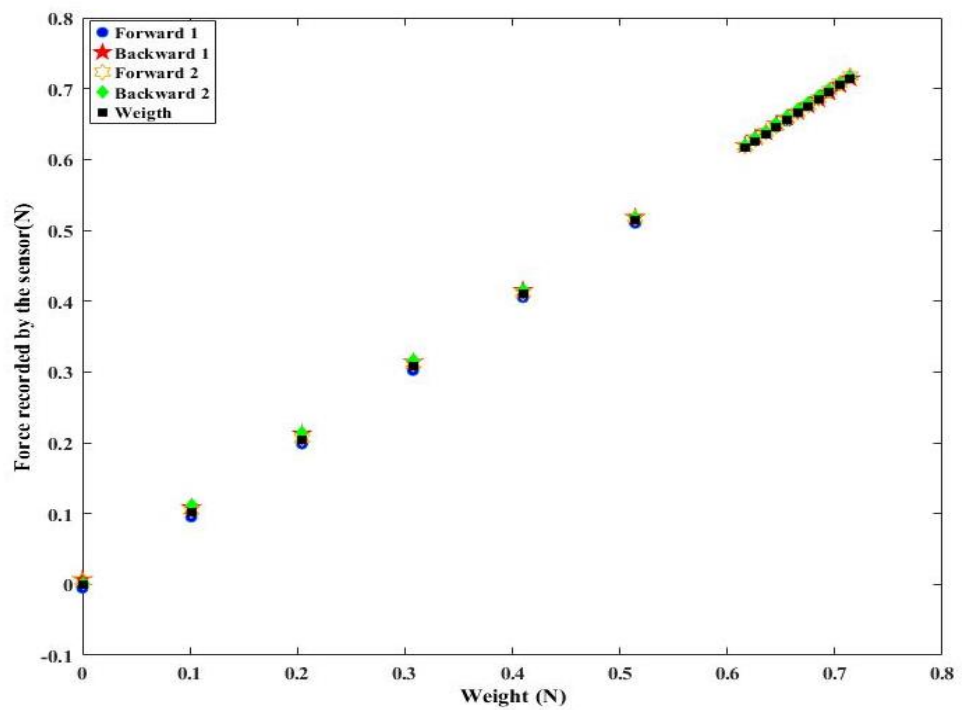


Figure A-8. Calibration test of the force sensor between 0.6 and 0.8 N

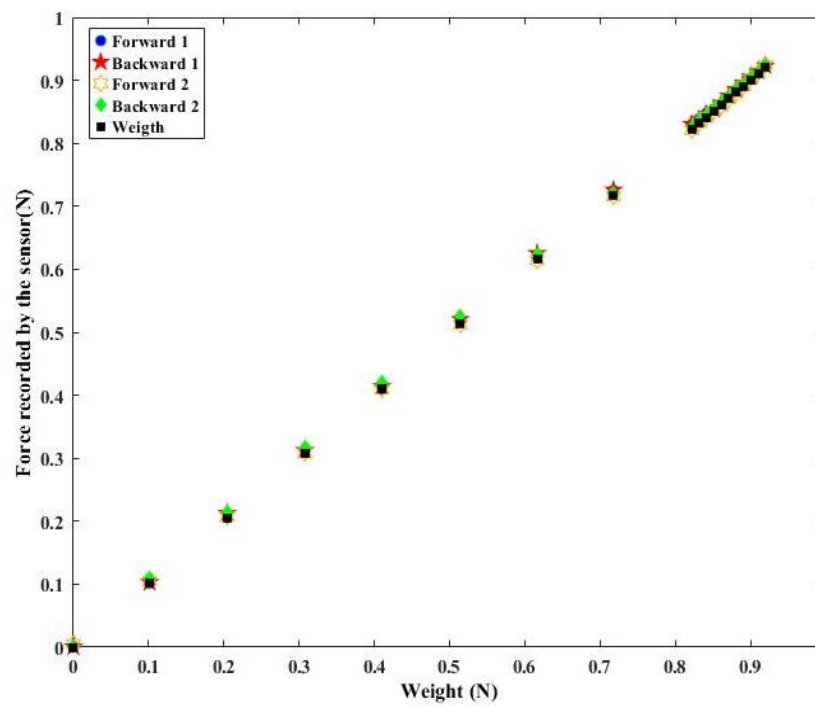


Figure A-10. Calibration test of the force sensor between 0.8 and 1 N

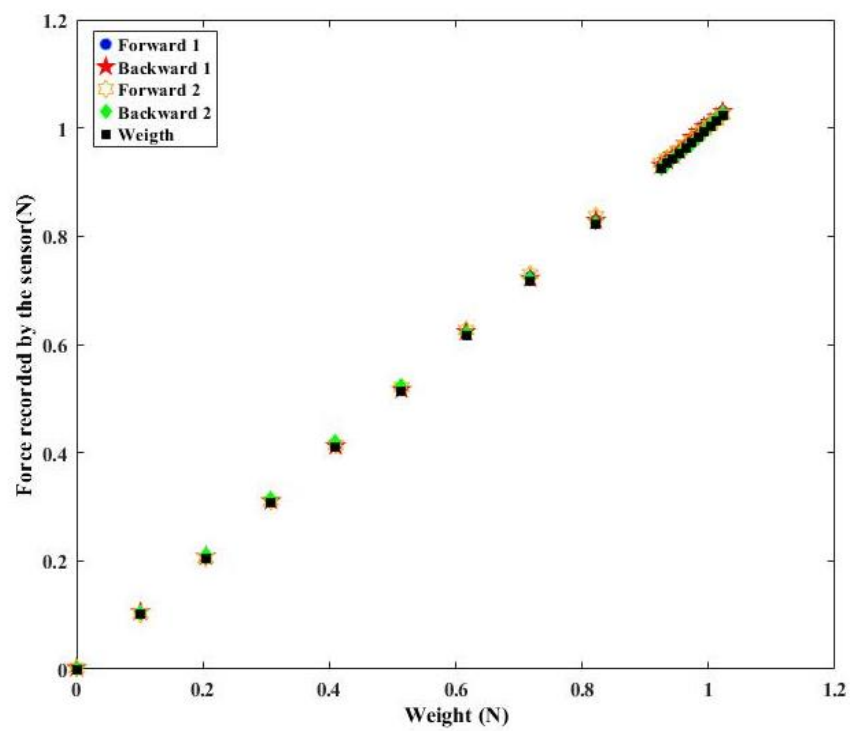


Figure A-11. Calibration test of the force sensor between 0.9 and 1.1 N

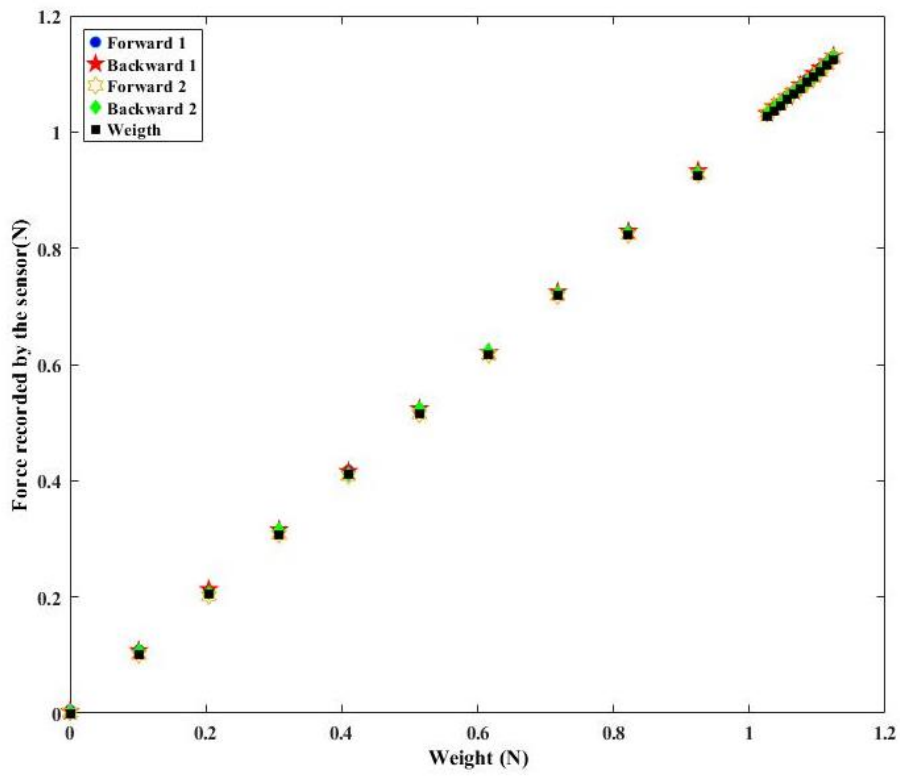


Figure A-12. Calibration test of the force sensor between 1 and 1.2 N

## Appendix B

MATLAB optimiser function: Fmincon

```
function [X,FVAL,EXITFLAG,OUTPUT,LAMBDA,GRAD,HESSIAN] =  
fmincon(FUN,X,A,B,Aeq,Beq,LB,UB,NONLCON,options,varargin)
```

```
defaultopt = struct( ...  
    'Algorithm','interior-point', ...  
    'AlwaysHonorConstraints','bounds', ...  
    'DerivativeCheck','off', ...  
    'Diagnostics','off', ...  
    'DiffMaxChange',Inf, ...  
    'DiffMinChange',0, ...  
    'Display','final', ...  
    'FinDiffRelStep',[], ...  
    'FinDiffType','forward', ...  
    'ProblemdefOptions', struct, ...  
    'FunValCheck','off', ...  
    'GradConstr','off', ...  
    'GradObj','off', ...  
    'HessFcn',[], ...  
    'Hessian',[], ...  
    'HessMult',[], ...  
    'HessPattern','sparse(ones(numberOfVariables))', ...  
    'InitBarrierParam',0.1, ...  
    'InitTrustRegionRadius','sqrt(numberOfVariables)', ...  
    'MaxFunEvals',[], ...  
    'MaxIter',[], ...  
    'MaxPCGIter',[], ...  
    'MaxProjCGIter','2*(numberOfVariables-numberOfEqualities)', ...  
  
    'MaxSQPIter','10*max(numberOfVariables,numberOfInequalities+numberOfBou  
nds)', ...  
    'ObjectiveLimit',-1e20, ...  
    'OutputFcn',[], ...  
    'PlotFcns',[], ...  
    'PrecondBandWidth',0, ...  
    'RelLineSrchBnd',[], ...  
    'RelLineSrchBndDuration',1, ...  
    'ScaleProblem','none', ...  
    'SubproblemAlgorithm','ldl-factorization', ...
```

```

'TolCon',1e-6, ...
'TolConSQP',1e-6, ...
'TolFun',1e-6, ...
'TolFunValue',1e-6, ...
'TolPCG',0.1, ...
'TolProjCG',1e-2, ...
'TolProjCGAbs',1e-10, ...
'TolX',[], ...
'TypicalX','ones(numberOfVariables,1)', ...
'UseParallel',false ...
);

% If just 'defaults' passed in, return the default options in X
if nargin==1 && narginout <= 1 && strcmpi(FUN,'defaults')
    X = defaultopt;
    return
end

if nargin < 10
    options = [];
    if nargin < 9
        NONLCON = [];
        if nargin < 8
            UB = [];
            if nargin < 7
                LB = [];
                if nargin < 6
                    Beq = [];
                    if nargin < 5
                        Aeq = [];
                        if nargin < 4
                            B = [];
                            if nargin < 3
                                A = [];
                            end
                        end
                    end
                end
            end
        end
    end
end

end
end
end
end
end
end
end

if nargin == 1
    if isa(FUN,'struct')
        [FUN,X,A,B,Aeq,Beq,LB,UB,NONLCON,options] =
separateOptimStruct(FUN);
    else % Single input and non-structure.
        error(message('optimlib:fmincon:InputArg'));
    end
end
end

```

```

% No options passed. Set options directly to defaultopt after
allDefaultOpts = isempty(options);

% Prepare the options for the solver
options = prepareOptionsForSolver(options, 'fmincon');

% Check for non-double inputs
msg = isoptimargdbl('FMINCON',{ 'X0','A','B','Aeq','Beq','LB','UB'}, ...
    X, A, B, Aeq, Beq, LB, UB);
if ~isempty(msg)
    error('optimlib:fmincon:NonDoubleInput',msg);
end

% Check for complex X0
if ~isreal(X)
    error('optimlib:fmincon:ComplexX0', ...
        getString(message('optimlib:commonMsgs:ComplexX0','Fmincon')));
end

% Set options to default if no options were passed.
if allDefaultOpts
    % Options are all default
    options = defaultopt;
end

if nargin > 4
    computeLambda = true;
else
    computeLambda = false;
end

activeSet = 'active-set';
sqp = 'sqp';
trustRegionReflective = 'trust-region-reflective';
interiorPoint = 'interior-point';
sqpLegacy = 'sqp-legacy';

sizes.xShape = size(X);
XOUT = X(:);
sizes.nVar = length(XOUT);
% Check for empty X
if sizes.nVar == 0
    error(message('optimlib:fmincon:EmptyX'));
end

display = optimget(options,'Display',defaultopt,'fast',allDefaultOpts);
flags.detailedExitMsg = contains(display,'detailed');
switch display
    case {'off','none'}
        verbosity = 0;

```

```

    case {'notify','notify-detailed'}
        verbosity = 1;
    case {'final','final-detailed'}
        verbosity = 2;
    case {'iter','iter-detailed'}
        verbosity = 3;
    case 'testing'
        verbosity = 4;
    otherwise
        verbosity = 2;
end

% Set linear constraint right hand sides to column vectors
% (in particular, if empty, they will be made the correct
% size, 0-by-1)
B = B(:);
Beq = Beq(:);

% Check for consistency of linear constraints, before evaluating
% (potentially expensive) user functions

% Set empty linear constraint matrices to the correct size, 0-by-n
if isempty(Aeq)
    Aeq = reshape(Aeq,0,sizes.nVar);
end
if isempty(A)
    A = reshape(A,0,sizes.nVar);
end

[lin_eq,Aeqcol] = size(Aeq);
[lin_ineq,Acol] = size(A);
% These sizes checks assume that empty matrices have already been made the
% correct size
if Aeqcol ~= sizes.nVar
    error(message('optimlib:fmincon:WrongNumberOfColumnsInAeq', sizes.nVar))
end
if lin_eq ~= length(Beq)
    error(message('optimlib:fmincon:AeqAndBeqInconsistent'))
end
if Acol ~= sizes.nVar
    error(message('optimlib:fmincon:WrongNumberOfColumnsInA', sizes.nVar))
end
if lin_ineq ~= length(B)
    error(message('optimlib:fmincon:AeqAndBinInconsistent'))
end
% End of linear constraint consistency check

Algorithm = optimget(options,'Algorithm',defaultopt,'fast',allDefaultOpts);

% Option needed for processing initial guess

```



```

AlwaysHonorConstraints =
optimget(options,'AlwaysHonorConstraints',defaultopt,'fast',allDefaultOpts);

% Determine algorithm user chose via options. (We need this now
% to set OUTPUT.algorithm in case of early termination due to
% inconsistent bounds.)
if ~any(strcmpi(Algorithm,{activeSet,sqp,trustRegionReflective,interiorPoint,
sqpLegacy}))
    error(message('optimlib:fmincon:InvalidAlgorithm'));
end
OUTPUT.algorithm = Algorithm;

[XOUT,l,u,msg] = checkbounds(XOUT,LB,UB,sizes.nVar);
if ~isempty(msg)
    EXITFLAG = -2;
    [FVAL,LAMBDA,GRAD,HESSIAN] = deal([]);

    OUTPUT.iterations = 0;
    OUTPUT.funcCount = 0;
    OUTPUT.stepsize = [];
    if strcmpi(OUTPUT.algorithm,activeSet) || strcmpi(OUTPUT.algorithm,sqp)||
strcmpi(OUTPUT.algorithm,sqpLegacy)
        OUTPUT.lssteplength = [];
    else % trust-region-reflective, interior-point
        OUTPUT.cgiterations = [];
    end
    if strcmpi(OUTPUT.algorithm,interiorPoint) ||
strcmpi(OUTPUT.algorithm,activeSet) || ...
strcmpi(OUTPUT.algorithm,sqp) || strcmpi(OUTPUT.algorithm,sqpLegacy)
        OUTPUT.constrviolation = [];
    end
    OUTPUT.firstorderopt = [];
    OUTPUT.message = msg;

    X(:) = XOUT;
    if verbosity > 0
        disp(msg)
    end
    return
end

% Get logical list of finite lower and upper bounds
finDiffFlags.hasLBs = isfinite(l);
finDiffFlags.hasUBs = isfinite(u);

lFinite = l(finDiffFlags.hasLBs);
uFinite = u(finDiffFlags.hasUBs);

% Create structure of flags and initial values, initialize merit function
% type and the original shape of X.
flags.meritFunction = 0;

```

```

initVals.xOrigShape = X;

diagnostics =
strcmpi(optimget(options, 'Diagnostics', defaultopt, 'fast', allDefaultOpts), 'on');
funValCheck =
strcmpi(optimget(options, 'FunValCheck', defaultopt, 'fast', allDefaultOpts), 'on');
derivativeCheck =
strcmpi(optimget(options, 'DerivativeCheck', defaultopt, 'fast', allDefaultOpts), 'on');

% Gather options needed for finitedifferences
% Write checked DiffMaxChange, DiffMinChage, FinDiffType, FinDiffRelStep,
% GradObj and GradConstr options back into struct for later use
options.DiffMinChange =
optimget(options, 'DiffMinChange', defaultopt, 'fast', allDefaultOpts);
options.DiffMaxChange =
optimget(options, 'DiffMaxChange', defaultopt, 'fast', allDefaultOpts);
if options.DiffMinChange >= options.DiffMaxChange
    error(message('optimlib:fmincon:DiffChangesInconsistent', sprintf( '%0.5g',
options.DiffMinChange ), sprintf( '%0.5g', options.DiffMaxChange )))
end
% Read in and error check option TypicalX
[typicalx, ME] =
getNumericOrStringFieldValue('TypicalX', 'ones(numberOfVariables,1)', ...
ones(sizes.nVar,1), 'a numeric value', options, defaultopt);
if ~isempty(ME)
    throw(ME)
end
checkoptionsize('TypicalX', size(typicalx), sizes.nVar);
options.TypicalX = typicalx;
options.FinDiffType =
optimget(options, 'FinDiffType', defaultopt, 'fast', allDefaultOpts);
options = validateFinDiffRelStep(sizes.nVar, options, defaultopt);
options.GradObj = optimget(options, 'GradObj', defaultopt, 'fast', allDefaultOpts);
options.GradConstr =
optimget(options, 'GradConstr', defaultopt, 'fast', allDefaultOpts);

flags.grad = strcmpi(options.GradObj, 'on');

% Notice that defaultopt.Hessian = [], so the variable "hessian" can be empty
hessian = optimget(options, 'Hessian', defaultopt, 'fast', allDefaultOpts);
% If calling trust-region-reflective with an unavailable Hessian option value,
% issue informative error message
if strcmpi(OUTPUT.algorithm, trustRegionReflective) && ...
    ~( isempty(hessian) || strcmpi(hessian, 'on') || strcmpi(hessian, 'user-supplied') ||
...
    strcmpi(hessian, 'off') || strcmpi(hessian, 'fin-diff-grads') )
    error(message('optimlib:fmincon:BadTRReflectHessianValue'))
end

if ~iscell(hessian) && ( strcmpi(hessian, 'user-supplied') || strcmpi(hessian, 'on') )
    flags.hess = true;

```

```

else
    flags.hess = false;
end

if isempty(NONLCON)
    flags.constr = false;
else
    flags.constr = true;
end

% Process objective function
if ~isempty(FUN) % will detect empty string, empty matrix, empty cell array
    % constrflag in optimfcnchk set to false because we're checking the objective,
    not constraint
    funfcn =
optimfcnchk(FUN, 'fmincon', length(varargin), funValCheck, flags.grad, flags.hess, false, Algorithm);
else
    error(message('optimlib:fmincon:InvalidFUN'));
end

% Process constraint function
if flags.constr % NONLCON is non-empty
    flags.gradconst = strcmpi(options.GradConstr, 'on');
    % hessflag in optimfcnchk set to false because hessian is never returned by
    nonlinear constraint
    % function
    %
    % constrflag in optimfcnchk set to true because we're checking the constraints
    confcn =
optimfcnchk(NONLCON, 'fmincon', length(varargin), funValCheck, flags.gradconst, false, true);
else
    flags.gradconst = false;
    confcn = {'', '', '', ''};
end

[rowAeq, colAeq] = size(Aeq);

if strcmpi(OUTPUT.algorithm, activeSet) || strcmpi(OUTPUT.algorithm, sqp) ||
strcmpi(OUTPUT.algorithm, sqpLegacy)
    % See if linear constraints are sparse and if user passed in Hessian
    if issparse(Aeq) || issparse(A)
        warning(message('optimlib:fmincon:ConvertingToFull', Algorithm))
    end
    if flags.hess % conflicting options
        flags.hess = false;
        warning(message('optimlib:fmincon:HessianIgnoredForAlg', Algorithm));
        if strcmpi(funfcn{1}, 'fungradhess')
            funfcn{1} = 'fungrad';
        elseif strcmpi(funfcn{1}, 'fun_then_grad_then_hess')

```

```

        funfcn{1}='fun_then_grad';
    end
end
elseif strcmpi(OUTPUT.algorithm,trustRegionReflective)
    % Look at constraint type and supplied derivatives, and determine if
    % trust-region-reflective can solve problem
    isBoundedNLP = isempty(NONLCON) && isempty(A) && isempty(Aeq); %
    problem has only bounds and no other constraints
    isLinEqNLP = isempty(NONLCON) && isempty(A) && isempty(lFinite) ...
        && isempty(uFinite) && colAeq > rowAeq;
    if isBoundedNLP && flags.grad
        % if only l and u then call sfminbx
    elseif isLinEqNLP && flags.grad
        % if only Aeq beq and Aeq has more columns than rows, then call sfminle
    else
        linkToDoc = addLink('Choosing the Algorithm', 'optim', 'helptargets.map', ...
            'choose_algorithm', false);
        if ~isBoundedNLP && ~isLinEqNLP
            error(message('optimlib:fmincon:ConstrTRR', linkToDoc))
        else
            % The user has a problem that satisfies the TRR constraint
            % restrictions but they haven't supplied gradients.
            error(message('optimlib:fmincon:GradOffTRR', linkToDoc))
        end
    end
end
end

% Process initial point
shiftedX0 = false; % boolean that indicates if initial point was shifted
if any(strcmpi(OUTPUT.algorithm,{activeSet,sqp,sqpLegacy}))
    if strcmpi(OUTPUT.algorithm,sqpLegacy)
        % Classify variables: finite lower bounds, finite upper bounds
        xIndices = classifyBoundsOnVars(l,u,sizes.nVar,false);
    end

    % Check that initial point strictly satisfies the bounds on the variables.
    violatedLowerBnds_idx = XOUT(finDiffFlags.hasLBs) < l(finDiffFlags.hasLBs);
    violatedUpperBnds_idx = XOUT(finDiffFlags.hasUBs) > u(finDiffFlags.hasUBs);
    if any(violatedLowerBnds_idx) || any(violatedUpperBnds_idx)
        finiteLbIdx = find(finDiffFlags.hasLBs);
        finiteUbIdx = find(finDiffFlags.hasUBs);
        XOUT(finiteLbIdx(violatedLowerBnds_idx)) =
            l(finiteLbIdx(violatedLowerBnds_idx));
        XOUT(finiteUbIdx(violatedUpperBnds_idx)) =
            u(finiteUbIdx(violatedUpperBnds_idx));
        X(:) = XOUT;
        shiftedX0 = true;
    end
elseif strcmpi(OUTPUT.algorithm,trustRegionReflective)
    %
    % If components of initial x not within bounds, set those components

```

```

% of initial point to a "box-centered" point
%
if isempty(Aeq)
    arg = (u >= 1e10); arg2 = (l <= -1e10);
    u(arg) = inf;
    l(arg2) = -inf;
    xinitOutOfBounds_idx = XOUT < l | XOUT > u;
    if any(xinitOutOfBounds_idx)
        shiftedX0 = true;
        XOUT = startx(u,l,XOUT,xinitOutOfBounds_idx);
        X(:) = XOUT;
    end
else
    % Phase-1 for fminle nearest feas. pt. to XOUT. Don't print a
    % message for this change in X0 for fminle.
    XOUT = feasibl(Aeq,Beq,XOUT);
    X(:) = XOUT;
end

elseif strcmpi(OUTPUT.algorithm,interiorPoint)
    % Variables: fixed, finite lower bounds, finite upper bounds
    xIndices = classifyBoundsOnVars(l,u,sizes.nVar,true);

    % If honor bounds mode, then check that initial point strictly satisfies the
    % simple inequality bounds on the variables and exactly satisfies fixed variable
    % bounds.
    if strcmpi(AlwaysHonorConstraints,'bounds') ||
    strcmpi(AlwaysHonorConstraints,'bounds-ineqs')
        violatedFixedBnds_idx = XOUT(xIndices.fixed) ~= l(xIndices.fixed);
        violatedLowerBnds_idx = XOUT(xIndices.finiteLb) <= l(xIndices.finiteLb);
        violatedUpperBnds_idx = XOUT(xIndices.finiteUb) >= u(xIndices.finiteUb);
        if any(violatedLowerBnds_idx) || any(violatedUpperBnds_idx) ||
        any(violatedFixedBnds_idx)
            XOUT = shiftInitPtToInterior(sizes.nVar,XOUT,l,u,Inf);
            X(:) = XOUT;
            shiftedX0 = true;
        end
    end
end

% Display that x0 was shifted in order to honor bounds
if shiftedX0
    if verbosity >= 3
        if strcmpi(OUTPUT.algorithm,interiorPoint)
            fprintf(getString(message('optimlib:fmincon:ShiftX0StrictInterior')));
            fprintf('\n');
        else
            fprintf(getString(message('optimlib:fmincon:ShiftX0ToBnds')));
            fprintf('\n');
        end
    end
end

```

```

end

% Evaluate function
initVals.g = zeros(sizes.nVar,1);
HESSIAN = [];

switch funfcn{1}
case 'fun'
    try
        initVals.f = feval(funfcn{3},X,varargin{:});
    catch userFcn_ME
        optim_ME = MException('optimlib:fmincon:ObjectiveError', ...
            getString(message('optimlib:fmincon:ObjectiveError')));
        userFcn_ME = addCause(userFcn_ME,optim_ME);
        rethrow(userFcn_ME)
    end
case 'fungrad'
    try
        [initVals.f,initVals.g] = feval(funfcn{3},X,varargin{:});
    catch userFcn_ME
        optim_ME = MException('optimlib:fmincon:ObjectiveError', ...
            getString(message('optimlib:fmincon:ObjectiveError')));
        userFcn_ME = addCause(userFcn_ME,optim_ME);
        rethrow(userFcn_ME)
    end
case 'fungradhess'
    try
        [initVals.f,initVals.g,HESSIAN] = feval(funfcn{3},X,varargin{:});
    catch userFcn_ME
        optim_ME = MException('optimlib:fmincon:ObjectiveError', ...
            getString(message('optimlib:fmincon:ObjectiveError')));
        userFcn_ME = addCause(userFcn_ME,optim_ME);
        rethrow(userFcn_ME)
    end
case 'fun_then_grad'
    try
        initVals.f = feval(funfcn{3},X,varargin{:});
    catch userFcn_ME
        optim_ME = MException('optimlib:fmincon:ObjectiveError', ...
            getString(message('optimlib:fmincon:ObjectiveError')));
        userFcn_ME = addCause(userFcn_ME,optim_ME);
        rethrow(userFcn_ME)
    end
    try
        initVals.g = feval(funfcn{4},X,varargin{:});
    catch userFcn_ME
        optim_ME = MException('optimlib:fmincon:GradientError', ...
            getString(message('optimlib:fmincon:GradientError')));
        userFcn_ME = addCause(userFcn_ME,optim_ME);
        rethrow(userFcn_ME)
    end
end

```

```

case 'fun_then_grad_then_hess'
    try
        initVals.f = feval(funfcn{3},X,varargin{:});
    catch userFcn_ME
        optim_ME = MException('optimlib:fmincon:ObjectiveError', ...
            getString(message('optimlib:fmincon:ObjectiveError')));
        userFcn_ME = addCause(userFcn_ME,optim_ME);
        rethrow(userFcn_ME)
    end
    try
        initVals.g = feval(funfcn{4},X,varargin{:});
    catch userFcn_ME
        optim_ME = MException('optimlib:fmincon:GradientError', ...
            getString(message('optimlib:fmincon:GradientError')));
        userFcn_ME = addCause(userFcn_ME,optim_ME);
        rethrow(userFcn_ME)
    end
    try
        HESSIAN = feval(funfcn{5},X,varargin{:});
    catch userFcn_ME
        optim_ME = MException('optimlib:fmincon:HessianError', ...
            getString(message('optimlib:fmincon:HessianError')));
        userFcn_ME = addCause(userFcn_ME,optim_ME);
        rethrow(userFcn_ME)
    end
otherwise
    error(message('optimlib:fmincon:UndefinedCallType'));
end

% Check that the objective value is a scalar
if numel(initVals.f) ~= 1
    error(message('optimlib:fmincon:NonScalarObj'))
end

% Check that the objective gradient is the right size
initVals.g = initVals.g(:);
if numel(initVals.g) ~= sizes.nVar
    error('optimlib:fmincon:InvalidSizeOfGradient', ...

getString(message('optimlib:commonMsgs:InvalidSizeOfGradient',sizes.nVar)));
end

% Evaluate constraints
switch confcn{1}
case 'fun'
    try
        [ctmp,ceqtmp] = feval(confcn{3},X,varargin{:});
    catch userFcn_ME
        if strcmpi('MATLAB:maxlhs',userFcn_ME.identifier)
            error(message('optimlib:fmincon:InvalidHandleNonlcon'))
        else

```

```

        optim_ME = MException('optimlib:fmincon:NonlconError', ...
            getString(message('optimlib:fmincon:NonlconError')));
        userFcn_ME = addCause(userFcn_ME,optim_ME);
        rethrow(userFcn_ME)
    end
end
initVals.ncineq = ctmp(:);
initVals.nceq = ceqtmp(:);
initVals.gnc = zeros(sizes.nVar,length(initVals.ncineq));
initVals.gnceq = zeros(sizes.nVar,length(initVals.nceq));
case 'fungrad'
try
    [ctmp,ceqtmp,initVals.gnc,initVals.gnceq] = feval(confcn{3},X,varargin{:});
catch userFcn_ME
    optim_ME = MException('optimlib:fmincon:NonlconError', ...
        getString(message('optimlib:fmincon:NonlconError')));
    userFcn_ME = addCause(userFcn_ME,optim_ME);
    rethrow(userFcn_ME)
end
initVals.ncineq = ctmp(:);
initVals.nceq = ceqtmp(:);
case 'fun_then_grad'
try
    [ctmp,ceqtmp] = feval(confcn{3},X,varargin{:});
catch userFcn_ME
    optim_ME = MException('optimlib:fmincon:NonlconError', ...
        getString(message('optimlib:fmincon:NonlconError')));
    userFcn_ME = addCause(userFcn_ME,optim_ME);
    rethrow(userFcn_ME)
end
initVals.ncineq = ctmp(:);
initVals.nceq = ceqtmp(:);
try
    [initVals.gnc,initVals.gnceq] = feval(confcn{4},X,varargin{:});
catch userFcn_ME
    optim_ME = MException('optimlib:fmincon:NonlconFunOrGradError', ...
        getString(message('optimlib:fmincon:NonlconFunOrGradError')));
    userFcn_ME = addCause(userFcn_ME,optim_ME);
    rethrow(userFcn_ME)
end
case ''
    % No nonlinear constraints. Reshaping of empty quantities is done later
    % in this file, where both cases, (i) no nonlinear constraints and (ii)
    % nonlinear constraints that have one type missing (equalities or
    % inequalities), are handled in one place
    initVals.ncineq = [];
    initVals.nceq = [];
    initVals.gnc = [];
    initVals.gnceq = [];
otherwise
    error(message('optimlib:fmincon:UndefinedCallType'));

```



```

end

% Check for non-double data typed values returned by user functions
if ~isempty( isoptimargdbl('FMINCON', {'f','g','H','c','ceq','gc','gceq'}, ...
    initVals.f, initVals.g, HESSIAN, initVals.ncineq, initVals.nceq, initVals.gnc,
    initVals.gnceq) )

error('optimlib:fmincon:NonDoubleFunVal',getString(message('optimlib:common
Msgs:NonDoubleFunVal','FMINCON')));
end

sizes.mNonlinEq = length(initVals.nceq);
sizes.mNonlinIneq = length(initVals.ncineq);

% Make sure empty constraint and their derivatives have correct sizes (not 0-by-
0):
if isempty(initVals.ncineq)
    initVals.ncineq = reshape(initVals.ncineq,0,1);
end
if isempty(initVals.nceq)
    initVals.nceq = reshape(initVals.nceq,0,1);
end
if isempty(initVals.gnc)
    initVals.gnc = reshape(initVals.gnc,sizes.nVar,0);
end
if isempty(initVals.gnceq)
    initVals.gnceq = reshape(initVals.gnceq,sizes.nVar,0);
end
[cgrow,cgcol] = size(initVals.gnc);
[ceqgrow,ceqgcol] = size(initVals.gnceq);

if cgrow ~= sizes.nVar || cgcol ~= sizes.mNonlinIneq
    error(message('optimlib:fmincon:WrongSizeGradNonlinIneq', sizes.nVar,
    sizes.mNonlinIneq))
end
if ceqgrow ~= sizes.nVar || ceqgcol ~= sizes.mNonlinEq
    error(message('optimlib:fmincon:WrongSizeGradNonlinEq', sizes.nVar,
    sizes.mNonlinEq))
end

if diagnostics
    % Do diagnostics on information so far
    diagnose('fmincon',OUTPUT,flags.grad,flags.hess,flags.constr,flags.gradconst,...
        XOUT,sizes.mNonlinEq,sizes.mNonlinIneq,lin_eq,lin_ineq,l,u,funfcn,confcn);
end

% Create default structure of flags for finitedifferences:
% This structure will (temporarily) ignore some of the features that are
% algorithm-specific (e.g. scaling and fault-tolerance) and can be turned
% on later for the main algorithm.
finDiffFlags.fwdFinDiff = strcmpi(options.FinDiffType,'forward');

```

```

finDiffFlags.scaleObjConstr = false; % No scaling for now
finDiffFlags.chkFunEval = false; % No fault-tolerance yet
finDiffFlags.chkComplexObj = false; % No need to check for complex values
finDiffFlags.isGrad = true; % Scalar objective

% For parallel finite difference (if needed) we need to send the function
% handles now to the workers. This avoids sending the function handles in
% every iteration of the solver. The output from 'setOptimFcnHandleOnWorkers'
% is a onCleanup object that will perform cleanup task on the workers.
UseParallel = optimget(options,'UseParallel',defaultopt,'fast',allDefaultOpts);
ProblemdefOptions = optimget(options,
'ProblemdefOptions',defaultopt,'fast',allDefaultOpts);
FromSolve = false;
if ~isempty(ProblemdefOptions) && isfield(ProblemdefOptions, 'FromSolve')
    FromSolve = ProblemdefOptions.FromSolve;
end
cleanupObj =
setOptimFcnHandleOnWorkers(UseParallel,funfcn,confcn,FromSolve);

% Check derivatives
if derivativeCheck && ... % User wants to check derivatives...
    (flags.grad || ... % of either objective or ...
    flags.gradconst && sizes.mNonlinEq+sizes.mNonlinIneq > 0) % nonlinear
constraint function.
    validateFirstDerivatives(funfcn,confcn,X, ...
    l,u,options,finDiffFlags,sizes,varargin{:});
end

% Flag to determine whether to look up the exit msg.
flags.makeExitMsg = logical(verbosity) || nargout > 3;

% call algorithm
if strcmpi(OUTPUT.algorithm,activeSet) % active-set
    defaultopt.MaxIter = 400; defaultopt.MaxFunEvals = '100*numberofvariables';
    defaultopt.TolX = 1e-6;
    defaultopt.Hessian = 'off';
    problemInfo = []; % No problem related data
    [X,FVAL,LAMBDA,EXITFLAG,OUTPUT,GRAD,HESSIAN]=...
    nlconst(funfcn,X,l,u,full(A),B,full(Aeq),Beq,confcn,options,defaultopt, ...
    finDiffFlags,verbosity,flags,initVals,problemInfo,varargin{:});
elseif strcmpi(OUTPUT.algorithm,trustRegionReflective) % trust-region-reflective
    if (strcmpi(funfcn{1}, 'fun_then_grad_then_hess') || strcmpi(funfcn{1},
'fungradhess'))
        Hstr = [];
    elseif (strcmpi(funfcn{1}, 'fun_then_grad') || strcmpi(funfcn{1}, 'fungrad'))
        n = length(XOUT);
        Hstr = optimget(options,'HessPattern',defaultopt,'fast',allDefaultOpts);
        if ischar(Hstr)
            if strcmpi(Hstr,'sparse(ones(numberofvariables))')
                Hstr = sparse(ones(n));
            end
        end
    end
end

```

```

        else
            error(message('optimlib:fmincon:InvalidHessPattern'))
        end
    end
    checkoptionsize('HessPattern', size(Hstr), n);
end

defaultopt.MaxIter = 400; defaultopt.MaxFunEvals = '100*numberOfvariables';
defaultopt.TolX = 1e-6;
defaultopt.Hessian = 'off';
% Trust-region-reflective algorithm does not compute constraint
% violation as it progresses. If the user requests the output structure,
% we need to calculate the constraint violation at the returned
% solution.
if nargout > 3
    computeConstrViolForOutput = true;
else
    computeConstrViolForOutput = false;
end

if isempty(Aeq)
    defaultopt.MaxPCGIter = 'max(1,floor(numberOfVariables/2))';
    [X,FVAL,LAMBDA,EXITFLAG,OUTPUT,GRAD,HESSIAN] = ...

sfminbx(funfcn,X,l,u,verbosity,options,defaultopt,computeLambda,initVals.f,initV
als.g, ...

HESSIAN,Hstr,flags.detailedExitMsg,computeConstrViolForOutput,flags.makeEx
itMsg,varargin{:});
else
    defaultopt.MaxPCGIter = [];
    [X,FVAL,LAMBDA,EXITFLAG,OUTPUT,GRAD,HESSIAN] = ...

sfminle(funfcn,X,sparse(Aeq),Beq,verbosity,options,defaultopt,computeLambda,in
itVals.f, ...

initVals.g,HESSIAN,Hstr,flags.detailedExitMsg,computeConstrViolForOutput,fla
gs.makeExitMsg,varargin{:});
end
elseif strcmpi(OUTPUT.algorithm,'interior-point')
    defaultopt.MaxIter = 1000; defaultopt.MaxFunEvals = 3000; defaultopt.TolX =
1e-10;
    defaultopt.Hessian = 'bfgs';
    mEq = lin_eq + sizes.mNonlinEq + nnz(xIndices.fixed); % number of equalities
    % Interior-point-specific options. Default values for lbfgs memory is 10, and
    % ldl pivot threshold is 0.01
    options = getIpOptions(options,sizes.nVar,mEq,flags.constr,defaultopt,10,0.01);

    [X,FVAL,EXITFLAG,OUTPUT,LAMBDA,GRAD,HESSIAN] =
barrier(funfcn,X,A,B,Aeq,Beq,l,u,confcn,options.HessFcn, ...

```

```

initVals.f,initVals.g,initVals.ncineq,initVals.nceq,initVals.gnc,initVals.gnceq,HESS
IAN, ...
    xIndices,options,finDiffFlags,flags.makeExitMsg,varargin{:});
elseif strcmpi(OUTPUT.algorithm,sqp)
    defaultopt.MaxIter = 400; defaultopt.MaxFunEvals = '100*numberofvariables';
    defaultopt.TolX = 1e-6; defaultopt.Hessian = 'bfgs';
    % Validate options used by sqp
    options = getSQPOptions(options,defaultopt,sizes.nVar);
    % Call algorithm
    [X,FVAL,EXITFLAG,OUTPUT,LAMBDA,GRAD,HESSIAN] =
sqpInterface(funfcn,X,full(A),full(B),full(Aeq),full(Beq), ...

full(l),full(u),confcn,initVals.f,full(initVals.g),full(initVals.ncineq),full(initVals.nceq
), ...

full(initVals.gnc),full(initVals.gnceq),sizes,options,finDiffFlags,verbosity,flags.mak
eExitMsg,varargin{:});
else % sqpLegacy
    defaultopt.MaxIter = 400; defaultopt.MaxFunEvals = '100*numberofvariables';
    defaultopt.TolX = 1e-6; defaultopt.Hessian = 'bfgs';
    % Validate options used by sqp
    options = getSQPOptions(options,defaultopt,sizes.nVar);
    % Call algorithm
    [X,FVAL,EXITFLAG,OUTPUT,LAMBDA,GRAD,HESSIAN] =
sqpLineSearch(funfcn,X,full(A),full(B),full(Aeq),full(Beq), ...

full(l),full(u),confcn,initVals.f,full(initVals.g),full(initVals.ncineq),full(initVals.nceq
), ...
    full(initVals.gnc),full(initVals.gnceq),xIndices,options,finDiffFlags, ...
    verbosity,flags.detailedExitMsg,flags.makeExitMsg,varargin{:});
end

delete(cleanupObj);

```

## Appendix C

FTIR test on the ink before and after curing process

The FTIR analysis can reveal whether the ink fully cured after being exposed by UV light. The result (see figure) indicates that the ink was fully cured, and therefore the peaks between 1500 and 1600  $\text{cm}^{-1}$  disappeared.

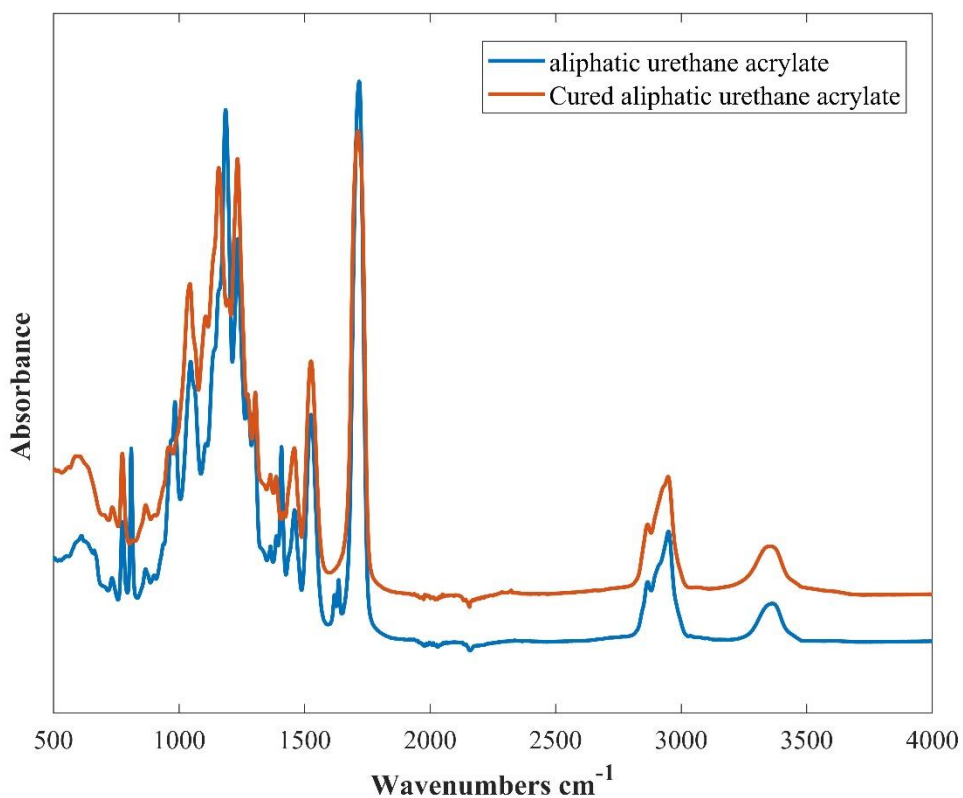


Figure C-1. FTIR analysis of ink and cured ink

